

LIGHT CURVES OF HYDROGEN-POOR SUPERLUMINOUS SUPERNOVAE FROM THE PALOMAR TRANSIENT FACTORY

ANNALISA DE CIA^{1,2}, A. GAL-YAM¹, A. RUBIN¹, G. LELOUDAS^{1,3}, P. VREESWIJK¹, D. A. PERLEY⁴, R. QUIMBY^{5,6}, LIN YAN^{7,8}, M. SULLIVAN⁹, A. FLÖRS², J. SOLLERMAN¹⁰, D. BERSIER⁴, S. B. CENKO^{11,12}, M. GAL-YAM¹³, K. MAGUIRE¹⁴, E. O. OFEK¹, S. PRENTICE⁴, S. SCHULZE¹, J. SPYROMILIO², S. VALENTI²⁰, I. ARCAVI^{15,16}, A. CORSI¹⁷, D. A. HOWELL^{15,16}, P. MAZZALI^{4,18}, M. M. KASLIWAL¹⁹, F. TADDIA¹⁰, O. YARON¹

¹ Department of Particle Physics and Astrophysics, Weizmann Institute of Science, Rehovot 76100, Israel

² European Southern Observatory, Karl-Schwarzschild Str. 2, D-85748 Garching bei München, Germany, adecia@eso.org

³ Dark Cosmology Centre, Niels Bohr Institute, University of Copenhagen, Juliane Maries Vej 30, DK-2100, Copenhagen, Denmark

⁴ Astrophysics Research Institute, Liverpool John Moores University, Liverpool Science Park, 146 Brownlow Hill, Liverpool L35RF, UK

⁵ Department of Astronomy, San Diego State University, San Diego, CA 92182, USA

⁶ Kavli IPMU (WPI), UTIAS, The University of Tokyo, Kashiwa, Chiba 277-8583, Japan

⁷ MS100-22, Caltech/IPAC, California Institute of Technology, Pasadena, CA 91125, USA

⁸ Caltech Optical Observatories, California Institute of Technology, Pasadena, CA 91125, USA

⁹ Department of Physics and Astronomy, University of Southampton, Southampton SO17 1BJ, UK

¹⁰ The Oskar Klein Centre, Department of Astronomy, Stockholm University, AlbaNova, SE-10691, Stockholm, Sweden

¹¹ Astrophysics Science Division, NASA Goddard Space Flight Center, Mail Code 661, Greenbelt, MD 20771, USA

¹² Joint Space-Science Institute, University of Maryland, College Park, MD 20742, USA

¹³ The Schwartz/Reisman Science Education Center, Weizmann Institute of Science, Rehovot, Israel

¹⁴ Astrophysics Research Centre, School of Mathematics and Physics, Queen's University Belfast, Belfast BT7 1NN, UK

¹⁵ Las Cumbres Observatory, 6740 Cortona Dr. Suite 102, Goleta, CA 93117, USA

¹⁶ Department of Physics, University of California, Santa Barbara, CA 93106-9530, USA

¹⁷ Department of Physics and Astronomy, Texas Tech University, Box 1051, Lubbock, TX 79409-1051, USA

¹⁸ Max-Planck-Institut für Astrophysik, Karl-Schwarzschild-Str. 1, D-85748 Garching, Germany

¹⁹ Astronomy Department, California Institute of Technology, Pasadena, CA 91125, USA

²⁰ Department of Physics, University of California, Davis, CA 95616, USA

ABSTRACT

We investigate the light-curve properties of a sample of 26 spectroscopically confirmed hydrogen-poor superluminous supernovae (SLSNe-I) in the Palomar Transient Factory (PTF) survey. These events are brighter than SNe Ib/c and SNe Ic-BL, on average, by about 4 and 2 mag, respectively. The peak absolute magnitudes of SLSNe-I in rest-frame g band span $-22 \lesssim M_g \lesssim -20$ mag, and these peaks are not powered by radioactive ^{56}Ni , unless strong asymmetries are at play. The rise timescales are longer for SLSNe than for normal SNe Ib/c, by roughly 10 days, for events with similar decay times. Thus, SLSNe-I can be considered as a separate population based on photometric properties. After peak, SLSNe-I decay with a wide range of slopes, with no obvious gap between rapidly declining and slowly declining events. The latter events show more irregularities (bumps) in the light curves at all times. At late times, the SLSN-I light curves slow down and cluster around the ^{56}Co radioactive decay rate. Powering the late-time light curves with radioactive decay would require between 1 and 10M_\odot of Ni masses. Alternatively, a simple magnetar model can reasonably fit the majority of SLSNe-I light curves, with four exceptions, and can mimic the radioactive decay of ^{56}Co , up to ~ 400 days from explosion. The resulting spin values do not correlate with the host-galaxy metallicities. Finally, the analysis of our sample cannot strengthen the case for using SLSNe-I for cosmology.

1. INTRODUCTION

Since the advent of wide-field untargeted transient surveys, a class of superluminous supernovae (SLSNe)

that are over 10 times more luminous than regular SNe (see Gal-Yam 2012, for a review), with absolute magnitudes $\lesssim -21$ mag, has emerged. The first few

objects showed a striking diversity, e.g. SN 2005ap (Quimby et al. 2007), SN 2006gy (Ofek et al. 2007; Smith et al. 2007), and SN 2007bi (Gal-Yam et al. 2009), leading to a natural division between H-rich events (SLSNe-II) and H-poor events (SLSNe-I). Most SLSNe-II show narrow lines (SLSN-II_n) and are powered by the interaction of the SN ejecta with the circumstellar medium (CSM; e.g., Chugai & Danziger 1994; Chevalier & Fransson 1994; Chevalier & Irwin 2011; Ofek et al. 2013; Inserra et al. 2018). SLSNe-I are less well-understood, and the physical processes that dominate these explosions are still under debate.

Quimby et al. (2011) inspected the first sample of SLSNe-I, and found that they have UV-bright light curves over extended periods of time. Quimby et al. also showed similarity in their spectral features, and suggested that their progenitors may have initial masses $90 < M < 130 \text{ M}_\odot$, perhaps exploding as core-collapse SNe with massive ejecta interacting with a H-poor CSM. Asymmetry in the ejecta can hide signatures of hydrogen or helium in SLSN-I spectra (Kozyreva & Blinnikov 2015), as well as ionization (Mazzali et al. 2016). Gal-Yam (2012) proposed that a group of slowly declining events (SLSNe-R), similar to SN 2007bi, have late-time light curves that are powered by radioactivity and could be associated with pair-instability SNe (PISN; Barkat et al. 1967; Heger & Woosley 2002; Gal-Yam et al. 2009), but this is widely debated (Dessart et al. 2012; Nicholl et al. 2013). Inserra et al. (2013) showed that the late-time decay of a few SLSNe slows down to a 'tail' that could be explained if the light curves were powered by the spin-down of a newly born magnetar (Kasen & Bildsten 2010). Nicholl et al. (2015a) studied a sample of SLSNe and suggested that the ejecta mass is the main driver of the observed diversity. More recently, Nicholl et al. (2017) fitted a magnetar model to the literature sample of SLSNe-I.

Early-time bumps (pre-peak or double peaks, or excess emission) have been observed in some SLSNe light curves, such as SN 2006oz (Leloudas et al. 2012), LSQ 14bdq (Nicholl et al. 2015b), PTF 12dam and iPTF 13dcc (Vreeswijk et al. 2017), and DES 14X3taz (Smith et al. 2016). These early bumps can be explained by shock-cooling or CSM interaction models (e.g Nakar & Sari 2010; Rabinak & Waxman 2011; Chatzopoulos et al. 2012; Piro 2015). Such early bumps or double-peaked light curves may in fact be common among SLSNe (Nicholl & Smartt 2016). Late-time bumps (postpeak) have also been observed in a few cases, such as for SN 2007bi (Gal-Yam et al. 2009), iPTF 13ehe (Yan et al. 2015), PS1-14bj (Lunnan et al. 2016), and SN 2015bn (Nicholl et al. 2016). Wiggles in the late-time decay have often been observed in a hand-

ful of slowly declining SLSNe by Inserra et al. (2017). Such late-time bumps cannot be explained by magnetar and radioactive decay models. Late-time emergence of hydrogen emission has been detected in a few cases (e.g., iPTF 15esb; Yan et al. 2015, 2017), and in these cases it was explained with substantial mass loss that occurred shortly before the progenitors of the SLSNe exploded (Yan et al. 2015, 2017). Indeed, Liu et al. (2017) showed that the light curves of iPTF 15esb could be explained with a multiple-shell CSM interaction model. The diversity observed so far in H-poor SLSNe seems to indicate that multiple processes may contribute to powering their light curves.

In this paper, we present a sample of 26 SLSNe-I from the Palomar Transient Factory (PTF; Law et al. 2009; Rau et al. 2009) and its successor the intermediate Palomar Transient Factory (iPTF). This is the largest sample of SLSNe-I homogeneously selected from a single survey available so far. Here we characterize and discuss the properties of the light curves of these events, and compare them to a large PTF sample of SNe Ib/c and Ic-BL (with broad lines). We address the question on how luminous SLSNe-I are, and whether they can be considered a separate population based on their light-curve properties. We investigate whether Type SLSNe-R are a separate class of events, and whether we can use SLSNe-I for cosmology. The spectra of (i)PTF SLSNe, and the host galaxies of PTF SLSNe up to 2012 are studied in Quimby et al. (2018) and Perley et al. (2016), respectively.

The paper is organized as follows. In Sect. 2 and 3 we describe the SLSN sample and observations, respectively. We characterize the SN light curves in Sect. 4, discuss our results in Sect. 5, and present our conclusions in Sect. 6. We adopt the cosmological parameters $H_0 = 70 \text{ km s}^{-1} \text{ Mpc}^{-1}$, $\Omega_m = 0.3$, and $\Omega_\Lambda = 0.7$ throughout the paper.

2. THE PTF SAMPLE OF SLSNE

PTF was a wide-field (7.26 deg^2 field of view), non-targeted survey designed to investigate the optical transient and variable sky (Law et al. 2009; Rau et al. 2009), carried out using the refurbished *CFH12k* camera (Rahmer et al. 2008), mounted on the Palomar Observatory 48-inch Samuel Oschin Telescope (P48), in California. The PTF survey is optimized for the discovery of SNe of different types. Since its start in 2009, PTF has discovered and classified over 3000 SNe. The classification and follow-up observations of these SNe are performed through a wide network of telescopes (Gal-Yam et al. 2011), as described below for our sample. The selection of SN candidates for spectroscopic classification within the PTF survey is not free of biases. For example, SLSN searches may have given more

weight to candidates that were brighter than their host galaxies. Nevertheless, PTF has discovered a large number of SLSNe-II as well, which can explode in normal host galaxies (e.g. Perley et al. 2016), reassuring us that such selection biases are not dominant.

The 26 SLSNe discussed in this paper are all the hydrogen-poor SLSNe discovered between 2009 and 2013 by the (i)PTF survey. The sample is shown in Table 1. This significantly increases the sample of about 50 currently known H-poor SLSNe with reported spectral classification in the literature (either published or with spectra reported in Astronomer’s Telegrams; e.g. Nicholl et al. 2015a; Schulze et al. 2018; Lunman et al. 2018), 10 of which have been discovered by PTF and are part of this work as well.

The PTF SLSNe in our sample have been spectroscopically classified as SLSNe-I by Quimby et al. (2018). This sample is thus spectroscopically selected and assumes no luminosity thresholds. The sample of PTF SLSN host galaxies of Perley et al. (2016) is slightly different because that work also applied a luminosity cut, while PTF 12hni and PTF 12gty are presented here for the first time. PTF 12hni is classified as an SLSN-I by Quimby et al. (2018) with some uncertainty, and having possible matches to SN Ia and SN Ic. In addition, three other events are reported as possible SLSNe by Quimby et al. (2018), namely PTF 09q, PTF 10gvb, and PTF 11mnb, but are most likely not SLSNe, and therefore we do not include these in our sample.¹

What makes the PTF sample unique is not only the fact that it is homogeneously selected from a single survey, but also that its average redshift is low ($< z = 0.27$; see Sect. 2.1). A higher- z ($0.3 < z < 1.6$) sample of 17 SLSNe-I from the Pan-STARRS1 Medium Deep Survey (PS1; Kaiser et al. 2010) is presented by Lunman et al. (2018). In addition, the light-curve coverage of the PTF sample often extends to late times, beyond 100 days after the peak for half of the sample. The currently known H-poor SLSNe in the literature typically lack photometry later than 120 days after peak (e.g. Nicholl et al. 2015a). Jerkstrand et al. (2017) and Inserra et al. (2017) have studied a small sample of slow-evolving SLSNe, with data coverage up to 400 days after peak.

As a comparison sample, we also select all Type Ib, Ib/c, Ic, and Ic-BL SNe discovered between 2009 and

¹ For PTF 09q there is a single spectrum available, which is well consistent with an SN Ic, and its host galaxy is a massive galaxy (Quimby et al. 2018). Three spectra are available for PTF 10gvb, but one is mostly featureless and lacks the typical SLSN O II features, and the other two are well-matched with an SN Ic-BL (Quimby et al. 2018). PTF 11mnb is most likely a SN Ic, as studied in detail by Taddia et al. (2018a).

Table 1. The PTF sample of 26 hydrogen-poor SLSNe.

PTF ID	R.A. (hh:mm:ss)	Decl. ($^{\circ} : ' : ''$)	z	Type	A_V^a (mag)
09as	12:59:15.78	+27:16:38.5	0.1864	I	0.02
09atu	16:30:24.55	+23:38:25.0	0.5014	I	0.13
09cnd	16:12:08.94	+51:29:16.2	0.2585	I	0.06
09cwl	14:49:10.08	+29:25:11.4	0.3502	I	0.04
10aagc	09:39:56.93	+21:43:16.9	0.2067	I	0.07
10bfz	12:54:41.27	+15:24:17.0	0.1699	I	0.05
10bjp	10:06:34.30	+67:59:19.0	0.3585	I	0.17
10cwr	11:25:46.67	-08:49:41.2	0.2301	I	0.10
10hgj	16:37:47.04	+06:12:32.3	0.0982	I	0.22
10nmn	15:50:02.79	-07:24:42.1	0.1236	I/R	0.42
10uhf	16:52:46.68	+47:36:22.0	0.2879	I	0.05
10vqv	03:03:06.84	-01:32:34.9	0.4520	I	0.17
10vwg	18:59:32.86	+19:24:25.7	0.1901	I/R	1.41
11dij	13:50:57.77	+26:16:42.8	0.1429	I	0.03
11hrq	00:51:47.22	-26:25:10.0	0.0571	I/R	0.04
11rks	01:39:45.51	+29:55:27.0	0.1924	I	0.11
12dam	14:24:46.20	+46:13:48.3	0.1075	I/R	0.03
12gty	16:01:15.23	+21:23:17.4	0.1768	I	0.18
12hni	22:31:55.86	-06:47:49.0	0.1056	I	0.16
12mxx	22:30:16.68	+27:58:21.9	0.3274	I	0.12
13ajg	16:39:03.95	+37:01:38.4	0.7403	I	0.04
13bdl	12:36:56.14	+13:07:45.5	0.4030	I	0.13
13bjz	10:38:19.83	+24:24:51.0	0.2712	I	0.06
13cjq	00:14:27.18	+24:17:08.8	0.3962	I	0.13
13dcc	02:57:02.50	-00:18:44.0	0.4308	I/R	0.18
13ehe	06:53:21.50	+67:07:56.0	0.3434	I/R	0.14

^aGalactic foreground extinction.

2013 by PTF. These SNe are studied in more detail in Arcavi et al. (2010), Corsi et al. (2016), Prentice et al. (2016), and Taddia et al. (2018b), and will be presented in full in forthcoming publications (Barbarino et al. 2018, in preparation; Fremling et al. 2018, in preparation; Huang et al. 2018, in preparation; Karamehmetoglu et al. 2018, in preparation; Schulze et al. 2018, in preparation).

We derive the rest-frame g -band absolute magnitudes, M_g , from the apparent r magnitudes m_r including the k -correction term as K_{gr} described in Sect. 3.12 and listed in Table C2 ($M_g = m_r - DM(z) - K_{gr}$, where $DM(z)$ is the distance modulus for a given redshift z , and m_r is corrected for foreground Galactic extinction, reported in Table 1). Figure 1 shows the rest-frame M_g light curves of all the 26 SLSNe in our sample.

2.1. The redshift distribution

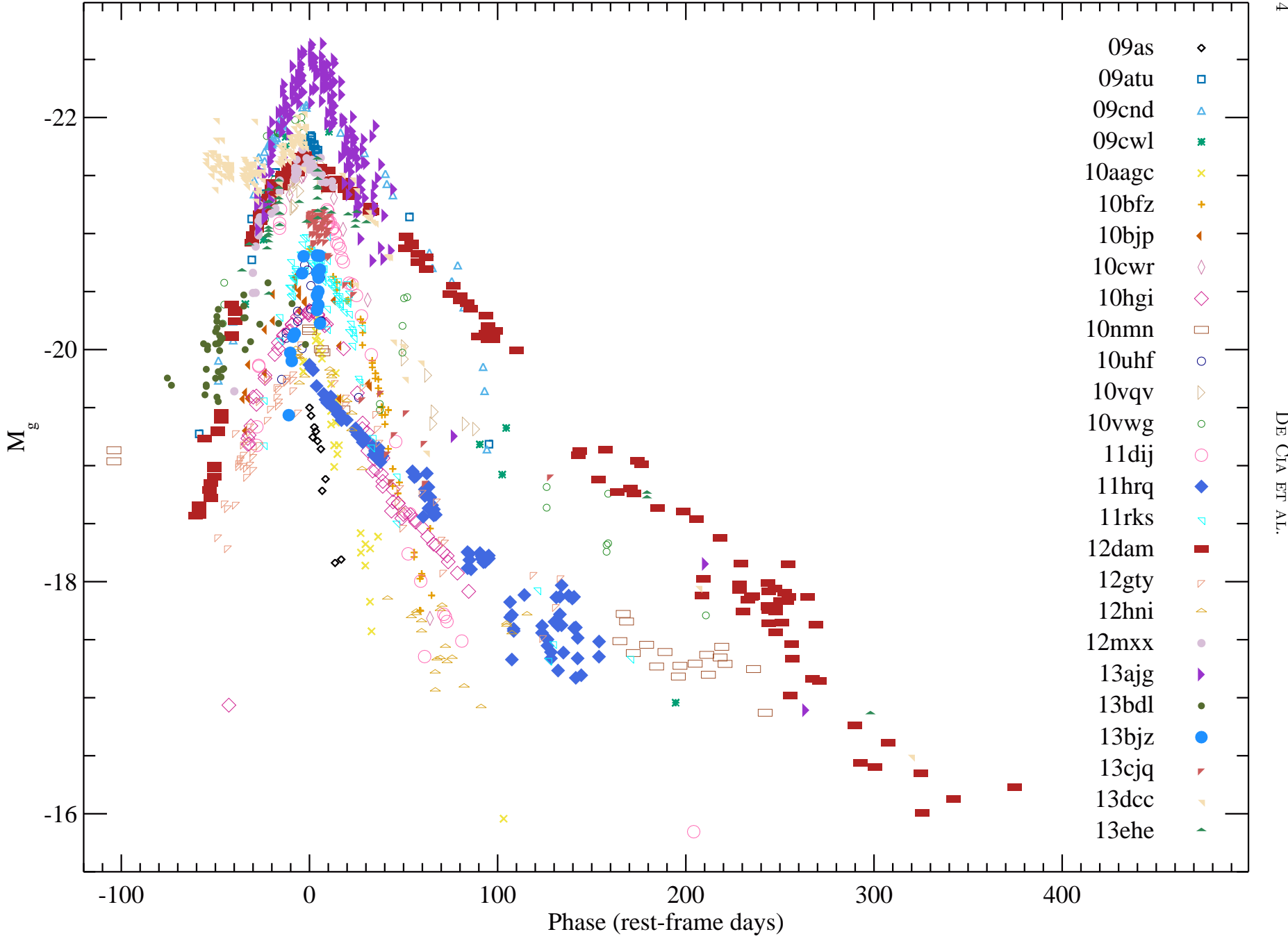


Figure 1. Rest-frame M_g light curves of the 26 H-poor SLSNe in our sample. The error bars are omitted here for readability, but are shown in Figs. B1 to B5.

Although most normal SNe are observed in the nearby universe ($z \lesssim 0.2$), the most luminous ones can be detected out to higher redshift. SNe Type Ia, for instance, are currently discovered out to $z \sim 2$ in deep imaging (Jones et al. 2013). A few SLSNe have been studied out to $z \sim 4$ in the deepest surveys (Cooke et al. 2012), although in limited detail compared to nearby targets. Recently, a small sample of $z \sim 2$ SLSNe has been studied by Moriya et al. (2018) and Curtin et al. (2018). In the future, the James Webb Space Telescope is expected to be able to detect SLSNe out to $z \sim 20$ (Abbott et al. 2017). The PTF survey typically discovers SLSNe below $z \lesssim 1$.

The redshifts in our SLSN sample are all measured spectroscopically and normally measured from narrow Mg II absorption lines in the SN spectra. The typical uncertainties on the redshift estimates are of the order of 0.0005, given the typical resolution of the follow-up spectra (described in Quimby et al. 2018). The redshifts in Table 1 are taken from Quimby et al. (2018) for all events up to 2012, except for PTF 10vvg for which we adopt the slightly more accurate redshift of Perley et al. (2016). We adopt the redshifts of Vreeswijk et al. (2014) for PTF 13ajg and of Yan et al. (2015) for PTF 13ehe. For the other 2013 events, we directly measure the redshifts from the Mg II narrow absorption lines in the spectra. In PTF 13ehe, the most common spectral features are very weak. The redshift measurement is based on a weak O III 5007 emission line, and its uncertainty is of the order of 0.001.

Figure 2 shows the redshift distribution of our sample, where the mean redshift is $\langle z \rangle = 0.27$ with standard deviation $\sigma_z = 0.15$. The volume-weighted mean is $\langle z \rangle = 0.33$.²

The mean redshift of the PTF H-poor SLSN sample presented here is comparable to the "golden" SLSN sample of Nicholl et al. (2015a, $\langle z \rangle = 0.22$, while $\langle z \rangle = 0.63$ for their "silver" sample), and the SLSN host sample of Leloudas et al. (2015, $\langle z \rangle = 0.34$ with a standard deviation of 0.2). On the other hand, SLSNe discovered by PS1 tend to be at higher redshifts, typically $z > 0.5$ (McCrum et al. 2015), and in particular $0.3 < z < 1.6$ (Lunnan et al. 2018).

The drop of the redshift distribution above $z \sim 0.5$ in our sample is an observational selection effect due to the limiting magnitude of the PTF survey ($m_{r,\text{lim}} \sim 20.5$ mag, Cao et al. 2016). This limit hampers further investigations of the evolution of the sample properties

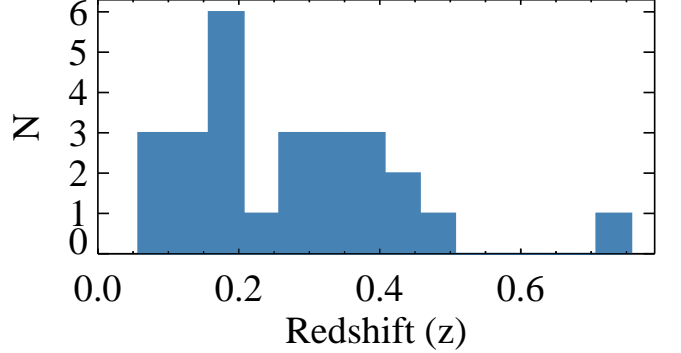


Figure 2. Redshift distribution of the sample of hydrogen-poor SLSNe presented in Table 1.

with redshift.

3. OBSERVATIONS AND DATA PROCESSING

3.1. Palomar P48 discovery and imaging

As part of the standard PTF operations, SN candidates are discovered in P48 images using image subtraction in Mould-R (r) or the Sloan Digital Sky Survey (SDSS, York et al. 2000; SDSS Collaboration et al. 2016) g' filter. The best SN candidates are then classified spectroscopically and followed-up with other telescopes. The raw P48 images are initially processed by the Infrared Processing and Analysis Center (IPAC, Laher et al. 2014). The photometric calibration and system are described in Ofek et al. (2012). Image-subtraction point-spread function (PSF) photometry is performed with a custom routine (a pipeline written by one of us (M.S.) and used extensively in PTF; e.g. Sullivan et al. 2006; Ofek et al. 2014a; Firth et al. 2015; Dimitriadis et al. 2017). This pipeline constructs deep reference images - either before the SN explosion or after the SN has faded - and astrometrically aligns the images using the Automated Astrometry described in Hogg et al. (2008) and the Naval Observatory Mergered Astrometric Dataset (NOMAD, Zacharias et al. 2004). The image PSFs are then matched in order to perform the image subtraction and then to extract the PSF photometry of the SN only (where the contribution of the reference image has been subtracted). The fluxes are calibrated against the SDSS Data Release 10 (Ahn et al. 2014) when available, and otherwise against the photometric catalog of Ofek et al. (2012), and making no assumption on the SLSN colors.

The formal uncertainties derived with the MS pipeline only include statistical uncertainties, but not uncertainties from poor image subtraction or calibration. As a result, the formal uncertainties are slightly underestimated. For example, under excellent data coverage, we can observe a larger scatter than that accounted for by the formal uncertainties. The best example is for

² A Gaussian fit through the redshift distribution data prefers a mean redshift $\langle z \rangle = 0.16$ with a standard deviation $\sigma_z = 0.20$ for a z bin size of 0.05. The mean $\langle z \rangle$ is 0.11 and 0.17 for bin sizes of 0.01 and 0.1, respectively.

iPTF 13ajg, which shows a scatter of ~ 0.5 mag around peak. We quantify the additional source of uncertainty by assuming a $\chi^2_\nu = 1$ for the light-curve fit around the peak of iPTF 13ajg (see Sect. 4.1). The additional required uncertainty is 0.05 mag, which we add to all formal errors derived with the MS pipeline (i.e. for the data taken with the P48, P60, and LT telescopes; see below), to account for poor image subtraction or calibration.

Nondetections, and in particular the last nondetection limits before the SN discoveries, are not included in our analysis. The reason for this is that nondetections are largely dominated by noisy data and are uninformative. In addition, in most cases the SLSNe-I were discovered long after explosions. For the case of PTF 12dam co-adds of the prediscovey nondetections are presented by Vreeswijk et al. (2017). The analysis presented in this paper is independent of the nondetection limits. Thus, we leave the treatment of prediscovey limits, which is beyond the scope of this paper, for future case-by-case studies.

3.2. Palomar P60 imaging

Follow-up imaging was obtained with the Palomar 60-inch telescope (P60; Cenko et al. 2006). The filters employed for our observations are Johnson B (Bessell 1990), Kron R (similar to Cousins R_C , Bessell 1990), Sloan i' and z' (Fukugita et al. 1996), and Gunn g (Thuan & Gunn 1976). The SN photometry is extracted with the same routine described above for the P48 data processing, but calibrated using the AAVSO Photometric All-Sky Survey (APASS; Henden et al. 2009) for the B filter or for fields that are not covered by the SDSS footprint.

3.3. Keck/LRIS imaging

We observed PTF SLSNe at late times using the Low-Resolution Imaging Spectrometer (LRIS) on the Keck I telescope to monitor the late-time evolution of the light curve or to produce a deep reference image (after the SN has faded) for image subtraction or host galaxy study (Perley et al. 2016). Images were processed using standard techniques via the custom pipeline LPIPE³ and co-added using SWarp. Photometry was performed after image subtraction of the reference image (taken from Perley et al. 2016), with the custom-made IRAF routine `mkdifflc` (Gal-Yam et al. 2004, 2008).

3.4. Liverpool Telescope imaging

Follow-up imaging was also obtained with the 2m robotic Liverpool Telescope (LT; Steele et al. 2004) at

the Roque de los Muchachos Observatory on La Palma, Spain, with the RATCAM and IO:O optical imagers in g , r , and i filters (similar to SDSS). The images were processed following Maguire et al. (2014) and using the image-subtraction PSF photometry custom routine described above for the P48 Telescope.

3.5. Las Cumbres Observatory imaging

The LCO (previously known as LCOGT; Brown et al. 2013) data have been reduced using a custom pipeline (Valenti et al. 2016). The pipeline employs standard procedures (PYRAF, DAOPHOT) in a Python framework. Host galaxy flux was removed using image subtraction technique (High Order Transform of PSF ANd Template Subtraction, HOTPANTS⁴). PSF magnitudes were computed on the subtracted images and transformed to the standard SDSS filter system (for gri) via standard star observations taken during clear nights.

3.6. Discovery Channel Telescope imaging

We imaged several of the SLSNe in our sample with the Large Monolithic Imager (LMI) mounted on the 4.3 m Discovery Channel Telescope (DCT) in Happy Jack, AZ. The LMI images were processed using a custom IRAF pipeline for basic detrending (bias subtraction and flat fielding), and individual dithered images were combined using SWarp (Bertin et al. 2002). SN magnitudes were measured using aperture photometry with the inclusion radius matched to the FWHM of the image PSF. Photometric calibration was performed relative to point sources from the SDSS (York et al. 2000; SDSS Collaboration et al. 2016).

No DCT reference images are available for image subtraction, so we account for the contribution of the host galaxies by subtracting the host magnitudes from the observed fluxes, and we include this into the photometric uncertainty budget. The SLSNe iPTF 13dcc and 13ehe were observed with the DCT. The host galaxy of iPTF 13dcc has $B = 26.3 \pm 0.2$ and $i = 25.0 \pm 0.2$ (Perley et al. 2018, in preparation), and we assume $g = 26.3 \pm 0.2$ and $r = 25.0 \pm 0.2$ for the subtraction of the host galaxy contribution to the r -band data point, which is a reasonable assumption given typical host galaxy colors (Perley et al. 2016). The host galaxy of iPTF 13ehe has $B = 25.0 \pm 0.1$ and $R = 24.0 \pm 0.1$. (Perley et al. 2018, in preparation), which we use to subtract the host-galaxy contribution. For both SLSNe, this host-galaxy correction affects significantly (by 0.2 mag) only the last r -band epoch of their light curves. In both cases, the DCT data points are consistent with the photometry from other facilities, including late-time *Hubble Space*

³ www.astro.caltech.edu/~dperley/programs/lpipe.html

⁴ www.astro.washington.edu/users/becker/v2.0/hotpants.html

Telescope (HST) photometry (Sec. 3.9).

3.7. *Swift/UVOT imaging*

A number of supernovae in our sample were observed with the UltraViolet/Optical Telescope (UVOT; Roming et al. 2005) on board the *Swift* Gamma-ray Burst Explorer (Gehrels et al. 2004). Data were processed using the standard UVOT pipeline, and photometry was extracted at the supernova location using a 3'' radius. Photometric calibration was calculated using the zero point measurements from Poole et al. (2008) and Breeveld et al. (2010). The magnitudes reported in Tables D6 to D70 are all on the AB system. No attempt has been made to correct for underlying contributions from the host galaxy emission. At these redshifts, the host galaxy contribution should not significantly affect the observed UV flux in most cases. This may not be true for some cases, in particular for PTF 12dam and its luminous underlying starburst host galaxy (Chen et al. 2015; Thöne et al. 2015; Perley et al. 2016; Cikota et al. 2017). However, even in this case, the host galaxy brightness in the *F225W* filter is 19.94 ± 0.17 (Perley et al. 2016), which is 1–2 mag fainter than the unsubtracted SN photometry (Nicholl et al. 2013; Chen et al. 2015).

3.8. *Palomar P200/Large Format Camera (LFC) imaging*

Follow-up imaging was obtained with the Palomar 200-inch Hale Telescope with the LFC⁵. The data reduction was performed with standard IRAF tasks. The SN magnitudes were derived by extracting aperture photometry at different radii, for the SN images and the reference image, and subtracting the host contribution. For the case of PTF 09cnd, we measure the photometry using both the image-subtraction routine `mkdifflc` and aperture photometry, and take the average between the two results. For the case of PTF 10cwr no reference image is available, so we extract aperture photometry with a 3'' radius and subtract the host magnitude reported by Perley et al. (2016) and include this into the photometric uncertainty budget.

3.9. *HST*

The SLSNe iPTF 13dcc and iPTF 13ehe were observed with the Advanced Camera for Surveys (ACS) in the Wide Field Channel on board the HST, with the *F625W* filter, as part of the GO-13858 program (PI A. De Cia). The data were reduced using the CALACS software, which contains corrections for degradation of the charge transfer efficiency and electronic artifacts

(bias-shift and -striping effects). Cosmic rays were removed using the LA Cosmic routine (van Dokkum 2001). The images were then processed with DrizzlePac 2.0,⁶ with inverse variance map (IVM) weighting and assuming a pixel scale of 0.033'' and a pixel fraction of 0.6.

The SN PSF is resolved from the more extended host galaxies. For iPTF 13dcc, the PSF of the host has an FWHM of 3.2 pixels (0.11''), while field stars have 2.4 pixels (0.08''). iPTF 13ehe is separated from its host galaxy. The SN PSFs were fitted and thus isolated from their host galaxies using a custom IDL routine. The PSF SN photometry was then extracted assuming HST zeropoints and applying a correction for an aperture of 0.5'' radius.

3.10. *Literature data collection*

We complement the photometric dataset of the SLSNe in our sample with the data published in Quimby et al. (2011), Pastorello et al. (2010), Inserra et al. (2013), Nicholl et al. (2013), Chen et al. (2015), and Vreeswijk et al. (2014). The literature photometry is showed in Figs. B1 to B5. The purpose of including the literature data in this paper is to collect the most complete available light curves for the SLSNe in our sample. The *r*-band photometry is used to calculate the rest-frame *g*-band photometry, which is reported in Tables D7 to D71. Because the sources of our observations are already diverse, the inclusion of literature data does not affect significantly the quality of our dataset.

The full light curve of PTF 10nnm will be presented by Yaron et al. (2018, in preparation), including a wider coverage of the SN peak, which is not presented in this paper.

We exclude from the analysis a couple of published photometry datapoints in cases of disagreement with the photometry secured with other (multiple) telescopes, namely for iPTF 13ajg (P60 *R*-band data at MJD 56429 from Vreeswijk et al. 2014, excluded) and for PTF 09cnd (*Wise R*-band data at MJD 55089 from Quimby et al. 2011, excluded). The new measurements supersede the earlier ones.

3.11. *On the diversity of the dataset*

The dataset used in this paper was collected from a diversity of facilities, and the photometry is derived with different pipelines and methods. The quoted uncertainties assess the quality of the photometry for each facility or measurement method. The contribution of the host galaxy light to the SN measured flux is taken into account and reflected in the quoted uncertainties. An

⁵ www.astro.caltech.edu/palomar/about/telescopes/hale.html

⁶ <http://drizzlepac.stsci.edu>

exception to this is for the UV photometry (*Swift*), for which the contribution from the host galaxy is not subtracted, but should be minimal (Sect. 3.7). Often the filter transmission curves of similar filters are different for different facilities or catalogs for calibration, such as r , R , and R_c for example. However, we did not correct for these differences because they depend on the source spectra and their evolution, and these differences are typically very small, normally well below 0.1 mag.

In Figs. B1 to B5, all photometry are shown together. When enough data are available, the photometry from different telescopes can be directly cross-checked, and we do not find evident discrepancies. Further corrections to the photometry, such as foreground extinction and k -corrections, and their uncertainties, are described below.

3.12. Foreground dust extinction and k -corrections

We derive Galactic foreground optical extinction A_V using the maps of Schlafly & Finkbeiner (2011) through the Galactic Dust Reddening and Extinction Service at the NASA/IPAC Infrared Science Archive, assuming a standard extinction law and an extinction to reddening ratio $A_V/E(B-V) = 3.1$.⁷ The mean uncertainty in the Galactic foreground extinction A_V for our sample is of 0.009 mag, and we do not include this uncertainty in the photometric budget. The adopted A_V values are listed in Table 1. We calculate the extinction A_λ at the central wavelength of each filter using the reddening curve of Cardelli et al. (1989) and including the update for the near-UV given by O'Donnell (1994). Both apparent and absolute magnitudes reported in this paper are corrected for Galactic foreground extinction.

Host-galaxy extinction is not considered. SLSN host galaxies tend to be faint and have low metallicity (Neill et al. 2011; Leloudas et al. 2015; Lunman et al. 2015; Perley et al. 2016; Chen et al. 2017; Schulze et al. 2018), and therefore we expect them to have negligible dust extinction in the red bands, with possible regions that may be locally more dusty, affecting mostly the UV (e.g. Cikota et al. 2017). On the other hand, SN Ib/c host galaxies can show significant extinction (mean $< E(B-V) > \sim 0.2$ and < 0.6 mag for $\sim 80\%$ of SNe Type Ic, Ib, and Ic-BL; Taddia et al. 2015; Prentice et al. 2016), but determining it case by case for our comparison sample is often not possible and is beyond the scope of this paper.

We calculate the k -corrections K_{gr} for the SLSN sample from observed PTF r to rest-frame g (SDSS filter system) using spectral series of PTF 12dam and

iPTF 13ajg (Vreeswijk et al. 2014, 2017; Quimby et al. 2018) and following Hogg et al. (2002). Using individual spectra for each SLSNe was not possible here, due to the paucity of sufficient spectral coverage at all epochs for the SLSNe in our sample. The spectral coverage of PTF 12 dam is frequently sampled and spans from -25 to 321 rest-frame days after the peak, while the spectra of iPTF 13ajg are reliable until 60 days after peak. In the overlapping interval, there is good agreement between the k -corrections calculated from the two series of spectra. This indicates some level of similarity between the spectra, which is also confirmed by the spectral analysis of the PTF SLSN-I sample (Quimby et al. 2018). The spectra of the more slowly evolving SLSNe-I change more slowly. However, the k -corrections based on PTF 12dam and iPTF 13ajg are similar, so the differences in k -corrections for faster and slower SLSNe-I should be small. Given this similarity, and due to the general lack of spectral series as complete as those for PTF 12dam, we apply the k -corrections derived from the spectra of PTF 12dam and their evolution to all of the SLSNe in our sample.

The spectra were not warped to match the observed photometry of the individual SLSNe. This could have led to more accurate k -corrections. However, the uncertainty from the fact that we use the spectrum of PTF 12dam as a reference for the k -correction for all individual SLSNe is likely larger than the precision that could be gained by such a procedure. In addition, to make a reliable warping, photometry in at least two bands (and much preferably three) would be necessary, and this was not always available. The spectra of PTF 12dam themselves were carefully flux calibrated. To ensure a smooth evolution of the k -correction with time, we interpolate the individual k -correction values and obtain a smooth k -correction evolution in time for each SLSN, through a third-order polynomial fit of the individual k -correction values.

The residuals from the third-order polynomial fit of the k -correction values with time can be used to estimate the uncertainties on the k -corrections, which are between 0.004 and 0.05 mag in our sample, with an average of 0.02 mag. These values show the scatter around the best-fit k -correction curve. Fitting the k -correction through individual points ensures that potential outliers, e.g. due to inaccurate flux calibration of the reference spectra, become negligible because the fit is driven by the majority of the points. The dominant source of uncertainty on the k -correction is likely the fact that we use the spectrum of PTF 12dam as a reference for the k -correction for all SLSNe, but this cannot be trivially estimated. Using different SLSN spectra as a reference for the k -correction in a different but comparable sample of SLSNe, the uncertainties on the k -corrections are

⁷ The background and further cautionary notes are reported at <http://irsa.ipac.caltech.edu/applications/DUST/docs/background.html>

0.01–0.1 mag (Wiis, private communication, MSc thesis, Table 4.1.1), although these are potentially slightly overestimated because they are derived with linear fits to the k -correction data. We do not include the uncertainties on the k -correction in our photometry uncertainty budget.

Table C2 lists the values of the adopted smooth k -correction at the epochs of the PTF 12dam spectra, applied to the redshifts of the SLSNe of our sample. Our k -correction values are in agreement with those of Nicholl et al. (2015b, $K_{gr} = -0.3$ before peak for LSQ 14bdq at $z = 0.347$). The k -corrections that we apply rely on the assumption that the spectra of our SLSN sample are similar to those of PTF 12dam out to late epochs. At late times, the assumption of similarity among the spectra is less certain. We therefore recommend exercising caution in trusting our k -corrections at late epochs.

For the comparison with the Ib/c sample at maximum light, we calculate the k -correction from the observed r to rest-frame r using the spectrum at the peak of PTF 10tqv and following Hogg et al. (2002). We then derive the rest-frame g by applying a color correction from the observed mean $g - r = 0.36$ mag of a large sample of Type Ib/c SNe of Prentice et al. (2016). Where necessary, we convert $B - V$ measurements from Prentice et al. (2016) at V peak to $g - r$ and adopt the weighted average, and otherwise directly use the observed $g - r$ at the g peak. The standard deviation on the $g - r$ distribution is 0.34 mag (0.25 and 0.23 mag for the $g - r$ and $B - V$ distributions). Since $g - r$ evolves significantly for SNe Ib/c (e.g. Taddia et al. 2015; Prentice et al. 2016), the r to g conversion used here for SNe Ib/c is most reliable around SNe peaks.

4. CHARACTERIZING THE LIGHT CURVES

The light curves of PTF H-poor SLSNe sometimes show complex features, such as bumps/plateau, double peaks, and a change of the decay rate. Besides, the data are often sparse. We use the following independent diagnostics to characterize different properties of the light curves.

1. *SN peak magnitudes* – derived with a second-order polynomial fit to the data around the peak (see Sect. 4.1).
2. *Early- and late-time decay rates* – derived with two independent linear fits to the data at early and late times after peak (see Sect. 4.2).
3. *Rise and fall times by 1 mag*, $t_{\text{rise}}^{\Delta 1\text{mag}}$ and $t_{\text{fall}}^{\Delta 1\text{mag}}$ – the times that the SN takes to rise and fall by 1 mag from the peak (see Sect. 4.4), measured

on light curves which have been smoothed using interpolation (see Sect. 4.3).

4. *Half-flux rise and fall times* $t_{\text{rise},1/2}$, $t_{\text{fall},1/2}$ – the times for the SN fluxes to rise from half-flux to peak, and to fall from peak to half-flux (see Sect. 4.5), measured on light curves that have been smoothed using interpolation (see Sect. 4.3).

The derived quantities are listed in Table A1 and the details for each diagnostic are reported below.

4.1. Peak-magnitude distribution

We calculate the absolute magnitudes using the distance modulus for a given z (e.g. Hogg 1999). At the z considered here (~ 0.3), the difference in distance modulus obtained from different cosmology models is negligible compared to the uncertainties in the observed apparent magnitudes. The redshifts of the SLSNe are derived in most cases to three decimal digits (see Table 1). In fact, here we are interested only in the relative luminosity distances between different SNe, and the relative uncertainties are even smaller. The uncertainties on the absolute magnitudes are therefore largely dominated by the uncertainties on the observed apparent magnitudes, and we do not make any attempt to include uncertainties due to the distance estimate.

We determine the peak times and magnitudes by fitting a second-order polynomial to the rest-frame g -band magnitudes around the maximum brightness, typically between –30 and 30 days around the approximate peak, or adjusting this interval to adapt to the data coverage. The fitted curves and the relevant time intervals are shown in Figures B1 to B5.

Figure 3, top panel, shows the peak-magnitude distribution of H-poor SLSNe (solid blue), Type Ic-BL SNe (shaded yellow), and Type Ib, Ic, and Ib/c SNe (solid orange), all from the PTF survey, for a brightness bin of 0.2 mag. Note that only SNe where the peak could be observed and constrained are included in this plot. When calculating the number of SNe for each brightness bin, it is important to consider the observational biases. Although SLSNe are bright enough to be observed at larger distances, many normal SNe could actually be exploding at those distances, but be too faint to be detected (Malmquist bias). To compare the numbers of SNe in a fair way, it is therefore necessary to normalize the numbers to the same comoving volume. We calculate the volumetric correction V_c for each SN as the ratio between the volume probed by the most luminous SLSN in our sample ($M_{g,\text{max}} = -22.42$ mag at peak) and the volume probed by the individual SN, given the limiting magnitude of the PTF survey of $m_{\text{lim}} = 20.5$ mag (Cao et al. 2016), i.e., the maximum luminosity distance at which each SN would have been observed with this

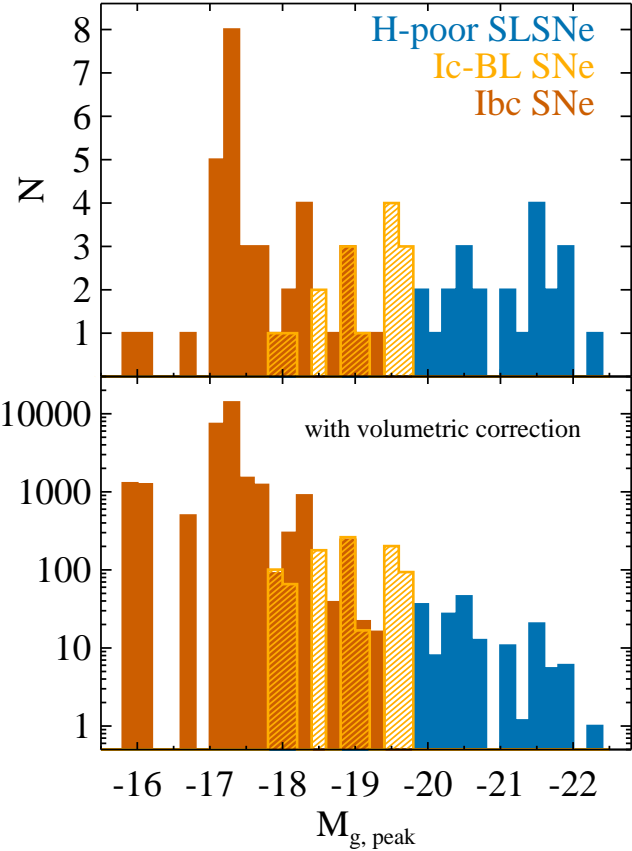


Figure 3. Peak-magnitude distribution of the labelled types of PTF SNe, for rest-frame g absolute magnitudes. The bottom panel shows the peak-magnitude distribution after volumetric correction (i.e. corrected for Malmquist bias).

limiting magnitude. The volumetric correction factor V_c is then expressed as follows:

$$V_c = V_{\max}/V_{\max,i} = \left(\frac{D_{L,\max}}{1 + z_{\max}} \right)^3 / \left(\frac{D_{L,\max,i}}{1 + z_i} \right)^3, \quad (1)$$

where the luminosity distance of the brightest SN in the sample is $D_{L,\max} = 10^{((m_{\lim} - M_{g,\max}) + 5)/5}$, and the luminosity distance for each individual SN is $D_{L,\max,i} = 10^{((m_{\lim} - M_{g,i}) + 5)/5}$. Figure 3, bottom panel, shows the peak-magnitude distribution after the volumetric correction. The mean peak magnitude of the SLSN sample is $\langle M_{g,\text{peak}} \rangle = -21.14$ mag with a standard deviation of 0.75 mag.

4.2. The postpeak early- and late-time decay rates

The light curves of H-poor SLSNe can show a change in decay rate (e.g. Inserra et al. 2013). Here we independently characterize the postpeak early- and late-time decay rates of H-poor SLSNe with linear fits to the early-time and late-time data separately. We study the early decay with a linear fit to the rest-frame g magnitudes in a time interval between the peak and typically 60 days after peak. In some cases, this interval was adjusted to

the data coverage, or to avoid changes of slope. The selected time intervals and the resulting linear fits to the data are displayed in Figs. B1 to B5 (solid curves). We define the late-time decay as typically beyond 60 days after peak and characterize the decay rate with a linear fit to the data, in the same way as we did for the early-time decay. The linear fits to the late-time decays are displayed in Figs. B1 to B5 (solid curves, typically beyond 60 days after peak).

Figure 4 shows the distribution of the early-time decay slopes (top panel) and the late-time decay slopes (bottom panel). SLSNe that were originally classified as sub-type R within the PTF survey are marked separately in this figure and compared to the rest of the sample. The original criterion for being classified as an SLSN-R was either a slow decline or spectral similarity with SN 2007bi, with no quantitative threshold. We do not intend to use these criteria as a meaningful classification, but rather to test this classification scheme, because it is often used in the literature (e.g. Gal-Yam 2012; Inserra et al. 2017).

The decay rate of most SLSNe slows down from early to late times. The decay rates and the times of transition from a faster to a slower decay (the intersections between the early- and late-time linear fits) are reported in Table A1.

4.3. Light-curve smoothing

We smooth the SN light curves to be able to further measure the rise and decay times more easily. We model the observed light curves with a nonparametric model, as follows. We first fit a first-order polynomial to the rest-frame g -band flux light curves locally. Then, we consider a fitting interval of 5 days (at phases until 5 days after peak), 10 days (at phases beyond 50 days after peak), and proportional to the phase (0.2 times) otherwise. For the interpolations, we use a Gaussian smoothing kernel that weights the fluxes according to their phase distance to each interpolated point. The smoothing algorithm also uses the uncertainties on the photometry to weight the data points. In order to avoid mathematical artifacts, a few auxiliary points are added to the observations. The light-curve smoothing algorithm is described in more detail in Rubin et al. (2016). In a few cases, to avoid unphysical wiggles in the smoothed light curves for poorly sampled regions, we binned scattered data during small time intervals. Namely, we binned the data for PTF 10aagc between 32 and 44 rest-frame days after peak; PTF 09cwl between 122 and 141; PTF 10vwg between 44 and 62; PTF 11rks at 55, and between 144 and 154; and PTF 12gty between 141 and 158. We adopt the formal error on the smoothed fluxes computed by the smoothing algorithm, and assume a minimum uncertainty of 10% of the flux

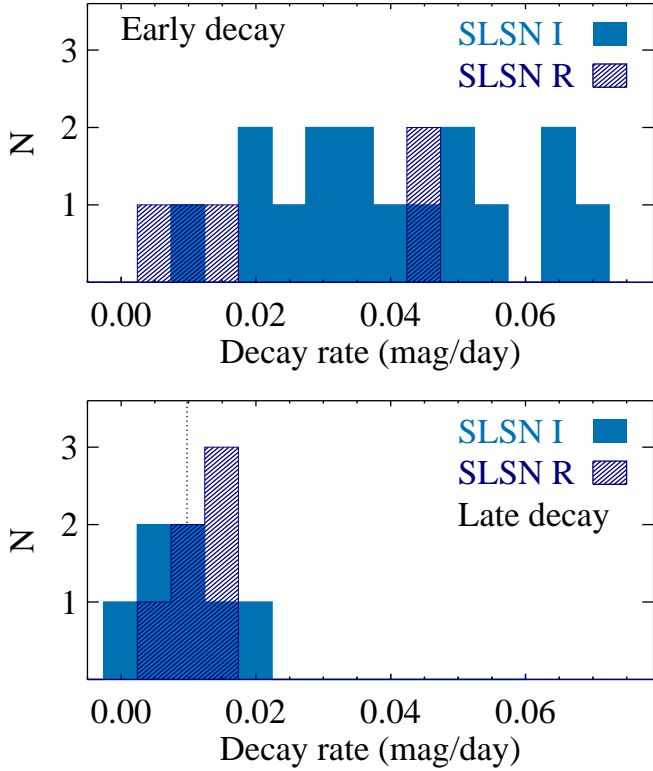


Figure 4. Postpeak decay slope distribution at early times (typically below 60 days, top panel) and at late times (typically beyond 60 days, bottom panel). At late times, all observed SLSNe cluster around the ^{56}Co to ^{56}Fe decay rate of 0.0098 mag day $^{-1}$ (dotted vertical line).

in those cases where the formal errors are smaller.

The light-curve smoothing fits to the data in flux space, including the auxiliary points, are shown in Figs. B6 to B9. The collection of all smoothed light curves, normalized by the peak magnitude, is shown in Fig. 5. Even when normalized to the peak, there is a wide variety of light-curve behaviors among H-poor SLSNe, and the scatter is too large to reduce them to a single template. Remarkably, there is no clear gap between fast- and slow-decaying SLSNe.

4.4. Times to rise and decay by 1 mag from the peak

We derive the times to rise (and decay) by 1 mag to (from) the peak, $t_{\text{rise}}^{\Delta 1\text{mag}}$ ($t_{\text{fall}}^{\Delta 1\text{mag}}$) by inspecting the smooth light curves (Sect. 4.3). Figures B11 to B14 display the time intervals within 1 mag from the peak. Table A1 lists the resulting rise and decay times. The errors are estimated starting from the errors on the smoothed light curves (Sect. 4.3). We create a pseudo-random normal distribution of the smoothed flux errors around the smoothed light curves, through n Monte Carlo realizations, and we estimate n rise (and decay) times. We finally derive the uncertainties on the rise (decay) times from the standard deviation of the distri-

Table 2. Normalizations and slopes of the linear fits of the correlations between rise times and decay times (Figs. 6 and 7). Note. r and ρ are the Pearson and Spearman correlation coefficients, respectively, and are listed with their respective null probability (p_r and p_ρ).

Type	A		B		r	p_r	ρ	p_ρ
	$t_{\text{rise}}^{\Delta 1\text{mag}} = A + B \times t_{\text{fall}}^{\Delta 1\text{mag}}$	$t_{\text{rise},1/2}^{\Delta 1\text{mag}} = A + B \times t_{\text{fall},1/2}$	r	p_r				
SLSN	12.93 ± 6.55	0.36 ± 0.15	0.69	0.057	0.76	0.028		
SLSN	17.32 ± 6.22	0.21 ± 2.06	0.39	0.270	0.44	0.206		

bution of rise (and decay) times and assuming a minimum uncertainty of 2 days. We test for convergence of our results by varying the number of Monte Carlo realizations n between 10, 100, 1000, and 10,000, and eventually use $n = 1000$.

In Fig. 6 we investigate the cross-correlations between $t_{\text{fall}}^{\Delta 1\text{mag}}$, $t_{\text{rise}}^{\Delta 1\text{mag}}$, their sum, and the peak magnitude. There is a clear correlation between $t_{\text{fall}}^{\Delta 1\text{mag}}$ and $t_{\text{rise}}^{\Delta 1\text{mag}}$.

We fit this correlation linearly, assuming $t_{\text{rise}}^{\Delta 1\text{mag}} = A + B \times t_{\text{fall}}^{\Delta 1\text{mag}}$ and including the observed uncertainties in both x and y axes, for each SN type. SNe where the data are not sufficient to constrain $t_{\text{rise}}^{\Delta 1\text{mag}}$ and $t_{\text{fall}}^{\Delta 1\text{mag}}$ are excluded from this fit, as reported in Table A1. The results of this fit are shown in Fig. 6 (dotted curves) and reported in Table 2. We also compute the Pearson and Spearman correlation coefficients, which measure the strength (tightness and monotonicity) of a correlation not taking the observed uncertainty into account, and their null probabilities. These are listed in Table 2.

We also find a trend between the peak magnitudes and $t_{\text{rise}}^{\Delta 1\text{mag}}$, $t_{\text{fall}}^{\Delta 1\text{mag}}$, and the peak width.

4.5. Times to rise and decay by half-flux

We further characterize the rise and decay times using the method of Prentice et al. (2016), who measured the time required to double or halve the flux with respect to the peak flux of a sample of stripped-envelope SNe (Ib/c). We derive $t_{\text{rise},1/2}$ and $t_{\text{fall},1/2}$, the time to double and halve the flux, respectively, for the PTF SN sample considered in this paper, using the smoothed flux light curves (Sect. 4.3). The resulting $t_{\text{rise},1/2}$ and $t_{\text{fall},1/2}$ are reported in Table A1. We calculated the uncertainties in the same way as for the rise and decay times by 1 mag (Sect. 4.4).

Figure 7 shows the comparison of $t_{\text{rise},1/2}$ and $t_{\text{fall},1/2}$ among the different samples and SN types, and compares it with the results of Prentice et al. (2016). We linearly fit the correlations between rise and decay times for each SN type in the same way as for the rise and decay times by 1 mag (Sect. 4.4). The results of the fit are

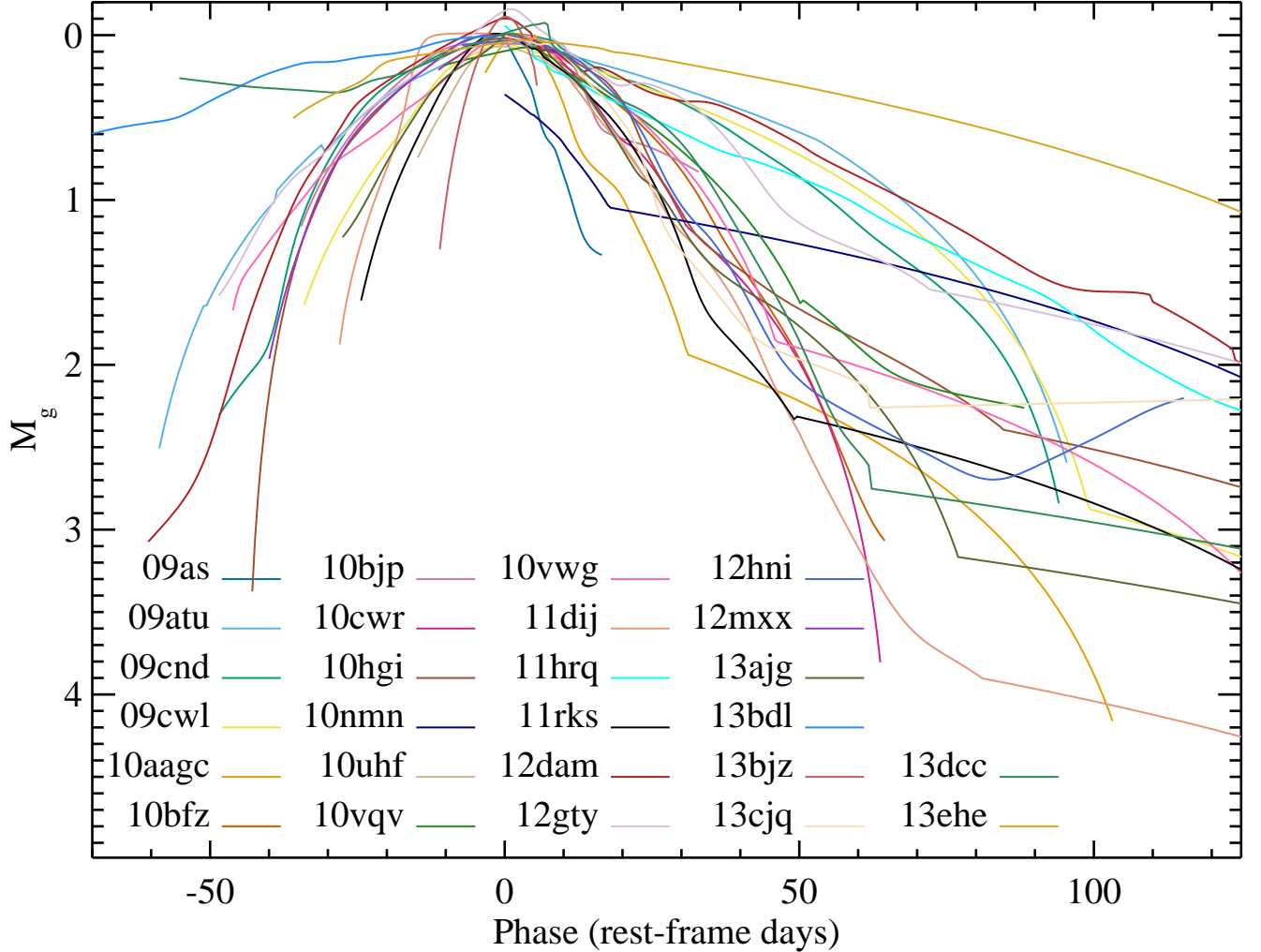


Figure 5. Rest-frame g -band smoothed light curves of the SLSNe in our sample, normalized at peak. PTF 10nmn is normalized with respect to the peak magnitude, which is taken from Yaron et al. (2018, in preparation) and is not presented in this paper. The peak magnitudes are derived with a second-order polynomial fit to the data (Figs. B1 to B5) and reported in Table A1.

shown in Fig. 7 (dotted curves) and reported in Table 2.

5. DISCUSSION

In this paper, we study 26 hydrogen-poor SLSNe at "low" redshift ($< z > = 0.27$), all spectroscopically classified as an SLSN-I and discovered by the (i)PTF survey. Here we characterize their light curves and discuss their (dis)similarity to SNe Ib/c and Ic-BL.

5.1. Peak-magnitude distribution

Figure 3, top panel, shows the distribution of the rest-frame g -band absolute peak magnitudes of SLSNe, SNe Ib/c, and Ic-BL. These SNe are all discovered by the PTF survey and separated into these three classes through spectroscopic classification (Quimby et al. 2018; Schulze et al. 2018). The k -correction has been applied as described in Sect. 3.12.

Clearly, not all peak magnitudes of SLSNe are brighter than < -21 mag. This threshold was an operational definition that was used to start characterizing SLSNe in the early days of their discovery (Quimby et al. 2011; Gal-Yam 2012). In fact, spectroscopically classified SLSNe-I from PTF span a wider range in absolute peak magnitudes, $-22.5 \lesssim M_{g,\text{peak}} \lesssim -20$ mag. The mean absolute peak magnitude in the PTF sample is $< M_{g,\text{peak}} > = -21.14$ mag, with a standard deviation of 0.75 mag, which is about 2 and 4 mag brighter than the mean for SNe Ic-BL and SN Ib/c in our sample, respectively. The SLSN mean peak magnitude in the PTF sample is similar to what Lunnan et al. (2018) found for the higher- z sample from PS1, and thus we confirm no evidence for evolution of the SLSN peak luminosities with z on the currently available data.

Furthermore, the peak magnitudes of SLSNe-I are all brighter than SNe Ib/c. The gap between the brightest

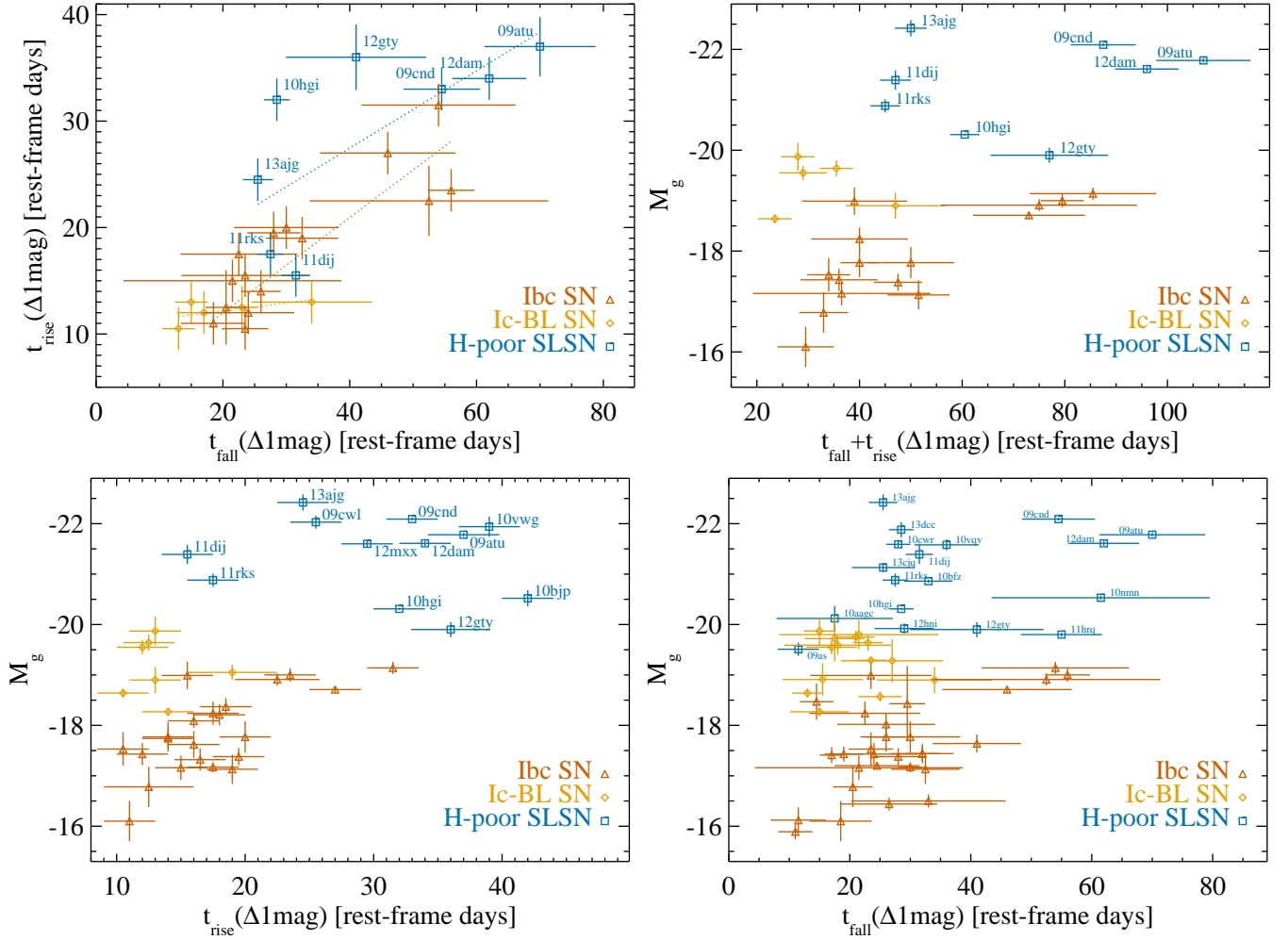


Figure 6. Times to rise and decay by 1 mag to and from the peak, and peak magnitudes (rest-frame g). The dotted curves show linear fits to the data in our sample.

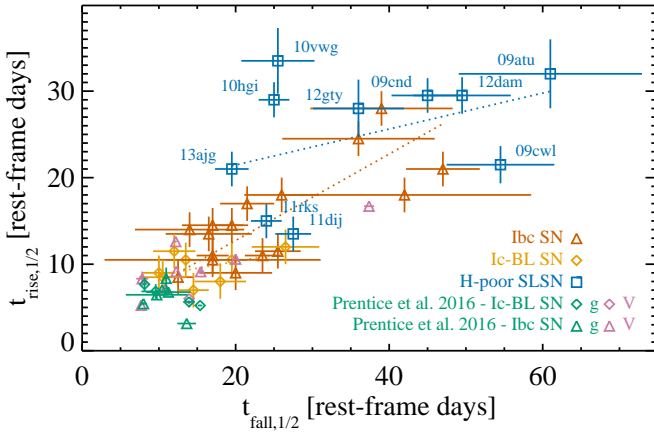


Figure 7. Times to rise and decay by half-flux. The dotted curves show the linear fit to the data in our sample.

SN Ibc and the faintest SLSN-I is of about 0.5 mag, although somewhat uncertain given the limited size of the samples and the uncertainty on the host-galaxy extinction for the SNe Ib/c. SNe Ic-BL are typically brighter

than SNe Ib/c and fill this gap. The distribution of peak magnitudes is continuous from SNe Ib/c to SNe Ic-BL and SLSNe. There is very little overlap between the SLSN population and SNe Ic-BL.

It is crucial to take into consideration the fact that fainter SNe can be observed and counted only out to smaller distances. When applying the volumetric correction to compensate for this bias (Fig. 3, bottom panel), the peak magnitude distribution decays smoothly and exponentially from SNe Ib/c to Ic-BL and to SLSNe. Another important bias to keep in mind is spectroscopic completeness. Because SNe Ib/c exist in the same parameter space as Type Ia or IIP SNe, some of them may be not selected for spectroscopic classification and therefore missing from those that we sample.

We conclude that the peak magnitudes of SLSNe are brighter than those of SNe Ib/c and Ic-BL. However, there is no evidence for SLSNe being drawn from a separate population when considering only the peak-magnitude distribution and taking the volumetric cor-

rection into consideration. Further evidence for the difference between SLSNe and SNe Ib/c comes from the rise and decay timescales, which we discuss in Sect. 5.4.

5.2. Observed colors

Figure 8 shows the evolution of the observed $g - r$ color for individual SLSNe. The $g - r$ color seems to increase at early epochs, until a few tens of days after peak. The mean observed $\langle g - r \rangle$ at peak is 0.24 mag, with a standard deviation of 0.37 mag. At later times, the $g - r$ color evolution seems to stabilize at around ~ 0.5 mag, and perhaps higher.

This $g - r$ evolution in SLSNe is overall similar to that in SN Ib/c (see Figures 22–25 of Prentice et al. 2016). The $g - r$ color in SLSNe may, however, rise for a longer time (up to ~ 50 days after peak, while SNe Ib/c reach a plateau at 10–20 days after peak), and to lower $g - r$ (the color plateau in SNe Ib/c spans roughly between 0.5–1 mag). However, we caution against a direct comparison of the observed $g - r$ between nearby SNe and SLSN, given their higher redshift. Indeed, after k -correction, the rest-frame $g - r$ colors at peak in SLSNe span roughly between −0.6 and 0.0 mag. The observed-frame colors are reported here only as an observational reference. In Sect. 5.9 we further discuss rest-frame $g - r$ colors at peak in SLSNe.

5.3. Decay rates

Figure 4 shows the postpeak decay rates at early times (top panel, typically before 60 days after peak) and late times (bottom panel, typically beyond 60 days after peak), as derived in Sect. 4.2. The two distributions are quite different, indicating that at early times, SLSNe decay faster than at late times. The mean SLSN decay rates are 0.04 and 0.013 mag day $^{-1}$ at early and late times, respectively, with standard deviations of 0.02 and 0.005 mag day $^{-1}$. All SLSNe with available data in our sample slow down their decay rate from early to late times. Moreover, their late-time decay rate settles around ~ 1 mag decay per 100 days. This rate is similar to the radioactive decay of ^{56}Co to stable ^{56}Fe (more specifically, 102.3 days mag $^{-1}$; Wheeler & Benetti 2000; Nadyozhin 1994). While at late times all SLSNe-I with available data show this slow decay, some selection biases may be present, because fast decays at late times may fall below the detection thresholds and not be measurable.

The late-time decays expected within the magnetar scenario can, under certain circumstances, mimic the radioactive ^{56}Co decay (e.g. Moriya et al. 2017). We further discuss this in Sect. 5.8.

The SLSN PTF 12hni is excluded from the late-time decay distribution because it exhibits a clear rebrightening (in all covered filters) and thus a negative de-

cay rate, starting at about 75 days after peak, as reported in Table A1. This could represent a case where interaction with the CSM re-energizes the light curve at late times, through the transformation of kinetic energy into luminosity. This typically requires a high optical depth, and one may naively not expect to observe broad lines and absorption features in this case (see, however, Moriya & Tominaga 2012). The rebrightening of PTF 12hni was not covered by spectral observations (Quimby et al. 2018).

In Fig. 4, we distinguish between classical H-poor SLSNe and those SNe originally classified as SLSNe-R within the PTF survey due to their slow decay early after the peak (consistent with radioactive decay, or spectrally similar to SN 2007bi). We stress again that we do not intend to use these criteria as a meaningful classification, but rather to test this classification scheme. At late times, the decay rates of SLSNe-R indeed cluster around the radioactive nickel decay rate, which is expected given the way SLSNe-R were originally selected. However, at early times, a couple of SLSNe-R have steeper decay slopes. Moreover, there is no evidence for a bimodal distribution in the decay properties in Fig. 5, where all smoothed light curves are plotted together, after being normalized around the peak. Therefore, there is no clear separation between SLSNe-R and classical SLSNe-I. This casts doubt on the existence of SLSN-R as a separate class, as initially suggested by Gal-Yam (2012).

Nevertheless, we note that early-time light-curve features are more common in SLSNe-R than in classical SLSNe-I. While none of the classical SLSNe-I show these features, three out of five SLSNe-R with early-time coverage (10nmn, Yaron et al. 2018 in preparation; 12dam and 13dcc, Vreeswijk et al. 2017) and possibly a fourth case (13ehe, Yan et al. 2015) have an early plateau or bumps of different strengths. At late times, the light-curve decay in SLSNe-R shows wiggles and bumps in virtually all events. Similar conclusions have also been drawn by Nicholl & Smartt (2016) and Inserra et al. (2017). In the case of the hybrid SLSN iPTF 15esb (late-time emergence of H emission), Liu et al. (2017) showed that the double peak of the light curves could be explained with a multiple-shell CSM interaction model. On the other hand, classical SLSNe-I might show fewer late-time features, the only clear example being PTF 12hni and perhaps PTF 12gtv, which are the least luminous among our sample. However, the paucity of late-time data for such events prevents us from drawing firm conclusions. For this reason, we keep open the possibility that two separate subclasses of SLSNe-I exist (slowly/rapidly declining), until further evidence is collected. The light curves of all potential SLSNe-R from PTF are shown together in

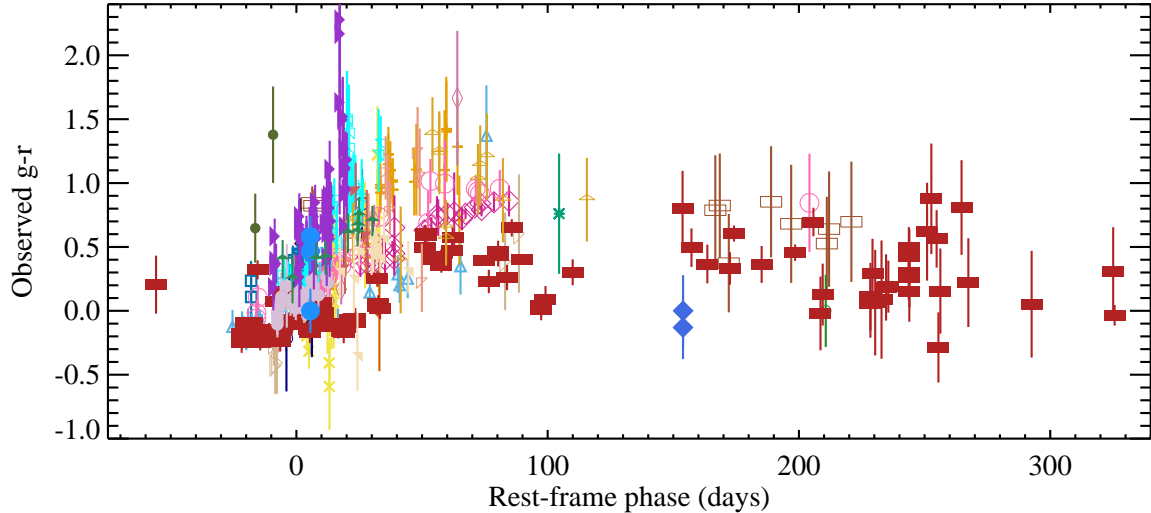


Figure 8. Observed $g - r$ color of the SLSNe in our sample. The symbols and colors are as in Fig. 1.

Fig. 9. The presence of bumps in the light curves indicate that either CSM interaction or multiple sources are responsible for powering the light curve, as also found by Vreeswijk et al. (2017) and Inserra et al. (2017).

5.4. Rise and decay times

In Fig. 6, we compare the rise and decay timescales ($t_{\text{rise}}^{\Delta 1\text{mag}}$ and $t_{\text{fall}}^{\Delta 1\text{mag}}$; Sect. 4.4) and peak magnitudes for PTF SLSNe-I and PTF SNe Type Ib/c and Ic-BL SNe.

The peak magnitudes are brighter for SLSNe-I than for SNe Ib/c and Ic-BL, as discussed in Sect. 5.1. We find possible mild trends between M_g and $t_{\text{rise}}^{\Delta 1\text{mag}}$ and between M_g and $t_{\text{fall}}^{\Delta 1\text{mag}}$, albeit with a very large scatter, and mostly when all SNe are considered. Indeed, neither luminous and fast-evolving events nor faint and slow-evolving ones are observed. A correlation between peak luminosity and rise time was observed for SNe IIn by Ofek et al. (2014a) and is consistent with the explanation of CSM interaction. The predictions for this correlation are in Ofek et al. (2014b).

The SLSNe in our sample tend to have longer rise timescales than SNe Ib/c; see below. Most SNe Ib/c and Ic-BL also tend to decay faster than SLSNe, although there are a few exceptions of slow-decaying, long-lived SNe Ib/c (e.g., PTF 11bov, also known as SN 2011bm; Valenti et al. 2012).

We find a correlation between $t_{\text{rise}}^{\Delta 1\text{mag}}$ and $t_{\text{fall}}^{\Delta 1\text{mag}}$ for SLSNe (Fig. 6, top left panel). The parameters and strength of this correlation are reported in Table 2. Such a correlation is expected for both magnetar and nickel decay models (e.g. Nicholl et al. 2015a). This correlation is continuous and does not show two separate classes of SLSNe-I, in contrast to the findings of Nicholl et al. (2015a). Interestingly, SLSNe and "normal" SNe Ibc follow separate $t_{\text{rise}}^{\Delta 1\text{mag}} - t_{\text{fall}}^{\Delta 1\text{mag}}$ correlations. Although the correlation is not strong, there is an

evident offset toward longer rise times for SLSNe with respect to SNe Ib/c. The offset is roughly a 10 day longer rise timescale for SLSNe. Finally, this correlation has a large scatter, and moreover, in some cases (PTF 11dij and PTF 11rks), the measured rise and decay times are similar to those of SNe Ib/c. Therefore, the above-mentioned correlation cannot be used to distinguish between SLSNe-I and SNe Ib/c, but only as an indicator of the average properties of the two populations.

As a sanity check, we further study the rise and decay times with a different approach, by considering the time to rise and decay by half-flux from the peak ($t_{\text{rise},1/2}$ and $t_{\text{fall},1/2}$, Sect. 4.5). Again, the rise and decay times correlate continuously for SLSNe-I and the correlations are different for the three different classes of SNe. (The parameters and strength of this correlation are reported in Table 2.)

The difference between the correlations of the rise with the decay timescales for SLSNe and SNe Ib/c (and Ic-BL) is evident using both independent methods ($\Delta 1$ mag and half-flux). This suggests that SLSNe have longer rise timescales than SNe Ib/c, even for similar decay timescales. Observationally, we conclude that SLSNe show overall different light-curve properties from SNe Ib/c and Ic-BL. Therefore, SLSNe can be considered as a separate population, not only from a spectroscopic (Quimby et al. 2018) but also from a photometric perspective.

5.5. Bolometric correction

We use the spectral information derived from a well-observed event to estimate the bolometric luminosity L_{bol} from single-band photometry. We adopt the conversion from the rest-frame g -band to the bolometric luminosity derived for PTF 12dam by Vreeswijk et al.

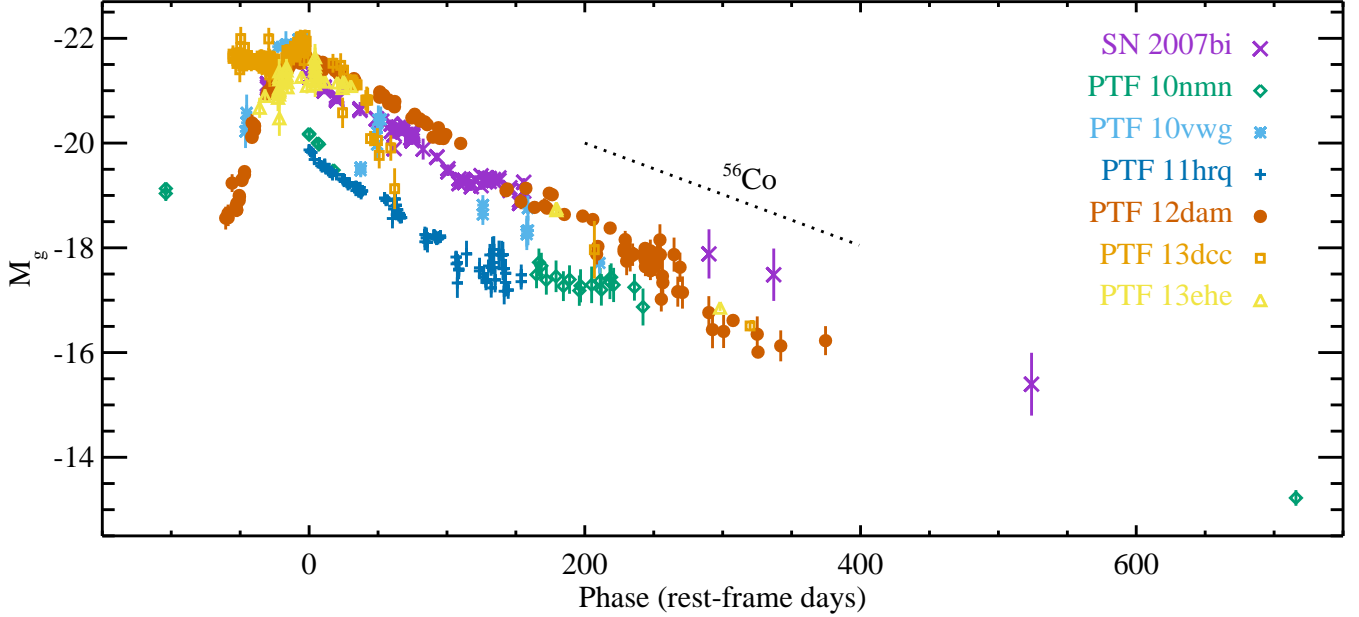


Figure 9. Rest-frame M_g light curves of the SLSNe originally classified as SLSNe of the R type.

(2017) up to 334 rest-frame days after peak. The bolometric light curve of PTF 12dam was constructed from the observed spectral series and blackbody models of the UV/optical data. More details on this derivation are explained in Vreeswijk et al. (2017). We apply the bolometric correction from absolute magnitudes to the bolometric luminosity of PTF 12dam to all SLSNe in our sample, i.e. by basically adding a constant to the rest-frame g -band absolute magnitudes, where this constant evolves with the SN phase. This is valid under the assumption of spectral similarity among SLSNe-I. While there are strong indications for such similarity in our sample (Quimby et al. 2018), this is not always guaranteed, especially at late times when the spectral coverage is typically poorer than around peak. A solid case-by-case bolometric correction can in principle only be attempted for the few best observed cases with sufficient spectral coverage. Due to the paucity of such complete datasets, this cannot be done for the full sample and is beyond the scope of the current paper. Nevertheless, given the overall similarity among the spectra in our sample, it is still informative, as a first approximation for the study of the energetics, to use a simple bolometric correction to derive the bolometric luminosities. Because the relative shapes of the light curves does not change between different SLSNe in bolometric luminosity, we do not show the individual light curves. We report the bolometric luminosities at peak in Table 3. The total radiated energy is then derived by integrating the bolometric light curves. Because the bolometric light curves are defined over a limited time interval, the

derived radiated energies are lower limits.

5.6. Ni masses

We investigate whether the peaks and light curve decays of SLSNe-I could be powered by Ni decay, using two independent methods. First, we derive a very rough estimate of what the required nickel masses would be if the SN peaks were completely powered by nickel. We use the relation $L_{\text{peak}} = \alpha E_{\text{Ni}} = (6.45 \times 10^{43} e^{-(t_{\text{peak}}/\tau_{\text{Ni}})} + 1.43 \times 10^{43} e^{-(t_{\text{peak}}/\tau_{\text{Co}})}) \times M_{\text{Ni}}/M_{\odot}$ (Nadyozhin 1994; Stritzinger & Leibundgut 2005), where $\tau_{\text{Ni}} = 8.8$ days and $\tau_{\text{Co}} = 111.3$ days, and assume no deviation from the Arnett rule ($\alpha = 1$, Arnett 1979). The time of explosion is quite uncertain in our sample, because the rise times are often not well-covered.⁸ Thus, we use a representative $t_{\text{peak}} = 70$ days. For a few SLSNe-I that show indications for a longer rise time, we assume an explosion time of 100 days before peak (namely for PTF 10nmn, PTF 11hrq, and PTF 13dcc), and we assume the literature explosion time of 66 days before the peak for PTF 12dam (Vreeswijk et al. 2017). The uncertainties in this Ni mass calculation are of about 20% for an uncertainty in explosion date of about 30%. The Ni mass that we derive with this method for PTF 12dam is similar to what has been derived by Vreeswijk et al. (2017) with a more detailed Ni decay model of the full light curve. In this exercise, the main assumption is that the light

⁸ In most cases, the SN empirical-model fit of Bazin et al. (2011) does not provide satisfactory results.

curves are totally powered by radioactive Ni decay, while in fact there may be a significant contribution from CSM interaction, magnetars, or other sources. The derived nickel masses are therefore upper limits of the true values, for a peak time of 70 days after explosion. The results are reported in Table 3.

Second, we derive what the required nickel masses would roughly be if the SN late-time decay would be completely powered by nickel. In this case, we compare the SLSN decay, if sufficient photometry is available, to the decay of SN 1987A. For this SN, the well-studied decay is thought to be powered by the radioactive decay of 0.07 M_{\odot} of ^{56}Ni (Fransson & Kozma 2002; Seitenzahl et al. 2014). To compare the SLSNe light curves with SN 1987A, we assume an explosion date for the SLSNe and shift the bolometric light curves to that of SN 1987A (taken from Pun et al. 1995), using the same method as Gal-Yam et al. (2009). We shifted the light curve of SN 1987A to match the potential transition from the diffusive phase to the radioactive decay in the SLSN light curves or to the late-time decay. The explosion dates are quite uncertain. We assume the same explosion dates as discussed above. While the assumption on the explosion dates are not secure, here we are only interested in a zero-order estimate of the Ni masses from the tails. Figure 10 shows the comparison between the SLSN light curves and SN 1987A. The Ni masses derived from the light-curve decay are labeled on the figure and reported in Table 3. These masses are upper limits, because they are calculated assuming that the late-time light curves are powered only by radioactive Ni, with no other contribution. The typical uncertainties on these nickel masses are large, roughly of the order of 50% (accounting for a shift in explosion date of up to 100 days). Despite the large uncertainties, these estimates are useful for the comparison with the nickel masses derived from the peaks.

In Table 3, we compare the nickel masses that we derived above with the two methods, one based purely on the peak luminosity and one based purely on the late-time decay. It is evident that the nickel masses derived from the peak luminosities are much higher than the nickel masses derived from the SN decay, both for fast- and slow-evolving SLSNe-I. This suggests that the SLSN peaks are not powered by nickel. This confirms the results of Inserra et al. (2013). In addition, the large ejecta masses required for powering the SLSN-I peaks with Ni radioactivity would increase the diffusion times, and therefore the light curves would show broader peaks than what is observed. A different component, such as magnetar spin-down or CSM interaction, is likely causing the high peak luminosities of most SLSNe-I. A factor of 5 discrepancy between the Ni masses required for the peak and the late-time decay was also found for

SN 1998bw, which was possible to reconcile only with asymmetry of the ejecta (Dessart et al. 2017). Strong evidence for asphericity of this event, based on the spectra, was found by Mazzali et al. (2001), Maeda et al. (2002), and Maeda et al. (2006). If asymmetry is relevant for SLSNe-I as well, the discrepancy between the nickel masses derived from the peak and the late-time decay may be partly mitigated (perhaps by a factor of 5 for asymmetries levels similar to SN 1998bw).

When data coverage is available, we observe a late-time decay of SLSNe-I, which is close to the radioactive decay of ^{56}Co to stable ^{56}Fe , as observed from the late-time decay slopes (Sect. 4.2). The nickel masses derived from this late-time decay are between ≤ 1 and $\leq 10 M_{\odot}$. This suggests that while nickel production is not the main source powering the light curve peaks, a nickel component could be important, and perhaps dominant, at late times. While the derived Ni masses are upper limits, producing up to $10 M_{\odot}$ of Ni is challenging in classical SN models. The PISN model can produce 1– $10 M_{\odot}$ of nickel from progenitor stars with cores of 90– $105 M_{\odot}$ (Heger & Woosley 2002).

In the case of PTF 10hgi, the only data point at late times seems fainter than what would be predicted from the decay rate of ^{56}Co (Fig. 10). The current ^{56}Ni mass estimated from the light-curve decay is $M_{\text{Ni}} \sim 2 M_{\odot}$. However, estimating the Ni mass directly by scaling the SN 1987A light curve to the fainter data point at late times would provide $M_{\text{Ni}} \sim 0.2 M_{\odot}$.

5.7. Radioactive decay

One potential power source of SLSN-I light curves is radioactive decay of ^{56}Co to stable ^{56}Fe (e.g. Gal-Yam et al. 2009). The half-life time of the ^{56}Co decay is 77.2 days (Junde et al. 2011). As we discussed above, it is rather unlikely that the SLSN peaks are powered by radioactive decay because of the discrepancy between the Ni masses required by the peak luminosities and those required by the late-time decays. One possibility is that the late-time light curves are powered by radioactive decay. Indeed, we showed in Sect. 4.2 that whenever observable, the SLSN-I light curves tend to slow down, and at late times settle around the 0.01 mag days $^{-1}$ decay rate, which is typical of radioactive ^{56}Co decay with full trapping. On the other hand, Inserra et al. (2017) argued that SLSNe tend to decay faster than the radioactive rate, and therefore could not easily be associated with ^{56}Co decay. However, the escape of γ -rays can increase the decay rate. In this section, we investigate under which conditions γ -ray escape can efficiently induce a light-curve decline that is faster than the nominal radioactive decay rate.

The radioactive decay energy (RDE) deposition is the heating/excitation/ionization of the SN ejecta because

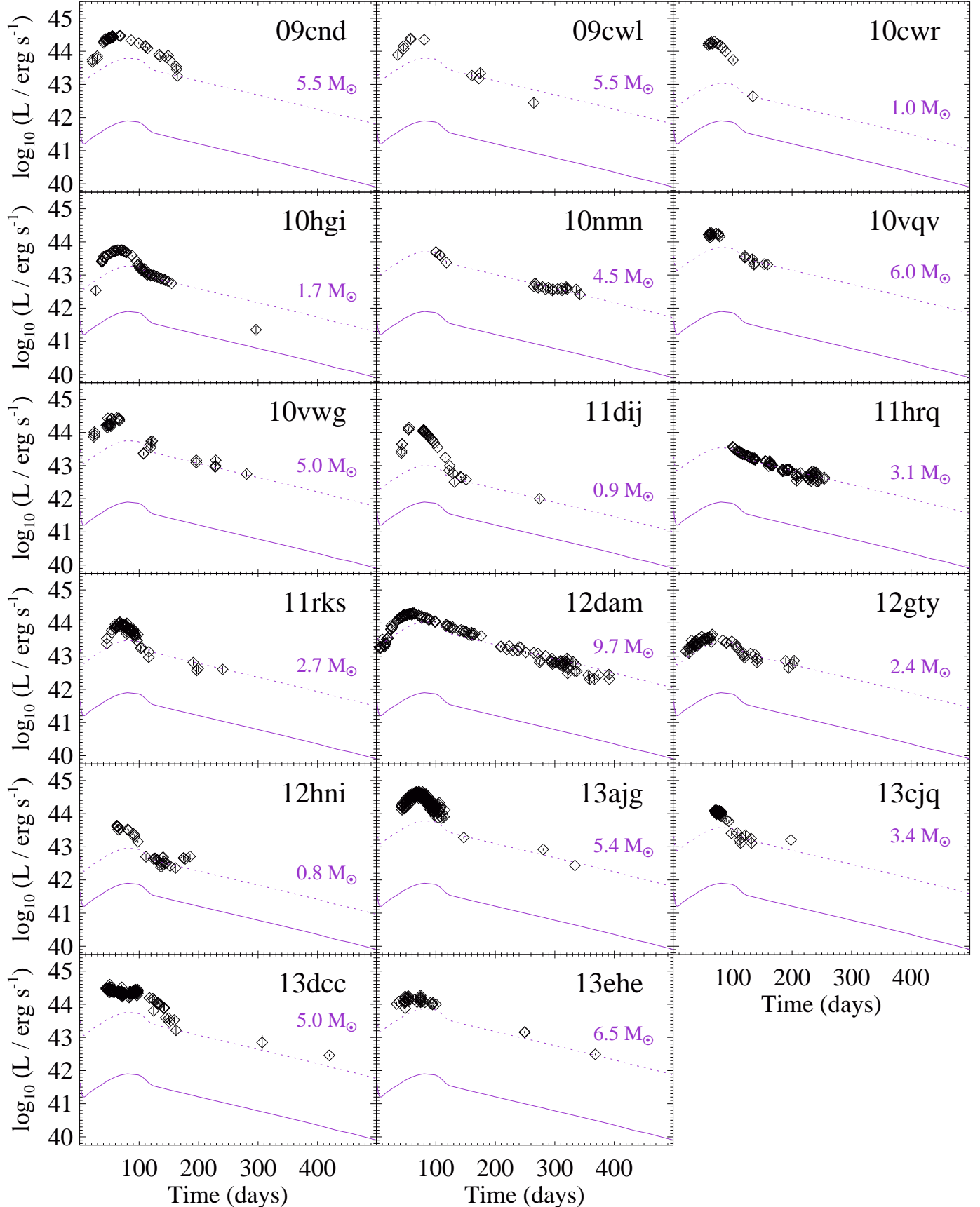


Figure 10. Bolometric light curve of SN 1987A (solid curve) is scaled (dashed curves) to match the decay of SLSNe-I (black diamonds) at late times, after bolometric correction. The M_{Ni} roughly estimated from this comparison are labeled. The time reference is in rest-frame days after explosion.

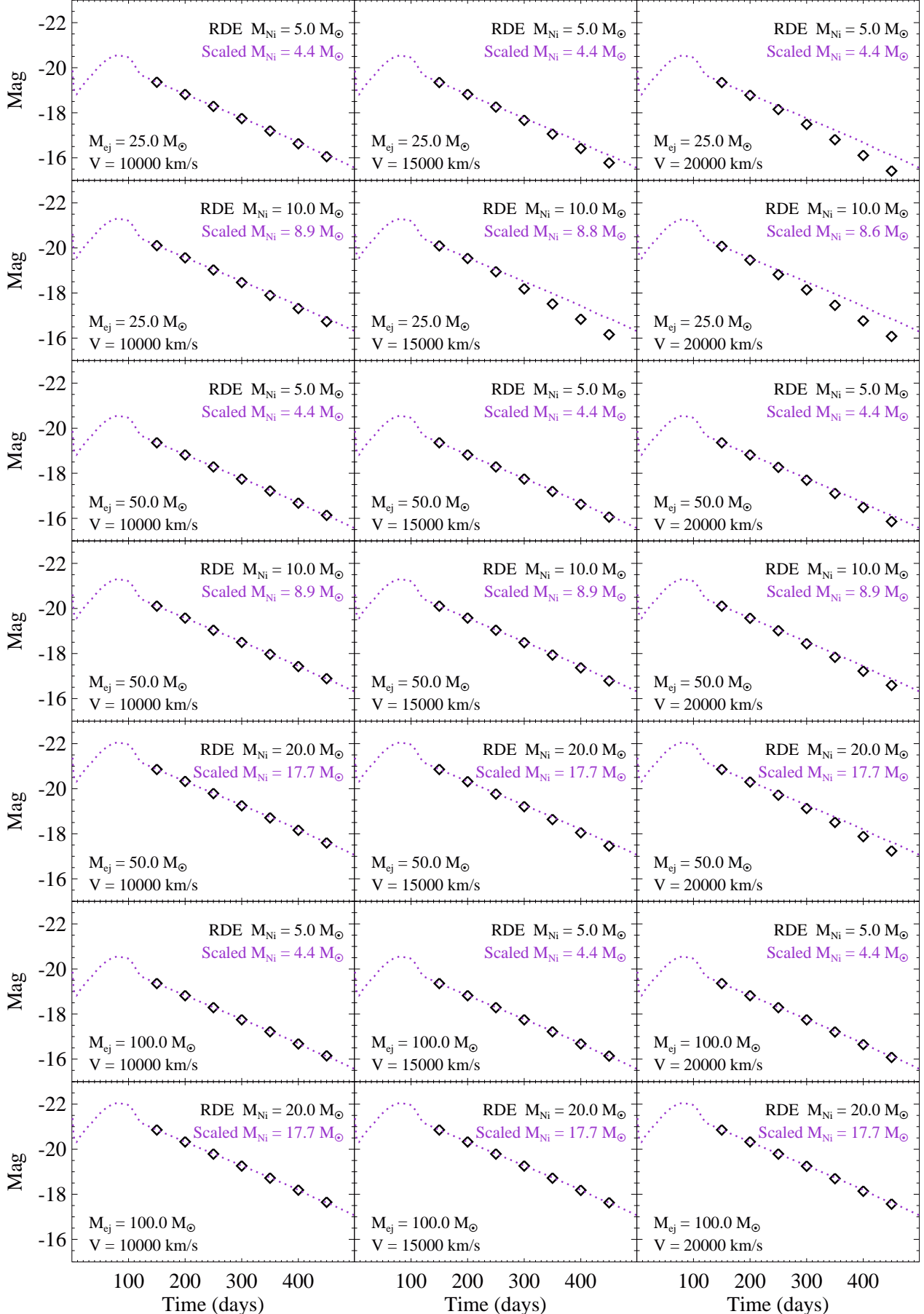


Figure 11. Simulated light curves using RDE deposition (black diamonds) for stars with different initial parameters (black labels). A comparison with the SN 1987A light curve, scaled up to match the simulated magnitudes at 150 days, and the associated Ni masses are shown (purple label and dotted curve). Time is measured in rest-frame days after explosion.

Table 3. Radiated energy and nickel mass estimates from the peak luminosity and the late-time decay.

PTF ID	$\log L_{\text{bol,peak}}$ (erg s $^{-1}$)	$\log E_{\text{rad}}$ (erg)	$M_{\text{Ni,peak}}$ [M $_{\odot}$]	$M_{\text{Ni,decay}}$ [M $_{\odot}$]
09as	43.4	≥ 49.3	≤ 3.4	–
09atu	44.3	≥ 51.2	≤ 28.3	–
09cnd	44.5	≥ 51.3	≤ 37.3	≤ 5.5
09cwl	44.4	≥ 51.2	≤ 33.7	≤ 5.5
10aagc	43.7	≥ 50.0	≤ 6.5	–
10bfz	44.0	≥ 50.4	≤ 12.1	–
10bjp	43.8	≥ 50.5	≤ 8.8	–
10cwr	44.3	≥ 50.8	≤ 23.5	≤ 1.0
10hgj	43.7	≥ 50.5	≤ 7.2	≤ 1.7
10nmn	43.7	≥ 50.6	≤ 8.3	≤ 4.5
10uhf	43.9	≥ 50.3	≤ 9.8	–
10vqv	44.2	≥ 50.8	≤ 21.4	≤ 6.0
10vwg	44.4	≥ 51.2	≤ 32.0	≤ 5.0
11dij	44.2	≥ 50.8	≤ 21.0	≤ 0.9
11hrq	43.6	≥ 50.2	≤ 6.2	≤ 3.1
11rks	43.9	≥ 50.6	≤ 10.7	≤ 2.7
12dam	44.3	≥ 51.2	≤ 24.6	≤ 9.7
12gty	43.7	≥ 50.5	≤ 5.9	≤ 2.4
12hni	43.6	≥ 50.1	≤ 4.8	≤ 0.8
12mxx	44.2	≥ 50.8	≤ 22.6	–
13ajg	44.6	≥ 51.2	≤ 49.5	≤ 5.4
13bdl	43.9	≥ 50.6	≤ 9.6	–
13bjz	44.0	≥ 50.0	≤ 12.1	–
13cjq	44.1	≥ 50.7	≤ 15.2	≤ 3.4
13dcc	44.5	≥ 51.3	≤ 48.6	≤ 5.0
13ehe	44.2	≥ 51.2	≤ 18.3	≤ 6.5

of radioactive emission of γ -rays (and e^+) and the subsequent acceleration of electrons through Compton scattering (Jeffery 1999). This phenomenon is important for SNe Ia as well as for core-collapse SNe. After a diffusion phase when the γ -rays are fully trapped, a transition to a quasi-steady state marks the beginning of a regime where the decay is dominated by RDE deposition (and the diffusion timescale is much larger than the dynamical and radioactive timescales). At the transition point, the SN luminosity is purely determined by the total amount of radioactive material. The quasi-steady state decay is then exponential, starting with a radioactive slope that corresponds to full trapping. In time, the γ -rays can start to escape, and the decay can appear faster. We investigate here whether γ -ray escape is important for massive star progenitors.

We simulate the quasi-steady state decay from pure RDE deposition for stars with a density profile that has

an inner plateau and decays exponentially (similar to the ‘s25e12’ profile of Dessart & Hillier 2011), where the ^{56}Ni mass is distributed in the inner ejecta. We consider total ejecta masses between 25 and 100 M $_{\odot}$, ^{56}Ni masses between 5 and 20 M $_{\odot}$, and maximum expansion velocity between 10,000 and 20,000 km s $^{-1}$. The total ejecta mass and maximum expansion velocity determine the absolute value of the density profile at each point. These simulations cannot treat the diffusive phase, but only the light-curve decay beyond maximum light and beyond the transition to the quasi-steady state. As a sanity check, we reproduce the observed radioactive light-curve phase of SN 1987A given an expansion velocity of 6000 km s $^{-1}$, the same density profile as we used for SLSNe, total ejecta mass of 10 M $_{\odot}$, and $M(^{56}\text{Ni}) = 0.07$ M $_{\odot}$.

Figure 11 shows the resulting light curves of our RDE deposition simulations for different initial parameters. In all cases, we observe \sim 100% gamma-ray trapping at \sim 150 days after the explosion. At later times the luminosity can decrease more rapidly because of the reduced trapping due to lower densities. This effect is stronger for high expansion velocities and high $M_{\text{Ni}}/M_{\text{ej}}$ ejected masses. Within this set of simulations, the deviation from a pure radioactive ^{56}Co decay ranges from 0.01 (still fully trapped) to a maximum of 0.27 mag (\sim 50% escape fraction) at about 450 days after explosion, with a decay rate of 1.33 mag in 100 days.

The contours in Figure 12 show the energy deposition fraction (where 100% means full trapping) from our RDE deposition simulations for the cases of 5 and 10 M $_{\odot}$ of nickel. These results confirm that massive star progenitors, with high SN ejecta velocities and high Ni fraction in the ejecta, have limited trapping and therefore can decay faster than the radioactive exponential decline. Figure 12 can also be used to roughly estimate the total ejecta masses in case the expansion velocity and the trapping are known from the spectra and light curves, respectively.

An additional factor that can efficiently limit the trapping (and induce faster decays) is the potential mixing of ^{56}Ni in the outer layers. While this can be a dominant effect, we do not attempt to model it here, because this is highly dependent on the geometry of the mixing, which cannot be constrained.

5.8. Magnetar modeling

We investigate whether the SLSN-I light curves could be powered by the spin-down of a magnetar. We consider an analytic magnetar model sourced from Arnett (1982) and Kasen & Bildsten (2010). The fitting technique is described in detail in Rubin et al. (2018, in preparation). The main model parameters are the initial pulsar spin P , the magnetic field B , the diffusion timescale $t_m \approx M_{\text{ej}}^{3/4} E_k^{1/4}$ (where M_{ej} and E_k are the

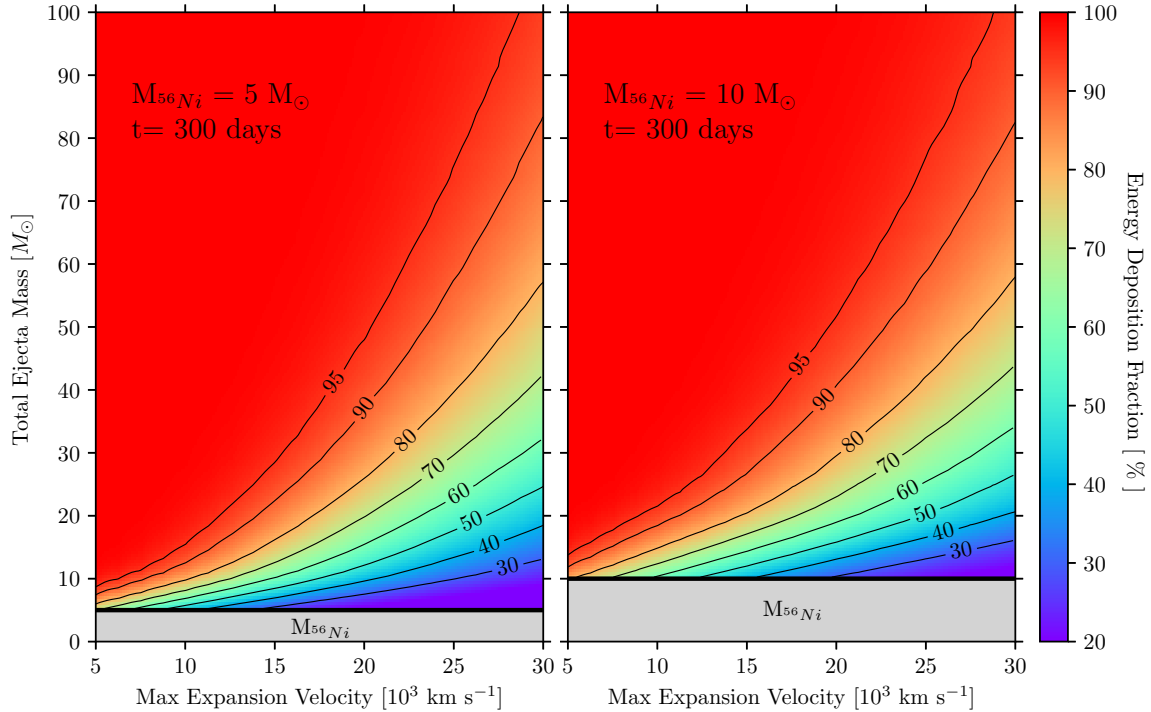


Figure 12. Contours show the energy deposition fraction (100% means full trapping) for different ejecta velocities and total ejecta masses, and in the cases of $5 M_{\odot}$ and $10 M_{\odot}$ of nickel (left and right panels, respectively). The color scale displays an interpolation of the contours.

ejected mass and kinetic energy, respectively), and the explosion time t_{\exp} . This is a basic modeling, that includes neither photon escape nor multiple components. The uncertainties are derived with a Monte Carlo treatment and shown in Figs. B18 to B31. The treatment of the opacity is the same as in Inserra et al. (2013).

Figures B16 and B17 show a fit of the magnetar model described above to the bolometric SLSN-I light curves. The best-fit parameters are reported in Table 4, and displayed in Fig. 13. In most cases, we obtain a satisfactory overall description of the light curves, with the exception of PTF 10hgi, PTF 10vwg, and PTF 11rks, for which we observe a different decay than predicted from our magnetar fit. In addition, the magnetar model does not describe well the light curve of PTF 11dij, both for the late-time decay and the early rise.⁹ The confidence levels of the best-fit parameters are shown in Figs. B18 to B31.

Recently, Nicholl et al. (2017) has modeled a large literature SLSN-I sample with a magnetar model, including several published (i)PTF objects. The spin values P that we obtain are mostly consistent with the values of Nicholl et al. (2017). For PTF 12dam, we find a spin value $P = 1.87^{+0.07}_{-0.08}$ ms, which is a bit lower than

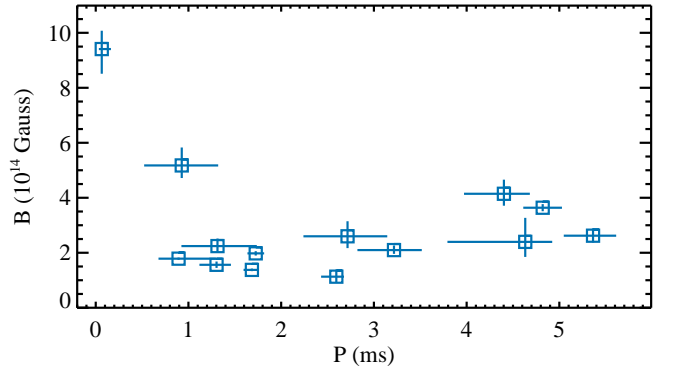


Figure 13. Magnetic field strength and magnetar initial spin, as listed in Table 4.

the ~ 2.3 ms values that were derived by Nicholl et al. (2017) and Vreeswijk et al. (2017), and also lower than that by Chen et al. (2015). The magnetic fields B that we obtain are in all cases higher than what was derived by Nicholl et al. (2017). For PTF 13ajg, our B value is more similar to that found by Vreeswijk et al. (2014). For PTF 12dam, our B value is more similar to those found by Chen et al. (2015) and Vreeswijk et al. (2017).

The late-time luminosities expected from the spin-down of a magnetar decline as t^{-2} (e.g. Woosley 2010). In principle, such model may also be able to mimic the ^{56}Co decay of about 1 mag per 100 days, which we ob-

⁹ Forcing the explosion date to be before -28 days improves the fit at late times, but cannot well explain the data around peak and at ~ 50 days after peak.

serve in SLSN-I late-time light curves. In the case of pure dipole radiation, the magnetar light curves start to have the same decay rate around 200 days postpeak. At later times, e.g. 400 days postpeak, the magnetar model is expected to have a decay rate that is noticeably slower than from the 1 mag/100 days (e.g. Inserra et al. 2013). However, the capability of a magnetar to mimic a radioactive decay would require a pure dipole radiation and a narrow set of fine-tuned parameters, in particular for the magnetic field and Ni masses (Moriya et al. 2017). In Fig. 14 we display the space parameter where a magnetar (in the dipole case) can mimic the radioactive ^{56}Co decay from Moriya et al. (2017), and compare it with the results from our magnetar fit on the SLSN light curves. The reference time intervals are derived from the observed times after peak where the SLSN decay follows the radioactive rate (Fig. 10), and using the explosion times from the magnetar fits to the data (Figs. B16 and B17). The magnetic field B is taken from the magnetar fit, while the Ni masses are taken from scaling the late-time light-curve decays (Sect. 5.6). The SLSNe for which these measurements are available are lying in the parameter space where the magnetar decay mimics the radioactive decay of ^{56}Co , with the marginal exception of PTF 11rks, for which a magnetar model does not describe the data well. Given that we do observe radiative-like light-curve decays at late times in SLSNe, it is perhaps not surprising that most of the derived magnetar parameters that we derive fulfill the radiative-mimicking criteria. These results indicate that we cannot disentangle between the magnetar and the radioactive decay models at these epochs, up to 400 days after explosion, but that observations at later times can be extremely powerful in disentangling between the two models.

Intriguingly, a correlation between the magnetar initial spin and the host galaxy metallicity was found by Chen et al. (2017). In Fig. 15 we show these quantities for our SLSN data using the host metallicities derived in Perley et al. (2016, ; PP04 N2 scale) and compare them to the correlation of Chen et al. (2017). We cannot confirm the existence of such a correlation in the PTF sample, or at least we find a large scatter (more than a factor of 10) in the derived spin periods, for a similar metallicity range.

5.9. Cosmology tests

Because SLSNe can be observed out to large distances, as far out to $z \sim 4$ (Cooke et al. 2012) and likely well beyond with future facilities, the prospects of using SLSNe for cosmological distance determinations is of primary interest. Indeed, Inserra & Smartt (2014) suggested that SLSNe-I may be standardizable, based on *i*) the narrowness of the peak magnitude distribution, *ii*) a

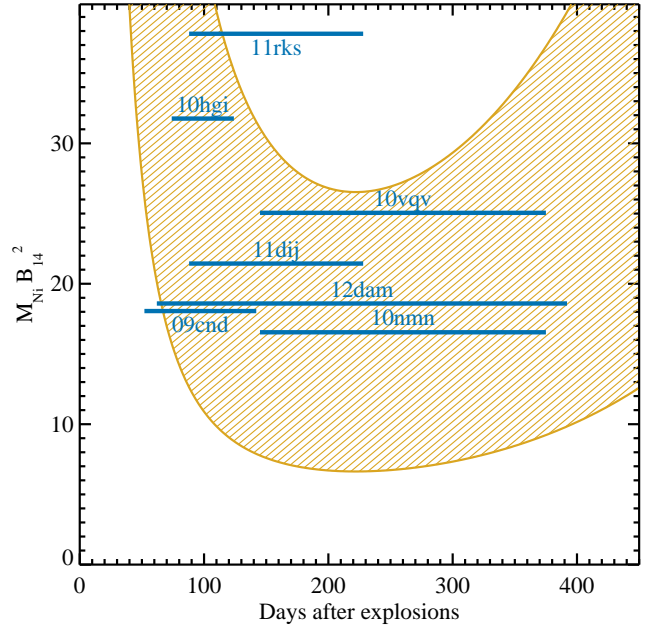


Figure 14. Parameter space where a magnetar (in the dipole case) can mimic the radioactive ^{56}Co decay (shaded area; Moriya et al. 2017). The horizontal lines mark the epochs when SLSNe are observed to decay consistently with the radioactive decay.

Table 4. Resulting parameter from a magnetar fit to the bolometric light curves. Note. The last column lists the host-galaxy metallicity from Perley et al. (2016).

ID	B (10^{14} G)	P (ms)	τ_m (days)	t_{exp} (days)	$12 + \log[\text{O}/\text{H}]$ (PP04 N2)
09cnd	$1.56_{-0.11}^{+0.12}$	$1.30_{-0.18}^{+0.16}$	$63.0_{-3.0}^{+3.2}$	$-45.0_{-1.0}^{+1.0}$	$8.22_{-0.15}^{+0.09}$
09cwl	$2.24_{-0.20}^{+0.27}$	$1.31_{-0.39}^{+0.42}$	$57.7_{-8.1}^{+6.2}$	$-37.1_{-2.2}^{+4.4}$	—
10bjp	$2.40_{-0.55}^{+0.87}$	$4.63_{-0.84}^{+0.29}$	$38.3_{-7.0}^{+8.8}$	$-46.6_{-2.6}^{+3.0}$	$8.14_{-0.10}^{+0.06}$
10cwr	$9.41_{-0.90}^{+0.67}$	$0.06_{-0.03}^{+0.10}$	$34.8_{-1.0}^{+0.9}$	$-12.6_{-0.8}^{+0.6}$	$7.96_{-0.24}^{+0.12}$
10hgi	$3.64_{-0.13}^{+0.13}$	$4.82_{-0.21}^{+0.21}$	$39.0_{-2.1}^{+1.9}$	$-42.0_{-1.3}^{+1.1}$	$8.27_{-0.06}^{+0.05}$
10nmm	$1.78_{-0.04}^{+0.04}$	$0.89_{-0.22}^{+0.40}$	$48.5_{-1.9}^{+2.4}$	$-104.7_{-1.0}^{+0.4}$	$8.16_{-0.04}^{+0.03}$
10vqv	$2.10_{-0.14}^{+0.17}$	$3.22_{-0.39}^{+0.30}$	$29.9_{-4.9}^{+6.1}$	$-28.5_{-2.3}^{+2.3}$	$8.28_{-0.05}^{+0.04}$
10vwg	$2.60_{-0.43}^{+0.55}$	$2.72_{-0.48}^{+0.43}$	$29.1_{-4.8}^{+6.5}$	$-34.1_{-7.1}^{+2.8}$	—
11dij	$5.18_{-0.46}^{+0.65}$	$0.93_{-0.41}^{+0.39}$	$39.2_{-1.3}^{+1.4}$	$-27.6_{-0.8}^{+0.4}$	$7.93_{-0.20}^{+0.10}$
11rks	$4.15_{-0.43}^{+0.51}$	$4.40_{-0.43}^{+0.28}$	$26.7_{-1.7}^{+1.7}$	$-22.8_{-1.3}^{+1.1}$	$8.14_{-0.18}^{+0.13}$
12dam	$1.38_{-0.05}^{+0.05}$	$1.68_{-0.09}^{+0.08}$	$76.8_{-2.2}^{+2.1}$	$-56.0_{-0.8}^{+0.8}$	$8.07_{-0.01}^{+0.01}$
12gty	$2.62_{-0.25}^{+0.27}$	$5.36_{-0.32}^{+0.25}$	$54.0_{-4.2}^{+4.1}$	$-58.5_{-2.3}^{+2.0}$	—
12mxx	$1.13_{-0.19}^{+0.26}$	$2.59_{-0.16}^{+0.08}$	$44.3_{-4.2}^{+5.0}$	$-48.4_{-1.9}^{+2.1}$	$8.19_{-0.19}^{+0.13}$
13ajg	$1.98_{-0.08}^{+0.08}$	$1.73_{-0.09}^{+0.09}$	$33.8_{-1.3}^{+1.3}$	$-28.7_{-0.8}^{+1.4}$	—

weak correlation between the peak magnitude (at rest-frame 400 nm) and its decay after a certain time, and *iii*) the dependence of the peak magnitude (at rest-frame 400 nm) on the SLSN-I color (rest-frame 400–520 nm). We test similar correlations in the current sample.

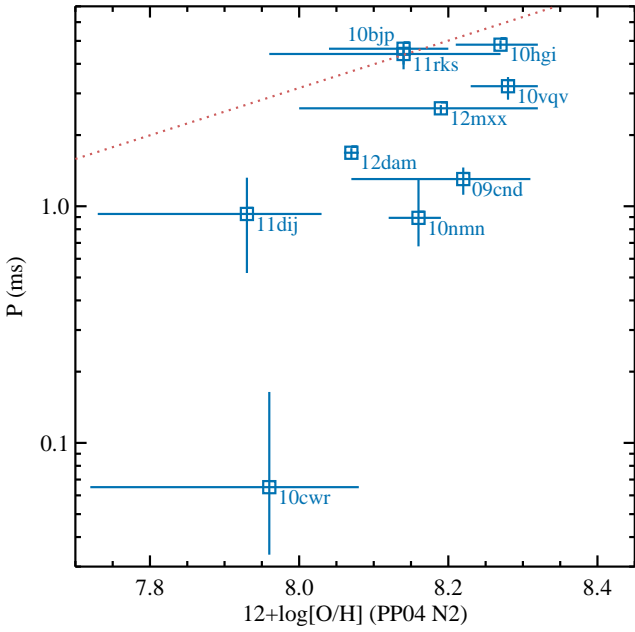


Figure 15. Magnetar spin and host-galaxy metallicity. The red dotted line shows the spin-metallicity correlation found by Chen et al. (2017).

i) We use the rest-frame g band as a proxy for the rest-frame 400 nm band of Inserra & Smartt (2014). The peak magnitudes of the SLSNe in our sample are widely distributed around their mean value ($< M_g > = -21.14$ mag), with a standard deviation of 0.75 mag, which is almost twice as in the sample of Inserra & Smartt (2014).

ii) Figure 16 shows the distribution of the rest-frame g peak magnitude, $M_{g,\text{peak}}$, with its decay, ΔM_g , at 10, 20, and 30 days after the peak. These were all calculated from the smoothed light curves (Sect. 4.3) and can therefore be slightly different from the $M_{g,\text{peak}}$ calculated with the second-order polynomial around the peak (Sect. 4.1). As a comparison, SLSNe-I and also Type Ic and Ic-BL SNe from PTF are shown in Fig. 16. There are very weak correlations, highlighted by the linear fits to the data. However, none of these trends are significant correlations. In every case, the Pearson correlation coefficient is $|r| < 0.3$, and the intrinsic scatter is up to ~ 0.8 mag for SLSNe-I; see Fig. 16. The intrinsic scatter of the correlation is the scatter required for the correlation to have $\chi^2 \sim 1$ (Bedregal et al. 2006; Williams et al. 2010), and it is a way of discriminating the observational scatter from what is intrinsic to the correlation. The data and fit results for SLSNe-I are reported in Tables 5 and 6, respectively.

iii) In Fig. 17 and Table 7, we compare the rest-frame g peak magnitude with the rest-frame $g - r$ color at peak. The rest-frame r was derived from the observed i -band photometry using the same techniques as described

Table 5. Rest-frame g magnitude at peak and its decay from the peak after 10, 20, and 30 days, calculated from the smoothed light curves (Sect. 4.3).

PTF ID	$M_{g,\text{peak}}$	$\Delta M_{g,10}$	$\Delta M_{g,20}$	$\Delta M_{g,30}$
09atu	-21.8 ± 0.1	0.1 ± 0.1	0.2 ± 0.2	0.3 ± 0.2
09cnd	-22.1 ± 0.1	0.1 ± 0.1	0.3 ± 0.1	0.4 ± 0.1
09cwl	-22.0 ± 0.1	0.1 ± 0.1	0.2 ± 0.1	0.3 ± 0.2
10aagc	-20.1 ± 0.1	0.7 ± 0.5	1.2 ± 0.5	2.0 ± 0.6
10cwr	-21.6 ± 0.1	0.2 ± 0.1	0.7 ± 0.1	1.2 ± 0.1
10hgi	-20.3 ± 0.1	0.1 ± 0.1	0.4 ± 0.1	1.1 ± 0.2
10vqv	-21.5 ± 0.1	0.2 ± 0.2	0.5 ± 0.2	0.8 ± 0.2
10vwg	-21.9 ± 0.1	0.2 ± 0.1	0.5 ± 0.2	1.0 ± 0.3
11dij	-21.4 ± 0.1	0.0 ± 0.1	0.4 ± 0.1	0.9 ± 0.1
11rks	-20.9 ± 0.1	0.2 ± 0.1	0.5 ± 0.1	1.2 ± 0.1
12dam	-21.7 ± 0.1	0.3 ± 0.1	0.4 ± 0.1	0.5 ± 0.1
12gty	-20.1 ± 0.1	0.3 ± 0.1	0.5 ± 0.1	0.6 ± 0.2
12hni	-19.9 ± 0.1	0.1 ± 0.1	0.4 ± 0.1	1.0 ± 0.2
13ajg	-22.4 ± 0.1	0.3 ± 0.1	0.8 ± 0.1	1.2 ± 0.1
13cjq	-21.1 ± 0.1	0.1 ± 0.2	0.5 ± 0.2	1.3 ± 0.4
13dcc	-22.0 ± 0.1	0.4 ± 0.1	0.6 ± 0.1	1.1 ± 0.1
13ehe	-21.3 ± 0.1	0.1 ± 0.2	0.1 ± 0.2	0.2 ± 0.2

Table 6. Fit parameters of the $M_{g,\text{peak}} = A + B \times \Delta M_g$ relation for SLSNe at different epochs (days after peak, see Fig. 16 and Table 5). Note. σ_{int} is the intrinsic scatter (see text). r and ρ are the Pearson and Spearman correlation coefficients, respectively, and are listed with their respective null probability (p_r and p_ρ).

t	A	B	σ_{int}	r	p_r	ρ	p_ρ
10	–	–	–	-0.24	0.37	-0.23	0.39
20	-20.9 ± 0.5	-1.2 ± 1.1	0.75	-0.10	0.71	-0.11	0.69
30	-21.7 ± 0.5	0.4 ± 0.5	0.76	0.14	0.60	0.15	0.57

for the r to rest-frame g conversion. The k -correction values are listed in Table C4. Both the rest-frame g - and r -band peaks were estimated by fitting a second-order polynomial to the data around peak. We could then constrain the rest-frame $g - r$ for a subsample of SLSNe-I, as listed in Table 7.

The correlation $M_{g,\text{peak}} = A + B \times (g - r)_{\text{peak}}$ is weak, with a Pearson correlation coefficient of 0.59 (null probability $p_r = 0.04$) and a Spearman correlation coefficient of 0.57 (null probability $p_\rho = 0.04$). The normalization and slope are $A = -19.5 \pm 1.2$ and $B = 7.5 \pm 3.8$. In this case, the intrinsic scatter is consistent with zero. While this may suggest a potentially real correlation, it may simply be the consequence of the large error bars that we measure for $g - r$. A larger statistical sample is needed to further investigate the solidity of this relation.

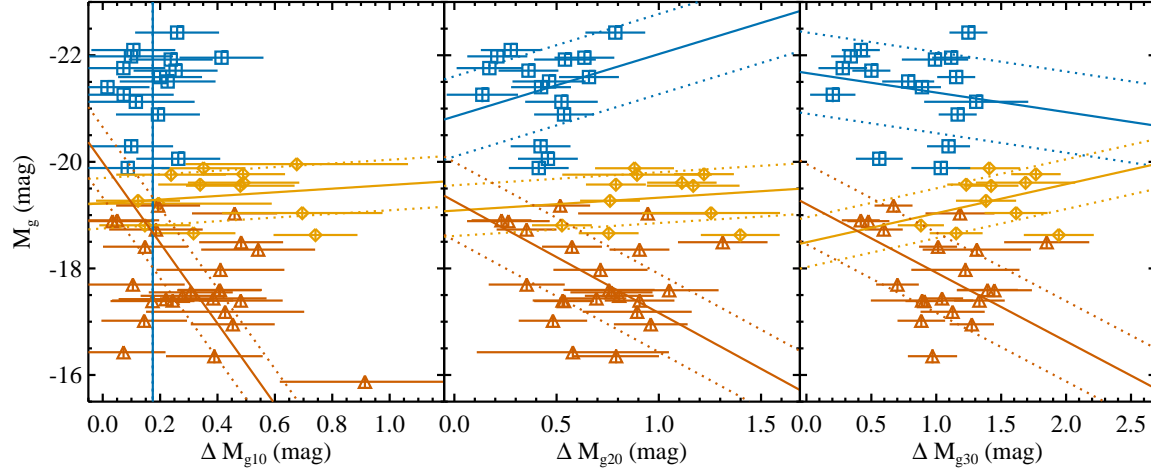


Figure 16. Rest-frame g magnitude at peak and its decay from the peak after 10 (left), 20 (middle), and 30 days (right panel). Blue squares show SLSNe-I, gold diamonds show SNe Ic-BL, and orange triangles SNe Ic, all from PTF. The solid and dotted lines show linear fits through the data and the intrinsic scatter, respectively.

Table 7. Rest-frame g and rest-frame $g - r$ magnitudes at peak for the SLSNe in our sample (see Fig. 17).

PTF ID	$M_{g,\text{peak}}$	$g - r(\text{peak})$
09atu	-21.78 ± 0.04	-0.24 ± 0.15
09cnd	-22.09 ± 0.03	-0.37 ± 0.07
10cwr	-21.59 ± 0.06	-0.25 ± 0.14
10hgj	-20.31 ± 0.02	-0.29 ± 0.16
11dij	-21.39 ± 0.19	-0.41 ± 0.19
11rks	-20.88 ± 0.13	-0.06 ± 0.19
12dam	-21.61 ± 0.05	-0.46 ± 0.15
12gtv	-19.90 ± 0.15	0.11 ± 0.23
12mxx	-21.60 ± 0.08	-0.06 ± 0.16
13ajg	-22.42 ± 0.16	-0.34 ± 0.19
13dcc	-21.88 ± 0.15	-0.64 ± 0.47
13ehe	-21.26 ± 0.20	-0.09 ± 0.22

The possible dust reddening $E(B - V)$ of the SLSN-I host galaxies is not taken into account here. While this should we expect the reddening to be small (e.g. Perley et al. 2016), there may be regions that are locally more dusty (e.g. Cikota et al. 2017). However, a case-to-case characterization of the host-galaxies' $E(B - V)$ is not possible here and is beyond the scope of this paper.

While we find the same overall trends as Inserra & Smartt (2014), the diagnostics above show mostly weaker correlations than reported by their work. One exception is the relation between the peak magnitude and $g - r$ at peak, for which we find a similar Pearson correlation coefficient to Inserra & Smartt (2014).

We further investigate possible correlations of M_g with other variables, such as the early decay slope or host

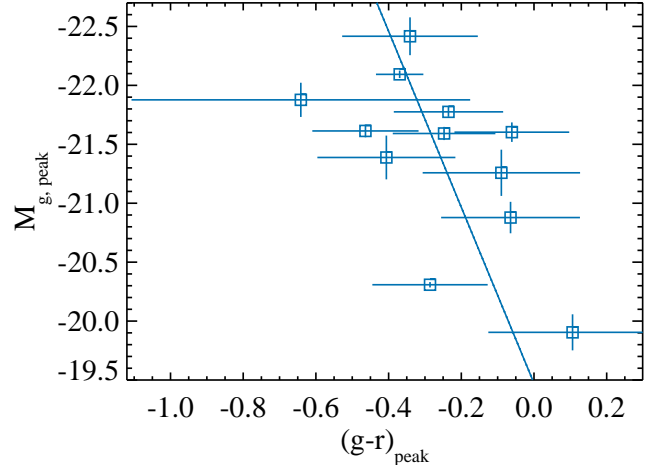


Figure 17. Rest-frame g peak magnitude versus the rest-frame $g - r$ color at peak, for PTF SLSNe. The solid line shows a linear fit to the data. The Pearson correlation coefficient is $r = 0.6$.

metallicity, with no convincing results. The weak trends of M_g with the rise and decay times are shown in Fig. 6. We therefore cannot strengthen the claim that SLSNe might be standardizable candles with the current data. Future transient surveys may clarify this issue with much improved statistics (e.g. Scovacricchi et al. 2016).

6. CONCLUSIONS

We study a sample of 26 SLSNe-I, all discovered by the PTF survey with light-curve coverage out to late times, well beyond 100 days after peak for half of the sample. Based on our analysis, we conclude the following.

1. The absolute peak magnitudes of PTF spectroscopically classified SLSNe-I are $-22.5 \lesssim M_g \lesssim -20$ mag (Sect. 4.1 and 5.1). The mean SLSN-I

- peak magnitude is -21.14 mag, which is brighter than the mean magnitudes of SNe Ic-BL and SNe Ib/c by about 2 and 4 mag, respectively. When including volumetric corrections, the peak-magnitude distribution evolves smoothly from SNe Ib/c to SNe Ic-BL, and to SLSNe-I. There is only very little overlap between the faintest SLSNe-I and the brightest SNe Ic-BL.
2. At early times (< 60 days after peak) SLSNe-I tend to decay faster (0.04 mag day $^{-1}$ on average) and with a wider range of decay rates than at late times (> 60 days); see Sect. 4.2 and 5.3.
 3. At late times, all SLSN-I light curves for which sufficient data are available cluster around the decay rate of ~ 1 mag per 100 days, which is consistent with the radioactive decay of ^{56}Co to stable ^{56}Fe (Sect. 4.2 and 5.3).
 4. We observe no gap between fast- and slow-declining SLSNe-I. Nevertheless, virtually all slow-declining events (SLSN-R) show early- and late-time bumps/plateau which are not as common in classical SLSNe-I. Thus, the possibility is still open that SLSN-I/R represent a subclass of SLSN-I (Sect. 4.2 and 5.3).
 5. SLSNe-I rise more slowly than SNe Ib/c and Ic-BL (i.e. SLSNe have longer rise timescales $t_{\text{rise}}^{\Delta 1\text{mag}}$ by roughly 10 days), even for similar decay times. Indeed, the rise times correlate differently with the decay times for SLSNe-I and SNe Ib/c (Sect. 4.4, 4.5, and 5.4).
 6. This implies that the light curves of SLSNe-I are different from SNe Ib/c and Ic-BL, and therefore SLSNe-I can be considered as a separate population photometrically, as well as spectroscopically.
 7. The peaks of SLSNe-I are not powered by the production of radioactive nickel, unless there are strong asymmetries in the ejecta (Sect. 5.6).
 8. Late-time light curves can be explained with the radioactive decay of Ni masses ranging from 1 to $10 M_{\odot}$. Radioactive decay might be an important powering source at these stages (Sect. 5.6).
 9. The slope of the late-time decay is in a few SLSNe-I faster than the radioactive decay. This can be explained by the escape of γ -rays from the massive ejecta. Our simulations of the radiative decay energy deposition for massive progenitors shows that the trapping is reduced for higher expansion velocities and higher Ni fractions of the ejected masses (Sect. 5.7).
 10. The majority of the SLSN-I light curves can reasonably well be reproduced also with a spinning-down magnetar model, with the exceptions of PTF 10hgi, PTF 10vvg, PTF 11dij, and PTF 11rks (Sect. 5.8). The derived magnetic fields lie in the parameter space where a magnetar model can mimic the radioactive decay of ^{56}Co .
 11. We cannot distinguish between a radioactively powered and magnetar light curves at this stage. Very late-time observations are needed to disentangle between the magnetar and radioactive models.
 12. We find no correlation between the magnetar spin and the host metallicity (Sect. 5.8).
 13. We find similar correlations to those claimed to make SLSN-I standardizable candles (Inserra & Smartt 2014); see Sect. 5.9. These correlations are significantly weaker, except for the correlation between the rest-frame g -band peak magnitude with the rest-frame $g - r$ at peak. With the current data, we cannot strengthen the potential of exploiting SLSNe for cosmology.

We thank the referee for a useful and constructive report, which helped make the paper more robust. We thank L. Dessart, A. Jerkstrand, A. Kozyreva, and the SLSN MIAPP 2017 workshop participants for insightful discussions. A.D.C. acknowledges support by the Weizmann Institute of Science Koshland Center for Basic Research. Support for I.A. was provided by NASA through the Einstein Fellowship Program, grant PF6-170148. M.S. acknowledges support from EU/FP7-ERC grant No. [615929]. K.M. acknowledges support from the STFC through an Ernest Rutherford Fellowship. E.O.O. is grateful for support by grants from the Israel Science Foundation, Minerva, Israeli ministry of Science, the US-Israel Binational Science Foundation and the I-CORE Program of the Planning and Budgeting Committee and The Israel Science Foundation. A.C. acknowledges support from the NSF CAREER award 1455090. M.M.K. acknowledges support from the GROWTH project funded by the National Science Foundation under Grant No. 1545949. The intermediate Palomar Transient Factory project is a scientific collaboration among the California Institute of Technology, Los Alamos National Laboratory, the University of Wisconsin, Milwaukee, the Oskar Klein Center, the Weizmann Institute of Science, the TANGO Program of the University System of Taiwan, and the Kavli Institute for the Physics and Mathematics of the Universe. LANL participation in iPTF is supported by the

US Department of Energy as a part of the Laboratory Directed Research and Development program. A portion of this work was carried out at the Jet Propulsion Laboratory under a Research and Technology Development Grant, under contract with the National Aeronautics and Space Administration. This research has made use of the NASA/ IPAC Infrared Science Archive, which is operated by the Jet Propulsion Laboratory, California Institute of Technology, under contract with the National Aeronautics and Space Administration. This research has made use of NASA's Astrophysics Data System. This paper made use of Lowell Observatory's Discovery Channel Telescope (DCT). Lowell operates the DCT in partnership with Boston University, Northern Arizona University, the University of Maryland, and the University of Toledo. Partial support of the DCT was provided by Discovery Communications. Large Monolithic Imager (LMI) on DCT was built by Lowell Observatory using funds from the National Science Foundation.

dation (AST-1005313). This work makes use of observations taken with the LCO network. This research has made use of the NASA/IPAC Extragalactic Database (NED) which is operated by the Jet Propulsion Laboratory, California Institute of Technology, under contract with the National Aeronautics and Space Administration. Some of the data presented herein were obtained at the W.M. Keck Observatory, which is operated as a scientific partnership among the California Institute of Technology, the University of California and the National Aeronautics and Space Administration. The Observatory was made possible by the generous financial support of the W.M. Keck Foundation. The authors wish to recognize and acknowledge the very significant cultural role and reverence that the summit of Maunakea has always had within the indigenous Hawaiian community. We are most fortunate to have the opportunity to conduct observations from this mountain.

REFERENCES

- Abbott, T., Cooke, J., Curtin, C., et al. 2017, PASA, 34, e012
 Ahn, C. P., Alexandroff, R., Allende Prieto, C., et al. 2014, ApJS, 211, 17
 Arcavi, I., Gal-Yam, A., Kasliwal, M. M., et al. 2010, ApJ, 721, 777
 Arnett, W. D. 1979, ApJL, 230, L37
 —. 1982, ApJ, 253, 785
 Barkat, Z., Rakavy, G., & Sack, N. 1967, Physical Review Letters, 18, 379
 Bazin, G., Ruhlmann-Kleider, V., Palanque-Delabrouille, N., et al. 2011, A&A, 534, A43
 Bedregal, A. G., Aragón-Salamanca, A., & Merrifield, M. R. 2006, MNRAS, 373, 1125
 Bertin, E., Mellier, Y., Radovich, M., et al. 2002, in Astronomical Society of the Pacific Conference Series, Vol. 281, Astronomical Data Analysis Software and Systems XI, ed. D. A. Bohlender, D. Durand, & T. H. Handley, 228
 Bessell, M. S. 1990, PASP, 102, 1181
 Breeveld, A. A., Curran, P. A., Hoversten, E. A., et al. 2010, MNRAS, 406, 1687
 Brown, T. M., Baliber, N., Bianco, F. B., et al. 2013, PASP, 125, 1031
 Cao, Y., Nugent, P. E., & Kasliwal, M. M. 2016, PASP, 128, 114502
 Cardelli, J. A., Clayton, G. C., & Mathis, J. S. 1989, ApJ, 345, 245
 Cenko, S. B., Fox, D. B., Moon, D.-S., et al. 2006, PASP, 118, 1396
 Chatzopoulos, E., Wheeler, J. C., & Vinko, J. 2012, ApJ, 746, 121
 Chen, T.-W., Smartt, S. J., Yates, R. M., et al. 2017, MNRAS, 470, 3566
 Chen, T.-W., Smartt, S. J., Jerkstrand, A., et al. 2015, MNRAS, 452, 1567
 Chevalier, R. A., & Fransson, C. 1994, ApJ, 420, 268
 Chevalier, R. A., & Irwin, C. M. 2011, ApJL, 729, L6
 Chugai, N. N., & Danziger, I. J. 1994, MNRAS, 268, 173
 Cikota, A., De Cia, A., Schulze, S., et al. 2017, MNRAS, 469, 4705
 Cooke, J., Sullivan, M., Gal-Yam, A., et al. 2012, Nature, 491, 228
 Corsi, A., Gal-Yam, A., Kulkarni, S. R., et al. 2016, ApJ, 830, 42
 Curtin, C., Cooke, J., Moriya, T. J., et al. 2018, ArXiv e-prints, arXiv:1801.08241
 Dessart, L., & Hillier, D. J. 2011, MNRAS, 410, 1739
 Dessart, L., Hillier, D. J., Waldman, R., Livne, E., & Blondin, S. 2012, MNRAS, 426, L76
 Dessart, L., Hillier, D. J., Yoon, S.-C., Waldman, R., & Livne, E. 2017, ArXiv e-prints, arXiv:1703.08932
 Dimitriadis, G., Sullivan, M., Kerzendorf, W., et al. 2017, MNRAS, 468, 3798
 Firth, R. E., Sullivan, M., Gal-Yam, A., et al. 2015, MNRAS, 446, 3895
 Fransson, C., & Kozma, C. 2002, NewAR, 46, 487
 Fukugita, M., Ichikawa, T., Gunn, J. E., et al. 1996, AJ, 111, 1748
 Gal-Yam, A. 2012, Science, 337, 927
 Gal-Yam, A., Moon, D.-S., Fox, D. B., et al. 2004, ApJL, 609, L59
 Gal-Yam, A., Nakar, E., Ofek, E. O., et al. 2008, ApJ, 686, 408
 Gal-Yam, A., Mazzali, P., Ofek, E. O., et al. 2009, Nature, 462, 624
 Gal-Yam, A., Kasliwal, M. M., Arcavi, I., et al. 2011, ApJ, 736, 159
 Gehrels, N., Chincarini, G., Giommi, P., et al. 2004, ApJ, 611, 1005
 Heger, A., & Woosley, S. E. 2002, ApJ, 567, 532
 Henden, A. A., Welch, D. L., Terrell, D., & Levine, S. E. 2009, in American Astronomical Society Meeting Abstracts, Vol. 214, American Astronomical Society Meeting Abstracts 214, 407.02
 Hogg, D. W. 1999, ArXiv Astrophysics e-prints, astro-ph/9905116
 Hogg, D. W., Baldry, I. K., Blanton, M. R., & Eisenstein, D. J. 2002, ArXiv Astrophysics e-prints, astro-ph/0210394
 Hogg, D. W., Blanton, M., Lang, D., Mierle, K., & Roweis, S. 2008, in Astronomical Society of the Pacific Conference Series, Vol. 394, Astronomical Data Analysis Software and Systems XVII, ed. R. W. Argyle, P. S. Bunclark, & J. R. Lewis, 27
 Inserra, C., & Smartt, S. J. 2014, ApJ, 796, 87

- Inserra, C., Smartt, S. J., Jerkstrand, A., et al. 2013, *ApJ*, 770, 128
- Inserra, C., Nicholl, M., Chen, T.-W., et al. 2017, *MNRAS*, 468, 4642
- Inserra, C., Smartt, S. J., Gall, E. E. E., et al. 2018, *MNRAS*, 475, 1046
- Jeffery, D. J. 1999, ArXiv Astrophysics e-prints, astro-ph/9907015
- Jerkstrand, A., Smartt, S. J., Inserra, C., et al. 2017, *ApJ*, 835, 13
- Jones, D. O., Rodney, S. A., Riess, A. G., et al. 2013, *ApJ*, 768, 166
- Junde, H., Su, H., & Dong, Y. 2011, Nuclear Data Sheets, 112, 1513
- Kaiser, N., Burgett, W., Chambers, K., et al. 2010, in Society of Photo-Optical Instrumentation Engineers (SPIE) Conference Series, Vol. 7733, Society of Photo-Optical Instrumentation Engineers (SPIE) Conference Series, 0
- Kasen, D., & Bildsten, L. 2010, *ApJ*, 717, 245
- Kozyreva, A., & Blinnikov, S. 2015, *MNRAS*, 454, 4357
- Laher, R. R., Surace, J., Grillmair, C. J., et al. 2014, *PASP*, 126, 674
- Law, N. M., Kulkarni, S. R., Dekany, R. G., et al. 2009, *PASP*, 121, 1395
- Leloudas, G., Chatzopoulos, E., Dilday, B., et al. 2012, *A&A*, 541, A129
- Leloudas, G., Schulze, S., Krühler, T., et al. 2015, *MNRAS*, 449, 917
- Liu, L.-D., Wang, L.-J., Wang, S.-Q., & Dai, Z.-G. 2017, ArXiv e-prints, arXiv:1706.01783
- Lunnan, R., Chornock, R., Berger, E., et al. 2015, *ApJ*, 804, 90
- . 2016, *ApJ*, 831, 144
- . 2018, *ApJ*, 852, 81
- Maeda, K., Mazzali, P. A., & Nomoto, K. 2006, *ApJ*, 645, 1331
- Maeda, K., Nakamura, T., Nomoto, K., et al. 2002, *ApJ*, 565, 405
- Maguire, K., Sullivan, M., Pan, Y.-C., et al. 2014, *MNRAS*, 444, 3258
- Mazzali, P. A., Nomoto, K., Patat, F., & Maeda, K. 2001, *ApJ*, 559, 1047
- Mazzali, P. A., Sullivan, M., Pian, E., Greiner, J., & Kann, D. A. 2016, *MNRAS*, 458, 3455
- McCrumb, M., Smartt, S. J., Rest, A., et al. 2015, *MNRAS*, 448, 1206
- Moriya, T. J., Chen, T.-W., & Langer, N. 2017, *ApJ*, 835, 177
- Moriya, T. J., & Tominaga, N. 2012, *ApJ*, 747, 118
- Moriya, T. J., Tanaka, M., Yasuda, N., et al. 2018, ArXiv e-prints, arXiv:1801.08240
- Nadyozhin, D. K. 1994, *ApJS*, 92, 527
- Nakar, E., & Sari, R. 2010, *ApJ*, 725, 904
- Neill, J. D., Sullivan, M., Gal-Yam, A., et al. 2011, *ApJ*, 727, 15
- Nicholl, M., Guillochon, J., & Berger, E. 2017, *ApJ*, 850, 55
- Nicholl, M., & Smartt, S. J. 2016, *MNRAS*, 457, L79
- Nicholl, M., Smartt, S. J., Jerkstrand, A., et al. 2013, *Nature*, 502, 346
- . 2015a, *ApJL*, 807, L18
- . 2015b, *MNRAS*, 452, 3869
- Nicholl, M., Berger, E., Smartt, S. J., et al. 2016, *ApJ*, 826, 39
- O'Donnell, J. E. 1994, *ApJ*, 422, 158
- Ofek, E. O., Cameron, P. B., Kasliwal, M. M., et al. 2007, *ApJL*, 659, L13
- Ofek, E. O., Laher, R., Surace, J., et al. 2012, *PASP*, 124, 854
- Ofek, E. O., Fox, D., Cenko, S. B., et al. 2013, *ApJ*, 763, 42
- Ofek, E. O., Arcavi, I., Tal, D., et al. 2014a, *ApJ*, 788, 154
- Ofek, E. O., Zoglauer, A., Boggs, S. E., et al. 2014b, *ApJ*, 781, 42
- Pastorello, A., Smartt, S. J., Botticella, M. T., et al. 2010, *ApJL*, 724, L16
- Perley, D. A., Quimby, R. M., Yan, L., et al. 2016, *ApJ*, 830, 13
- Piro, A. L. 2015, *ApJL*, 808, L51
- Poole, T. S., Breeveld, A. A., Page, M. J., et al. 2008, *MNRAS*, 383, 627
- Prentice, S. J., Mazzali, P. A., Pian, E., et al. 2016, *MNRAS*, 458, 2973
- Pun, C. S. J., Kirshner, R. P., Sonneborn, G., et al. 1995, *ApJS*, 99, 223
- Quimby, R. M., Aldering, G., Wheeler, J. C., et al. 2007, *ApJL*, 668, L99
- Quimby, R. M., Kulkarni, S. R., Kasliwal, M. M., et al. 2011, *Nature*, 474, 487
- Quimby, R. M., De Cia, A., Gal-Yam, A., et al. 2018, ArXiv e-prints, arXiv:1802.07820
- Rabinak, I., & Waxman, E. 2011, *ApJ*, 728, 63
- Rahmer, G., Smith, R., Velur, V., et al. 2008, in Proc. SPIE, Vol. 7014, Ground-based and Airborne Instrumentation for Astronomy II, 70144Y
- Rau, A., Kulkarni, S. R., Law, N. M., et al. 2009, *PASP*, 121, 1334
- Roming, P. W. A., Kennedy, T. E., Mason, K. O., et al. 2005, *SSRv*, 120, 95
- Rubin, A., Gal-Yam, A., De Cia, A., et al. 2016, *ApJ*, 820, 33
- Schlafly, E. F., & Finkbeiner, D. P. 2011, *ApJ*, 737, 103
- Schulze, S., Krühler, T., Leloudas, G., et al. 2018, *MNRAS*, 473, 1258
- Scovacricchi, D., Nichol, R. C., Bacon, D., Sullivan, M., & Prajs, S. 2016, *MNRAS*, 456, 1700
- SDSS Collaboration, Albareti, F. D., Allende Prieto, C., et al. 2016, ArXiv e-prints, arXiv:1608.02013
- Seitenzahl, I. R., Timmes, F. X., & Magkotsios, G. 2014, *ApJ*, 792, 10
- Smith, M., Sullivan, M., D'Andrea, C. B., et al. 2016, *ApJL*, 818, L8
- Smith, N., Li, W., Foley, R. J., et al. 2007, *ApJ*, 666, 1116
- Steele, I. A., Smith, R. J., Rees, P. C., et al. 2004, in Society of Photo-Optical Instrumentation Engineers (SPIE) Conference Series, Vol. 5489, Ground-based Telescopes, ed. J. M. Oschmann, Jr., 679–692
- Stritzinger, M., & Leibundgut, B. 2005, *A&A*, 431, 423
- Sullivan, M., Howell, D. A., Perrett, K., et al. 2006, *AJ*, 131, 960
- Taddia, F., Sollerman, J., Leloudas, G., et al. 2015, *A&A*, 574, A60
- Taddia, F., Sollerman, J., Fremling, C., et al. 2018a, *A&A*, 609, A106
- Taddia, F., Stritzinger, M. D., Bersten, M., et al. 2018b, *A&A*, 609, A136
- Thöne, C. C., de Ugarte Postigo, A., García-Benito, R., et al. 2015, *MNRAS*, 451, L65
- Thuan, T. X., & Gunn, J. E. 1976, *PASP*, 88, 543
- Valenti, S., Taubenberger, S., Pastorello, A., et al. 2012, *ApJL*, 749, L28
- Valenti, S., Howell, D. A., Stritzinger, M. D., et al. 2016, *MNRAS*, 459, 3939
- van Dokkum, P. G. 2001, *PASP*, 113, 1420
- Vreeswijk, P. M., Savaglio, S., Gal-Yam, A., et al. 2014, *ApJ*, 797, 24
- Vreeswijk, P. M., Leloudas, G., Gal-Yam, A., et al. 2017, *ApJ*, 835, 58
- Wheeler, J. C., & Benetti, S. 2000, *Supernovae*, ed. A. N. Cox, 451
- Williams, M. J., Bureau, M., & Cappellari, M. 2010, *MNRAS*, 409, 1330
- Woosley, S. E. 2010, *ApJL*, 719, L204
- Yan, L., Quimby, R., Ofek, E., et al. 2015, *ApJ*, 814, 108
- Yan, L., Lunnan, R., Perley, D., et al. 2017, ArXiv e-prints, arXiv:1704.05061

York, D. G., Adelman, J., Anderson, Jr., J. E., et al. 2000, AJ,

120, 1579

Zacharias, N., Monet, D. G., Levine, S. E., et al. 2004, in
Bulletin of the American Astronomical Society, Vol. 36,
American Astronomical Society Meeting Abstracts, 1418

APPENDIX

A. SLSN-I LIGHT-CURVE PROPERTIES

The light-curve properties of the (i)PTF SLSN-I sample that we derived above (i.e. peak magnitude, early- and late-time decay, rise and decay timescales) are reported in Table A1.

Table A1. Light-curve properties of the H-poor SLSN sample

PTF ID	MJD_{peak}	Mg, peak (mag)	$\chi^2_{\nu, \text{peak}}/\nu$	Slope1 ^a (mag day ⁻¹)	$\chi^2_{\nu, \text{Slope1}}/\nu$	Slope2 ^a (mag day ⁻¹)	$\chi^2_{\nu, \text{Slope2}}/\nu$	Int ^b (days)	$t_{\text{rise}}^{1\text{mag}}$ (days)	$t_{\text{fall}}^{1\text{mag}}$ (days)	$t_{\text{rise},1/2}$ (days)	$t_{\text{fall},1/2}$ (days)
09as	54918.20	(-19.51 ± 0.13)	0.30/8	0.0830 ± 0.0121	0.27/9	—	—	—	11 ± 3	—	9 ± 3	
09atu	55062.32	-21.78 ± 0.04	0.20/22	0.0137 ± 0.0052	0.27/13	—	—	—	37 ± 2	70 ± 8	32 ± 3	61 ± 11
09cnd	55086.35	-22.09 ± 0.03	0.17/28	0.0226 ± 0.0018	0.61/8	—	—	—	33 ± 2	54 ± 6	29 ± 2	45 ± 4
09cwl	55067.25	-22.03 ± 0.13	0.44/3	0.0320 ± 0.0012	0.98/2	—	—	—	25 ± 2	—	21 ± 2	54 ± 7
10aagc	55499.48	-20.12 ± 0.25	1.69/28	0.0745 ± 0.0042	1.16/26	—	—	—	17 ± 9	—	11 ± 5	
10bfz	55227.46	(-20.86 ± 0.03)	0.15/5	0.0658 ± 0.0026	0.85/30	—	—	—	33 ± 4	—	28 ± 2	
10bjp	55252.52	-20.52 ± 0.16	0.41/9	0.0241 ± 0.0154	1.73/4	—	—	—	42 ± 2	—	—	—
10cwr	55281.23	-21.59 ± 0.06	0.46/10	0.0675 ± 0.0038	3.76/2	—	—	—	28 ± 2	—	23 ± 2	
10hgj	55367.43	-20.31 ± 0.02	0.09/22	0.0519 ± 0.0033	0.92/12	0.0211 ± 0.0011	0.93/12	37.7	32 ± 2	28 ± 2	29 ± 2	25 ± 2
10nmn	55384.20	-20.53 ± 0.04	0.02/2	—	—	0.0080 ± 0.0003	0.26/16	—	—	61 ± 18	—	—
10uhf	55452.25	-20.60 ± 0.22	1.50/12	0.0356 ± 0.0072	1.48/6	—	—	—	—	—	—	—
10vqv	55470.52	-21.58 ± 0.11	0.40/14	0.0338 ± 0.0043	0.12/6	0.0186 ± 0.0084	0.27/5	55.6	—	36 ± 5	—	29 ± 5
10vvg	55455.29	-21.94 ± 0.20	2.89/19	0.0451 ± 0.0019	9.48/8	0.0119 ± 0.0029	0.67/5	43.0	39 ± 2	—	33 ± 3	25 ± 4
11dij	55684.37	-21.39 ± 0.19	5.44/22	0.0550 ± 0.0005	4.92/30	0.0141 ± 0.0018	0.26/3	74.5	15 ± 2	31 ± 2	13 ± 2	27 ± 2
11hrq	55753.48	(-19.80 ± 0.04)	0.32/23	0.0156 ± 0.0006	0.45/45	0.0163 ± 0.0006	1.25/58	7.4	—	55 ± 6	—	37 ± 7
11rks	55935.14	-20.88 ± 0.13	1.84/50	0.0501 ± 0.0021	1.62/30	0.0085 ± 0.0072	1.39/2	60.0	17 ± 2	27 ± 2	15 ± 2	24 ± 2
12dam	56092.33	-21.61 ± 0.05	4.72/45	0.0137 ± 0.0002	4.84/17	0.0178 ± 0.0002	5.35/52	113.4	34 ± 2	62 ± 5	29 ± 2	49 ± 6
12gty	56143.36	-19.90 ± 0.15	0.80/20	0.0277 ± 0.0031	2.41/9	0.0115 ± 0.0028	0.88/7	54.9	36 ± 3	41 ± 11	28 ± 3	36 ± 5
12hni	56154.25	-19.92 ± 0.10	1.78/11	0.0470 ± 0.0016	1.21/11	-0.0217 ± 0.0071	0.52/4	74.1	—	29 ± 4	—	25 ± 2
12mxx	56292.14	-21.60 ± 0.08	0.93/30	—	—	—	—	—	29 ± 2	—	26 ± 2	—
13ajg	56410.35	-22.42 ± 0.16	1.00/69	0.0376 ± 0.0033	1.86/50	0.0096 ± 0.0008	10.32/1	87.6	24 ± 2	25 ± 2	21 ± 2	19 ± 2
13bdd	56493.22	-20.36 ± 0.22	0.66/28	—	—	—	—	—	—	—	—	—
13bjz	56438.17	-20.81 ± 0.18	2.53/15	—	—	—	—	—	—	—	8 ± 2	—
13cjg	56506.28	-21.13 ± 0.09	0.66/45	0.0409 ± 0.0056	2.71/7	0.0046 ± 0.0052	0.79/2	49.3	—	25 ± 5	—	23 ± 3
13dcc	56612.35	-21.88 ± 0.15	0.59/49	0.0476 ± 0.0044	1.96/15	0.0122 ± 0.0007	0.88/3	62.3	—	28 ± 2	—	24 ± 3
13ehe	56669.54	-21.26 ± 0.20	0.92/31	0.0062 ± 0.0065	1.29/4	0.0158 ± 0.0007	0.14/1	37.9	—	114 ± 7	—	97 ± 10

NOTE—SLSNe with best sampled data, where the light curves can be fully characterized in their rise and fall times, peaks, early- and late-time declines, are highlighted in bold. Peak magnitudes are in parenthesis for the cases where the peak is not sufficiently covered, so these represent magnitude upper limits. The peak magnitude for PTF 10nmn is taken from Yaron et al. (2018 in preparation), which includes a more complete coverage of the peak. In the case of PTF 12hni the late-time decay slope is negative because of the light curve rebrightening. The χ^2_{ν} are sometimes large because the formal errors in the observed magnitudes within the fitted time interval are very small (e.g. between 0.006 and 0.024 mag around peak for PTF 12dam). ^a Slopes of the postpeak early- and late-time linear fit to the data (Sect. 4.2). ^b Intersection between the postpeak early- and late-times linear fits to the data (in days after peak, Sect. 4.2).

B. APPENDIX FIGURES

The figures below show the light curves of (i)PTF SLSNe-I in our sample, their rise and decay timescales in flux and magnitudes, the magnetar fits to the data, and their confidence levels.

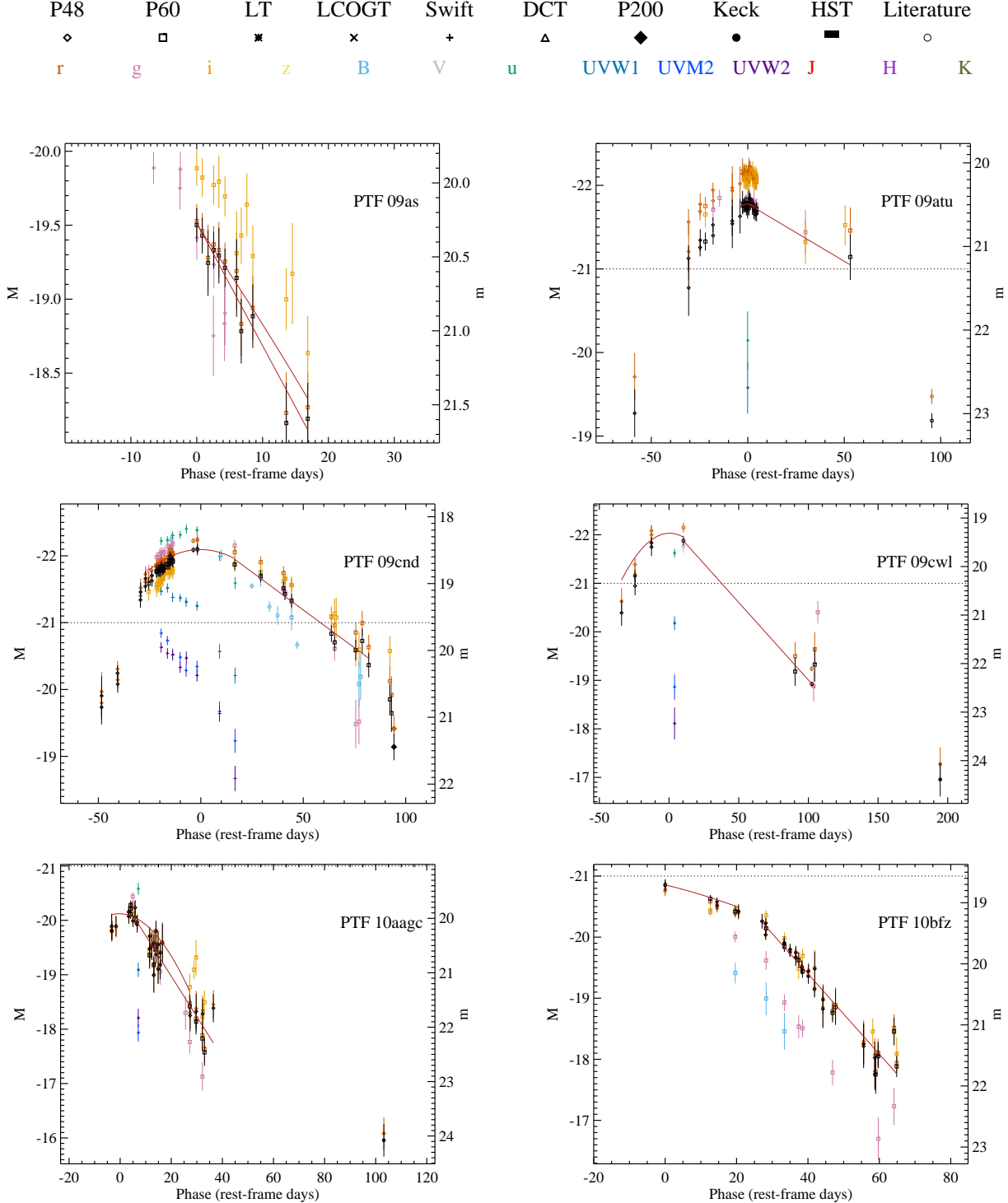


Figure B1. Light curves of (i)PTF SLSNe-I in our sample for individual observed filters and rest-frame M_g (black). Both apparent and absolute magnitudes are corrected for Galactic foreground dust extinction (see Sect. 3.12). The solid lines show the second-order polynomial fit around peak (Sect. 4.1) and the postpeak early- and late-time decay linear fits to the data (Sect. 4.2). The horizontal dotted line marks the $M = -21$ mag “historical” threshold for SLSNe, for comparison.

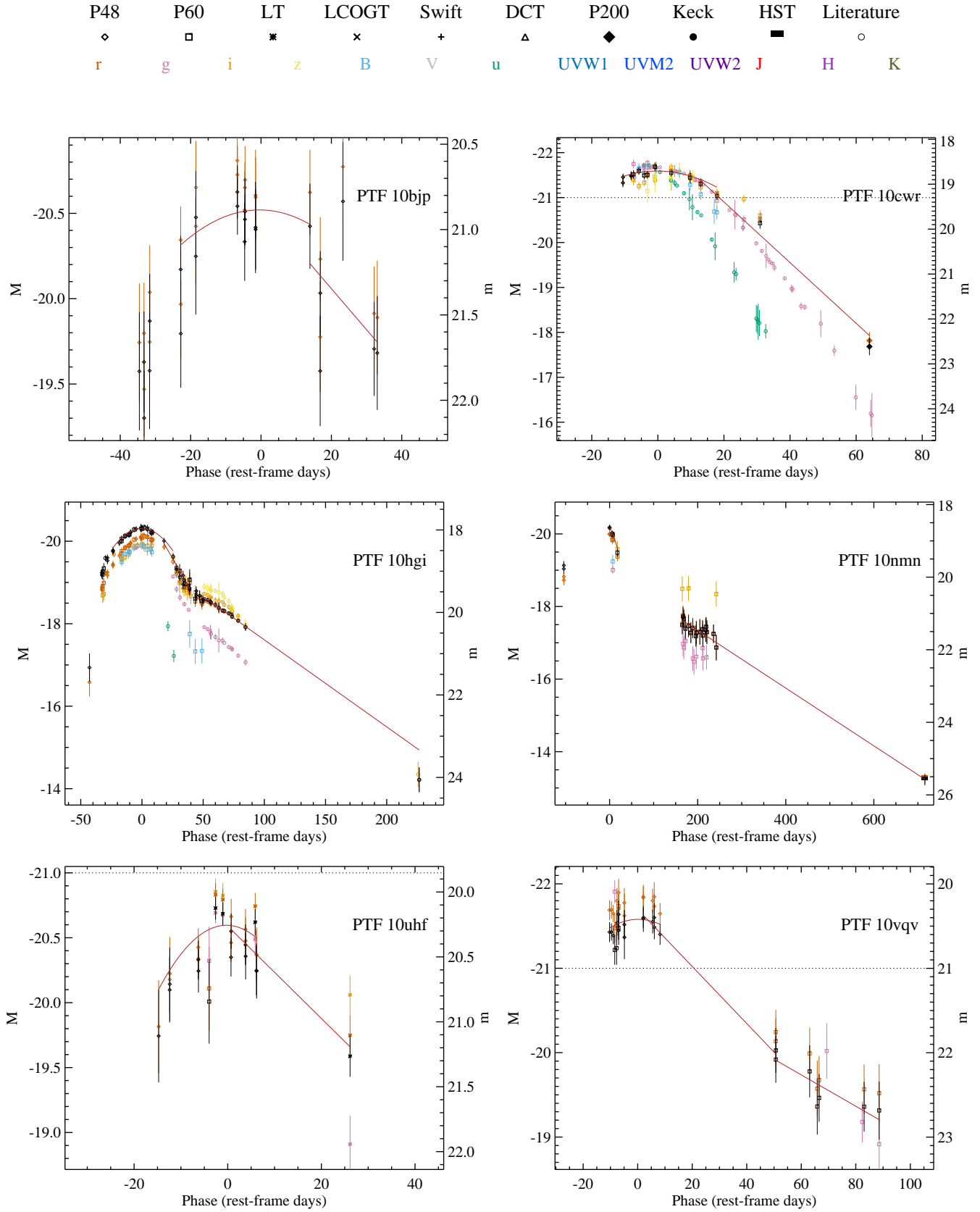


Figure B2. Continuation of Fig. B1.

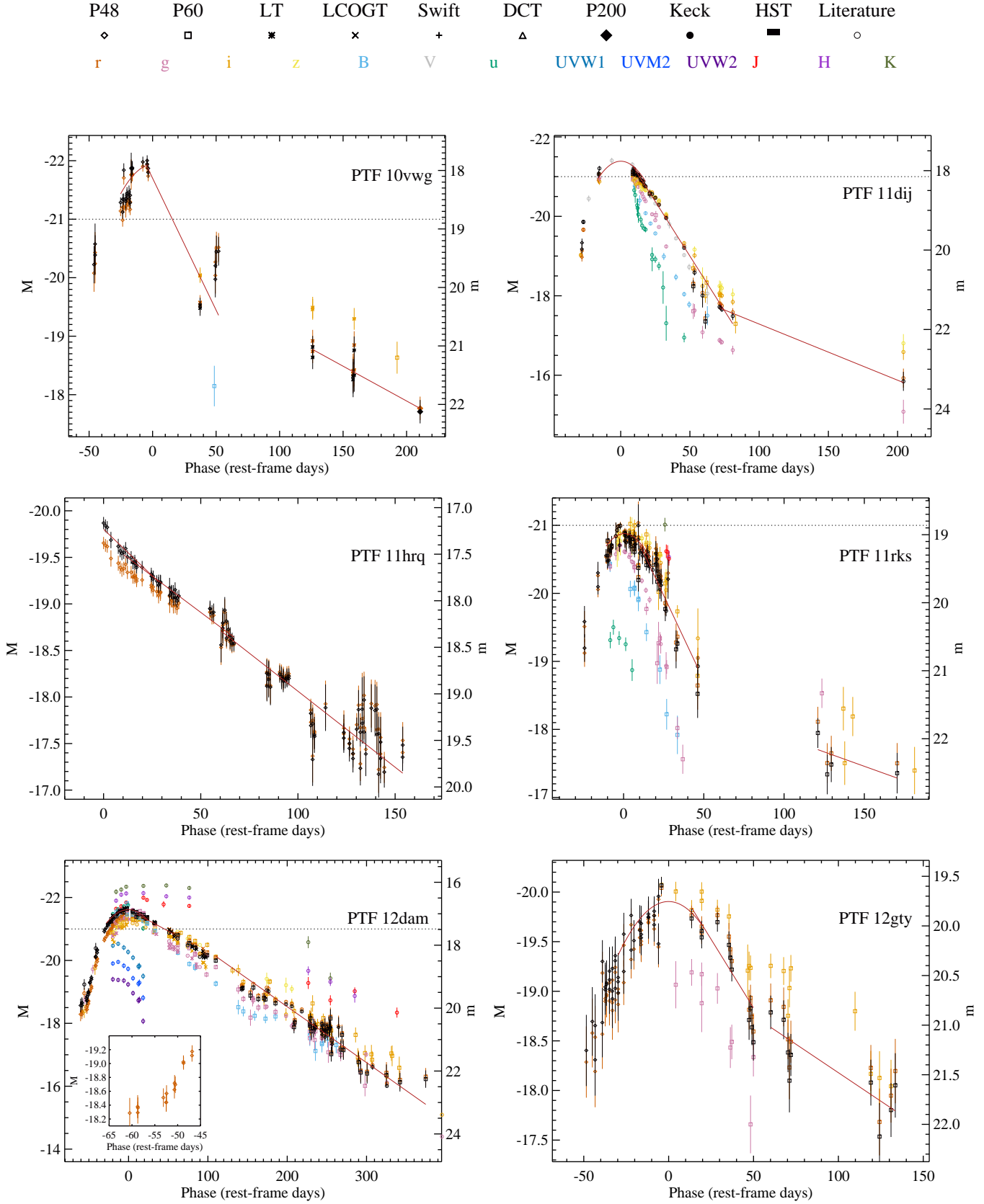


Figure B3. Continuation of Fig. B1.

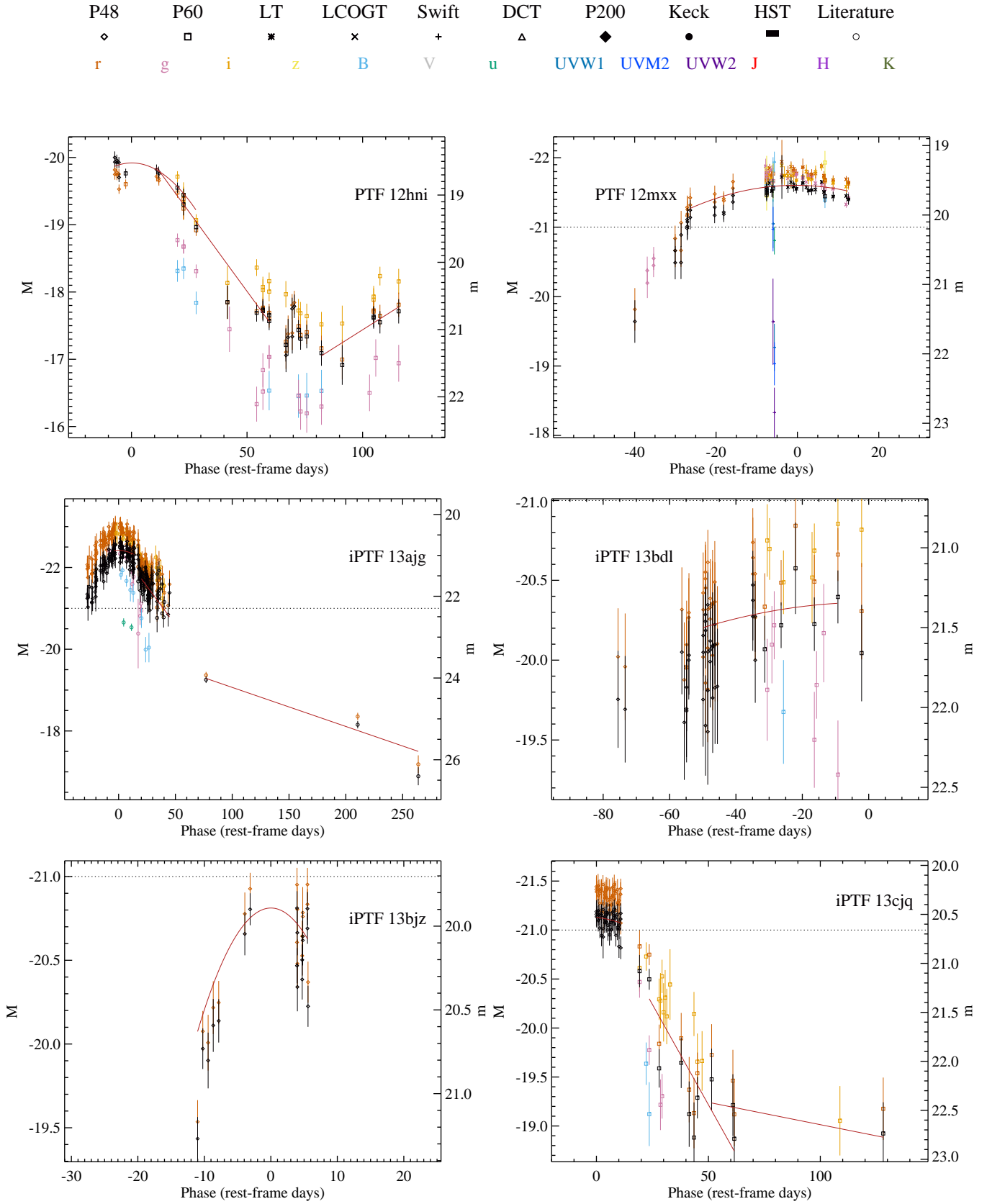


Figure B4. Continuation of Fig. B1.

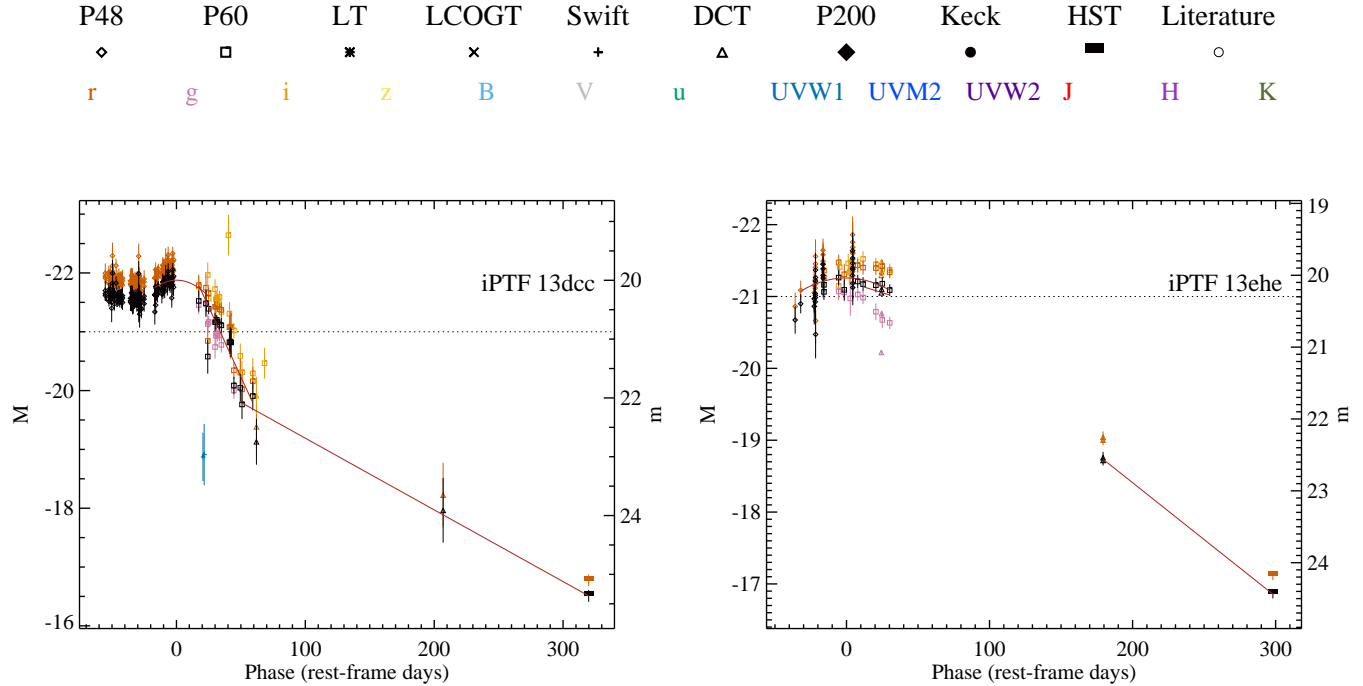


Figure B5. Continuation of Fig. B1.

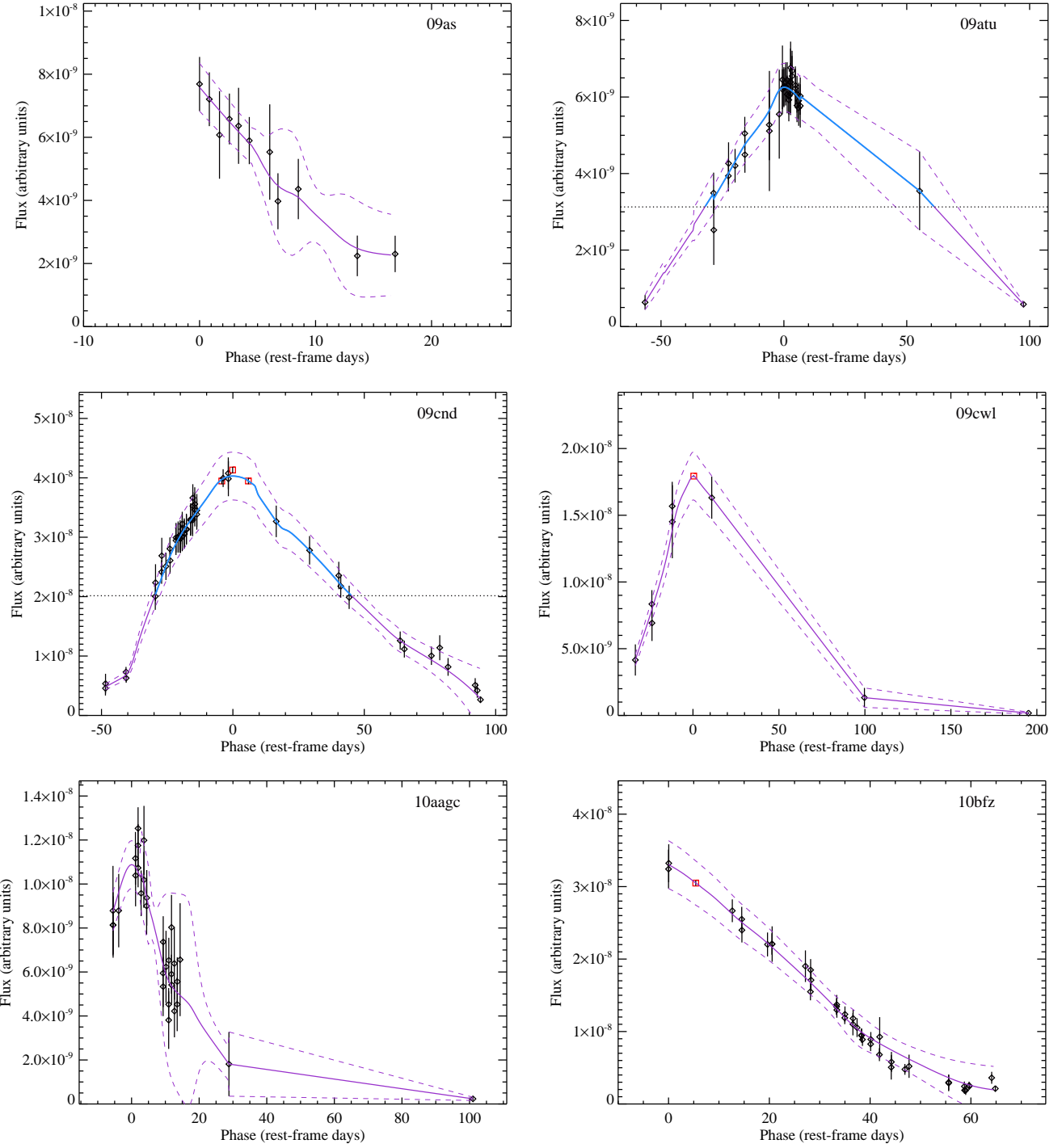


Figure B6. Rest-frame g -band light curves of the SLSNe-I in flux (black diamonds). The smoothed light curves (described in Sect. 4.3) are shown by the solid curves. The red squares indicate the auxiliary points introduced for the light-curve smoothing. The horizontal dotted line marks the half-flux limit, which is used to calculate the $t_{\text{rise},1/2}$ and $t_{\text{fall},1/2}$ timescales (Sect. 5.4), when the light curve is well-characterized between the half-flux limit and the peak (highlighted blue solid curves).

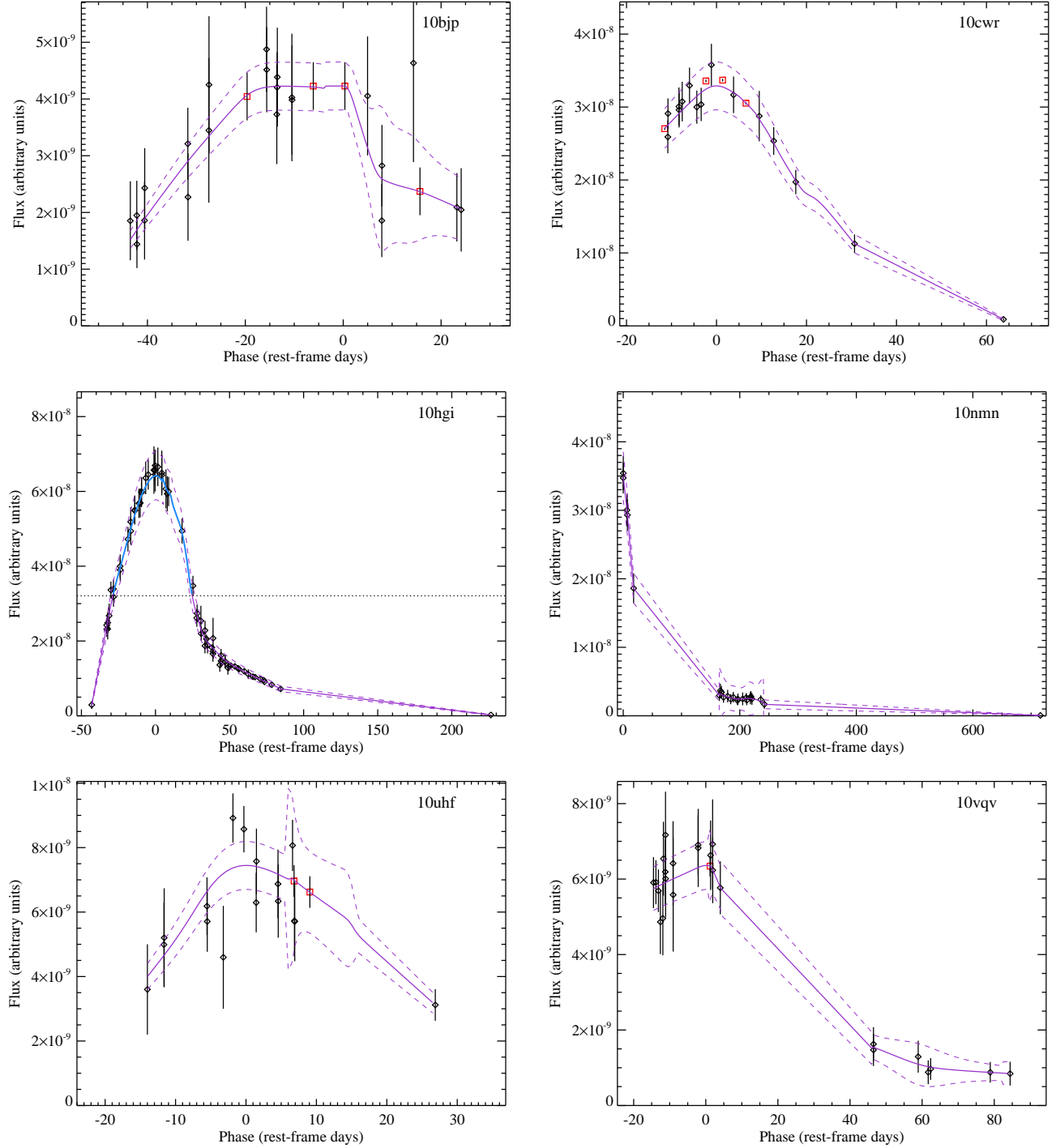


Figure B7. Continuation of Fig. B6.

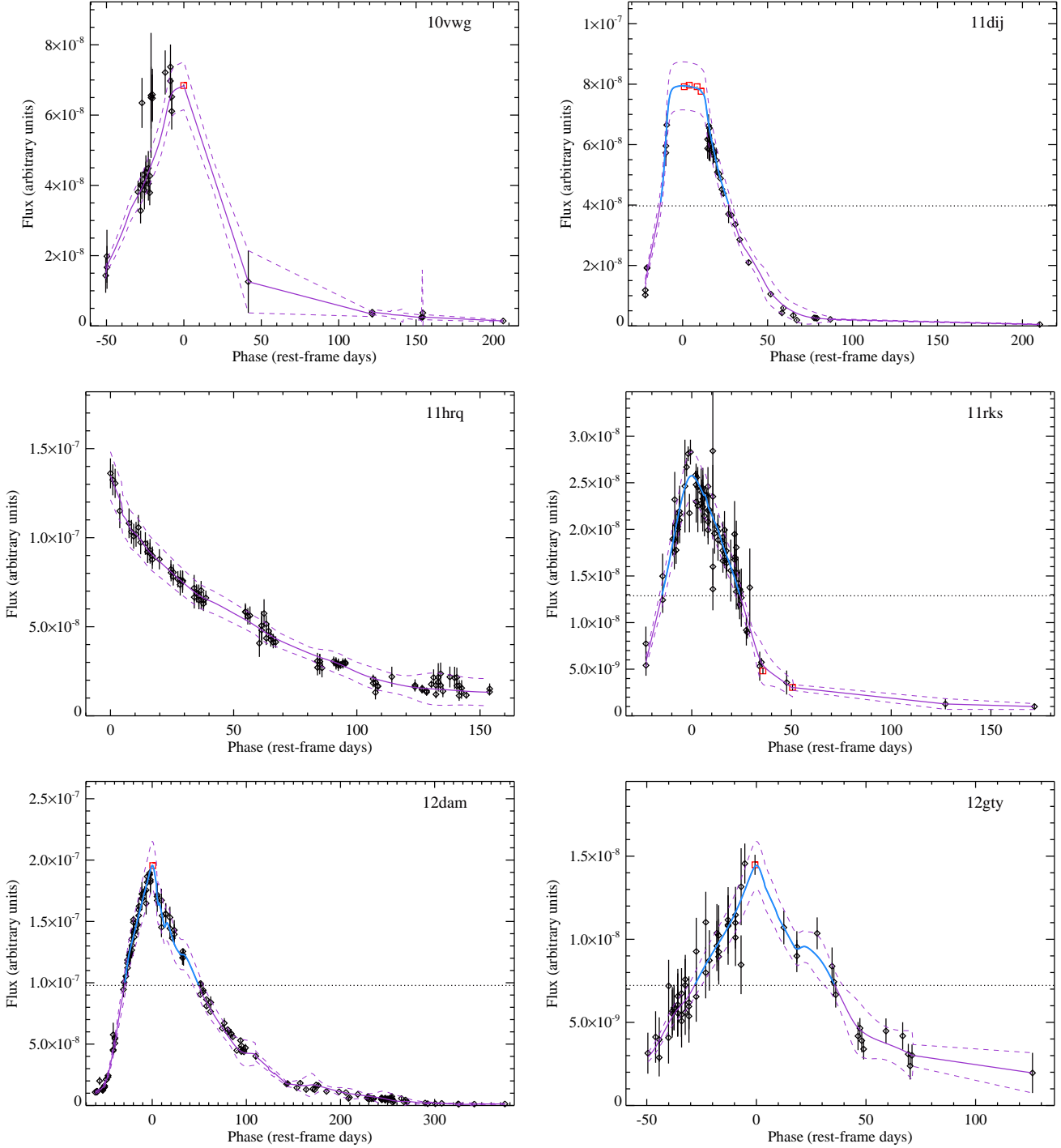


Figure B8. Continuation of Fig. B6.

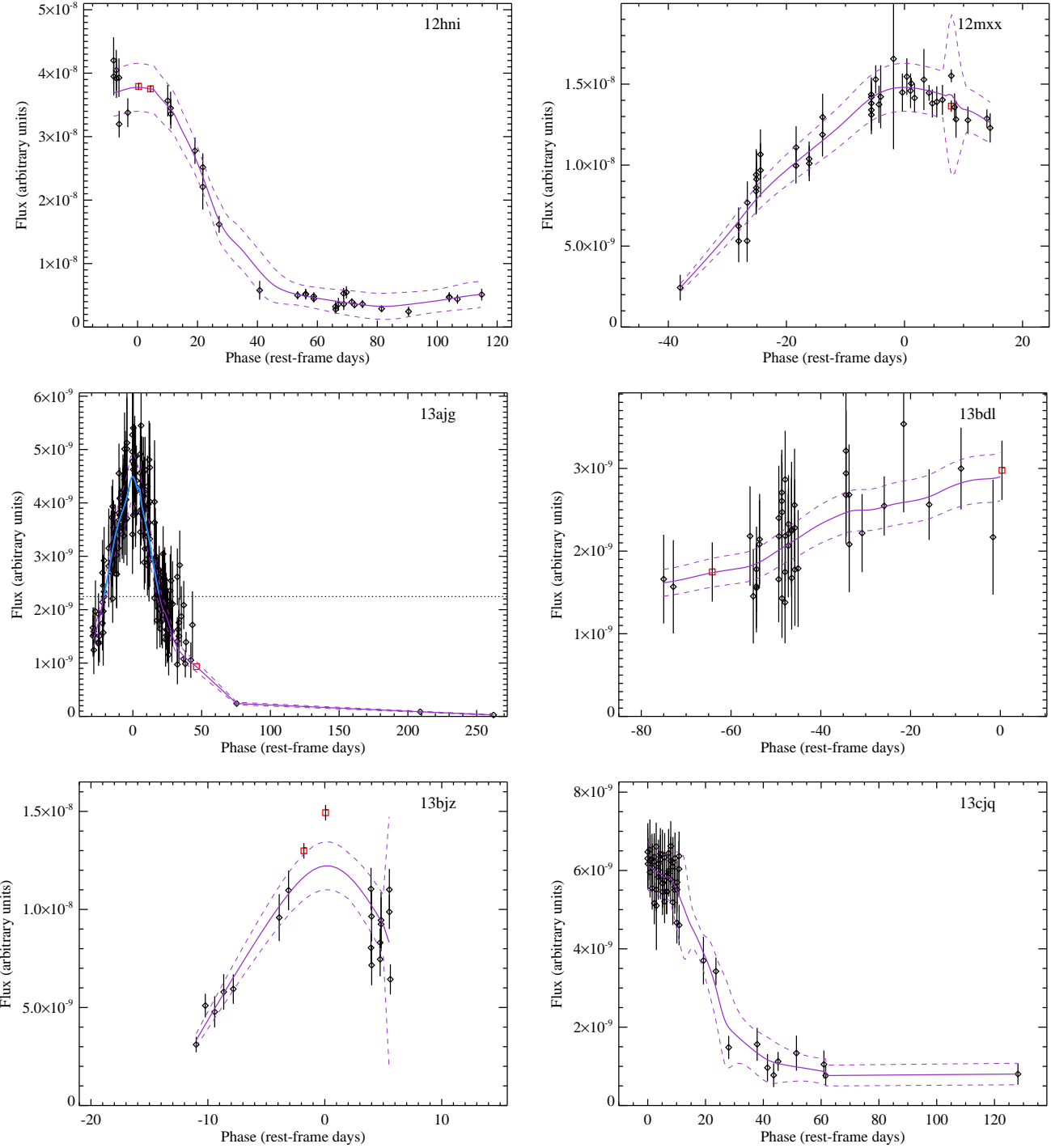


Figure B9. Continuation of Fig. B6.

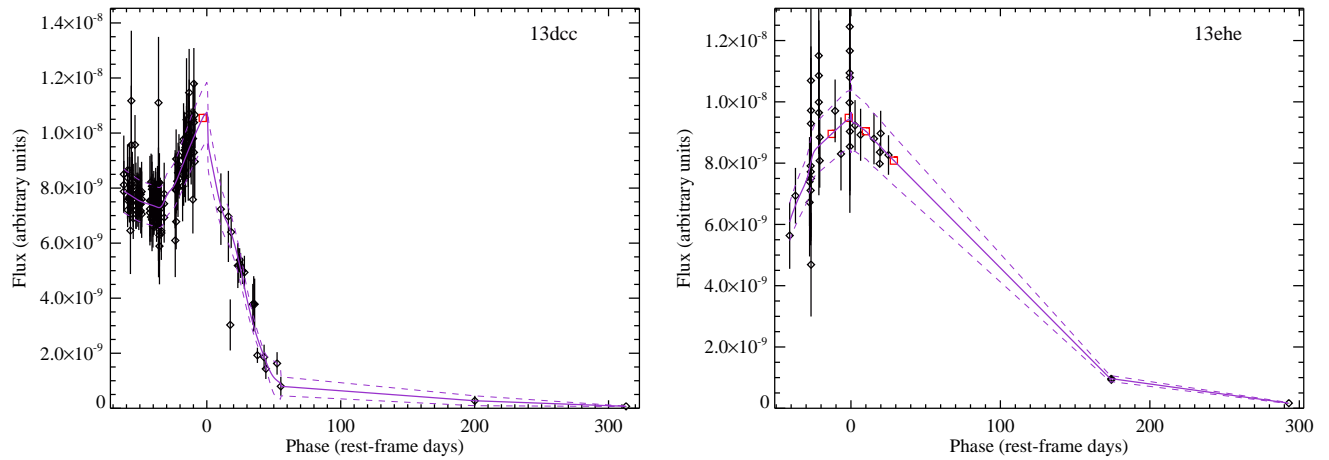


Figure B10. Continuation of Fig. B6.

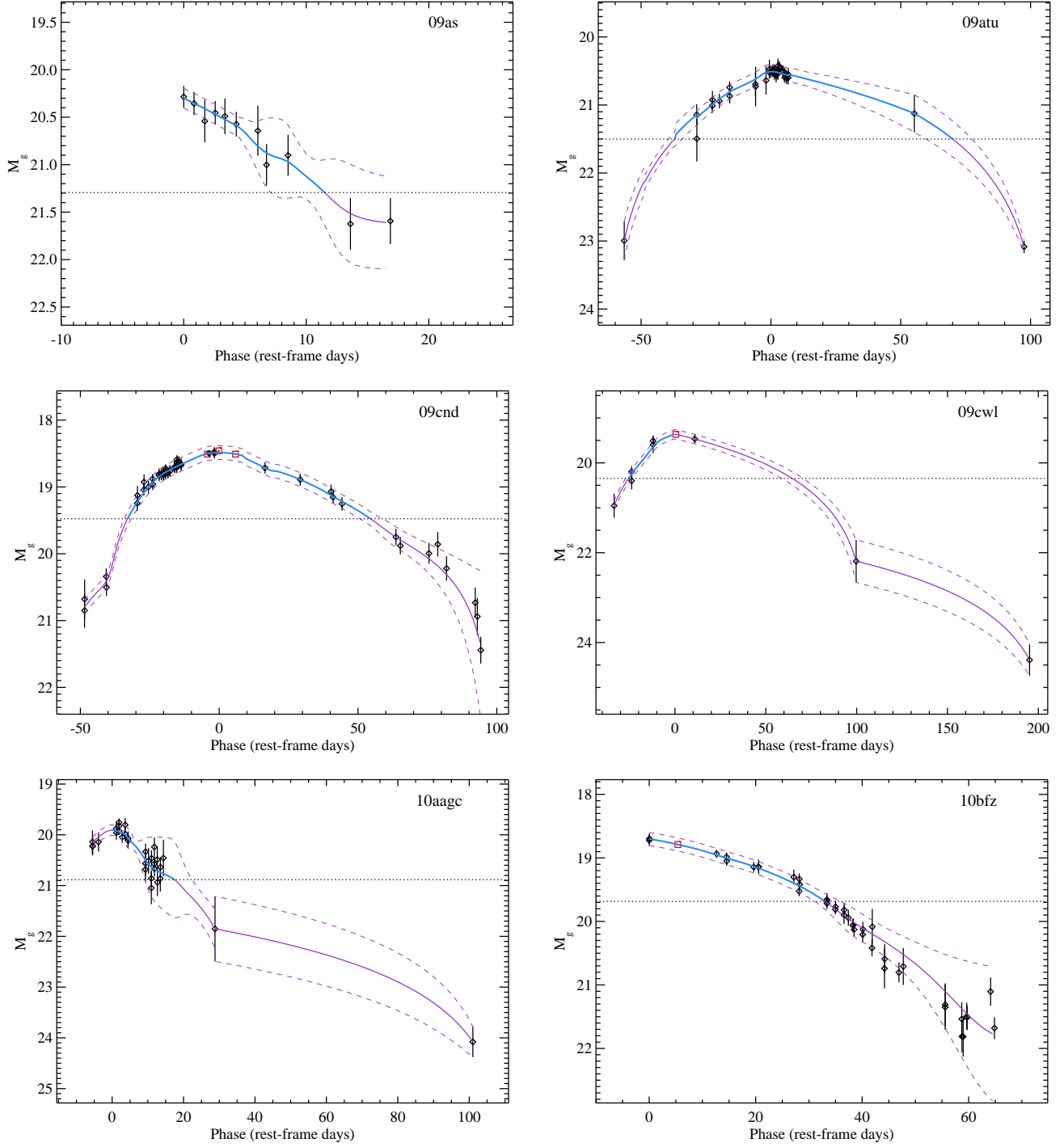
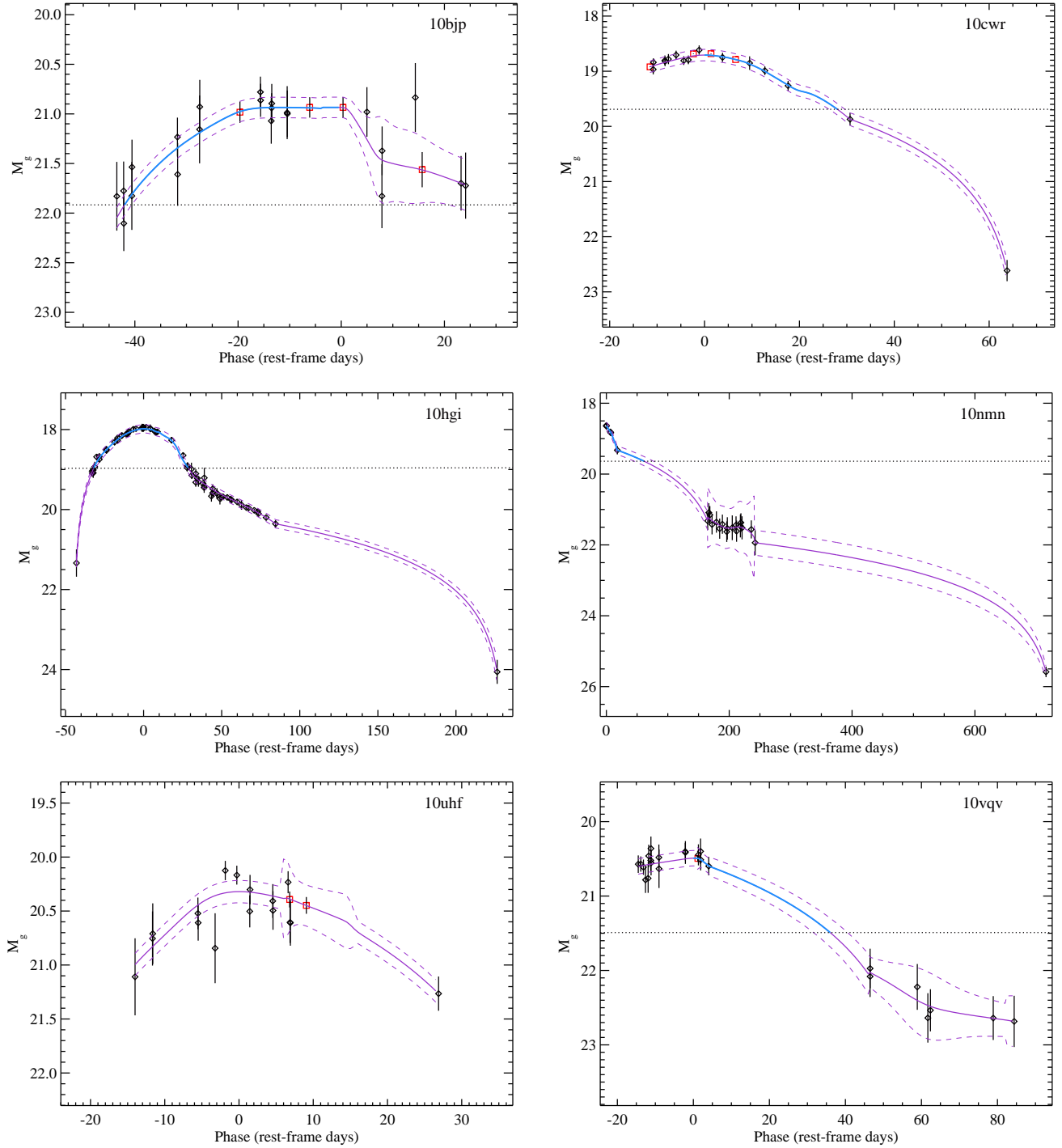


Figure B11. Same as Fig.B6, but for magnitudes. The horizontal dotted lines mark here the distance of 1 mag from peak, which is used to calculate the $t_{\text{rise}}^{\Delta 1 \text{mag}}$ and $t_{\text{fall}}^{\Delta 1 \text{mag}}$ timescales, when the light curves are well-characterized above this threshold (highlighted blue solid curves).

**Figure B12.** Continuation of Fig. B11.

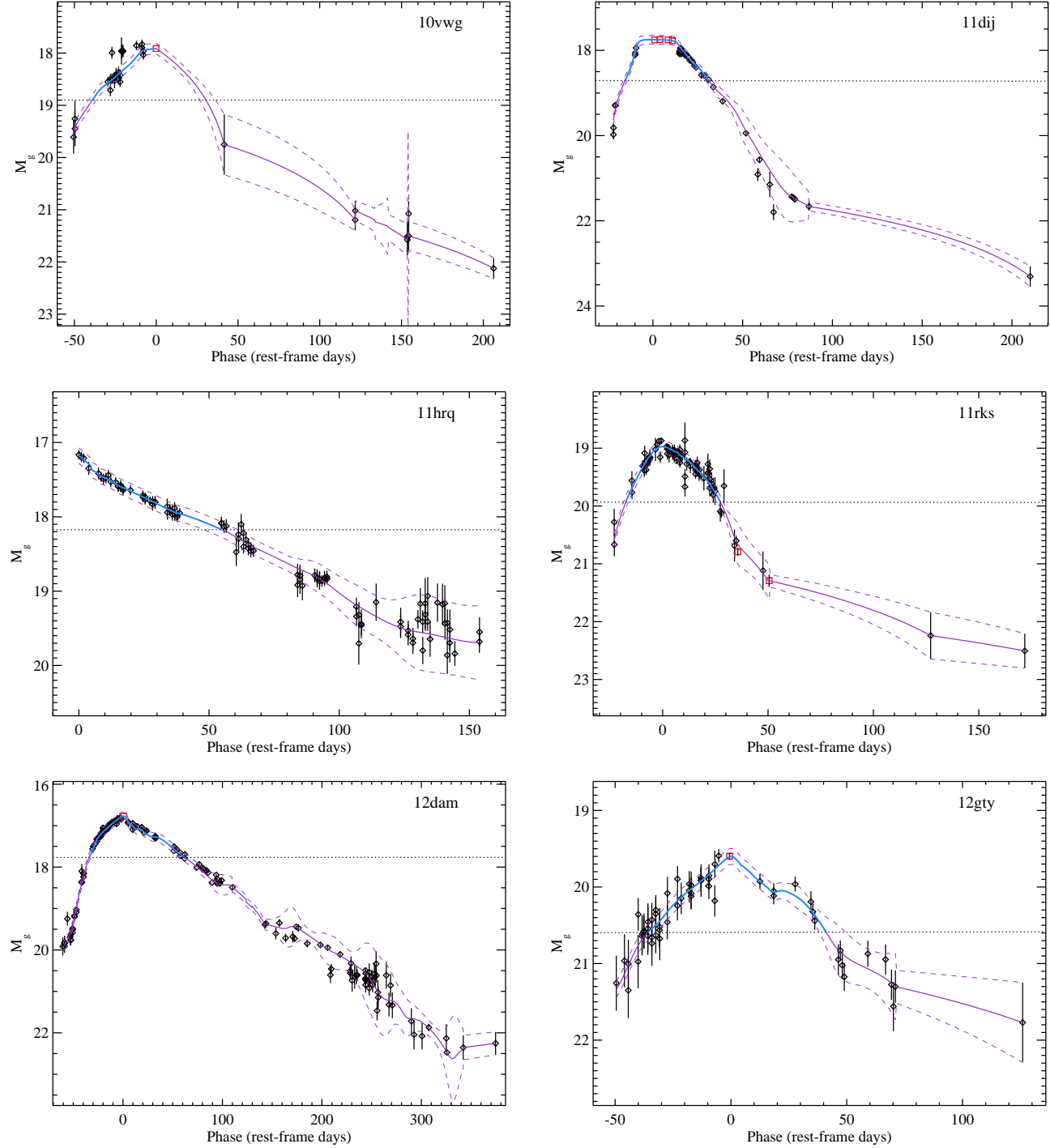
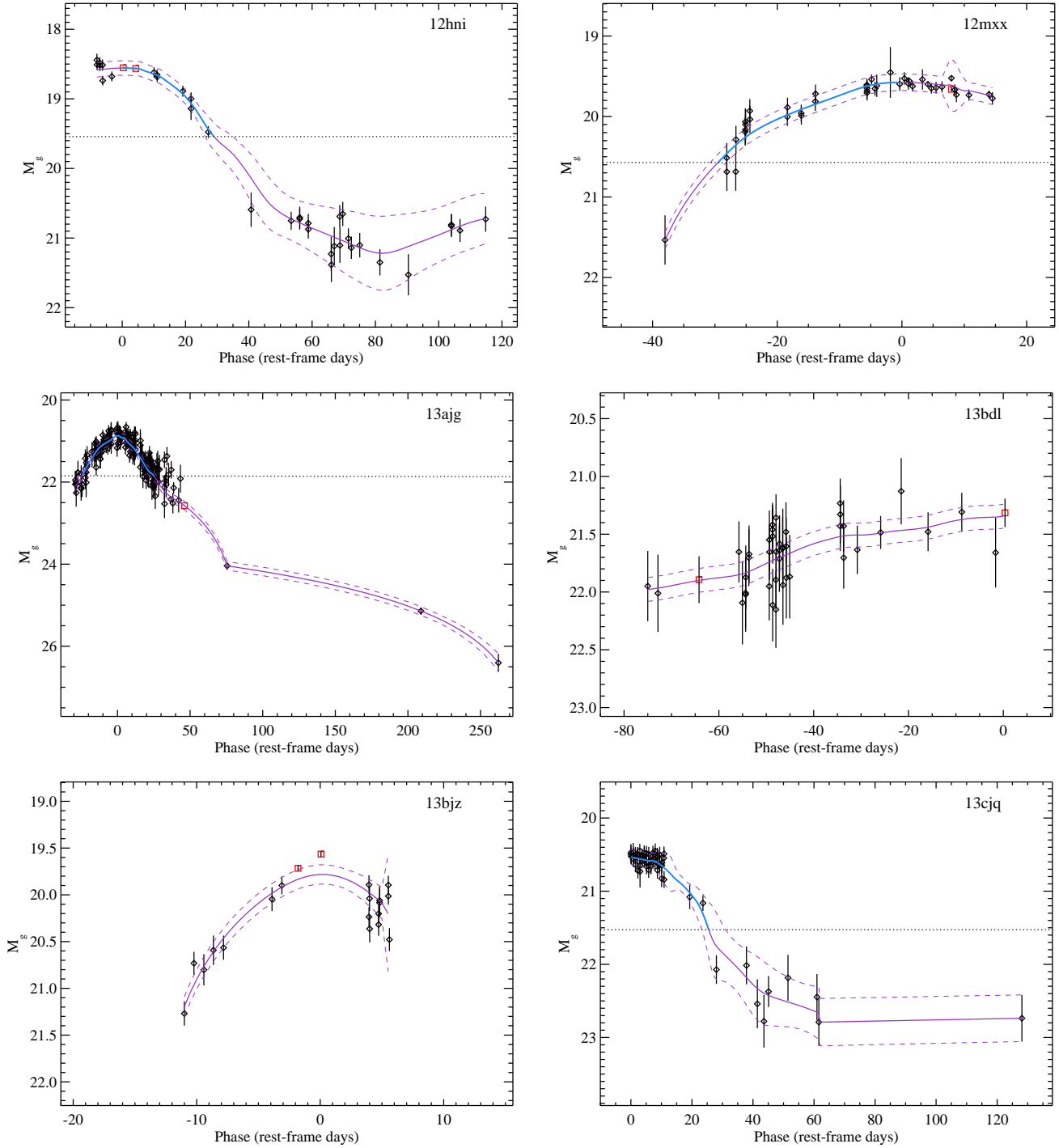


Figure B13. Continuation of Fig. B11.

**Figure B14.** Continuation of Fig. B11.

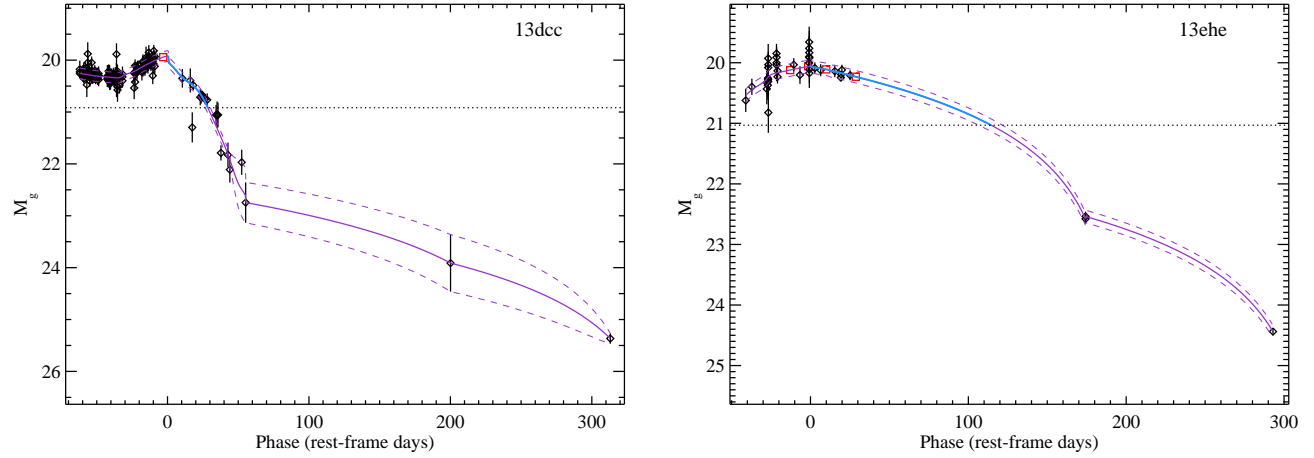


Figure B15. Continuation of Fig. B11.

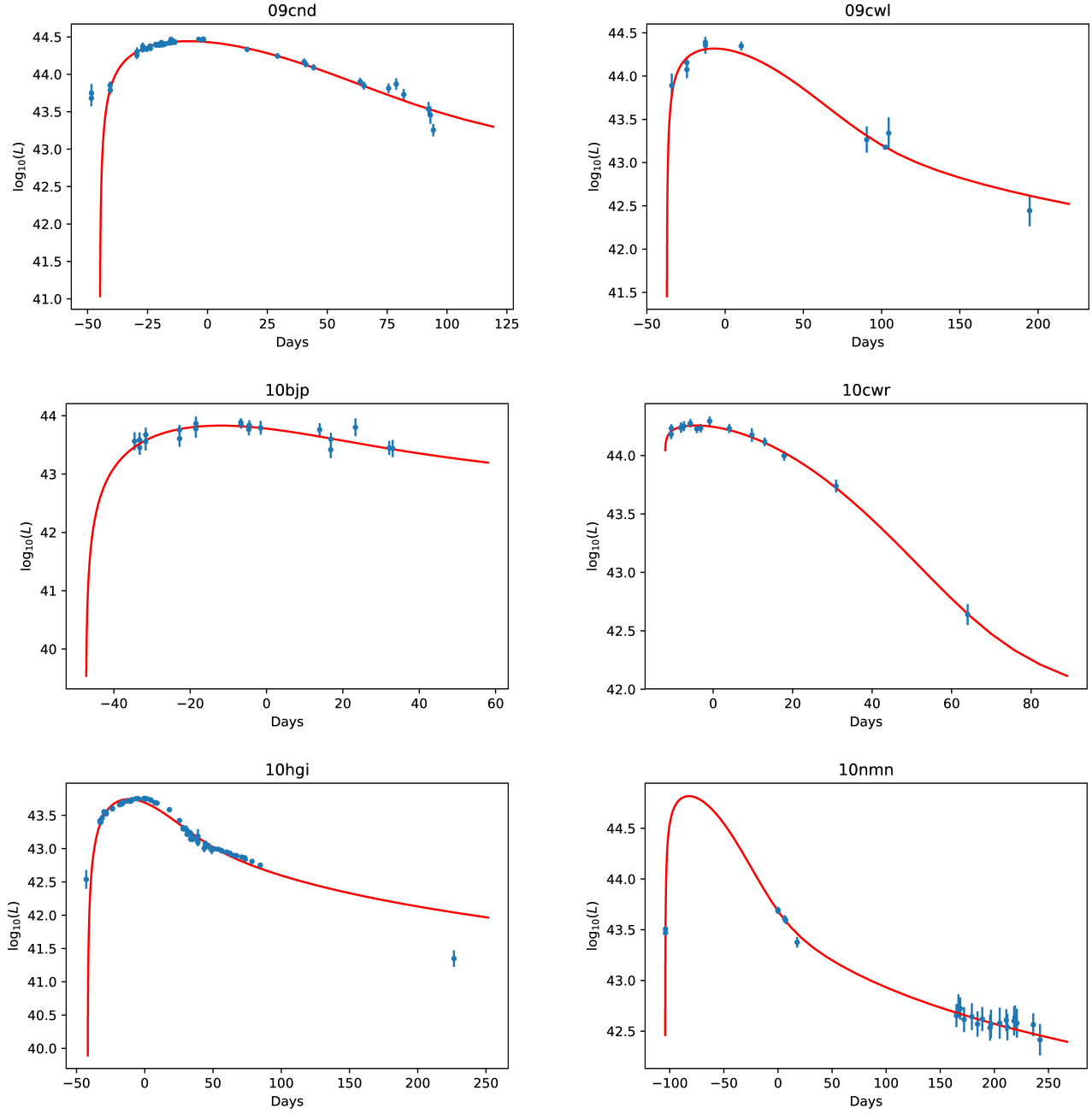


Figure B16. Magnetar fit to the bolometric light curves.

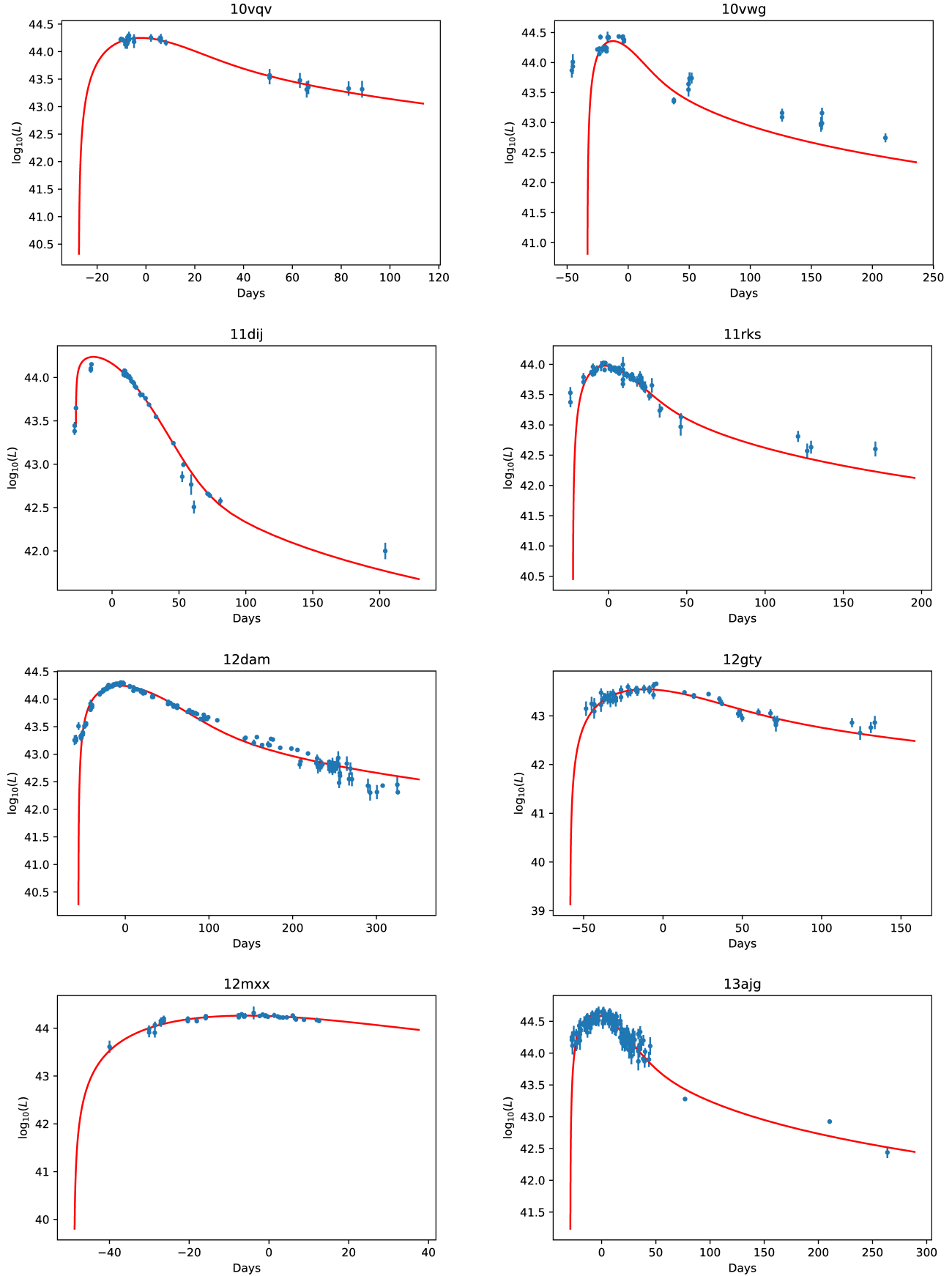


Figure B17. Continuation of Fig. B16.

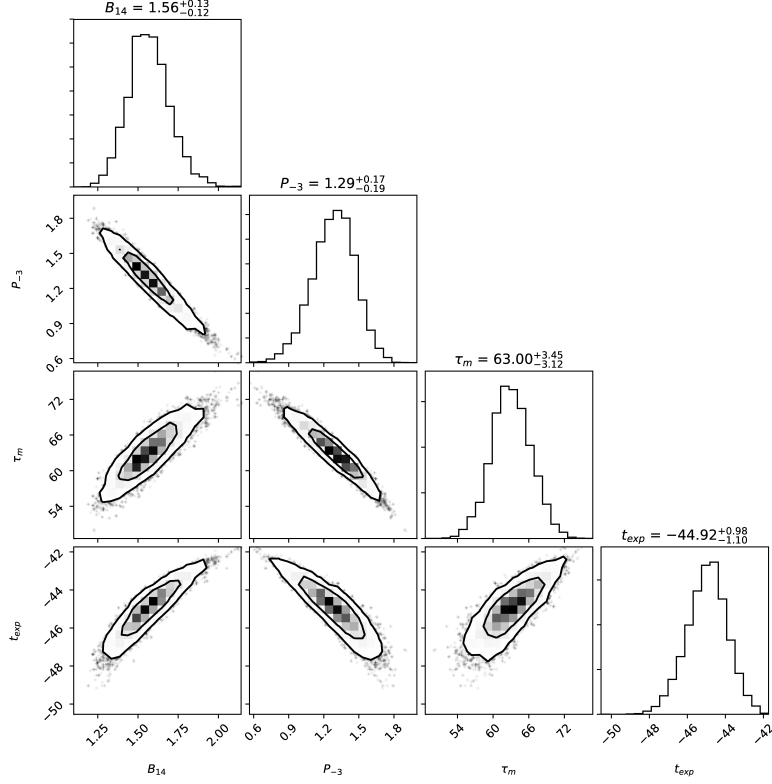


Figure B18. Confidence levels of the best-fit parameters for the magnetar model of PTF 09cnd.

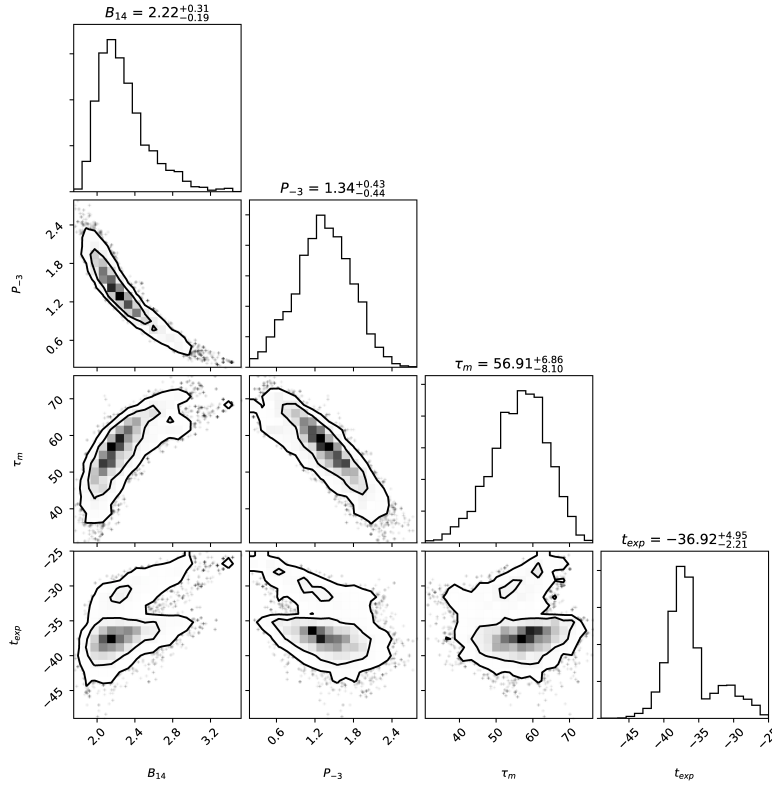


Figure B19. Confidence levels of the best-fit parameters for the magnetar model of PTF 09cwl.

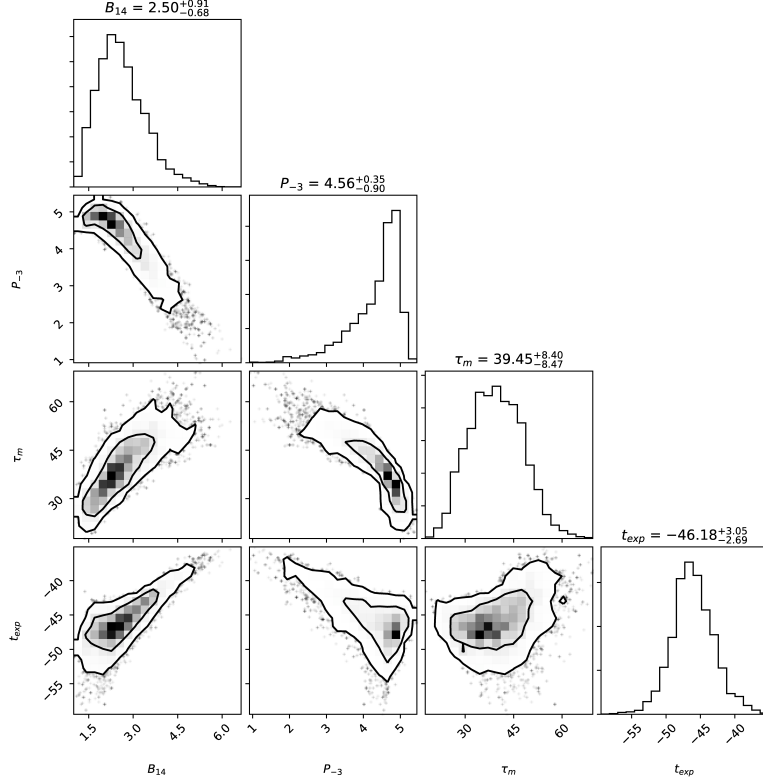


Figure B20. Confidence levels of the best-fit parameters for the magnetar model of PTF 10bjp.

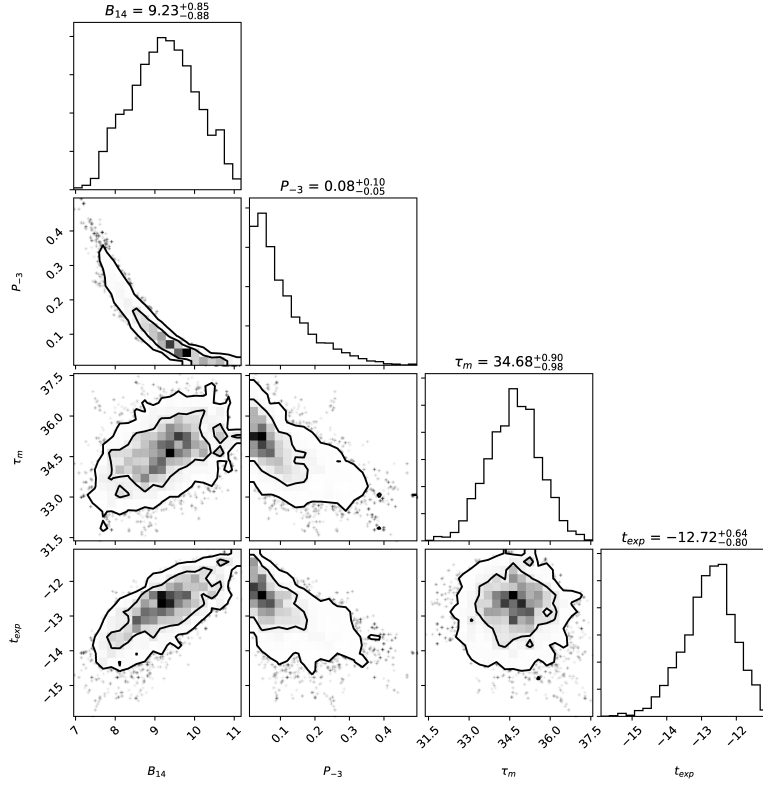


Figure B21. Confidence levels of the best-fit parameters for the magnetar model of PTF 10cwr.

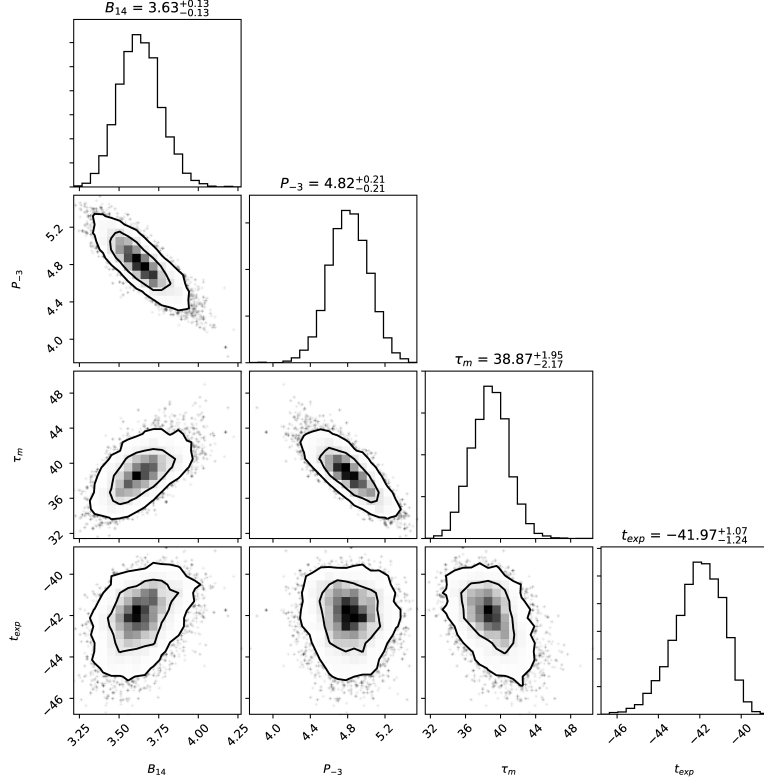


Figure B22. Confidence levels of the best-fit parameters for the magnetar model of PTF 10hgi.

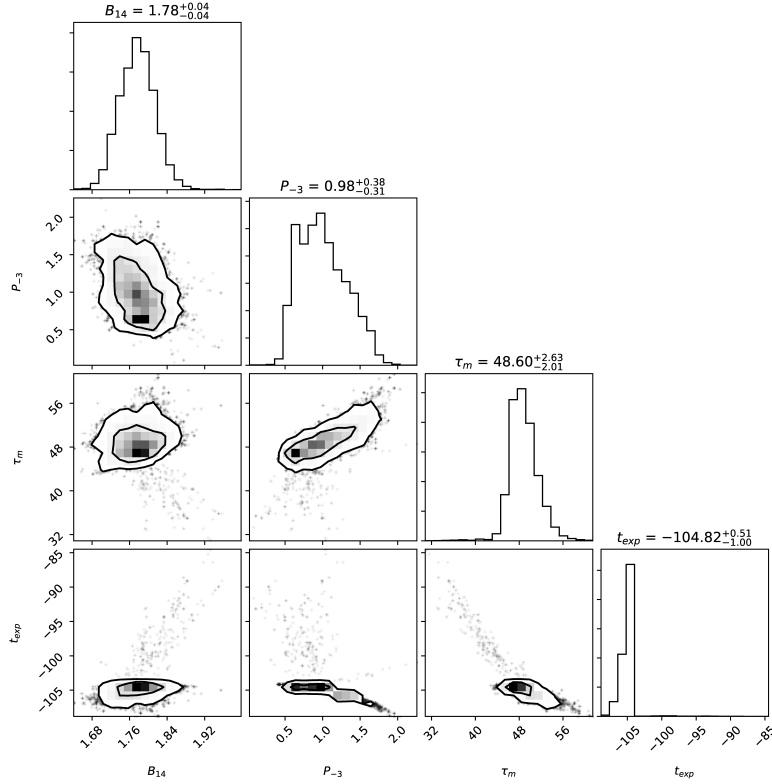


Figure B23. Confidence levels of the best-fit parameters for the magnetar model of PTF 10nmn.

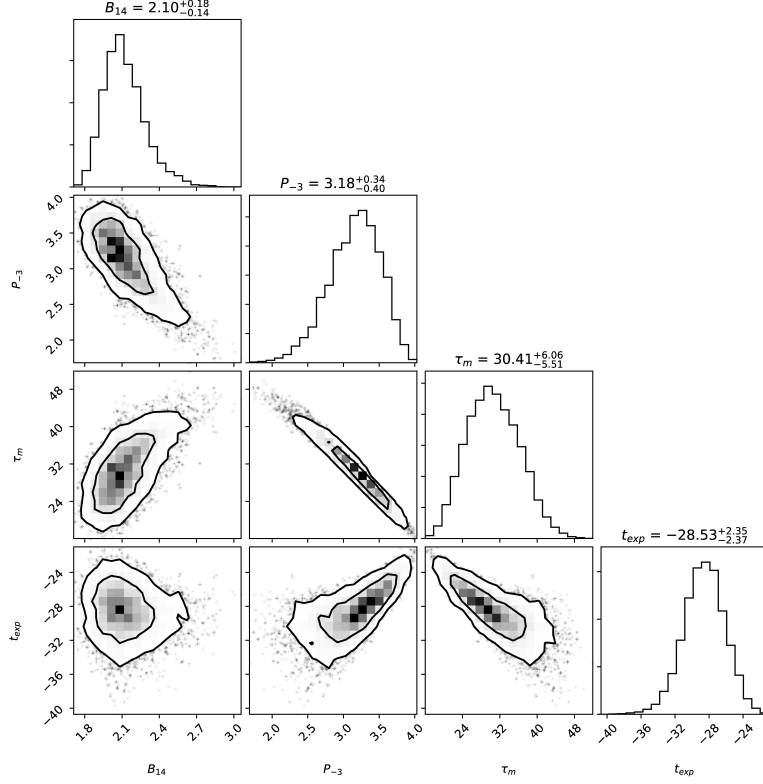


Figure B24. Confidence levels of the best-fit parameters for the magnetar model of PTF 10vqv.

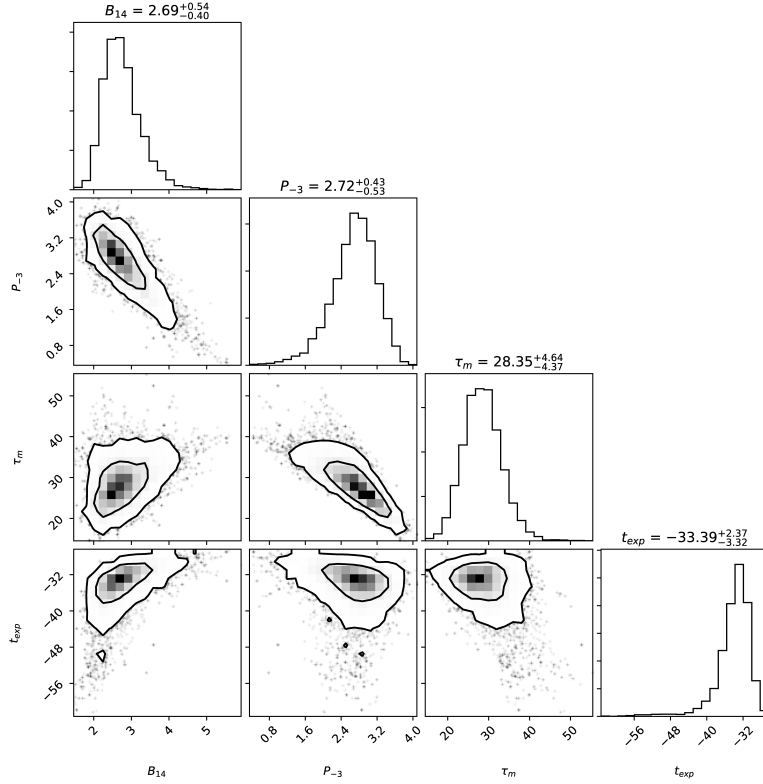


Figure B25. Confidence levels of the best-fit parameters for the magnetar model of PTF 10vwg.

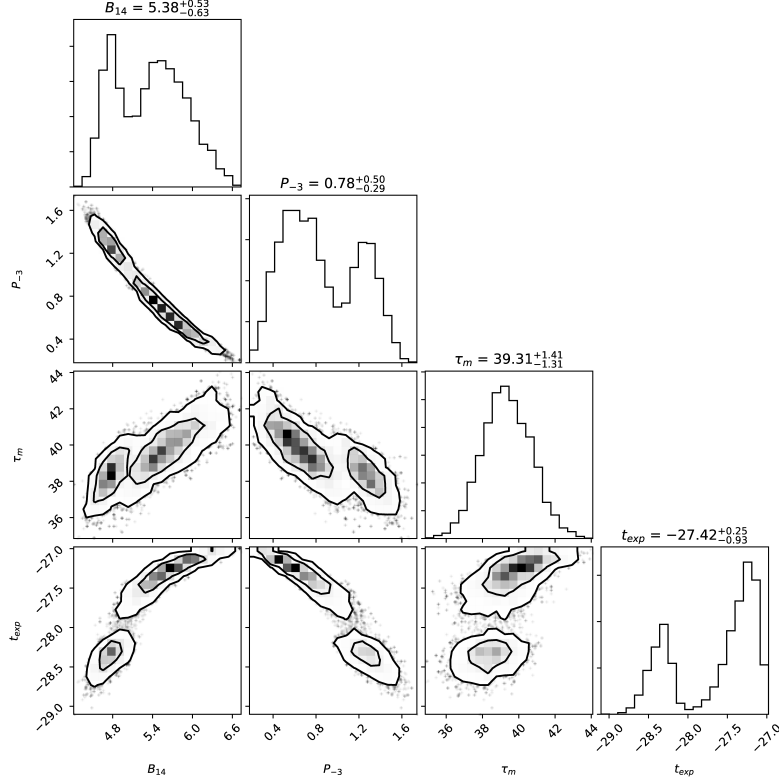


Figure B26. Confidence levels of the best-fit parameters for the magnetar model of PTF 11dij.

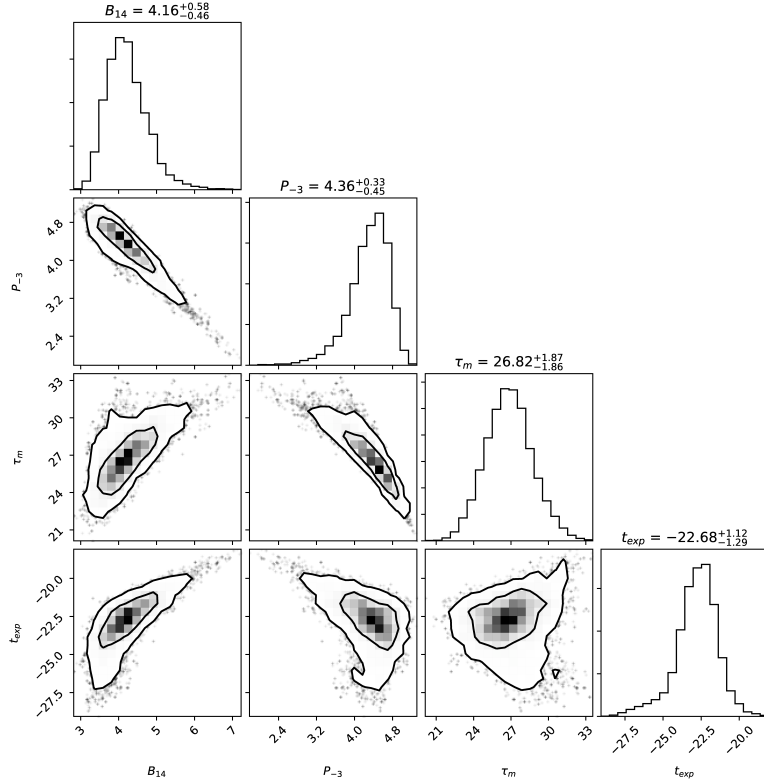


Figure B27. Confidence levels of the best-fit parameters for the magnetar model of PTF 11rks.

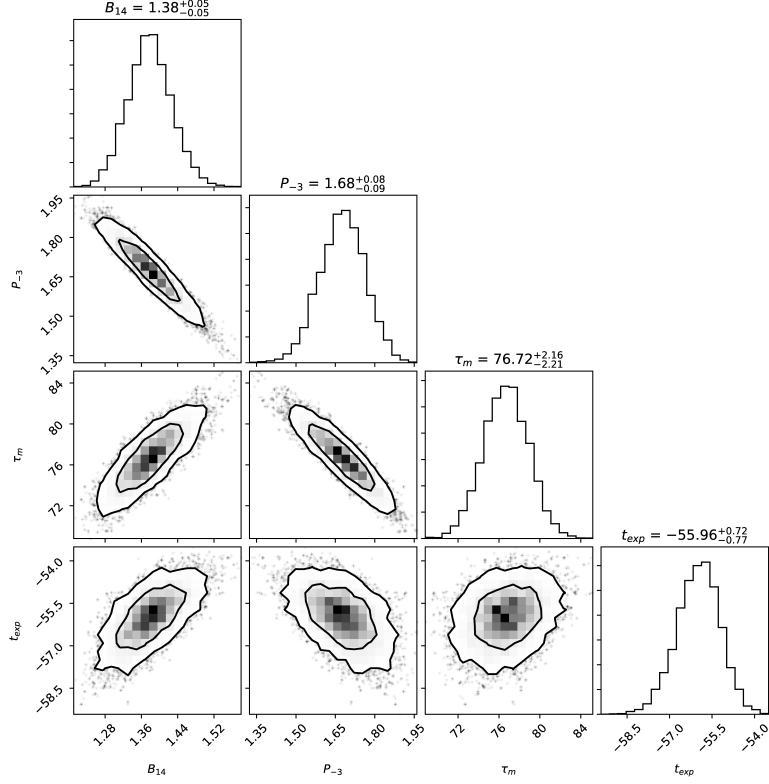


Figure B28. Confidence levels of the best-fit parameters for the magnetar model of PTF 12dam.

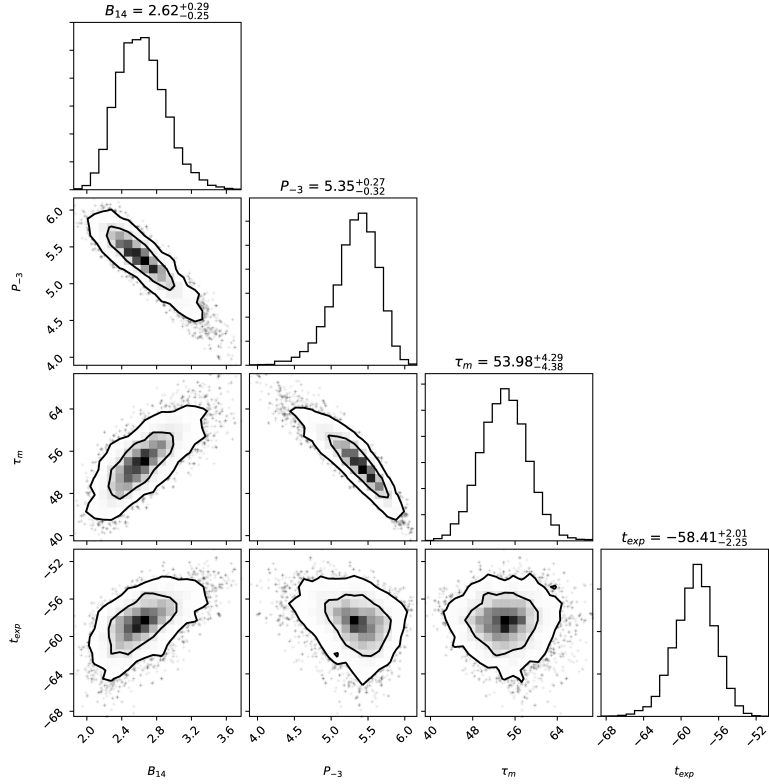


Figure B29. Confidence levels of the best-fit parameters for the magnetar model of PTF 12gty.

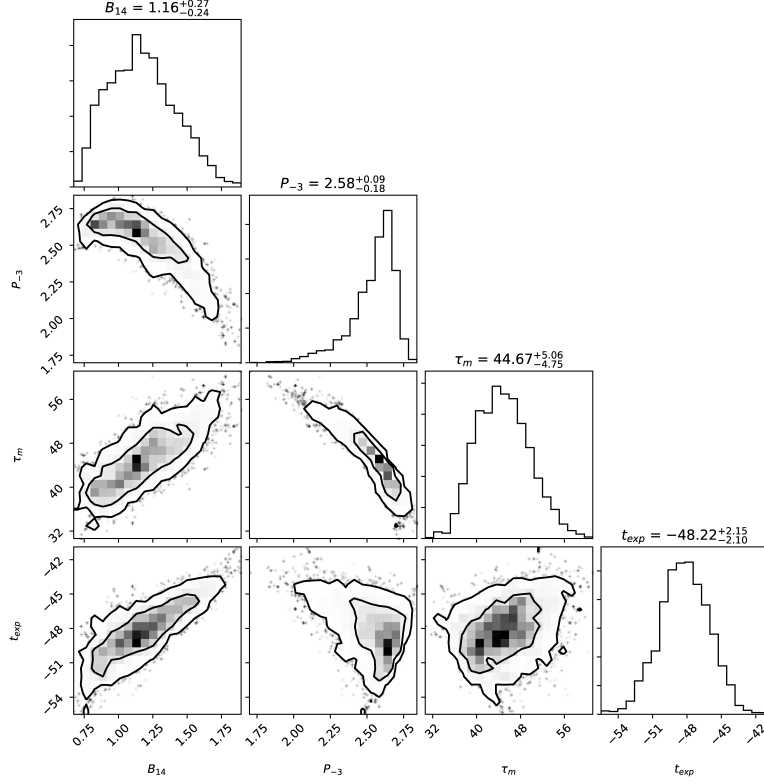


Figure B30. Confidence levels of the best-fit parameters for the magnetar model of PTF 12mxx.

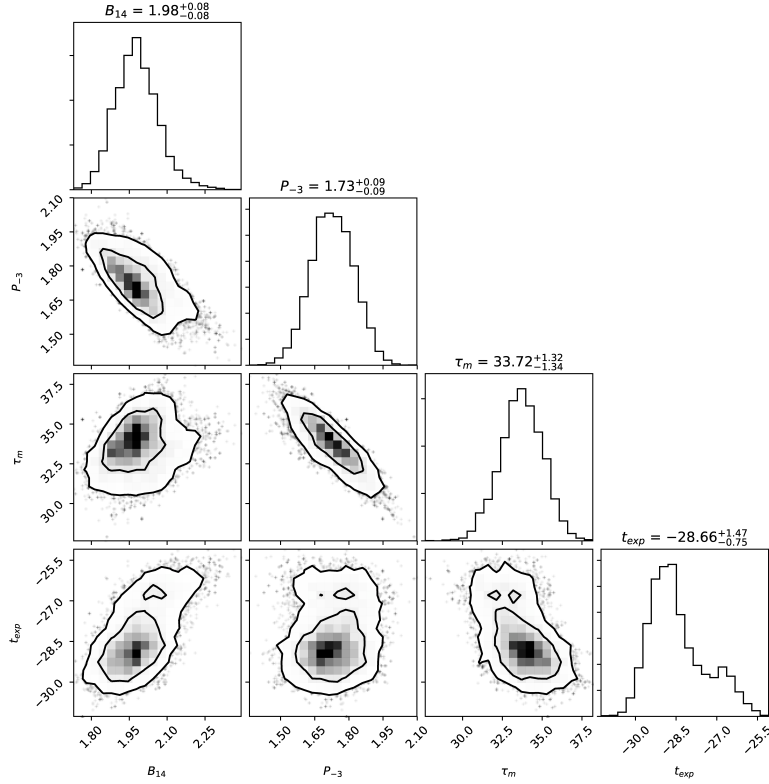


Figure B31. Confidence levels of the best-fit parameters for the magnetar model of PTF 13ajg.

C. K -CORRECTION TABLES

The k -corrections from r to rest-frame g (K_{gr}) and from i to rest-frame r (K_{ir}) for the (i)PTF SLSN sample are listed in the tables below.

Table C2. K_{gr} corrections

PTF ID	09as	09atu	09cnd	09cwl	10aagc	10bfz	10bjp	10cwr	10hgi	10nmn	10uhf	10vqv	10vwg	
z	0.1864	0.5014	0.2585	0.3502	0.2067	0.1699	0.3585	0.2301	0.0982	0.1236	0.2879	0.4520	0.1901	
phase	K_{gr}													
-25	0.00	-0.50	-0.13	-0.30	-0.04	0.04	-0.31	-0.08	0.20	0.16	-0.19	-0.42	-0.01	
-24	-0.00	-0.50	-0.14	-0.30	-0.04	0.04	-0.32	-0.09	0.20	0.15	-0.19	-0.42	-0.01	
-23	-0.00	-0.49	-0.14	-0.30	-0.05	0.03	-0.32	-0.09	0.19	0.15	-0.19	-0.42	-0.01	
-22	-0.01	-0.49	-0.14	-0.30	-0.05	0.03	-0.32	-0.09	0.19	0.14	-0.20	-0.42	-0.02	
-22	-0.01	-0.49	-0.14	-0.31	-0.05	0.03	-0.32	-0.10	0.18	0.14	-0.20	-0.42	-0.02	
-21	-0.02	-0.49	-0.15	-0.31	-0.06	0.02	-0.32	-0.10	0.18	0.13	-0.20	-0.42	-0.02	
-20	-0.02	-0.49	-0.15	-0.31	-0.06	0.02	-0.32	-0.10	0.17	0.13	-0.20	-0.42	-0.03	
-14	-0.04	-0.48	-0.17	-0.31	-0.08	-0.01	-0.32	-0.12	0.14	0.10	-0.22	-0.41	-0.05	
-8	-0.06	-0.46	-0.19	-0.32	-0.10	-0.03	-0.33	-0.14	0.11	0.07	-0.24	-0.41	-0.07	
-3	-0.08	-0.45	-0.20	-0.32	-0.12	-0.05	-0.33	-0.16	0.09	0.05	-0.25	-0.40	-0.09	
0	-0.10	-0.45	-0.21	-0.33	-0.13	-0.06	-0.33	-0.17	0.07	0.03	-0.26	-0.40	-0.10	
3	-0.10	-0.44	-0.22	-0.33	-0.14	-0.07	-0.34	-0.17	0.06	0.02	-0.26	-0.39	-0.11	
6	-0.11	-0.44	-0.23	-0.33	-0.15	-0.08	-0.34	-0.18	0.04	0.01	-0.27	-0.39	-0.12	
10	-0.13	-0.43	-0.23	-0.34	-0.16	-0.09	-0.34	-0.19	0.03	-0.01	-0.28	-0.39	-0.13	
16	-0.14	-0.42	-0.25	-0.34	-0.17	-0.11	-0.34	-0.21	0.00	-0.03	-0.29	-0.38	-0.15	
21	-0.15	-0.42	-0.26	-0.34	-0.18	-0.12	-0.35	-0.22	-0.01	-0.05	-0.30	-0.38	-0.16	
22	-0.16	-0.42	-0.26	-0.35	-0.19	-0.13	-0.35	-0.22	-0.01	-0.05	-0.30	-0.38	-0.16	
26	-0.17	-0.41	-0.27	-0.35	-0.20	-0.14	-0.35	-0.23	-0.03	-0.06	-0.31	-0.38	-0.17	
47	-0.20	-0.39	-0.30	-0.36	-0.23	-0.18	-0.36	-0.26	-0.09	-0.12	-0.34	-0.36	-0.21	
57	-0.22	-0.38	-0.31	-0.37	-0.24	-0.19	-0.36	-0.27	-0.11	-0.14	-0.35	-0.36	-0.22	
57	-0.22	-0.38	-0.31	-0.37	-0.24	-0.19	-0.36	-0.27	-0.11	-0.14	-0.35	-0.36	-0.22	
87	-0.24	-0.36	-0.34	-0.38	-0.27	-0.22	-0.37	-0.29	-0.16	-0.18	-0.37	-0.35	-0.25	
154	-0.23	-0.35	-0.34	-0.38	-0.26	-0.21	-0.38	-0.29	-0.18	-0.19	-0.38	-0.35	-0.24	
164	-0.23	-0.35	-0.33	-0.38	-0.25	-0.21	-0.38	-0.28	-0.18	-0.18	-0.37	-0.35	-0.23	
214	-0.19	-0.36	-0.31	-0.38	-0.22	-0.17	-0.37	-0.26	-0.15	-0.16	-0.35	-0.35	-0.20	
266	-0.18	-0.37	-0.29	-0.36	-0.21	-0.16	-0.37	-0.24	-0.13	-0.14	-0.33	-0.36	-0.18	
321	-0.21	-0.38	-0.29	-0.35	-0.24	-0.19	-0.36	-0.26	-0.15	-0.17	-0.32	-0.36	-0.22	

Table C3. Countinuation of Table C2.

PTF ID	11dij	11hrq	11rks	12dam	12gty	12hni	12mxx	13ajg	13bddl	13bjz	13cj	13dcc	13ehe
z	0.1429	0.0571	0.1924	0.1075	0.1768	0.1056	0.3274	0.7403	0.4030	0.2712	0.3962	0.4308	0.3434
phase	K_{gr}												
-25	0.11	0.26	-0.01	0.19	0.02	0.19	-0.26	-0.81	-0.37	-0.16	-0.36	-0.40	-0.29
-24	0.11	0.25	-0.01	0.18	0.02	0.19	-0.27	-0.80	-0.37	-0.16	-0.36	-0.39	-0.29
-23	0.10	0.25	-0.02	0.18	0.02	0.18	-0.27	-0.79	-0.37	-0.16	-0.36	-0.39	-0.29
-22	0.10	0.24	-0.02	0.17	0.01	0.18	-0.27	-0.78	-0.36	-0.17	-0.36	-0.39	-0.29
-22	0.09	0.24	-0.03	0.17	0.01	0.17	-0.27	-0.77	-0.36	-0.17	-0.36	-0.39	-0.30
-21	0.09	0.23	-0.03	0.16	0.01	0.17	-0.27	-0.76	-0.36	-0.17	-0.36	-0.39	-0.30
-20	0.08	0.23	-0.03	0.16	0.00	0.16	-0.27	-0.75	-0.36	-0.17	-0.36	-0.39	-0.30
-14	0.06	0.20	-0.05	0.13	-0.02	0.13	-0.28	-0.70	-0.36	-0.19	-0.36	-0.39	-0.31
-8	0.03	0.17	-0.08	0.10	-0.05	0.10	-0.29	-0.64	-0.36	-0.21	-0.36	-0.38	-0.31
-3	0.01	0.14	-0.09	0.07	-0.06	0.08	-0.30	-0.60	-0.36	-0.22	-0.36	-0.38	-0.32
0	-0.00	0.13	-0.11	0.06	-0.08	0.06	-0.31	-0.57	-0.36	-0.23	-0.35	-0.38	-0.32
3	-0.01	0.12	-0.11	0.04	-0.09	0.05	-0.31	-0.55	-0.36	-0.24	-0.35	-0.38	-0.33
6	-0.03	0.10	-0.13	0.03	-0.10	0.03	-0.32	-0.52	-0.36	-0.25	-0.35	-0.37	-0.33
10	-0.04	0.09	-0.14	0.02	-0.11	0.02	-0.32	-0.49	-0.36	-0.25	-0.35	-0.37	-0.33
16	-0.06	0.06	-0.15	-0.01	-0.13	-0.01	-0.33	-0.45	-0.35	-0.27	-0.35	-0.37	-0.34
21	-0.07	0.05	-0.16	-0.02	-0.14	-0.02	-0.34	-0.42	-0.35	-0.28	-0.35	-0.37	-0.34
22	-0.08	0.04	-0.16	-0.03	-0.14	-0.02	-0.34	-0.42	-0.35	-0.28	-0.35	-0.37	-0.34
26	-0.09	0.03	-0.17	-0.04	-0.15	-0.04	-0.34	-0.39	-0.35	-0.29	-0.35	-0.36	-0.35
47	-0.14	-0.03	-0.21	-0.10	-0.19	-0.10	-0.36	-0.29	-0.35	-0.32	-0.35	-0.36	-0.36
57	-0.15	-0.05	-0.23	-0.12	-0.20	-0.12	-0.37	-0.26	-0.35	-0.33	-0.35	-0.36	-0.37
57	-0.15	-0.05	-0.23	-0.12	-0.20	-0.12	-0.37	-0.26	-0.35	-0.33	-0.35	-0.36	-0.37
87	-0.19	-0.10	-0.25	-0.17	-0.23	-0.16	-0.38	-0.19	-0.35	-0.35	-0.35	-0.35	-0.38
154	-0.20	-0.14	-0.24	-0.18	-0.22	-0.18	-0.39	-0.20	-0.35	-0.36	-0.35	-0.35	-0.39
164	-0.19	-0.13	-0.23	-0.18	-0.21	-0.18	-0.39	-0.22	-0.35	-0.35	-0.36	-0.35	-0.39
214	-0.16	-0.11	-0.20	-0.15	-0.18	-0.15	-0.37	-0.31	-0.36	-0.33	-0.36	-0.36	-0.38
266	-0.14	-0.09	-0.19	-0.13	-0.16	-0.13	-0.35	-0.40	-0.36	-0.31	-0.36	-0.37	-0.36
321	-0.17	-0.11	-0.22	-0.16	-0.20	-0.16	-0.34	-0.40	-0.36	-0.30	-0.36	-0.36	-0.35

Table C4. K_{ri} corrections

PTF ID	09as	09atu	09cnd	09cwl	10aagc	10bfz	10bjp	10cwr	10hgi	10nmn	10uhf	10vqv	10vwg
z	0.1864	0.5014	0.2585	0.3502	0.2067	0.1699	0.3585	0.2301	0.0982	0.1236	0.2879	0.4520	0.1901
phase	K_{ri}												
-25	-0.16	-0.70	-0.26	-0.44	-0.20	-0.13	-0.46	-0.23	-0.05	-0.08	-0.30	-0.62	-0.17
-24	-0.16	-0.70	-0.26	-0.44	-0.20	-0.13	-0.46	-0.23	-0.05	-0.08	-0.30	-0.61	-0.17
-23	-0.16	-0.70	-0.26	-0.44	-0.20	-0.13	-0.46	-0.23	-0.06	-0.08	-0.30	-0.61	-0.17
-22	-0.16	-0.69	-0.26	-0.44	-0.20	-0.13	-0.46	-0.23	-0.06	-0.08	-0.30	-0.61	-0.17
-22	-0.16	-0.69	-0.26	-0.44	-0.20	-0.13	-0.46	-0.23	-0.06	-0.09	-0.30	-0.61	-0.17
-21	-0.16	-0.69	-0.26	-0.44	-0.20	-0.13	-0.46	-0.23	-0.06	-0.09	-0.30	-0.61	-0.17
-20	-0.16	-0.68	-0.26	-0.44	-0.20	-0.13	-0.46	-0.23	-0.06	-0.09	-0.30	-0.60	-0.17
-14	-0.16	-0.67	-0.26	-0.43	-0.20	-0.14	-0.45	-0.23	-0.07	-0.10	-0.30	-0.59	-0.17
-8	-0.16	-0.65	-0.26	-0.43	-0.20	-0.14	-0.45	-0.23	-0.08	-0.11	-0.30	-0.58	-0.17
-3	-0.17	-0.63	-0.26	-0.43	-0.20	-0.14	-0.44	-0.23	-0.09	-0.11	-0.30	-0.56	-0.17
0	-0.17	-0.62	-0.26	-0.42	-0.20	-0.14	-0.44	-0.23	-0.09	-0.12	-0.30	-0.56	-0.17
3	-0.17	-0.61	-0.26	-0.42	-0.19	-0.14	-0.44	-0.23	-0.10	-0.12	-0.30	-0.55	-0.17
6	-0.17	-0.60	-0.26	-0.42	-0.19	-0.15	-0.43	-0.22	-0.10	-0.13	-0.30	-0.55	-0.17
10	-0.17	-0.60	-0.26	-0.42	-0.19	-0.15	-0.43	-0.22	-0.11	-0.13	-0.30	-0.54	-0.17
16	-0.17	-0.58	-0.25	-0.41	-0.19	-0.15	-0.42	-0.22	-0.12	-0.14	-0.29	-0.53	-0.17
21	-0.17	-0.57	-0.25	-0.41	-0.19	-0.15	-0.42	-0.22	-0.12	-0.14	-0.29	-0.52	-0.17
22	-0.17	-0.57	-0.25	-0.41	-0.19	-0.15	-0.42	-0.22	-0.12	-0.14	-0.29	-0.52	-0.17
26	-0.17	-0.56	-0.25	-0.40	-0.19	-0.16	-0.42	-0.22	-0.13	-0.15	-0.29	-0.51	-0.17
47	-0.18	-0.52	-0.24	-0.39	-0.19	-0.17	-0.40	-0.21	-0.15	-0.17	-0.28	-0.48	-0.18
57	-0.18	-0.51	-0.24	-0.38	-0.19	-0.17	-0.39	-0.21	-0.17	-0.18	-0.28	-0.47	-0.18
57	-0.18	-0.51	-0.24	-0.38	-0.19	-0.17	-0.39	-0.21	-0.17	-0.18	-0.28	-0.47	-0.18
87	-0.18	-0.48	-0.23	-0.36	-0.19	-0.18	-0.37	-0.21	-0.19	-0.20	-0.26	-0.44	-0.18
154	-0.20	-0.45	-0.22	-0.32	-0.19	-0.20	-0.32	-0.20	-0.23	-0.22	-0.24	-0.42	-0.19
164	-0.20	-0.45	-0.22	-0.31	-0.19	-0.20	-0.32	-0.20	-0.23	-0.23	-0.23	-0.42	-0.19
214	-0.20	-0.45	-0.21	-0.29	-0.20	-0.20	-0.30	-0.20	-0.23	-0.22	-0.22	-0.42	-0.20
266	-0.20	-0.45	-0.22	-0.28	-0.20	-0.20	-0.30	-0.20	-0.20	-0.20	-0.23	-0.42	-0.20
321	-0.19	-0.43	-0.24	-0.30	-0.19	-0.18	-0.31	-0.22	-0.13	-0.16	-0.25	-0.40	-0.19

Table C5. Continuation of Table C4.

PTF ID	11dij	11hrq	11rks	12dam	12gty	12hni	12mxx	13ajg	13bddl	13bjz	13cj	13dcc	13ehe
z	0.1429	0.0571	0.1924	0.1075	0.1768	0.1056	0.3274	0.7403	0.4030	0.2712	0.3962	0.4308	0.3434
phase	K_{ri}												
-25	-0.09	0.02	-0.17	-0.06	-0.14	-0.06	-0.38	-0.98	-0.54	-0.28	-0.53	-0.58	-0.42
-24	-0.09	0.02	-0.17	-0.07	-0.14	-0.06	-0.38	-0.98	-0.54	-0.28	-0.53	-0.58	-0.42
-23	-0.09	0.02	-0.17	-0.07	-0.14	-0.07	-0.38	-0.97	-0.54	-0.28	-0.53	-0.58	-0.42
-22	-0.09	0.02	-0.17	-0.07	-0.14	-0.07	-0.38	-0.96	-0.54	-0.28	-0.53	-0.58	-0.42
-21	-0.10	0.01	-0.17	-0.07	-0.14	-0.07	-0.38	-0.95	-0.54	-0.28	-0.53	-0.58	-0.42
-20	-0.10	0.01	-0.17	-0.07	-0.14	-0.07	-0.38	-0.94	-0.54	-0.28	-0.53	-0.57	-0.42
-14	-0.10	0.00	-0.17	-0.08	-0.15	-0.08	-0.38	-0.90	-0.53	-0.28	-0.52	-0.56	-0.42
-8	-0.11	-0.01	-0.17	-0.09	-0.15	-0.09	-0.38	-0.86	-0.52	-0.28	-0.51	-0.55	-0.41
-3	-0.11	-0.01	-0.17	-0.10	-0.15	-0.10	-0.38	-0.82	-0.51	-0.27	-0.50	-0.54	-0.41
0	-0.12	-0.02	-0.17	-0.11	-0.15	-0.10	-0.38	-0.80	-0.50	-0.27	-0.50	-0.54	-0.41
3	-0.12	-0.02	-0.17	-0.11	-0.15	-0.11	-0.37	-0.78	-0.50	-0.27	-0.49	-0.53	-0.41
6	-0.12	-0.03	-0.18	-0.11	-0.15	-0.11	-0.37	-0.76	-0.50	-0.27	-0.49	-0.53	-0.41
10	-0.12	-0.03	-0.18	-0.12	-0.16	-0.12	-0.37	-0.74	-0.49	-0.27	-0.48	-0.52	-0.40
16	-0.13	-0.04	-0.18	-0.13	-0.16	-0.13	-0.37	-0.70	-0.48	-0.27	-0.47	-0.51	-0.40
21	-0.13	-0.05	-0.18	-0.13	-0.16	-0.13	-0.37	-0.68	-0.48	-0.27	-0.47	-0.50	-0.40
22	-0.13	-0.05	-0.18	-0.14	-0.16	-0.13	-0.37	-0.67	-0.47	-0.27	-0.47	-0.50	-0.40
26	-0.14	-0.05	-0.18	-0.14	-0.16	-0.14	-0.36	-0.65	-0.47	-0.27	-0.46	-0.50	-0.39
47	-0.15	-0.08	-0.18	-0.17	-0.17	-0.16	-0.35	-0.57	-0.45	-0.26	-0.44	-0.47	-0.38
57	-0.16	-0.09	-0.18	-0.18	-0.17	-0.17	-0.35	-0.53	-0.44	-0.26	-0.43	-0.46	-0.37
57	-0.16	-0.09	-0.18	-0.18	-0.17	-0.17	-0.35	-0.53	-0.44	-0.26	-0.43	-0.46	-0.37
87	-0.18	-0.12	-0.18	-0.20	-0.18	-0.20	-0.33	-0.46	-0.41	-0.25	-0.40	-0.44	-0.35
154	-0.21	-0.16	-0.19	-0.23	-0.20	-0.23	-0.29	-0.42	-0.37	-0.22	-0.36	-0.41	-0.31
164	-0.21	-0.16	-0.19	-0.24	-0.20	-0.24	-0.29	-0.42	-0.37	-0.22	-0.36	-0.40	-0.30
214	-0.21	-0.16	-0.20	-0.23	-0.20	-0.23	-0.27	-0.45	-0.36	-0.21	-0.35	-0.40	-0.28
266	-0.20	-0.13	-0.20	-0.21	-0.20	-0.20	-0.26	-0.49	-0.36	-0.22	-0.35	-0.40	-0.28
321	-0.16	-0.06	-0.19	-0.15	-0.18	-0.15	-0.27	-0.49	-0.37	-0.25	-0.37	-0.39	-0.29

Table D6. PTF 09as photometry data.

MJD	Phase	m	Filter	Telescope
54910.417	-6.56	19.71 ± 0.11	g	p48
54915.164	-2.56	19.85 ± 0.14	g	p48
54915.244	-2.49	19.72 ± 0.12	g	p48
54918.197	0.00	20.13 ± 0.11	r	p60
54918.199	0.00	19.80 ± 0.12	i	p60
54918.210	0.01	20.19 ± 0.15	g	p48
54919.195	0.84	20.19 ± 0.12	r	p60
54919.197	0.84	19.86 ± 0.13	i	p60
54920.235	1.72	20.38 ± 0.22	r	p60
54921.206	2.54	20.85 ± 0.27	g	p48
54921.248	2.57	20.29 ± 0.13	r	p60
54921.249	2.57	19.91 ± 0.13	i	p60
54921.294	2.61	20.37 ± 0.16	g	p48
54922.186	3.36	20.32 ± 0.19	r	p60
54922.187	3.36	19.89 ± 0.18	i	p60
54923.199	4.22	20.77 ± 0.25	g	p48
54923.283	4.29	20.40 ± 0.13	r	p60
54923.285	4.29	19.99 ± 0.14	i	p60
54923.286	4.29	20.70 ± 0.22	g	p48
54925.376	6.05	20.47 ± 0.26	r	p60
54925.377	6.05	20.37 ± 0.28	i	p60
54926.214	6.76	20.82 ± 0.22	r	p60
54926.215	6.76	20.25 ± 0.19	i	p60
54927.223	7.61	20.04 ± 0.21	i	p60
54928.297	8.51	20.72 ± 0.22	r	p60
54928.299	8.52	20.39 ± 0.21	i	p60
54934.333	13.60	21.42 ± 0.27	r	p60
54934.335	13.60	20.68 ± 0.21	i	p60
54935.427	14.52	20.51 ± 0.34	i	p60
54938.202	16.86	21.39 ± 0.24	r	p60
54938.204	16.87	21.05 ± 0.25	i	p60

D. PHOTOMETRIC DATA

All magnitudes are in the AB system. The absolute magnitudes in rest-frame g -band are derived from $M_g = m_r - DM - K_{gr}$, where DM is the distance modulus, m_r is corrected for foreground Galactic extinction (Table 1), and K_{gr} is the k -correction (Table C2), as described in Sect. 3.12. The photometric data in Tables D6 to D71 are available as machine-readable electronic tables in the online version of the paper (future link). The UV photometry from Swift was not corrected from host-galaxy contribution, but this should be minimal (see Sect. 3.7). The table references are: [I] Quimby et al. (2011); [II] Pastorello et al. (2010); [III] Inserra et al. (2013); [IV] Nicholl et al. (2013), Chen et al. (2015); [V] Vreeswijk et al. (2014).

Table D7. PTF 09as rest-frame g photometry data.

MJD	Phase	m_g	M_g	Telescope	Reference
54918.197	0.00	20.29 ± 0.11	-19.50	p60	
54919.195	0.84	20.36 ± 0.12	-19.43	p60	
54920.235	1.72	20.54 ± 0.22	-19.24	p60	
54921.248	2.57	20.45 ± 0.13	-19.33	p60	
54922.186	3.36	20.49 ± 0.19	-19.30	p60	
54923.283	4.29	20.57 ± 0.13	-19.21	p60	
54925.376	6.05	20.64 ± 0.26	-19.14	p60	
54926.214	6.76	21.00 ± 0.22	-18.78	p60	
54928.297	8.51	20.90 ± 0.22	-18.88	p60	
54934.333	13.60	21.62 ± 0.27	-18.16	p60	
54938.202	16.86	21.59 ± 0.24	-18.19	p60	

Table D8. PTF 09atu photometry data.

MJD	Phase	m	Filter	Tel	MJD	Phase	m	Filter	Tel
54974.325	-58.61	22.43 ± 0.29	r	p48	55064.163	1.23	20.09 ± 0.10	i	p60
55016.222	-30.70	20.58 ± 0.15	r	p48	55064.165	1.23	20.04 ± 0.10	i	p60
55016.321	-30.64	20.93 ± 0.33	r	p48	55066.154	2.55	20.32 ± 0.08	g	p60
55025.227	-24.71	20.45 ± 0.11	r	p48	55066.157	2.56	19.99 ± 0.08	r	p60
55025.343	-24.63	20.36 ± 0.13	r	p48	55066.160	2.56	20.01 ± 0.09	r	p60
55029.337	-21.97	20.39 ± 0.11	r	p60	55066.162	2.56	20.07 ± 0.10	i	p60
55029.339	-21.97	20.52 ± 0.15	i	p60	55066.165	2.56	19.98 ± 0.10	i	p60
55035.250	-18.03	20.20 ± 0.09	r	p48	55067.153	3.22	20.28 ± 0.11	g	p60
55035.339	-17.97	20.32 ± 0.11	r	p48	55067.156	3.22	20.09 ± 0.08	r	p60
55035.389	-17.94	20.38 ± 0.13	g	p60	55067.158	3.22	20.03 ± 0.08	r	p60
55040.356	-14.63	20.24 ± 0.10	g	p60	55067.161	3.22	20.13 ± 0.09	i	p60
55050.222	-8.06	20.17 ± 0.18	r	p48	55067.163	3.23	20.17 ± 0.09	i	p60
55050.297	-8.01	20.20 ± 0.29	r	p48	55068.188	3.91	20.33 ± 0.08	g	p60
55056.321	-4.00	20.12 ± 0.21	r	p48	55068.191	3.91	20.10 ± 0.09	r	p60
55058.193	-2.75	20.00 ± 0.09	r	p48	55068.193	3.91	20.07 ± 0.08	r	p60
55058.275	-2.69	19.96 ± 0.14	r	p48	55068.195	3.91	20.14 ± 0.09	i	p60
55059.163	-2.10	19.99 ± 0.08	r	p60	55068.197	3.91	20.02 ± 0.09	i	p60
55059.166	-2.10	20.00 ± 0.08	r	p60	55069.156	4.55	20.32 ± 0.08	g	p60
55059.168	-2.10	19.99 ± 0.09	i	p60	55069.159	4.55	20.09 ± 0.10	r	p60
55059.170	-2.10	20.10 ± 0.10	i	p60	55069.161	4.56	20.04 ± 0.08	r	p60
55060.211	-1.40	20.32 ± 0.09	g	p60	55069.163	4.56	20.11 ± 0.10	i	p60
55060.214	-1.40	19.97 ± 0.08	r	p60	55069.166	4.56	20.05 ± 0.09	i	p60
55060.216	-1.40	19.99 ± 0.08	r	p60	55107.182	29.88	20.65 ± 0.27	g	p60
55060.218	-1.40	20.10 ± 0.10	i	p60	55107.186	29.88	20.84 ± 0.27	i	p60
55060.221	-1.40	20.11 ± 0.10	i	p60	55138.095	50.47	20.64 ± 0.24	i	p60
55061.165	-0.77	20.31 ± 0.08	g	p60	55142.090	53.13	20.68 ± 0.28	r	p60
55061.168	-0.77	20.03 ± 0.08	r	p60					
55061.170	-0.77	19.96 ± 0.08	r	p60					
55061.172	-0.76	20.07 ± 0.12	i	p60					
55061.175	-0.76	20.11 ± 0.10	i	p60					
55062.158	-0.11	20.23 ± 0.07	g	p60					
55062.161	-0.11	20.04 ± 0.08	r	p60					
55062.163	-0.10	20.05 ± 0.10	r	p60					
55062.166	-0.10	20.19 ± 0.10	i	p60					
55062.168	-0.10	20.05 ± 0.09	i	p60					
55062.200	-0.08	22.38 ± 0.31	UVW1	Swift/UVOT					
55062.206	-0.08	21.90 ± 0.35	u	Swift/UVOT					
55063.160	0.56	19.98 ± 0.08	r	p60					
55063.163	0.56	20.03 ± 0.09	r	p60					
55063.165	0.56	20.12 ± 0.09	i	p60					
55063.167	0.56	20.07 ± 0.09	i	p60					
55063.232	0.61	19.97 ± 0.14	r	p48					
55063.277	0.64	19.91 ± 0.10	r	p48					
55064.155	1.22	20.31 ± 0.08	g	p60					
55064.158	1.22	19.93 ± 0.08	r	p60					
55064.161	1.23	19.95 ± 0.08	r	p60					

Table D9. PTF 09atu rest-frame g photometry data.

MJD	Phase	m_g	M_g	Telescope	Reference
54974.325	-58.61	23.00 ± 0.29	-19.27	p48	
55016.222	-30.70	21.14 ± 0.15	-21.13	p48	
55016.321	-30.64	21.50 ± 0.33	-20.77	p48	
55025.227	-24.71	21.01 ± 0.11	-21.26	p48	
55025.343	-24.63	20.93 ± 0.13	-21.34	p48	
55029.337	-21.97	20.94 ± 0.11	-21.33	p60	
55035.250	-18.03	20.74 ± 0.09	-21.53	p48	
55035.339	-17.97	20.87 ± 0.11	-21.40	p48	
55050.222	-8.06	20.69 ± 0.18	-21.57	p48	
55050.297	-8.01	20.73 ± 0.29	-21.54	p48	
55056.321	-4.00	20.64 ± 0.21	-21.63	p48	
55058.193	-2.75	20.52 ± 0.09	-21.75	p48	
55058.275	-2.69	20.48 ± 0.14	-21.79	p48	
55059.163	-2.10	20.51 ± 0.08	-21.76	p60	
55059.166	-2.10	20.51 ± 0.08	-21.76	p60	
55060.214	-1.40	20.49 ± 0.08	-21.78	p60	
55060.216	-1.40	20.51 ± 0.08	-21.76	p60	
55061.168	-0.77	20.54 ± 0.08	-21.73	p60	
55061.170	-0.77	20.48 ± 0.08	-21.79	p60	
55062.161	-0.11	20.55 ± 0.08	-21.72	p60	
55062.163	-0.10	20.57 ± 0.10	-21.70	p60	
55063.160	0.56	20.49 ± 0.08	-21.78	p60	
55063.163	0.56	20.54 ± 0.09	-21.73	p60	
55063.232	0.61	20.48 ± 0.14	-21.78	p48	
55063.277	0.64	20.42 ± 0.10	-21.84	p48	
55064.158	1.22	20.44 ± 0.08	-21.83	p60	
55064.161	1.23	20.46 ± 0.08	-21.81	p60	
55066.157	2.56	20.50 ± 0.08	-21.77	p60	
55066.160	2.56	20.51 ± 0.09	-21.75	p60	
55067.156	3.22	20.60 ± 0.08	-21.67	p60	
55067.158	3.22	20.54 ± 0.08	-21.73	p60	
55068.191	3.91	20.61 ± 0.09	-21.66	p60	
55068.193	3.91	20.57 ± 0.08	-21.70	p60	
55069.159	4.55	20.60 ± 0.10	-21.67	p60	
55069.161	4.56	20.55 ± 0.08	-21.72	p60	
55142.090	53.13	21.13 ± 0.28	-21.14	p60	
55205.556	95.40	23.08 ± 0.09	-19.18	p200	I

Table D10. PTF 09cnd photometry data.

MJD	Phase	m	Filter	Tel	MJD	Phase	m	Filter	Tel
55025.378	-48.45	20.66 ± 0.26	r	p48	55064.148	-17.64	18.54 ± 0.08	r	p60
55025.418	-48.41	20.49 ± 0.29	r	p48	55064.151	-17.64	18.76 ± 0.11	i	p60
55035.218	-40.63	20.15 ± 0.12	r	p48	55064.153	-17.64	18.74 ± 0.11	i	p60
55035.313	-40.55	20.31 ± 0.13	r	p48	55065.829	-16.30	19.41 ± 0.07	UVM2	Swift/UVOT
55049.254	-29.47	19.05 ± 0.12	r	p48	55065.830	-16.30	18.76 ± 0.07	UVW1	Swift/UVOT
55049.360	-29.39	18.93 ± 0.14	r	p48	55065.830	-16.30	18.13 ± 0.06	u	Swift/UVOT
55052.277	-27.07	18.85 ± 0.09	r	p48	55065.831	-16.30	19.66 ± 0.08	UVW2	Swift/UVOT
55052.360	-27.01	18.73 ± 0.12	r	p48	55066.141	-16.06	18.26 ± 0.08	g	p60
55054.345	-25.43	18.62 ± 0.09	g	p60	55066.145	-16.05	18.47 ± 0.09	r	p60
55054.347	-25.43	18.80 ± 0.10	r	p60	55066.147	-16.05	18.48 ± 0.08	r	p60
55054.348	-25.43	19.02 ± 0.13	i	p60	55066.149	-16.05	18.67 ± 0.11	i	p60
55056.245	-23.92	18.67 ± 0.07	r	p48	55066.152	-16.05	18.73 ± 0.11	i	p60
55056.335	-23.85	18.75 ± 0.09	r	p48	55067.140	-15.26	18.29 ± 0.08	g	p60
55059.147	-21.61	18.42 ± 0.08	g	p60	55067.144	-15.26	18.47 ± 0.08	r	p60
55059.151	-21.61	18.61 ± 0.09	r	p60	55067.146	-15.26	18.47 ± 0.09	r	p60
55059.153	-21.61	18.60 ± 0.09	r	p60	55067.148	-15.26	18.73 ± 0.11	i	p60
55059.156	-21.61	18.97 ± 0.13	i	p60	55067.151	-15.25	18.72 ± 0.11	i	p60
55059.158	-21.60	18.91 ± 0.13	i	p60	55067.226	-15.19	18.36 ± 0.07	r	p48
55060.198	-20.78	18.43 ± 0.08	g	p60	55067.270	-15.16	18.40 ± 0.07	r	p48
55060.201	-20.78	18.59 ± 0.09	r	p60	55068.139	-14.47	18.26 ± 0.08	g	p60
55060.204	-20.77	18.59 ± 0.09	r	p60	55068.143	-14.47	18.42 ± 0.08	r	p60
55060.206	-20.77	18.92 ± 0.12	i	p60	55068.145	-14.46	18.39 ± 0.08	r	p60
55060.208	-20.77	18.91 ± 0.12	i	p60	55068.147	-14.46	18.68 ± 0.11	i	p60
55061.151	-20.02	18.37 ± 0.08	g	p60	55068.150	-14.46	18.70 ± 0.11	i	p60
55061.155	-20.02	18.57 ± 0.09	r	p60	55068.259	-14.37	18.14 ± 0.09	B	p60
55061.158	-20.02	18.59 ± 0.08	r	p60	55069.015	-13.77	19.62 ± 0.09	UVM2	Swift/UVOT
55061.160	-20.01	18.87 ± 0.12	i	p60	55069.017	-13.77	18.90 ± 0.07	UVW1	Swift/UVOT
55061.162	-20.01	18.89 ± 0.13	i	p60	55069.019	-13.77	19.68 ± 0.08	UVW2	Swift/UVOT
55061.290	-19.91	18.60 ± 0.08	r	p48	55069.019	-13.77	18.06 ± 0.06	u	Swift/UVOT
55061.921	-19.41	19.30 ± 0.07	UVM2	Swift/UVOT	55069.138	-13.67	18.23 ± 0.07	g	p60
55061.930	-19.40	18.81 ± 0.06	UVW1	Swift/UVOT	55069.142	-13.67	18.44 ± 0.08	r	p60
55061.936	-19.40	18.14 ± 0.06	u	Swift/UVOT	55069.145	-13.67	18.42 ± 0.08	r	p60
55061.939	-19.40	19.57 ± 0.08	UVW2	Swift/UVOT	55069.147	-13.67	18.68 ± 0.11	i	p60
55062.145	-19.23	18.35 ± 0.08	g	p60	55069.149	-13.67	18.73 ± 0.11	i	p60
55062.149	-19.23	18.54 ± 0.08	r	p60	55073.635	-10.10	19.66 ± 0.08	UVM2	Swift/UVOT
55062.151	-19.23	18.58 ± 0.09	r	p60	55073.641	-10.10	18.91 ± 0.06	UVW1	Swift/UVOT
55062.153	-19.22	18.83 ± 0.12	i	p60	55073.645	-10.09	18.05 ± 0.06	u	Swift/UVOT
55062.156	-19.22	18.85 ± 0.12	i	p60	55073.647	-10.09	19.87 ± 0.08	UVW2	Swift/UVOT
55062.162	-19.22	18.51 ± 0.07	r	p48	55077.314	-7.18	19.86 ± 0.09	UVM2	Swift/UVOT
55063.144	-18.44	18.36 ± 0.08	g	p60	55077.316	-7.18	18.97 ± 0.07	UVW1	Swift/UVOT
55063.148	-18.43	18.57 ± 0.08	r	p60	55077.452	-7.07	17.96 ± 0.07	u	Swift/UVOT
55063.150	-18.43	18.56 ± 0.09	r	p60	55077.453	-7.07	19.73 ± 0.10	UVW2	Swift/UVOT
55063.153	-18.43	18.80 ± 0.12	i	p60	55084.014	-1.85	19.80 ± 0.09	UVM2	Swift/UVOT
55063.155	-18.43	18.82 ± 0.12	i	p60	55084.018	-1.85	19.03 ± 0.07	UVW1	Swift/UVOT
55064.142	-17.64	18.34 ± 0.08	g	p60	55084.020	-1.85	17.98 ± 0.06	u	Swift/UVOT
55064.146	-17.64	18.53 ± 0.08	r	p60	55084.022	-1.85	19.99 ± 0.09	UVW2	Swift/UVOT

Table D11. Continuation of Table D10.

MJD	Phase	m	Filter	Telescope
55084.213	-1.70	18.20 ± 0.07	r	p48
55084.257	-1.66	18.23 ± 0.08	r	p48
55097.812	9.11	20.47 ± 0.15	UVM2	Swift/UVOT
55097.814	9.11	19.71 ± 0.11	UVW1	Swift/UVOT
55097.815	9.11	18.37 ± 0.07	u	Swift/UVOT
55097.816	9.11	20.56 ± 0.12	UVW2	Swift/UVOT
55107.174	16.55	18.25 ± 0.08	g	p60
55107.176	16.55	18.40 ± 0.08	r	p60
55107.177	16.55	18.61 ± 0.11	i	p60
55107.376	16.71	20.91 ± 0.18	UVM2	Swift/UVOT
55107.379	16.71	20.07 ± 0.12	UVW1	Swift/UVOT
55107.382	16.71	18.77 ± 0.09	u	Swift/UVOT
55107.383	16.71	21.53 ± 0.19	UVW2	Swift/UVOT
55123.141	29.24	18.64 ± 0.10	g	p60
55123.143	29.24	18.55 ± 0.09	r	p60
55123.144	29.24	18.72 ± 0.12	i	p60
55123.147	29.24	18.71 ± 0.13	B	p60
55137.129	40.35	18.90 ± 0.11	g	p60
55137.131	40.35	18.71 ± 0.10	r	p60
55137.131	40.35	18.86 ± 0.13	i	p60
55138.077	41.10	18.95 ± 0.11	g	p60
55138.079	41.11	18.80 ± 0.09	r	p60
55138.080	41.11	18.82 ± 0.12	i	p60
55142.104	44.30	19.09 ± 0.12	g	p60
55142.106	44.31	18.89 ± 0.10	r	p60
55142.107	44.31	18.92 ± 0.13	i	p60
55142.110	44.31	19.31 ± 0.19	B	p60
55166.547	63.73	19.36 ± 0.12	r	p60
55166.549	63.73	19.40 ± 0.17	i	p60
55168.540	65.31	19.79 ± 0.18	g	p60
55168.542	65.31	19.49 ± 0.13	r	p60
55168.543	65.31	19.35 ± 0.22	i	p60
55169.539	66.10	19.41 ± 0.30	i	p60
55181.504	75.61	20.92 ± 0.36	g	p60
55181.505	75.61	19.60 ± 0.16	r	p60
55181.507	75.61	19.90 ± 0.24	i	p60
55183.502	77.20	20.88 ± 0.34	g	p60
55183.504	77.20	19.88 ± 0.26	i	p60
55183.508	77.20	20.30 ± 0.34	B	p60
55184.504	77.99	20.19 ± 0.35	B	p60
55185.495	78.78	19.46 ± 0.18	r	p60
55189.486	81.95	19.82 ± 0.18	r	p60
55202.474	92.27	20.33 ± 0.23	r	p60
55202.476	92.28	19.91 ± 0.23	i	p60
55203.448	93.05	20.54 ± 0.28	r	p60
55205.000	94.28	21.03 ± 0.20	r	P200

Table D12. PTF 09cnd rest-frame g photometry data.

MJD	Phase	m_g	M_g	Tel	Ref	MJD	Phase	m_g	M_g	Tel	Ref
55025.378	-48.45	20.85 ± 0.26	-19.73	p48		55185.495	78.78	19.86 ± 0.18	-20.73	p60	
55025.418	-48.41	20.68 ± 0.29	-19.91	p48		55189.486	81.95	20.22 ± 0.18	-20.37	p60	
55035.218	-40.63	20.34 ± 0.12	-20.24	p48		55202.474	92.27	20.73 ± 0.23	-19.85	p60	
55035.313	-40.55	20.50 ± 0.13	-20.08	p48		55203.448	93.05	20.94 ± 0.28	-19.64	p60	
55049.254	-29.47	19.25 ± 0.12	-21.34	p48		55205.000	94.28	21.44 ± 0.20	-19.14	P200	
55049.360	-29.39	19.13 ± 0.14	-21.46	p48							
55052.277	-27.07	19.04 ± 0.09	-21.54	p48							
55052.360	-27.01	18.93 ± 0.12	-21.66	p48							
55054.347	-25.43	19.00 ± 0.10	-21.58	p60							
55056.245	-23.92	18.88 ± 0.07	-21.71	p48							
55056.335	-23.85	18.96 ± 0.09	-21.63	p48							
55059.151	-21.61	18.83 ± 0.09	-21.76	p60							
55059.153	-21.61	18.81 ± 0.09	-21.77	p60							
55060.201	-20.78	18.81 ± 0.09	-21.78	p60							
55060.204	-20.77	18.81 ± 0.09	-21.78	p60							
55061.155	-20.02	18.79 ± 0.09	-21.79	p60							
55061.158	-20.02	18.81 ± 0.08	-21.77	p60							
55061.290	-19.91	18.82 ± 0.08	-21.77	p48							
55062.149	-19.23	18.76 ± 0.08	-21.83	p60							
55062.151	-19.23	18.80 ± 0.09	-21.78	p60							
55062.162	-19.22	18.73 ± 0.07	-21.86	p48							
55063.148	-18.43	18.79 ± 0.08	-21.80	p60							
55063.150	-18.43	18.78 ± 0.09	-21.80	p60							
55064.146	-17.64	18.76 ± 0.08	-21.83	p60							
55064.148	-17.64	18.76 ± 0.08	-21.82	p60							
55066.145	-16.05	18.70 ± 0.09	-21.88	p60							
55066.147	-16.05	18.71 ± 0.08	-21.88	p60							
55067.144	-15.26	18.70 ± 0.08	-21.88	p60							
55067.146	-15.26	18.71 ± 0.09	-21.88	p60							
55067.226	-15.19	18.59 ± 0.07	-21.99	p48							
55067.270	-15.16	18.63 ± 0.07	-21.95	p48							
55068.143	-14.47	18.65 ± 0.08	-21.93	p60							
55068.145	-14.46	18.62 ± 0.08	-21.96	p60							
55069.142	-13.67	18.68 ± 0.08	-21.91	p60							
55069.145	-13.67	18.65 ± 0.08	-21.93	p60							
55081.750	-3.65	18.50 ± 0.04	-22.09	Wise	I						
55084.213	-1.70	18.47 ± 0.07	-22.11	p48							
55084.257	-1.66	18.50 ± 0.08	-22.09	p48							
55107.176	16.55	18.71 ± 0.08	-21.87	p60							
55123.143	29.24	18.89 ± 0.09	-21.69	p60							
55137.131	40.35	19.07 ± 0.10	-21.52	p60							
55138.079	41.11	19.16 ± 0.09	-21.43	p60							
55142.106	44.31	19.25 ± 0.10	-21.33	p60							
55166.547	63.73	19.75 ± 0.12	-20.84	p60							
55168.542	65.31	19.88 ± 0.13	-20.70	p60							
55181.505	75.61	20.00 ± 0.16	-20.59	p60							

Table D13. PTF 09cwl photometry data.

MJD	Phase	m	Filter	Telescope
55021.255	-34.07	20.59 ± 0.27	r	p48
55034.210	-24.47	19.83 ± 0.13	r	p48
55034.308	-24.40	20.03 ± 0.19	r	p48
55050.185	-12.64	19.13 ± 0.12	r	p48
55050.268	-12.58	19.21 ± 0.19	r	p48
55072.574	3.94	22.04 ± 0.26	UVM2	Swift/UVOT
55072.578	3.94	20.86 ± 0.14	UVW1	Swift/UVOT
55072.581	3.95	19.50 ± 0.09	u	Swift/UVOT
55072.583	3.95	22.85 ± 0.33	UVW2	Swift/UVOT
55189.465	90.51	21.72 ± 0.29	r	p60
55207.416	103.81	22.28 ± 0.32	g	p60
55208.416	104.55	21.57 ± 0.35	r	p60
55211.405	106.76	20.76 ± 0.23	g	p60
55330.000	194.60	23.93 ± 0.35	r	Keck

Table D14. PTF 09cwl rest-frame g photometry data.

MJD	Phase	m_g	M_g	Telescope	Reference
55021.255	-34.07	20.95 ± 0.27	-20.39	p48	
55034.210	-24.47	20.20 ± 0.13	-21.15	p48	
55034.308	-24.40	20.40 ± 0.19	-20.95	p48	
55050.185	-12.64	19.51 ± 0.12	-21.83	p48	
55050.268	-12.58	19.60 ± 0.19	-21.75	p48	
55081.227	10.35	19.47 ± 0.10	-21.88	Wise	I
55189.465	90.51	22.16 ± 0.29	-19.18	p60	
55205.540	102.42	22.42 ± 0.05	-18.92	p200	I
55208.416	104.55	22.02 ± 0.35	-19.32	p60	
55330.000	194.60	24.39 ± 0.35	-16.96	Keck	

Table D15. PTF 10aagc photometry data.

MJD	Phase	<i>m</i>	Filter	Tel	MJD	Phase	<i>m</i>	Filter	Tel
55495.481	-3.31	19.88 ± 0.23	r	p48	55532.508	27.37	21.44 ± 0.29	r	p48
55495.506	-3.29	19.96 ± 0.16	r	p48	55534.353	28.90	20.71 ± 0.17	i	p60
55495.530	-3.27	19.96 ± 0.18	r	p48	55535.315	29.70	20.49 ± 0.33	i	p60
55497.524	-1.62	19.87 ± 0.19	r	p48	55535.318	29.70	21.55 ± 0.24	r	p60
55503.502	3.33	19.60 ± 0.11	r	p48	55535.394	29.76	21.37 ± 0.33	r	p48
55503.546	3.37	19.68 ± 0.14	r	p48	55538.307	32.18	21.58 ± 0.24	i	p60
55504.434	4.11	19.54 ± 0.09	r	p60	55538.309	32.18	21.86 ± 0.23	r	p60
55504.440	4.11	19.47 ± 0.08	r	p60	55538.316	32.18	22.50 ± 0.26	g	p60
55504.447	4.12	19.64 ± 0.09	r	p60	55538.433	32.28	21.40 ± 0.27	r	p48
55505.396	4.90	19.70 ± 0.11	i	p60	55539.304	33.00	21.32 ± 0.22	i	p60
55505.398	4.90	19.62 ± 0.11	i	p60	55539.306	33.00	22.11 ± 0.25	r	p60
55505.401	4.91	19.19 ± 0.07	g	p60	55543.493	36.47	21.29 ± 0.26	r	p48
55505.404	4.91	19.32 ± 0.08	g	p60	55624.000	103.19	23.65 ± 0.30	r	Keck
55505.531	5.01	19.76 ± 0.11	r	p48					
55506.501	5.82	19.69 ± 0.13	r	p48					
55506.545	5.85	19.51 ± 0.13	r	p48					
55507.498	6.64	19.82 ± 0.15	r	p48					
55507.544	6.68	19.78 ± 0.14	r	p48					
55508.020	7.08	21.10 ± 0.16	UVM2	Swift/UVOT					
55508.027	7.08	20.24 ± 0.13	UVW1	Swift/UVOT					
55508.032	7.09	18.95 ± 0.11	u	Swift/UVOT					
55508.034	7.09	20.95 ± 0.17	UVW2	Swift/UVOT					
55513.375	11.51	20.38 ± 0.27	i	p60					
55513.377	11.52	20.37 ± 0.24	r	p60					
55513.377	11.52	20.26 ± 0.25	r	p48					
55513.421	11.55	20.02 ± 0.16	r	p48					
55514.418	12.38	20.21 ± 0.25	r	p48					
55515.370	13.17	20.11 ± 0.15	i	p60					
55515.371	13.17	20.74 ± 0.32	r	p48					
55515.373	13.17	20.55 ± 0.16	r	p60					
55515.376	13.17	20.02 ± 0.11	g	p60					
55515.415	13.21	20.15 ± 0.16	r	p48					
55516.365	13.99	20.24 ± 0.14	i	p60					
55516.368	13.99	20.26 ± 0.15	r	p60					
55516.378	14.00	19.93 ± 0.18	r	p48					
55516.424	14.04	20.35 ± 0.16	r	p48					
55517.376	14.83	20.17 ± 0.25	r	p48					
55517.420	14.87	20.62 ± 0.27	r	p48					
55518.364	15.65	20.57 ± 0.24	g	p60					
55518.402	15.68	20.54 ± 0.26	r	p48					
55518.446	15.72	20.32 ± 0.20	r	p48					
55519.451	16.55	20.14 ± 0.36	r	p48					
55530.340	25.57	21.33 ± 0.31	g	p60					
55532.324	27.22	21.03 ± 0.25	i	p60					
55532.326	27.22	21.28 ± 0.22	r	p60					
55532.333	27.23	21.86 ± 0.22	g	p60					

Table D16. PTF 10aagc rest-frame g photometry data.

MJD	Phase	m_g	M_g	Telescope	Reference
55495.481	-3.31	20.14 ± 0.23	-19.90	p48	
55495.506	-3.29	20.22 ± 0.16	-19.81	p48	
55495.530	-3.27	20.22 ± 0.18	-19.81	p48	
55497.524	-1.62	20.14 ± 0.19	-19.90	p48	
55503.502	3.33	19.88 ± 0.11	-20.16	p48	
55503.546	3.37	19.96 ± 0.14	-20.08	p48	
55504.434	4.11	19.82 ± 0.09	-20.21	p60	
55504.440	4.11	19.76 ± 0.08	-20.28	p60	
55504.447	4.12	19.92 ± 0.09	-20.11	p60	
55505.531	5.01	20.05 ± 0.11	-19.99	p48	
55506.501	5.82	19.98 ± 0.13	-20.06	p48	
55506.545	5.85	19.80 ± 0.13	-20.23	p48	
55507.498	6.64	20.11 ± 0.15	-19.92	p48	
55507.544	6.68	20.07 ± 0.14	-19.97	p48	
55513.377	11.52	20.68 ± 0.24	-19.35	p60	
55513.377	11.52	20.56 ± 0.25	-19.47	p48	
55513.421	11.55	20.33 ± 0.16	-19.70	p48	
55514.418	12.38	20.51 ± 0.25	-19.52	p48	
55515.371	13.17	21.05 ± 0.32	-18.99	p48	
55515.373	13.17	20.86 ± 0.16	-19.18	p60	
55515.415	13.21	20.46 ± 0.16	-19.57	p48	
55516.368	13.99	20.57 ± 0.15	-19.46	p60	
55516.378	14.00	20.24 ± 0.18	-19.80	p48	
55516.424	14.04	20.67 ± 0.16	-19.37	p48	
55517.376	14.83	20.49 ± 0.25	-19.55	p48	
55517.420	14.87	20.94 ± 0.27	-19.10	p48	
55518.402	15.68	20.86 ± 0.26	-19.18	p48	
55518.446	15.72	20.64 ± 0.20	-19.40	p48	
55519.451	16.55	20.46 ± 0.36	-19.58	p48	
55532.326	27.22	21.62 ± 0.22	-18.42	p60	
55532.508	27.37	21.79 ± 0.29	-18.25	p48	
55535.318	29.70	21.90 ± 0.24	-18.14	p60	
55535.394	29.76	21.71 ± 0.33	-18.32	p48	
55538.309	32.18	22.21 ± 0.23	-17.83	p60	
55538.433	32.28	21.75 ± 0.27	-18.29	p48	
55539.306	33.00	22.46 ± 0.25	-17.57	p60	
55543.493	36.47	21.65 ± 0.26	-18.39	p48	
55624.000	103.19	24.08 ± 0.30	-15.96	Keck	

Table D17. PTF 10bfz photometry data.

MJD	Phase	m	Filter	Tel	MJD	Phase	m	Filter	Tel
55227.463	-0.00	18.52 ± 0.09	r	p48	55283.303	47.73	20.38 ± 0.29	r	p60
55227.507	0.04	18.49 ± 0.08	r	p48	55292.501	55.59	21.01 ± 0.36	r	p48
55242.264	12.65	18.74 ± 0.06	g	p60	55292.502	55.59	20.97 ± 0.34	r	p48
55242.266	12.65	18.69 ± 0.06	r	p60	55295.494	58.15	20.88 ± 0.21	i	p60
55242.267	12.65	18.90 ± 0.08	i	p60	55296.146	58.71	21.20 ± 0.26	r	p48
55244.452	14.52	18.73 ± 0.07	r	p48	55296.189	58.74	21.47 ± 0.25	r	p48
55244.496	14.56	18.80 ± 0.07	r	p48	55296.452	58.97	21.47 ± 0.31	r	p60
55250.437	19.64	19.15 ± 0.09	g	p60	55297.237	59.64	21.15 ± 0.22	r	p48
55250.438	19.64	18.88 ± 0.08	r	p60	55297.321	59.71	22.46 ± 0.35	g	p60
55250.440	19.64	18.88 ± 0.08	i	p60	55297.330	59.72	21.17 ± 0.19	r	p60
55250.442	19.64	19.70 ± 0.17	B	p60	55302.474	64.12	21.92 ± 0.30	g	p60
55251.464	20.51	18.87 ± 0.07	r	p48	55302.483	64.12	20.76 ± 0.22	r	p60
55251.510	20.55	18.87 ± 0.11	r	p48	55302.485	64.13	20.89 ± 0.22	i	p60
55259.240	27.16	19.02 ± 0.12	r	p48	55303.333	64.85	21.33 ± 0.17	r	p60
55260.407	28.16	19.24 ± 0.08	r	p48	55303.335	64.85	21.25 ± 0.27	i	p60
55260.451	28.20	19.05 ± 0.08	r	p48					
55260.539	28.27	19.54 ± 0.16	g	p60					
55260.540	28.27	19.13 ± 0.09	r	p60					
55260.542	28.27	18.98 ± 0.08	i	p60					
55260.545	28.28	20.12 ± 0.27	B	p60					
55266.465	33.34	19.38 ± 0.09	r	p48					
55266.511	33.38	19.36 ± 0.10	r	p48					
55266.534	33.40	20.22 ± 0.14	g	p60					
55266.536	33.40	19.42 ± 0.09	r	p60					
55266.538	33.40	19.35 ± 0.09	i	p60					
55266.541	33.40	20.66 ± 0.30	B	p60					
55268.376	34.97	19.51 ± 0.08	r	p48					
55268.420	35.01	19.47 ± 0.09	r	p48					
55270.268	36.59	19.59 ± 0.14	r	p48					
55270.311	36.62	19.51 ± 0.10	r	p48					
55271.226	37.41	20.62 ± 0.19	g	p60					
55271.229	37.41	19.64 ± 0.13	r	p60					
55271.230	37.41	19.85 ± 0.17	i	p60					
55272.255	38.29	19.75 ± 0.11	r	p48					
55272.298	38.32	19.75 ± 0.10	r	p48					
55272.481	38.48	20.65 ± 0.15	g	p60					
55272.484	38.48	19.82 ± 0.10	r	p60					
55272.486	38.48	19.64 ± 0.11	i	p60					
55274.380	40.10	19.90 ± 0.12	r	p48					
55274.424	40.14	19.81 ± 0.12	r	p48					
55276.422	41.85	20.10 ± 0.13	r	p48					
55276.483	41.90	19.77 ± 0.28	r	p48					
55279.162	44.19	20.42 ± 0.31	r	p48					
55279.206	44.23	20.27 ± 0.23	r	p48					
55282.335	46.90	21.37 ± 0.21	g	p60					
55282.336	46.90	20.48 ± 0.16	r	p60					

Table D18. PTF 10bfz rest-frame g photometry data.

MJD	Phase	m_g	M_g	Telescope	Reference
55227.463	-0.00	18.72 ± 0.09	-20.84	p48	
55227.507	0.04	18.70 ± 0.08	-20.87	p48	
55242.266	12.65	18.94 ± 0.06	-20.63	p60	
55244.452	14.52	18.98 ± 0.07	-20.58	p48	
55244.496	14.56	19.05 ± 0.07	-20.51	p48	
55250.438	19.64	19.14 ± 0.08	-20.42	p60	
55251.464	20.51	19.14 ± 0.07	-20.42	p48	
55251.510	20.55	19.14 ± 0.11	-20.42	p48	
55259.240	27.16	19.30 ± 0.12	-20.26	p48	
55260.407	28.16	19.52 ± 0.08	-20.04	p48	
55260.451	28.20	19.33 ± 0.08	-20.23	p48	
55260.540	28.27	19.42 ± 0.09	-20.15	p60	
55266.465	33.34	19.68 ± 0.09	-19.88	p48	
55266.511	33.38	19.66 ± 0.10	-19.91	p48	
55266.536	33.40	19.72 ± 0.09	-19.85	p60	
55268.376	34.97	19.81 ± 0.08	-19.75	p48	
55268.420	35.01	19.77 ± 0.09	-19.79	p48	
55270.268	36.59	19.90 ± 0.14	-19.67	p48	
55270.311	36.62	19.82 ± 0.10	-19.74	p48	
55271.229	37.41	19.94 ± 0.13	-19.62	p60	
55272.255	38.29	20.06 ± 0.11	-19.50	p48	
55272.298	38.32	20.06 ± 0.10	-19.51	p48	
55272.484	38.48	20.13 ± 0.10	-19.44	p60	
55274.380	40.10	20.21 ± 0.12	-19.36	p48	
55274.424	40.14	20.12 ± 0.12	-19.44	p48	
55276.422	41.85	20.42 ± 0.13	-19.15	p48	
55276.483	41.90	20.08 ± 0.28	-19.48	p48	
55279.162	44.19	20.74 ± 0.31	-18.82	p48	
55279.206	44.23	20.59 ± 0.23	-18.97	p48	
55282.336	46.90	20.80 ± 0.16	-18.76	p60	
55283.303	47.73	20.71 ± 0.29	-18.85	p60	
55292.501	55.59	21.35 ± 0.36	-18.21	p48	
55292.502	55.59	21.31 ± 0.34	-18.25	p48	
55296.146	58.71	21.54 ± 0.26	-18.03	p48	
55296.189	58.74	21.81 ± 0.25	-17.75	p48	
55296.452	58.97	21.81 ± 0.31	-17.75	p60	
55297.237	59.64	21.49 ± 0.22	-18.07	p48	
55297.330	59.72	21.51 ± 0.19	-18.05	p60	
55302.483	64.12	21.10 ± 0.22	-18.46	p60	
55303.333	64.85	21.68 ± 0.17	-17.88	p60	

Table D19. PTF 10bjp photometry data.

MJD	Phase	m	Filter	Telescope
55205.547	-34.57	21.37 ± 0.35	r	p48
55207.341	-33.25	21.32 ± 0.30	r	p48
55207.386	-33.22	21.65 ± 0.28	r	p48
55209.503	-31.66	21.37 ± 0.34	r	p48
55209.548	-31.63	21.08 ± 0.28	r	p48
55221.515	-22.82	20.77 ± 0.20	r	p48
55221.560	-22.79	21.15 ± 0.32	r	p48
55227.346	-18.53	20.69 ± 0.34	r	p48
55227.391	-18.49	20.46 ± 0.27	r	p48
55243.366	-6.74	20.30 ± 0.16	r	p48
55243.412	-6.70	20.39 ± 0.17	r	p48
55246.213	-4.64	20.59 ± 0.23	r	p48
55246.309	-4.57	20.46 ± 0.15	r	p48
55246.353	-4.54	20.42 ± 0.20	r	p48
55250.405	-1.55	20.51 ± 0.27	r	p48
55250.449	-1.52	20.52 ± 0.24	r	p48
55271.409	13.91	20.49 ± 0.25	r	p48
55275.363	16.82	21.34 ± 0.32	r	p48
55275.407	16.85	20.88 ± 0.25	r	p48
55284.156	23.29	20.34 ± 0.35	r	p48
55296.199	32.16	21.20 ± 0.28	r	p48
55297.395	33.04	21.22 ± 0.33	r	p48

Table D20. PTF 10bjp rest-frame g photometry data.

MJD	Phase	m_g	M_g	Telescope	Reference
55205.547	-34.57	21.83 ± 0.35	-19.57	p48	
55207.341	-33.25	21.78 ± 0.30	-19.63	p48	
55207.386	-33.22	22.10 ± 0.28	-19.30	p48	
55209.503	-31.66	21.83 ± 0.34	-19.58	p48	
55209.548	-31.63	21.54 ± 0.28	-19.87	p48	
55221.515	-22.82	21.23 ± 0.20	-20.17	p48	
55221.560	-22.79	21.61 ± 0.32	-19.80	p48	
55227.346	-18.53	21.16 ± 0.34	-20.25	p48	
55227.391	-18.49	20.93 ± 0.27	-20.48	p48	
55243.366	-6.74	20.78 ± 0.16	-20.62	p48	
55243.412	-6.70	20.86 ± 0.17	-20.54	p48	
55246.213	-4.64	21.07 ± 0.23	-20.33	p48	
55246.309	-4.57	20.94 ± 0.15	-20.46	p48	
55246.353	-4.54	20.90 ± 0.20	-20.51	p48	
55250.405	-1.55	20.99 ± 0.27	-20.42	p48	
55250.449	-1.52	21.00 ± 0.24	-20.41	p48	
55271.409	13.91	20.98 ± 0.25	-20.42	p48	
55275.363	16.82	21.83 ± 0.32	-19.58	p48	
55275.407	16.85	21.37 ± 0.25	-20.03	p48	
55284.156	23.29	20.84 ± 0.35	-20.57	p48	
55296.199	32.16	21.70 ± 0.28	-19.71	p48	
55297.395	33.04	21.72 ± 0.33	-19.68	p48	

Table D21. PTF 10cwr photometry data.

MJD	Phase	<i>m</i>	Filter	Tel	MJD	Phase	<i>m</i>	Filter	Tel
55268.233	-10.57	18.69 ± 0.09	r	p48	55319.275	30.92	19.49 ± 0.12	r	p60
55268.277	-10.53	18.56 ± 0.07	r	p48	55360.000	64.03	22.20 ± 0.19	r	P200
55271.264	-8.11	18.52 ± 0.09	r	p48					
55271.315	-8.06	18.53 ± 0.08	r	p48					
55272.168	-7.37	18.14 ± 0.10	g	p60					
55272.169	-7.37	18.49 ± 0.09	r	p60					
55272.170	-7.37	18.68 ± 0.12	i	p60					
55274.161	-5.75	18.26 ± 0.07	g	p60					
55274.163	-5.75	18.41 ± 0.08	r	p60					
55274.164	-5.75	18.81 ± 0.09	i	p60					
55274.167	-5.75	18.20 ± 0.12	B	p60					
55276.156	-4.13	18.18 ± 0.07	g	p60					
55276.157	-4.13	18.51 ± 0.08	r	p60					
55276.159	-4.13	18.74 ± 0.08	i	p60					
55276.162	-4.12	18.29 ± 0.13	B	p60					
55277.344	-3.16	18.12 ± 0.07	g	p60					
55277.345	-3.16	18.49 ± 0.08	r	p60					
55277.347	-3.16	18.58 ± 0.08	i	p60					
55277.348	-3.16	18.99 ± 0.27	z	p60					
55277.349	-3.16	18.18 ± 0.10	B	p60					
55280.146	-0.88	18.42 ± 0.19	g	p60					
55280.147	-0.88	18.31 ± 0.08	r	p60					
55280.149	-0.88	18.68 ± 0.08	i	p60					
55280.150	-0.88	18.68 ± 0.34	z	p60					
55286.211	4.05	18.43 ± 0.08	r	p60					
55286.213	4.05	18.40 ± 0.08	i	p60					
55286.215	4.05	18.68 ± 0.27	z	p60					
55289.217	6.49	18.55 ± 0.19	z	p60					
55289.221	6.49	18.29 ± 0.11	B	p60					
55293.228	9.75	18.52 ± 0.12	r	p60					
55293.230	9.75	18.65 ± 0.10	i	p60					
55293.233	9.75	18.56 ± 0.13	B	p60					
55294.271	10.60	18.68 ± 0.15	z	p60					
55297.175	12.96	18.59 ± 0.07	g	p60					
55297.177	12.96	18.65 ± 0.08	r	p60					
55297.181	12.96	18.84 ± 0.09	i	p60					
55297.182	12.96	18.78 ± 0.13	B	p60					
55302.207	17.05	19.16 ± 0.27	B	p60					
55303.207	17.86	18.96 ± 0.08	g	p60					
55303.211	17.87	18.91 ± 0.09	r	p60					
55303.212	17.87	19.00 ± 0.09	i	p60					
55303.213	17.87	19.11 ± 0.30	z	p60					
55303.214	17.87	19.18 ± 0.15	B	p60					
55313.246	26.02	19.10 ± 0.09	i	p60					
55313.252	26.03	19.38 ± 0.10	g	p60					
55319.274	30.92	19.46 ± 0.11	i	p60					

Table D22. PTF 10cwr rest-frame g photometry data.

MJD	Phase	m_g	M_g	Telescope	Reference
55268.233	-10.57	18.97 ± 0.09	-21.33	p48	
55268.277	-10.53	18.84 ± 0.07	-21.46	p48	
55271.264	-8.11	18.80 ± 0.09	-21.49	p48	
55271.315	-8.06	18.82 ± 0.08	-21.48	p48	
55272.169	-7.37	18.78 ± 0.09	-21.52	p60	
55274.163	-5.75	18.71 ± 0.08	-21.59	p60	
55276.157	-4.13	18.81 ± 0.08	-21.49	p60	
55277.345	-3.16	18.79 ± 0.08	-21.50	p60	
55280.147	-0.88	18.62 ± 0.08	-21.68	p60	
55286.211	4.05	18.75 ± 0.08	-21.55	p60	
55293.228	9.75	18.85 ± 0.12	-21.44	p60	
55297.177	12.96	18.99 ± 0.08	-21.31	p60	
55303.211	17.87	19.26 ± 0.09	-21.04	p60	
55319.275	30.92	19.87 ± 0.12	-20.43	p60	
55360.000	64.03	22.61 ± 0.19	-17.68	P200	

Table D23. PTF 10hgi photometry data.

MJD	Phase	m	Filter	Tel	MJD	Phase	m	Filter	Tel
55320.381	-42.85	21.40 ± 0.34	r	p48	55372.277	4.41	17.89 ± 0.08	r	p48
55331.441	-32.77	19.10 ± 0.08	r	p48	55372.289	4.42	18.15 ± 0.15	i	p60
55331.485	-32.73	19.15 ± 0.09	r	p48	55372.290	4.42	17.88 ± 0.10	r	p60
55332.190	-32.09	19.36 ± 0.18	i	p60	55372.295	4.43	18.03 ± 0.13	B	p60
55332.192	-32.09	19.15 ± 0.12	r	p60	55375.368	7.22	17.94 ± 0.09	r	p60
55332.195	-32.09	19.35 ± 0.18	i	p60	55375.368	7.22	18.22 ± 0.13	i	p60
55332.197	-32.09	19.08 ± 0.12	r	p60	55375.370	7.23	18.02 ± 0.13	B	p60
55333.220	-31.15	19.32 ± 0.17	i	p60	55376.320	8.09	18.15 ± 0.12	i	p60
55333.221	-31.15	19.00 ± 0.13	r	p60	55376.321	8.09	17.96 ± 0.08	r	p60
55336.438	-28.22	18.74 ± 0.08	r	p48	55376.322	8.09	18.09 ± 0.12	B	p60
55336.482	-28.18	18.81 ± 0.09	r	p48	55377.331	9.01	17.94 ± 0.07	r	p48
55341.434	-23.67	18.54 ± 0.08	r	p48	55387.302	18.09	18.12 ± 0.07	r	p48
55341.477	-23.64	18.57 ± 0.08	r	p48	55398.237	28.05	18.78 ± 0.09	r	p48
55347.195	-18.43	18.33 ± 0.07	r	p48	55401.243	30.79	19.06 ± 0.25	i	p60
55349.243	-16.56	18.48 ± 0.10	i	p60	55401.244	30.79	18.80 ± 0.16	r	p60
55349.245	-16.56	18.28 ± 0.08	r	p60	55404.276	33.55	19.12 ± 0.11	r	p48
55349.246	-16.56	18.23 ± 0.09	B	p60	55404.322	33.59	18.91 ± 0.12	r	p48
55349.251	-16.56	18.49 ± 0.11	i	p60	55405.242	34.43	19.19 ± 0.19	i	p60
55349.253	-16.55	18.22 ± 0.08	r	p60	55406.183	35.28	19.11 ± 0.12	r	p60
55349.266	-16.54	18.33 ± 0.09	B	p60	55408.251	37.17	19.30 ± 0.17	i	p60
55352.243	-13.83	18.15 ± 0.07	r	p48	55410.184	38.93	19.24 ± 0.13	r	p48
55352.288	-13.79	18.43 ± 0.09	i	p60	55410.227	38.97	19.20 ± 0.11	r	p48
55352.289	-13.79	18.14 ± 0.07	r	p60	55410.275	39.01	19.00 ± 0.25	r	p60
55352.291	-13.79	18.14 ± 0.08	B	p60	55410.277	39.01	20.07 ± 0.33	B	p60
55355.366	-10.99	18.37 ± 0.09	i	p60	55411.295	39.94	19.38 ± 0.19	i	p60
55355.367	-10.99	18.09 ± 0.07	r	p60	55415.294	43.58	19.28 ± 0.17	i	p60
55355.369	-10.99	18.07 ± 0.08	B	p60	55415.296	43.58	19.44 ± 0.14	r	p60
55356.290	-10.15	18.30 ± 0.09	i	p60	55415.297	43.58	20.50 ± 0.30	B	p60
55356.292	-10.15	18.09 ± 0.07	r	p60	55416.177	44.38	19.36 ± 0.12	r	p48
55356.293	-10.14	18.10 ± 0.08	B	p60	55416.221	44.42	19.26 ± 0.11	r	p48
55357.227	-9.29	18.02 ± 0.07	r	p48	55419.182	47.12	19.37 ± 0.12	r	p48
55357.282	-9.24	18.03 ± 0.07	r	p48	55419.226	47.16	19.36 ± 0.13	r	p48
55360.343	-6.46	18.17 ± 0.08	i	p60	55421.270	49.02	19.46 ± 0.16	i	p60
55360.345	-6.45	17.95 ± 0.07	r	p60	55421.272	49.02	19.49 ± 0.15	r	p60
55360.346	-6.45	17.99 ± 0.08	B	p60	55421.274	49.03	20.48 ± 0.30	B	p60
55362.234	-4.73	17.93 ± 0.07	r	p48	55422.224	49.89	19.45 ± 0.10	r	p48
55363.361	-3.71	18.15 ± 0.09	i	p60					
55363.365	-3.70	17.94 ± 0.08	B	p60					
55367.277	-0.14	17.88 ± 0.07	r	p48					
55367.301	-0.12	18.12 ± 0.10	i	p60					
55367.302	-0.12	17.90 ± 0.07	r	p60					
55367.304	-0.12	17.93 ± 0.09	B	p60					
55367.320	-0.10	17.86 ± 0.07	r	p48					
55369.358	1.75	18.18 ± 0.12	i	p60					
55369.359	1.75	17.86 ± 0.08	r	p60					
55369.380	1.77	17.94 ± 0.09	B	p60					

Table D24. PTF 10hg1 rest-frame g photometry data.

MJD	Phase	m_g	M_g	Tel	Ref	MJD	Phase	m_g	M_g	Tel	Ref
55320.381	-42.85	21.34 ± 0.34	-16.94	p48		55415.296	43.58	19.67 ± 0.14	-18.61	p60	
55331.441	-32.77	19.04 ± 0.08	-19.24	p48		55416.177	44.38	19.58 ± 0.12	-18.69	p48	
55331.485	-32.73	19.09 ± 0.09	-19.18	p48		55416.221	44.42	19.48 ± 0.11	-18.79	p48	
55332.192	-32.09	19.09 ± 0.12	-19.19	p60		55419.182	47.12	19.60 ± 0.12	-18.67	p48	
55332.197	-32.09	19.01 ± 0.12	-19.26	p60		55419.226	47.16	19.60 ± 0.13	-18.68	p48	
55333.221	-31.15	18.93 ± 0.13	-19.34	p60		55421.272	49.02	19.73 ± 0.15	-18.55	p60	
55334.570	-29.92	18.68 ± 0.07	-19.59	PS1	III	55422.224	49.89	19.69 ± 0.10	-18.58	p48	
55336.438	-28.22	18.67 ± 0.08	-19.60	p48		55423.390	50.95	19.68 ± 0.03	-18.59	LT	III
55336.482	-28.18	18.74 ± 0.09	-19.53	p48		55426.420	53.71	19.70 ± 0.05	-18.58	LT	III
55341.434	-23.67	18.49 ± 0.08	-19.78	p48		55428.870	55.94	19.74 ± 0.07	-18.53	FTN	III
55341.477	-23.64	18.52 ± 0.08	-19.75	p48		55429.430	56.45	19.76 ± 0.06	-18.51	LT	III
55347.195	-18.43	18.31 ± 0.07	-19.96	p48		55433.380	60.05	19.81 ± 0.05	-18.47	LT	III
55349.245	-16.56	18.27 ± 0.08	-20.01	p60		55436.400	62.80	19.88 ± 0.12	-18.39	LT	III
55349.253	-16.55	18.21 ± 0.08	-20.06	p60		55439.820	65.91	19.95 ± 0.04	-18.32	FTN	III
55352.243	-13.83	18.15 ± 0.07	-20.12	p48		55441.370	67.33	19.96 ± 0.04	-18.31	LT	III
55352.289	-13.79	18.15 ± 0.07	-20.12	p60		55445.370	70.97	20.02 ± 0.04	-18.26	LT	III
55355.367	-10.99	18.11 ± 0.07	-20.16	p60		55447.800	73.18	20.05 ± 0.04	-18.22	FTN	III
55356.292	-10.15	18.11 ± 0.07	-20.16	p60		55448.380	73.71	20.10 ± 0.04	-18.17	LT	III
55357.227	-9.29	18.06 ± 0.07	-20.22	p48		55453.770	78.62	20.20 ± 0.05	-18.07	FTN	III
55357.282	-9.24	18.06 ± 0.07	-20.21	p48		55460.360	84.62	20.36 ± 0.09	-17.92	LT	III
55360.345	-6.45	17.99 ± 0.07	-20.28	p60		55616.230	226.55	24.06 ± 0.30	-14.22	WHT	III
55362.234	-4.73	17.98 ± 0.07	-20.30	p48							
55366.450	-0.90	17.96 ± 0.10	-20.32	PS1	III						
55367.277	-0.14	17.96 ± 0.07	-20.32	p48							
55367.302	-0.12	17.98 ± 0.07	-20.30	p60							
55367.320	-0.10	17.94 ± 0.07	-20.34	p48							
55369.359	1.75	17.94 ± 0.08	-20.33	p60							
55372.277	4.41	17.98 ± 0.08	-20.29	p48							
55372.290	4.42	17.97 ± 0.10	-20.30	p60							
55375.368	7.22	18.04 ± 0.09	-20.23	p60							
55376.321	8.09	18.07 ± 0.08	-20.21	p60							
55377.331	9.01	18.06 ± 0.07	-20.22	p48							
55387.302	18.09	18.27 ± 0.07	-20.01	p48							
55395.390	25.46	18.65 ± 0.08	-19.63	LT	III						
55398.237	28.05	18.96 ± 0.09	-19.32	p48							
55398.470	28.26	18.91 ± 0.09	-19.37	LT	III						
55401.244	30.79	18.99 ± 0.16	-19.28	p60							
55401.500	31.02	19.15 ± 0.09	-19.13	LT	III						
55404.276	33.55	19.32 ± 0.11	-18.95	p48							
55404.322	33.59	19.10 ± 0.12	-19.17	p48							
55405.390	34.56	19.22 ± 0.06	-19.06	LT	III						
55406.183	35.28	19.31 ± 0.12	-18.97	p60							
55409.400	38.21	19.35 ± 0.03	-18.93	LT	III						
55410.184	38.93	19.45 ± 0.13	-18.82	p48							
55410.227	38.97	19.41 ± 0.11	-18.86	p48							
55410.275	39.01	19.21 ± 0.25	-19.07	p60							

Table D25. PTF 10nmn photometry data.

MJD	Phase	m	Filter	Telescope
55267.413	-103.94	19.79 ± 0.14	r	p48
55267.456	-103.90	19.70 ± 0.12	r	p48
55384.200	0.00	18.54 ± 0.07	r	p48
55384.245	0.04	18.52 ± 0.07	r	p48
55391.275	6.30	18.72 ± 0.15	i	p60
55391.277	6.30	18.67 ± 0.08	r	p60
55392.213	7.13	18.63 ± 0.14	i	p60
55392.215	7.13	18.69 ± 0.08	r	p60
55392.217	7.14	19.12 ± 0.19	B	p60
55392.220	7.14	19.40 ± 0.10	g	p60
55404.163	17.77	18.99 ± 0.23	i	p60
55404.165	17.77	19.15 ± 0.12	r	p60
55569.533	164.95	20.09 ± 0.35	i	p60
55569.535	164.95	20.99 ± 0.26	r	p60
55571.530	166.72	20.76 ± 0.26	r	p60
55571.542	166.73	21.43 ± 0.34	g	p60
55573.525	168.50	20.82 ± 0.25	r	p60
55573.537	168.51	21.53 ± 0.32	g	p60
55577.547	172.08	21.10 ± 0.28	r	p60
55577.551	172.08	21.35 ± 0.27	g	p60
55585.491	179.15	20.08 ± 0.34	i	p60
55585.502	179.16	21.03 ± 0.30	r	p60
55591.474	184.47	21.22 ± 0.28	r	p60
55596.461	188.91	21.10 ± 0.27	r	p60
55596.474	188.92	21.83 ± 0.34	g	p60
55599.499	191.62	21.93 ± 0.35	g	p60
55604.440	196.01	21.31 ± 0.29	r	p60
55605.438	196.90	21.22 ± 0.32	r	p60
55605.451	196.91	21.78 ± 0.34	g	p60
55614.507	204.97	21.21 ± 0.35	r	p60
55621.393	211.10	21.14 ± 0.25	r	p60
55621.416	211.12	21.54 ± 0.27	g	p60
55622.389	211.99	21.31 ± 0.30	r	p60
55622.402	212.00	21.83 ± 0.34	g	p60
55629.383	218.21	21.16 ± 0.33	r	p60
55630.368	219.09	21.07 ± 0.26	r	p60
55631.380	219.99	21.80 ± 0.34	g	p60
55632.363	220.86	21.22 ± 0.33	r	p60
55649.350	235.98	21.27 ± 0.26	r	p60
55656.296	242.17	20.24 ± 0.35	i	p60
55656.312	242.18	21.65 ± 0.35	r	p60
56188.500	715.82	25.25 ± 0.15	r	HST

Table D26. PTF 10nmn rest-frame g photometry data.

MJD	Phase	m_g	M_g	Telescope	Reference
55267.413	-103.94	19.77 ± 0.14	-19.04	p48	
55267.456	-103.90	19.68 ± 0.12	-19.13	p48	
55384.200	0.00	18.65 ± 0.07	-20.16	p48	
55384.245	0.04	18.63 ± 0.07	-20.18	p48	
55391.277	6.30	18.81 ± 0.08	-20.00	p60	
55392.215	7.13	18.83 ± 0.08	-19.98	p60	
55404.165	17.77	19.33 ± 0.12	-19.48	p60	
55569.535	164.95	21.32 ± 0.26	-17.49	p60	
55571.530	166.72	21.09 ± 0.26	-17.72	p60	
55573.525	168.50	21.15 ± 0.25	-17.66	p60	
55577.547	172.08	21.42 ± 0.28	-17.38	p60	
55585.502	179.16	21.35 ± 0.30	-17.46	p60	
55591.474	184.47	21.54 ± 0.28	-17.27	p60	
55596.461	188.91	21.42 ± 0.27	-17.39	p60	
55604.440	196.01	21.63 ± 0.29	-17.18	p60	
55605.438	196.90	21.53 ± 0.32	-17.27	p60	
55614.507	204.97	21.52 ± 0.35	-17.29	p60	
55621.393	211.10	21.44 ± 0.25	-17.37	p60	
55622.389	211.99	21.61 ± 0.30	-17.20	p60	
55629.383	218.21	21.46 ± 0.33	-17.35	p60	
55630.368	219.09	21.37 ± 0.26	-17.44	p60	
55632.363	220.86	21.52 ± 0.33	-17.29	p60	
55649.350	235.98	21.56 ± 0.26	-17.25	p60	
55656.312	242.18	21.94 ± 0.35	-16.87	p60	
56188.500	715.82	25.58 ± 0.15	-13.23	HST	

Table D27. PTF 10uhf photometry data.

MJD	Phase	m	Filter	Telescope
55433.249	-14.75	20.75 ± 0.36	r	p48
55436.275	-12.40	20.38 ± 0.25	r	p48
55436.319	-12.37	20.34 ± 0.28	r	p48
55444.149	-6.29	20.14 ± 0.15	r	p48
55444.196	-6.25	20.22 ± 0.17	r	p48
55447.135	-3.97	20.45 ± 0.32	r	p60
55447.136	-3.97	20.12 ± 0.26	g	p60
55448.900	-2.60	19.76 ± 0.08	g	LT
55448.900	-2.60	19.78 ± 0.10	i	LT
55448.900	-2.60	19.74 ± 0.09	r	LT
55450.900	-1.05	19.81 ± 0.10	i	LT
55450.900	-1.05	19.78 ± 0.08	g	LT
55450.900	-1.05	19.78 ± 0.09	r	LT
55453.149	0.70	20.10 ± 0.15	r	p48
55453.193	0.73	19.90 ± 0.14	r	p48
55457.136	3.79	20.00 ± 0.16	r	p48
55457.179	3.83	20.09 ± 0.18	r	p48
55459.800	5.86	19.83 ± 0.10	r	LT
55459.800	5.86	19.96 ± 0.11	g	LT
55460.138	6.12	20.19 ± 0.19	r	p48
55460.196	6.17	20.19 ± 0.21	r	p48
55485.900	26.13	21.54 ± 0.22	g	LT
55485.900	26.13	20.82 ± 0.16	r	LT
55485.900	26.13	20.57 ± 0.15	i	LT

Table D28. PTF 10uhf rest-frame g photometry data.

MJD	Phase	m_g	M_g	Telescope	Reference
55433.249	-14.75	21.11 ± 0.36	-19.74	p48	
55436.275	-12.40	20.75 ± 0.25	-20.10	p48	
55436.319	-12.37	20.71 ± 0.28	-20.14	p48	
55444.149	-6.29	20.52 ± 0.15	-20.33	p48	
55444.196	-6.25	20.61 ± 0.17	-20.24	p48	
55447.135	-3.97	20.84 ± 0.32	-20.01	p60	
55448.900	-2.60	20.12 ± 0.09	-20.73	LT	
55450.900	-1.05	20.17 ± 0.09	-20.69	LT	
55453.149	0.70	20.50 ± 0.15	-20.35	p48	
55453.193	0.73	20.30 ± 0.14	-20.55	p48	
55457.136	3.79	20.41 ± 0.16	-20.45	p48	
55457.179	3.83	20.50 ± 0.18	-20.36	p48	
55459.800	5.86	20.23 ± 0.10	-20.62	LT	
55460.138	6.12	20.61 ± 0.19	-20.25	p48	
55460.196	6.17	20.61 ± 0.21	-20.24	p48	
55485.900	26.13	21.27 ± 0.16	-19.59	LT	

Table D29. PTF 10vqv photometry data.

MJD	Phase	m	Filter	Telescope
55455.517	-10.33	20.02 ± 0.12	r	p48
55456.498	-9.65	20.02 ± 0.10	r	p48
55457.502	-8.96	20.06 ± 0.10	r	p48
55458.295	-8.42	20.23 ± 0.18	r	p60
55458.296	-8.42	19.68 ± 0.14	g	p60
55459.293	-7.73	20.21 ± 0.20	r	p60
55459.518	-7.57	19.91 ± 0.15	r	p48
55460.291	-7.04	19.97 ± 0.14	r	p60
55460.364	-6.99	19.81 ± 0.16	r	p48
55460.407	-6.96	20.00 ± 0.17	r	p48
55463.401	-4.90	19.93 ± 0.17	r	p48
55463.444	-4.87	20.09 ± 0.26	r	p48
55473.486	2.05	19.86 ± 0.12	r	p48
55473.529	2.08	19.87 ± 0.15	r	p48
55478.496	5.50	19.91 ± 0.14	r	p48
55479.334	6.07	19.86 ± 0.17	r	p48
55479.377	6.10	19.98 ± 0.14	r	p48
55482.429	8.20	20.06 ± 0.12	r	p48
55544.087	50.67	21.57 ± 0.28	r	p60
55544.095	50.67	21.46 ± 0.27	r	p60
55562.114	63.08	21.72 ± 0.31	r	p60
55566.151	65.86	22.14 ± 0.33	r	p60
55567.133	66.54	22.03 ± 0.28	r	p60
55571.203	69.34	21.57 ± 0.33	g	p60
55590.136	82.38	22.41 ± 0.24	g	p60
55591.128	83.07	22.14 ± 0.29	r	p60
55599.126	88.57	22.19 ± 0.34	r	p60
55599.130	88.58	22.67 ± 0.31	g	p60

Table D30. PTF 10vqv rest-frame g photometry data.

MJD	Phase	m_g	M_g	Telescope	Reference
55455.517	-10.33	20.57 ± 0.12	-21.43	p48	
55456.498	-9.65	20.57 ± 0.10	-21.43	p48	
55457.502	-8.96	20.61 ± 0.10	-21.39	p48	
55458.295	-8.42	20.78 ± 0.18	-21.22	p60	
55459.293	-7.73	20.76 ± 0.20	-21.24	p60	
55459.518	-7.57	20.46 ± 0.15	-21.54	p48	
55460.291	-7.04	20.52 ± 0.14	-21.48	p60	
55460.364	-6.99	20.36 ± 0.16	-21.64	p48	
55460.407	-6.96	20.55 ± 0.17	-21.45	p48	
55463.401	-4.90	20.48 ± 0.17	-21.52	p48	
55463.444	-4.87	20.63 ± 0.26	-21.37	p48	
55473.486	2.05	20.40 ± 0.12	-21.60	p48	
55473.529	2.08	20.41 ± 0.15	-21.58	p48	
55478.496	5.50	20.45 ± 0.14	-21.55	p48	
55479.334	6.07	20.40 ± 0.17	-21.60	p48	
55479.377	6.10	20.51 ± 0.14	-21.49	p48	
55482.429	8.20	20.60 ± 0.12	-21.40	p48	
55544.087	50.67	22.08 ± 0.28	-19.92	p60	
55544.095	50.67	21.97 ± 0.27	-20.03	p60	
55562.114	63.08	22.22 ± 0.31	-19.78	p60	
55566.151	65.86	22.64 ± 0.33	-19.36	p60	
55567.133	66.54	22.54 ± 0.28	-19.46	p60	
55591.128	83.07	22.64 ± 0.29	-19.36	p60	
55599.126	88.57	22.68 ± 0.34	-19.31	p60	

Table D31. PTF 10vwg photometry data.

MJD	Phase	<i>m</i>	Filter	Telescope
55400.401	-46.12	19.46 ± 0.32	r	p48
55401.359	-45.32	19.11 ± 0.35	r	p48
55401.403	-45.28	19.30 ± 0.34	r	p48
55425.290	-25.21	18.40 ± 0.09	r	p48
55427.211	-23.59	18.56 ± 0.11	r	p48
55427.261	-23.55	18.34 ± 0.10	r	p48
55428.257	-22.71	18.34 ± 0.10	r	p48
55428.300	-22.68	17.84 ± 0.12	r	p48
55430.180	-21.10	18.37 ± 0.14	r	p48
55430.242	-21.05	18.31 ± 0.11	r	p48
55431.246	-20.20	18.27 ± 0.11	r	p48
55431.290	-20.17	18.23 ± 0.12	r	p48
55433.160	-18.59	18.20 ± 0.11	r	p48
55433.207	-18.55	18.31 ± 0.12	r	p48
55434.247	-17.68	18.37 ± 0.10	r	p48
55434.290	-17.64	18.25 ± 0.12	r	p48
55435.252	-16.84	17.78 ± 0.26	r	p48
55435.296	-16.80	17.79 ± 0.14	r	p48
55436.268	-15.98	17.79 ± 0.11	r	p48
55436.320	-15.94	17.77 ± 0.12	r	p48
55446.151	-7.68	17.64 ± 0.09	r	p48
55450.149	-4.32	17.67 ± 0.08	r	p48
55450.192	-4.28	17.61 ± 0.09	r	p48
55451.155	-3.47	17.81 ± 0.09	r	p48
55451.199	-3.44	17.74 ± 0.09	r	p48
55499.800	37.40	19.97 ± 0.13	r	LT
55499.800	37.40	20.02 ± 0.13	r	LT
55499.800	37.40	19.57 ± 0.11	i	LT
55499.800	37.40	19.56 ± 0.13	i	LT
55513.129	48.60	21.24 ± 0.35	B	p60
55514.078	49.40	19.51 ± 0.31	r	p48
55514.121	49.43	19.27 ± 0.28	r	p48
55515.078	50.24	19.04 ± 0.28	r	p48
55517.119	51.95	19.02 ± 0.25	r	p48
55605.300	126.05	20.14 ± 0.18	i	LT
55605.300	126.05	20.80 ± 0.20	r	LT
55605.300	126.05	20.62 ± 0.19	r	LT
55605.300	126.05	20.11 ± 0.18	i	LT
55643.200	157.90	21.19 ± 0.30	r	LT
55643.200	157.90	21.13 ± 0.29	r	LT
55644.200	158.74	20.31 ± 0.19	i	LT
55644.200	158.74	20.69 ± 0.24	r	LT
55644.200	158.74	21.12 ± 0.28	r	LT
55684.440	192.55	20.97 ± 0.27	i	p60
55706.000	210.66	21.77 ± 0.20	r	P200

Table D32. PTF 10vvg rest-frame g photometry data.

MJD	Phase	m_g	M_g	Telescope	Reference
55400.401	-46.12	19.61 ± 0.32	-20.22	p48	
55401.359	-45.32	19.26 ± 0.35	-20.58	p48	
55401.403	-45.28	19.45 ± 0.34	-20.39	p48	
55425.290	-25.21	18.55 ± 0.09	-21.29	p48	
55427.211	-23.59	18.71 ± 0.11	-21.12	p48	
55427.261	-23.55	18.49 ± 0.10	-21.34	p48	
55428.257	-22.71	18.50 ± 0.10	-21.34	p48	
55428.300	-22.68	17.99 ± 0.12	-21.84	p48	
55430.180	-21.10	18.53 ± 0.14	-21.30	p48	
55430.242	-21.05	18.48 ± 0.11	-21.36	p48	
55431.246	-20.20	18.43 ± 0.11	-21.40	p48	
55431.290	-20.17	18.40 ± 0.12	-21.43	p48	
55433.160	-18.59	18.37 ± 0.11	-21.46	p48	
55433.207	-18.55	18.48 ± 0.12	-21.35	p48	
55434.247	-17.68	18.55 ± 0.10	-21.28	p48	
55434.290	-17.64	18.42 ± 0.12	-21.41	p48	
55435.252	-16.84	17.96 ± 0.26	-21.88	p48	
55435.296	-16.80	17.97 ± 0.14	-21.87	p48	
55436.268	-15.98	17.97 ± 0.11	-21.86	p48	
55436.320	-15.94	17.95 ± 0.12	-21.88	p48	
55446.151	-7.68	17.85 ± 0.09	-21.98	p48	
55450.149	-4.32	17.89 ± 0.08	-21.94	p48	
55450.192	-4.28	17.83 ± 0.09	-22.00	p48	
55451.155	-3.47	18.03 ± 0.09	-21.80	p48	
55451.199	-3.44	17.96 ± 0.09	-21.87	p48	
55499.800	37.40	20.30 ± 0.13	-19.53	LT	
55499.800	37.40	20.35 ± 0.13	-19.48	LT	
55514.078	49.40	19.86 ± 0.31	-19.97	p48	
55514.121	49.43	19.63 ± 0.28	-20.20	p48	
55515.078	50.24	19.39 ± 0.28	-20.44	p48	
55517.119	51.95	19.38 ± 0.25	-20.45	p48	
55605.300	126.05	21.20 ± 0.20	-18.64	LT	
55605.300	126.05	21.02 ± 0.19	-18.82	LT	
55643.200	157.90	21.58 ± 0.30	-18.26	LT	
55643.200	157.90	21.52 ± 0.29	-18.32	LT	
55644.200	158.74	21.08 ± 0.24	-18.76	LT	
55644.200	158.74	21.50 ± 0.28	-18.33	LT	
55706.000	210.66	22.12 ± 0.20	-17.71	P200	

Table D33. PTF 11dij photometry data.

MJD	Phase	m	Filter	Telescope
55652.370	-28.00	20.01 ± 0.11	r	p48
55652.429	-27.95	19.85 ± 0.11	r	p48
55666.197	-15.90	18.08 ± 0.08	r	p48
55666.240	-15.86	18.04 ± 0.07	r	p48
55694.324	8.71	17.95 ± 0.06	r	p60
55694.327	8.71	17.83 ± 0.06	g	p60
55694.329	8.71	18.05 ± 0.06	i	p60
55694.330	8.71	17.90 ± 0.06	r	p60
55694.334	8.72	17.98 ± 0.06	g	p60
55695.205	9.48	17.89 ± 0.08	r	p48
55695.249	9.52	17.96 ± 0.07	r	p48
55708.423	21.04	18.42 ± 0.09	i	p60
55708.425	21.05	18.42 ± 0.08	r	p60
55713.378	25.38	18.88 ± 0.11	g	p60
55744.294	52.43	20.32 ± 0.14	i	p60
55744.296	52.43	20.68 ± 0.15	r	p60
55744.299	52.43	21.30 ± 0.20	g	p60
55754.299	61.18	21.02 ± 0.17	i	p60
55754.301	61.19	21.55 ± 0.19	r	p60
55755.301	62.06	20.68 ± 0.17	i	p60
55766.273	71.66	21.00 ± 0.24	i	p60
55779.196	82.97	21.72 ± 0.24	i	p60

Table D34. PTF 11dij rest-frame g photometry data.

MJD	Phase	m_g	M_g	Telescope	Reference
55652.370	-28.00	19.98 ± 0.11	-19.17	p48	
55652.429	-27.95	19.82 ± 0.11	-19.33	p48	
55653.570	-26.95	19.29 ± 0.05	-19.86	PS1	III
55653.580	-26.94	19.30 ± 0.05	-19.85	PS1	III
55666.197	-15.90	18.11 ± 0.08	-21.05	p48	
55666.240	-15.86	18.06 ± 0.07	-21.09	p48	
55666.800	-15.37	17.94 ± 0.06	-21.21	PS1	III
55694.324	8.71	18.08 ± 0.06	-21.07	p60	
55694.330	8.71	18.02 ± 0.06	-21.13	p60	
55694.990	9.29	17.95 ± 0.06	-21.20	LT	III
55695.205	9.48	18.02 ± 0.08	-21.13	p48	
55695.249	9.52	18.08 ± 0.07	-21.07	p48	
55695.540	9.77	17.96 ± 0.02	-21.19	FTN	III
55695.920	10.10	18.05 ± 0.10	-21.10	LT	III
55695.950	10.13	18.06 ± 0.04	-21.09	LT	III
55696.930	10.99	18.05 ± 0.06	-21.10	LT	III
55697.960	11.89	18.12 ± 0.06	-21.03	LT	III
55698.360	12.24	18.11 ± 0.06	-21.04	FTN	III
55698.950	12.76	18.10 ± 0.03	-21.05	LT	III
55700.050	13.72	18.15 ± 0.08	-21.00	LT	III
55700.940	14.50	18.23 ± 0.02	-20.92	LT	III
55702.030	15.45	18.25 ± 0.02	-20.90	LT	III
55702.970	16.27	18.28 ± 0.02	-20.87	LT	III
55703.930	17.11	18.36 ± 0.03	-20.79	LT	III
55704.930	17.99	18.40 ± 0.02	-20.76	LT	III
55708.425	21.05	18.58 ± 0.08	-20.57	p60	
55710.290	22.68	18.59 ± 0.02	-20.56	FTN	III
55712.940	25.00	18.69 ± 0.02	-20.47	LT	III
55715.930	27.61	18.86 ± 0.02	-20.29	LT	III
55721.930	32.86	19.20 ± 0.04	-19.96	LT	III
55736.750	45.83	19.94 ± 0.04	-19.21	NTT	III
55744.296	52.43	20.91 ± 0.15	-18.24	p60	
55745.330	53.34	20.57 ± 0.07	-18.58	FTN	III
55751.930	59.11	21.15 ± 0.30	-18.00	LT	III
55754.301	61.19	21.80 ± 0.19	-17.35	p60	
55765.940	71.37	21.43 ± 0.06	-17.72	LT	III
55766.890	72.20	21.45 ± 0.07	-17.70	LT	III
55767.900	73.09	21.49 ± 0.06	-17.66	LT	III
55776.890	80.95	21.66 ± 0.10	-17.49	LT	III
55917.740	204.19	23.31 ± 0.24	-15.85	WHT	III

Table D35. PTF 11hrq photometry data.

MJD	Phase	m	Filter	Tel	MJD	Phase	m	Filter	Tel
55753.477	0.00	17.21 ± 0.07	r	p48	55820.294	63.21	18.07 ± 0.10	r	p48
55754.486	0.95	17.23 ± 0.07	r	p48	55820.338	63.25	18.25 ± 0.09	r	p48
55755.474	1.89	17.25 ± 0.07	r	p48	55821.324	64.18	18.15 ± 0.09	r	p48
55757.473	3.78	17.37 ± 0.09	r	p48	55822.289	65.10	18.27 ± 0.09	r	p48
55761.458	7.55	17.43 ± 0.08	r	p48	55822.332	65.14	18.22 ± 0.09	r	p48
55762.492	8.53	17.47 ± 0.07	r	p48	55823.301	66.05	18.31 ± 0.08	r	p48
55763.451	9.44	17.50 ± 0.07	r	p48	55823.345	66.09	18.25 ± 0.07	r	p48
55764.454	10.38	17.48 ± 0.07	r	p48	55824.379	67.07	18.30 ± 0.08	r	p48
55765.468	11.34	17.44 ± 0.07	r	p48	55842.266	83.99	18.60 ± 0.15	r	p48
55766.439	12.26	17.52 ± 0.07	r	p48	55842.309	84.03	18.73 ± 0.16	r	p48
55768.454	14.17	17.52 ± 0.07	r	p48	55843.265	84.94	18.66 ± 0.19	r	p48
55769.453	15.11	17.57 ± 0.07	r	p48	55843.308	84.98	18.61 ± 0.15	r	p48
55769.496	15.15	17.58 ± 0.07	r	p48	55844.227	85.85	18.74 ± 0.19	r	p48
55770.445	16.05	17.56 ± 0.07	r	p48	55849.258	90.61	18.59 ± 0.09	r	p48
55770.489	16.09	17.58 ± 0.07	r	p48	55850.215	91.51	18.62 ± 0.11	r	p48
55771.441	16.99	17.62 ± 0.06	r	p48	55850.272	91.57	18.64 ± 0.11	r	p48
55771.487	17.04	17.59 ± 0.06	r	p48	55851.209	92.45	18.67 ± 0.12	r	p48
55774.445	19.84	17.61 ± 0.07	r	p48	55851.254	92.50	18.64 ± 0.10	r	p48
55779.425	24.55	17.66 ± 0.07	r	p48	55852.206	93.40	18.67 ± 0.08	r	p48
55779.489	24.61	17.69 ± 0.06	r	p48	55853.203	94.34	18.63 ± 0.10	r	p48
55780.407	25.48	17.72 ± 0.07	r	p48	55853.247	94.38	18.64 ± 0.09	r	p48
55780.465	25.53	17.68 ± 0.06	r	p48	55854.206	95.29	18.61 ± 0.08	r	p48
55782.395	27.36	17.73 ± 0.06	r	p48	55854.252	95.33	18.64 ± 0.08	r	p48
55783.398	28.31	17.77 ± 0.09	r	p48	55866.166	106.60	19.00 ± 0.12	r	p48
55783.441	28.35	17.73 ± 0.07	r	p48	55866.210	106.64	19.13 ± 0.13	r	p48
55784.424	29.28	17.74 ± 0.09	r	p48	55867.163	107.55	19.50 ± 0.28	r	p48
55784.468	29.32	17.73 ± 0.07	r	p48	55867.207	107.59	19.11 ± 0.17	r	p48
55789.376	33.96	17.78 ± 0.11	r	p48	55868.160	108.49	19.23 ± 0.19	r	p48
55789.435	34.02	17.86 ± 0.10	r	p48	55868.204	108.53	19.25 ± 0.13	r	p48
55790.416	34.94	17.82 ± 0.07	r	p48	55874.190	114.19	18.94 ± 0.25	r	p48
55790.459	34.98	17.83 ± 0.07	r	p48	55884.116	123.58	19.26 ± 0.16	r	p48
55791.383	35.86	17.84 ± 0.10	r	p48	55884.160	123.62	19.20 ± 0.19	r	p48
55791.431	35.90	17.88 ± 0.08	r	p48	55887.163	126.47	19.37 ± 0.14	r	p48
55792.369	36.79	17.79 ± 0.08	r	p48	55887.218	126.52	19.31 ± 0.13	r	p48
55792.413	36.83	17.88 ± 0.09	r	p48	55889.111	128.31	19.48 ± 0.15	r	p48
55793.382	37.75	17.91 ± 0.07	r	p48	55889.112	128.31	19.42 ± 0.14	r	p48
55793.457	37.82	17.88 ± 0.07	r	p48	55891.146	130.23	19.16 ± 0.13	r	p48
55794.410	38.72	17.85 ± 0.07	r	p48	55892.138	131.17	18.95 ± 0.21	r	p48
55811.354	54.75	17.95 ± 0.08	r	p48	55893.094	132.08	19.19 ± 0.15	r	p48
55811.398	54.79	17.95 ± 0.07	r	p48	55893.130	132.11	19.58 ± 0.18	r	p48
55812.421	55.76	18.00 ± 0.09	r	p48	55894.113	133.04	18.94 ± 0.34	r	p48
55813.326	56.62	17.99 ± 0.09	r	p48	55894.165	133.09	19.10 ± 0.22	r	p48
55817.388	60.46	18.33 ± 0.19	r	p48	55895.095	133.97	19.19 ± 0.13	r	p48
55818.297	61.32	18.09 ± 0.16	r	p48	55895.139	134.01	18.85 ± 0.25	r	p48
55818.343	61.36	18.15 ± 0.16	r	p48	55896.103	134.92	19.43 ± 0.24	r	p48
55819.386	62.35	17.95 ± 0.14	r	p48	55899.097	137.75	18.93 ± 0.26	r	p48

Table D36. Continuation of Table D35.

MJD	Phase	<i>m</i>	Filter	Telescope
55901.130	139.68	18.96 ± 0.28	r	p48
55902.093	140.59	18.94 ± 0.24	r	p48
55902.138	140.63	19.21 ± 0.22	r	p48
55903.088	141.53	19.64 ± 0.25	r	p48
55903.114	141.55	19.21 ± 0.18	r	p48
55904.100	142.49	19.47 ± 0.27	r	p48
55904.146	142.53	19.30 ± 0.27	r	p48
55906.147	144.42	19.62 ± 0.17	r	p48
55916.115	153.85	19.46 ± 0.15	r	p48
55916.167	153.90	19.33 ± 0.20	r	p48

Table D37. PTF 11hrq rest-frame g photometry data.

MJD	Phase	m_g	M_g	Tel	Ref	MJD	Phase	m_g	M_g	Tel	Ref
55753.477	0.00	17.17 ± 0.07	-19.87	p48		55820.294	63.21	18.22 ± 0.10	-18.82	p48	
55754.486	0.95	17.19 ± 0.07	-19.84	p48		55820.338	63.25	18.40 ± 0.09	-18.63	p48	
55755.474	1.89	17.21 ± 0.07	-19.82	p48		55821.324	64.18	18.31 ± 0.09	-18.73	p48	
55757.473	3.78	17.35 ± 0.09	-19.69	p48		55822.289	65.10	18.43 ± 0.09	-18.61	p48	
55761.458	7.55	17.42 ± 0.08	-19.62	p48		55822.332	65.14	18.37 ± 0.09	-18.66	p48	
55762.492	8.53	17.46 ± 0.07	-19.57	p48		55823.301	66.05	18.46 ± 0.08	-18.57	p48	
55763.451	9.44	17.49 ± 0.07	-19.54	p48		55823.345	66.09	18.41 ± 0.07	-18.62	p48	
55764.454	10.38	17.48 ± 0.07	-19.55	p48		55824.379	67.07	18.46 ± 0.08	-18.58	p48	
55765.468	11.34	17.44 ± 0.07	-19.59	p48		55842.266	83.99	18.78 ± 0.15	-18.25	p48	
55766.439	12.26	17.53 ± 0.07	-19.50	p48		55842.309	84.03	18.92 ± 0.16	-18.12	p48	
55768.454	14.17	17.54 ± 0.07	-19.50	p48		55843.265	84.94	18.85 ± 0.19	-18.19	p48	
55769.453	15.11	17.59 ± 0.07	-19.45	p48		55843.308	84.98	18.79 ± 0.15	-18.24	p48	
55769.496	15.15	17.59 ± 0.07	-19.44	p48		55844.227	85.85	18.93 ± 0.19	-18.11	p48	
55770.445	16.05	17.58 ± 0.07	-19.46	p48		55849.258	90.61	18.79 ± 0.09	-18.25	p48	
55770.489	16.09	17.60 ± 0.07	-19.44	p48		55850.215	91.51	18.81 ± 0.11	-18.22	p48	
55771.441	16.99	17.64 ± 0.06	-19.39	p48		55850.272	91.57	18.84 ± 0.11	-18.20	p48	
55771.487	17.04	17.62 ± 0.06	-19.42	p48		55851.209	92.45	18.87 ± 0.12	-18.17	p48	
55774.445	19.84	17.64 ± 0.07	-19.39	p48		55851.254	92.50	18.84 ± 0.10	-18.20	p48	
55779.425	24.55	17.71 ± 0.07	-19.32	p48		55852.206	93.40	18.86 ± 0.08	-18.17	p48	
55779.489	24.61	17.74 ± 0.06	-19.30	p48		55853.203	94.34	18.82 ± 0.10	-18.21	p48	
55780.407	25.48	17.77 ± 0.07	-19.27	p48		55853.247	94.38	18.84 ± 0.09	-18.19	p48	
55780.465	25.53	17.74 ± 0.06	-19.30	p48		55854.206	95.29	18.81 ± 0.08	-18.22	p48	
55782.395	27.36	17.79 ± 0.06	-19.25	p48		55854.252	95.33	18.83 ± 0.08	-18.20	p48	
55783.398	28.31	17.83 ± 0.09	-19.20	p48		55866.166	106.60	19.21 ± 0.12	-17.82	p48	
55783.441	28.35	17.79 ± 0.07	-19.24	p48		55866.210	106.64	19.34 ± 0.13	-17.69	p48	
55784.424	29.28	17.81 ± 0.09	-19.23	p48		55867.163	107.55	19.71 ± 0.28	-17.33	p48	
55784.468	29.32	17.80 ± 0.07	-19.23	p48		55867.207	107.59	19.32 ± 0.17	-17.71	p48	
55789.376	33.96	17.86 ± 0.11	-19.17	p48		55868.160	108.49	19.44 ± 0.19	-17.59	p48	
55789.435	34.02	17.94 ± 0.10	-19.09	p48		55868.204	108.53	19.46 ± 0.13	-17.58	p48	
55790.416	34.94	17.90 ± 0.07	-19.13	p48		55874.190	114.19	19.15 ± 0.25	-17.89	p48	
55790.459	34.98	17.91 ± 0.07	-19.12	p48		55884.116	123.58	19.48 ± 0.16	-17.56	p48	
55791.383	35.86	17.93 ± 0.10	-19.11	p48		55884.160	123.62	19.41 ± 0.19	-17.62	p48	
55791.431	35.90	17.97 ± 0.08	-19.06	p48		55887.163	126.47	19.59 ± 0.14	-17.45	p48	
55792.369	36.79	17.88 ± 0.08	-19.15	p48		55887.218	126.52	19.53 ± 0.13	-17.50	p48	
55792.413	36.83	17.96 ± 0.09	-19.07	p48		55889.111	128.31	19.69 ± 0.15	-17.34	p48	
55793.382	37.75	18.00 ± 0.07	-19.03	p48		55889.112	128.31	19.64 ± 0.14	-17.39	p48	
55793.457	37.82	17.97 ± 0.07	-19.06	p48		55891.146	130.23	19.38 ± 0.13	-17.65	p48	
55794.410	38.72	17.95 ± 0.07	-19.09	p48		55892.138	131.17	19.17 ± 0.21	-17.86	p48	
55811.354	54.75	18.08 ± 0.08	-18.95	p48		55893.094	132.08	19.41 ± 0.15	-17.62	p48	
55811.398	54.79	18.09 ± 0.07	-18.95	p48		55893.130	132.11	19.80 ± 0.18	-17.23	p48	
55812.421	55.76	18.13 ± 0.09	-18.90	p48		55894.113	133.04	19.16 ± 0.34	-17.87	p48	
55813.326	56.62	18.12 ± 0.09	-18.91	p48		55894.165	133.09	19.32 ± 0.22	-17.72	p48	
55817.388	60.46	18.47 ± 0.19	-18.56	p48		55895.095	133.97	19.41 ± 0.13	-17.62	p48	
55818.297	61.32	18.24 ± 0.16	-18.79	p48		55895.139	134.01	19.07 ± 0.25	-17.97	p48	
55818.343	61.36	18.29 ± 0.16	-18.74	p48		55896.103	134.92	19.65 ± 0.24	-17.39	p48	
55819.386	62.35	18.10 ± 0.14	-18.93	p48		55899.097	137.75	19.15 ± 0.26	-17.88	p48	

Table D38. Continuation of Table D37.

MJD	Phase	m_g	M_g	Telescope	Reference
55901.130	139.68	19.18 ± 0.28	-17.86	p48	
55902.093	140.59	19.16 ± 0.24	-17.87	p48	
55902.138	140.63	19.43 ± 0.22	-17.60	p48	
55903.088	141.53	19.86 ± 0.25	-17.17	p48	
55903.114	141.55	19.43 ± 0.18	-17.61	p48	
55904.100	142.49	19.70 ± 0.27	-17.34	p48	
55904.146	142.53	19.52 ± 0.27	-17.52	p48	
55906.147	144.42	19.84 ± 0.17	-17.19	p48	
55916.115	153.85	19.68 ± 0.15	-17.35	p48	
55916.167	153.90	19.55 ± 0.20	-17.48	p48	

Table D39. PTF 11rks photometry data.

MJD	Phase	m	Filter	Tel	MJD	Phase	m	Filter	Tel
55906.082	-24.37	20.18 ± 0.23	r	p48	55946.092	9.19	18.65 ± 0.31	r	p48
55906.140	-24.32	20.57 ± 0.20	r	p48	55946.127	9.22	19.33 ± 0.20	i	p60
55916.092	-15.97	19.43 ± 0.16	r	p48	55946.129	9.22	19.45 ± 0.17	r	p60
55916.136	-15.93	19.63 ± 0.11	r	p48	55946.130	9.22	19.69 ± 0.16	B	p60
55922.137	-10.90	19.16 ± 0.10	r	p48	55946.134	9.22	18.91 ± 0.14	i	p60
55923.094	-10.10	19.23 ± 0.11	r	p48	55946.135	9.22	18.86 ± 0.15	r	p48
55923.138	-10.06	19.16 ± 0.09	r	p48	55946.136	9.22	19.28 ± 0.13	r	p60
55923.318	-9.91	18.93 ± 0.13	r	p60	55946.137	9.23	19.68 ± 0.15	B	p60
55924.105	-9.25	19.07 ± 0.08	r	p48	55947.136	10.06	19.05 ± 0.11	r	p48
55924.149	-9.21	19.22 ± 0.09	r	p48	55949.148	11.75	19.04 ± 0.09	r	p48
55925.090	-8.43	19.13 ± 0.09	i	p60	55949.195	11.79	19.09 ± 0.12	r	p48
55925.092	-8.42	19.16 ± 0.08	B	p60	55952.106	14.23	19.15 ± 0.10	r	p48
55925.093	-8.42	19.06 ± 0.07	g	p60	55952.117	14.24	18.86 ± 0.08	i	p60
55925.095	-8.42	19.05 ± 0.10	i	p60	55952.118	14.24	19.22 ± 0.08	r	p60
55925.096	-8.42	19.09 ± 0.08	r	p48	55952.120	14.24	20.17 ± 0.13	B	p60
55925.096	-8.42	19.19 ± 0.09	B	p60	55952.122	14.24	19.85 ± 0.09	g	p60
55925.098	-8.42	19.23 ± 0.06	g	p60	55952.151	14.27	19.07 ± 0.09	r	p48
55925.178	-8.35	19.07 ± 0.09	r	p48	55953.097	15.06	19.02 ± 0.10	r	p48
55926.096	-7.58	18.98 ± 0.08	r	p48	55953.141	15.10	19.17 ± 0.09	r	p48
55926.140	-7.55	19.03 ± 0.08	r	p48	55954.097	15.90	19.15 ± 0.14	r	p48
55926.275	-7.43	19.00 ± 0.14	r	p60	55954.141	15.94	19.21 ± 0.12	r	p48
55932.136	-2.52	18.98 ± 0.10	r	p48	55959.111	20.11	19.03 ± 0.18	r	p48
55936.107	0.81	18.82 ± 0.09	r	p48	55959.132	20.12	19.15 ± 0.15	i	p60
55936.150	0.85	18.91 ± 0.10	r	p48	55959.133	20.12	19.20 ± 0.18	r	p60
55937.087	1.64	18.83 ± 0.09	r	p48	55959.155	20.14	19.18 ± 0.15	r	p48
55937.131	1.67	18.92 ± 0.13	r	p48	55960.102	20.94	19.29 ± 0.16	r	p48
55939.149	3.36	18.83 ± 0.09	r	p48	55960.127	20.96	19.20 ± 0.16	i	p60
55939.186	3.40	18.91 ± 0.10	r	p48	55960.129	20.96	19.44 ± 0.15	r	p60
55940.090	4.15	18.92 ± 0.12	r	p48	55960.133	20.96	20.65 ± 0.30	g	p60
55940.142	4.20	18.88 ± 0.11	r	p48	55960.145	20.97	19.11 ± 0.16	r	p48
55940.145	4.20	18.71 ± 0.10	i	p60	55961.125	21.79	19.70 ± 0.27	i	p60
55940.146	4.20	18.83 ± 0.09	r	p60	55961.129	21.80	20.35 ± 0.31	g	p60
55940.148	4.20	19.53 ± 0.12	B	p60	55961.220	21.87	19.37 ± 0.20	r	p48
55940.150	4.20	19.05 ± 0.09	g	p60	55962.122	22.63	19.56 ± 0.13	r	p48
55941.089	4.99	18.97 ± 0.10	r	p48	55962.131	22.64	19.15 ± 0.10	i	p60
55943.197	6.76	18.81 ± 0.09	r	p48	55962.132	22.64	20.72 ± 0.21	B	p60
55943.243	6.80	18.93 ± 0.09	r	p48	55962.135	22.64	20.28 ± 0.09	g	p60
55943.262	6.81	18.85 ± 0.08	i	p60	55962.194	22.69	19.42 ± 0.16	r	p48
55943.263	6.82	19.00 ± 0.09	r	p60	55963.106	23.46	19.49 ± 0.24	r	p48
55943.265	6.82	19.51 ± 0.11	B	p60	55966.126	25.99	19.58 ± 0.17	i	p60
55943.267	6.82	19.24 ± 0.08	g	p60	55966.128	25.99	19.84 ± 0.18	r	p60
55943.269	6.82	18.73 ± 0.09	i	p60	55967.134	26.83	19.52 ± 0.08	i	p60
55943.271	6.82	19.04 ± 0.08	r	p60	55967.136	26.84	21.37 ± 0.23	B	p60
55943.272	6.82	19.53 ± 0.11	B	p60	55967.138	26.84	20.70 ± 0.10	g	p60
55943.275	6.83	19.23 ± 0.08	g	p60	55968.203	27.73	19.39 ± 0.29	r	p48
55944.142	7.55	18.93 ± 0.09	r	p48	55974.141	32.71	20.41 ± 0.28	r	p60

Table D40. Continuation of Table D39.

MJD	Phase	<i>m</i>	Filter	Telescope
55975.134	33.54	19.99 ± 0.09	i	p60
55975.135	33.54	20.33 ± 0.09	r	p60
55975.137	33.55	21.68 ± 0.28	B	p60
55975.140	33.55	21.60 ± 0.16	g	p60
55979.121	36.89	22.06 ± 0.21	g	p60
55990.150	46.14	20.94 ± 0.34	i	p60
55990.153	46.14	21.05 ± 0.35	r	p60
56079.481	121.05	21.58 ± 0.22	r	p60
56082.478	123.57	21.09 ± 0.22	g	p60
56086.460	126.91	22.19 ± 0.29	r	p60
56089.452	129.42	22.04 ± 0.26	r	p60
56098.432	136.95	21.42 ± 0.32	i	p60
56099.447	137.80	22.22 ± 0.32	i	p60
56105.407	142.80	21.54 ± 0.29	i	p60
56138.399	170.46	22.19 ± 0.30	r	p60
56151.333	181.31	22.33 ± 0.35	i	p60

Table D41. PTF 11rks rest-frame g photometry data.

MJD	Phase	m_g	M_g	Tel	Ref	MJD	Phase	m_g	M_g	Tel	Ref
55906.082	-24.37	20.28 ± 0.23	-19.58	p48		55949.148	11.75	19.26 ± 0.09	-20.60	p48	
55906.140	-24.32	20.67 ± 0.20	-19.20	p48		55949.195	11.79	19.31 ± 0.12	-20.55	p48	
55916.092	-15.97	19.56 ± 0.16	-20.30	p48		55951.730	13.92	19.33 ± 0.03	-20.53	FTN	III
55916.136	-15.93	19.76 ± 0.11	-20.10	p48		55952.106	14.23	19.38 ± 0.10	-20.48	p48	
55922.137	-10.90	19.31 ± 0.10	-20.56	p48		55952.118	14.24	19.45 ± 0.08	-20.42	p60	
55923.094	-10.10	19.39 ± 0.11	-20.48	p48		55952.151	14.27	19.29 ± 0.09	-20.57	p48	
55923.138	-10.06	19.31 ± 0.09	-20.55	p48		55953.097	15.06	19.25 ± 0.10	-20.61	p48	
55923.318	-9.91	19.09 ± 0.13	-20.78	p60		55953.141	15.10	19.40 ± 0.09	-20.47	p48	
55924.105	-9.25	19.22 ± 0.08	-20.64	p48		55954.097	15.90	19.38 ± 0.14	-20.48	p48	
55924.149	-9.21	19.38 ± 0.09	-20.49	p48		55954.141	15.94	19.45 ± 0.12	-20.42	p48	
55925.096	-8.42	19.25 ± 0.08	-20.61	p48		55954.440	16.19	19.46 ± 0.06	-20.40	LT	III
55925.178	-8.35	19.23 ± 0.09	-20.63	p48		55956.840	18.20	19.52 ± 0.21	-20.34	FTN	III
55926.096	-7.58	19.15 ± 0.08	-20.72	p48		55959.111	20.11	19.28 ± 0.18	-20.59	p48	
55926.140	-7.55	19.20 ± 0.08	-20.67	p48		55959.133	20.12	19.44 ± 0.18	-20.42	p60	
55926.275	-7.43	19.16 ± 0.14	-20.70	p60		55959.155	20.14	19.42 ± 0.15	-20.44	p48	
55929.420	-4.79	19.02 ± 0.20	-20.84	LT	III	55960.102	20.94	19.53 ± 0.16	-20.33	p48	
55930.420	-3.96	18.93 ± 0.04	-20.93	LT	III	55960.129	20.96	19.69 ± 0.15	-20.17	p60	
55931.340	-3.18	18.88 ± 0.03	-20.98	LT	III	55960.145	20.97	19.36 ± 0.16	-20.50	p48	
55932.136	-2.52	19.16 ± 0.10	-20.71	p48		55961.220	21.87	19.62 ± 0.20	-20.24	p48	
55932.720	-2.03	18.87 ± 0.05	-20.99	FTN	III	55962.122	22.63	19.81 ± 0.13	-20.05	p48	
55935.730	0.50	18.97 ± 0.02	-20.89	FTN	III	55962.194	22.69	19.67 ± 0.16	-20.19	p48	
55936.107	0.81	19.01 ± 0.09	-20.85	p48		55962.750	23.16	19.69 ± 0.04	-20.17	FTN	III
55936.150	0.85	19.10 ± 0.10	-20.76	p48		55963.106	23.46	19.74 ± 0.24	-20.12	p48	
55936.400	1.06	18.98 ± 0.03	-20.88	LT	III	55966.128	25.99	20.09 ± 0.18	-19.77	p60	
55937.087	1.64	19.03 ± 0.09	-20.84	p48		55966.740	26.50	20.12 ± 0.08	-19.74	FTN	III
55937.131	1.67	19.12 ± 0.13	-20.74	p48		55968.203	27.73	19.65 ± 0.29	-20.21	p48	
55939.149	3.36	19.03 ± 0.09	-20.83	p48		55974.141	32.71	20.69 ± 0.28	-19.18	p60	
55939.186	3.40	19.11 ± 0.10	-20.76	p48		55975.135	33.54	20.60 ± 0.09	-19.26	p60	
55939.320	3.51	19.05 ± 0.06	-20.81	LT	III	55990.153	46.14	21.34 ± 0.35	-18.52	p60	
55940.090	4.15	19.12 ± 0.12	-20.74	p48		55990.340	46.30	20.93 ± 0.15	-18.93	LT	III
55940.142	4.20	19.08 ± 0.11	-20.78	p48		56079.481	121.05	21.92 ± 0.22	-17.95	p60	
55940.146	4.20	19.03 ± 0.09	-20.83	p60		56086.460	126.91	22.52 ± 0.29	-17.34	p60	
55941.089	4.99	19.17 ± 0.10	-20.69	p48		56089.452	129.42	22.38 ± 0.26	-17.48	p60	
55941.320	5.19	19.06 ± 0.03	-20.80	LT	III	56138.399	170.46	22.51 ± 0.30	-17.36	p60	
55942.350	6.05	19.07 ± 0.03	-20.80	LT	III						
55943.197	6.76	19.02 ± 0.09	-20.84	p48							
55943.243	6.80	19.14 ± 0.09	-20.72	p48							
55943.263	6.82	19.20 ± 0.09	-20.66	p60							
55943.271	6.82	19.25 ± 0.08	-20.61	p60							
55944.142	7.55	19.14 ± 0.09	-20.72	p48							
55946.092	9.19	18.87 ± 0.31	-21.00	p48							
55946.129	9.22	19.67 ± 0.17	-20.20	p60							
55946.135	9.22	19.07 ± 0.15	-20.79	p48							
55946.136	9.22	19.49 ± 0.13	-20.37	p60							
55947.136	10.06	19.27 ± 0.11	-20.59	p48							
55948.750	11.42	19.23 ± 0.02	-20.63	FTN	III						

Table D42. PTF 12dam photometry data.

MJD	Phase	m	Filter	Tel	MJD	Phase	m	Filter	Tel
56025.328	-60.50	20.03 ± 0.22	r	p48	56070.436	-19.77	17.20 ± 0.06	r	p48
56027.257	-58.75	19.93 ± 0.17	r	p48	56070.469	-19.74	17.21 ± 0.06	r	p48
56027.286	-58.73	20.02 ± 0.16	r	p48	56072.340	-18.05	17.78 ± 0.03	i	LCOGT
56027.315	-58.70	19.95 ± 0.15	r	p48	56072.342	-18.05	17.43 ± 0.03	g	LCOGT
56033.489	-53.13	19.80 ± 0.13	r	p48	56072.343	-18.05	17.42 ± 0.04	g	LCOGT
56034.162	-52.52	19.87 ± 0.13	r	p48	56075.234	-15.43	17.24 ± 0.06	i	p60
56034.194	-52.49	19.87 ± 0.13	r	p48	56075.235	-15.43	17.13 ± 0.06	r	p60
56034.256	-52.44	19.74 ± 0.12	r	p48	56075.236	-15.43	16.67 ± 0.06	B	p60
56036.166	-50.71	19.69 ± 0.13	r	p48	56075.237	-15.43	17.05 ± 0.06	g	p60
56036.208	-50.67	19.59 ± 0.12	r	p48	56075.383	-15.30	17.38 ± 0.03	g	LCOGT
56036.371	-50.53	19.62 ± 0.12	r	p48	56075.385	-15.30	17.39 ± 0.05	g	LCOGT
56038.345	-48.74	19.29 ± 0.09	r	p48	56076.373	-14.41	17.04 ± 0.06	r	p48
56038.375	-48.72	19.31 ± 0.09	r	p48	56076.404	-14.38	17.07 ± 0.06	r	p48
56040.427	-46.86	19.20 ± 0.09	r	p48	56079.341	-11.73	17.20 ± 0.03	g	LCOGT
56040.458	-46.84	19.14 ± 0.09	r	p48	56079.342	-11.73	16.98 ± 0.05	g	LCOGT
56046.398	-41.47	18.47 ± 0.08	r	p48	56080.203	-10.95	17.12 ± 0.06	i	p60
56046.428	-41.44	18.49 ± 0.08	r	p48	56080.204	-10.95	16.94 ± 0.06	r	p60
56048.432	-39.64	18.26 ± 0.08	r	p48	56080.204	-10.95	16.74 ± 0.06	B	p60
56048.466	-39.60	18.35 ± 0.07	r	p48	56080.205	-10.95	16.69 ± 0.06	g	p60
56048.497	-39.58	18.27 ± 0.08	r	p48	56080.206	-10.95	17.12 ± 0.06	i	p60
56058.475	-30.57	17.67 ± 0.07	r	p48	56080.207	-10.94	16.96 ± 0.06	r	p60
56059.275	-29.84	17.61 ± 0.06	r	p48	56080.208	-10.94	16.77 ± 0.06	B	p60
56061.329	-27.99	17.55 ± 0.06	r	p48	56080.212	-10.94	16.64 ± 0.06	g	p60
56063.291	-26.22	17.45 ± 0.06	r	p48	56083.356	-8.10	16.96 ± 0.03	g	LCOGT
56063.322	-26.19	17.43 ± 0.06	r	p48	56083.357	-8.10	16.92 ± 0.05	g	LCOGT
56063.352	-26.16	17.49 ± 0.06	r	p48	56083.360	-8.10	16.92 ± 0.02	r	LCOGT
56065.441	-24.28	17.38 ± 0.07	r	p48	56083.361	-8.10	17.28 ± 0.03	i	LCOGT
56066.380	-23.43	17.36 ± 0.06	r	p48	56083.363	-8.09	17.33 ± 0.02	i	LCOGT
56066.414	-23.40	17.38 ± 0.06	r	p48	56085.210	-6.43	17.04 ± 0.06	i	p60
56066.448	-23.37	17.36 ± 0.06	r	p48	56085.211	-6.43	16.89 ± 0.06	r	p60
56068.219	-21.77	17.45 ± 0.06	i	p60	56085.212	-6.43	16.70 ± 0.06	B	p60
56068.221	-21.77	17.33 ± 0.06	r	p60	56085.213	-6.42	17.15 ± 0.06	i	p60
56068.222	-21.77	17.01 ± 0.06	B	p60	56085.214	-6.42	16.96 ± 0.06	r	p60
56068.224	-21.76	17.01 ± 0.06	g	p60	56085.215	-6.42	16.70 ± 0.06	B	p60
56068.226	-21.76	17.47 ± 0.06	i	p60	56085.216	-6.42	16.66 ± 0.06	g	p60
56068.227	-21.76	17.26 ± 0.06	r	p60	56086.442	-5.31	16.89 ± 0.05	g	LCOGT
56068.229	-21.76	17.08 ± 0.06	B	p60	56086.443	-5.31	16.91 ± 0.03	g	LCOGT
56068.230	-21.76	17.01 ± 0.06	g	p60	56086.444	-5.31	16.83 ± 0.02	r	LCOGT
56068.477	-21.54	17.29 ± 0.06	r	p48	56086.446	-5.31	16.86 ± 0.02	r	LCOGT
56070.264	-19.92	17.15 ± 0.02	r	LCOGT	56086.447	-5.31	17.28 ± 0.03	i	LCOGT
56070.265	-19.92	17.13 ± 0.02	r	LCOGT	56086.448	-5.31	17.28 ± 0.02	i	LCOGT
56070.267	-19.92	17.69 ± 0.02	i	LCOGT	56089.332	-2.71	16.94 ± 0.05	g	LCOGT
56070.268	-19.92	17.57 ± 0.03	i	LCOGT	56089.333	-2.70	16.93 ± 0.05	g	LCOGT
56070.269	-19.92	17.48 ± 0.04	g	LCOGT	56089.334	-2.70	16.80 ± 0.02	r	LCOGT
56070.271	-19.92	17.47 ± 0.04	g	LCOGT	56089.336	-2.70	16.81 ± 0.02	r	LCOGT
56070.401	-19.80	17.19 ± 0.06	r	p48	56089.337	-2.70	17.22 ± 0.01	i	LCOGT

Table D43. Continuation of Table D42.

MJD	Phase	m	Filter	Tel	MJD	Phase	m	Filter	Tel
56089.338	-2.70	17.23 ± 0.03	i	LCOGT	56118.257	23.41	17.00 ± 0.06	r	p60
56090.200	-1.92	16.99 ± 0.06	i	p60	56118.258	23.41	17.02 ± 0.06	B	p60
56090.201	-1.92	16.84 ± 0.06	r	p60	56118.259	23.41	16.86 ± 0.06	g	p60
56090.202	-1.92	16.40 ± 0.06	B	p60	56127.277	31.56	17.35 ± 0.07	g	p60
56090.203	-1.92	16.61 ± 0.06	g	p60	56128.378	32.55	17.33 ± 0.04	g	LCOGT
56090.204	-1.92	17.12 ± 0.06	i	p60	56128.379	32.55	17.35 ± 0.04	g	LCOGT
56090.205	-1.92	16.83 ± 0.06	r	p60	56128.380	32.55	17.12 ± 0.02	r	LCOGT
56090.206	-1.92	16.76 ± 0.06	B	p60	56128.381	32.55	17.14 ± 0.03	r	LCOGT
56090.221	-1.90	16.66 ± 0.06	g	p60	56128.383	32.56	17.46 ± 0.02	i	LCOGT
56093.433	1.00	16.94 ± 0.03	g	LCOGT	56128.384	32.56	17.43 ± 0.02	i	LCOGT
56093.434	1.00	16.94 ± 0.04	g	LCOGT	56129.199	33.29	17.31 ± 0.06	i	p60
56098.293	5.39	17.04 ± 0.06	i	p60	56129.200	33.29	17.15 ± 0.06	r	p60
56098.294	5.39	16.90 ± 0.06	r	p60	56129.201	33.29	17.28 ± 0.06	B	p60
56098.295	5.39	16.77 ± 0.06	B	p60	56129.202	33.29	17.10 ± 0.06	g	p60
56098.296	5.39	17.05 ± 0.06	i	p60	56131.266	35.16	17.42 ± 0.04	g	LCOGT
56098.297	5.39	16.87 ± 0.06	r	p60	56131.267	35.16	17.41 ± 0.04	g	LCOGT
56098.298	5.39	16.76 ± 0.06	B	p60	56149.243	51.39	17.75 ± 0.05	g	LCOGT
56098.299	5.39	16.66 ± 0.06	g	p60	56149.244	51.39	17.32 ± 0.02	r	LCOGT
56103.211	9.83	17.01 ± 0.06	i	p60	56149.244	51.39	17.85 ± 0.07	g	LCOGT
56103.212	9.83	16.88 ± 0.06	r	p60	56149.245	51.39	17.33 ± 0.01	r	LCOGT
56103.224	9.84	16.85 ± 0.06	g	p60	56149.246	51.39	17.59 ± 0.03	i	LCOGT
56103.225	9.84	17.07 ± 0.06	i	p60	56149.247	51.39	17.59 ± 0.02	i	LCOGT
56103.226	9.84	17.03 ± 0.06	r	p60	56152.241	54.10	17.85 ± 0.09	g	LCOGT
56103.227	9.84	16.73 ± 0.06	B	p60	56152.242	54.10	17.73 ± 0.05	g	LCOGT
56103.228	9.84	16.72 ± 0.06	g	p60	56152.243	54.10	17.38 ± 0.03	r	LCOGT
56108.209	14.34	17.04 ± 0.06	i	p60	56152.243	54.10	17.40 ± 0.02	r	LCOGT
56108.209	14.34	16.94 ± 0.06	r	p60	56152.244	54.10	17.58 ± 0.02	i	LCOGT
56108.210	14.34	16.87 ± 0.06	B	p60	56152.245	54.10	17.63 ± 0.02	i	LCOGT
56108.211	14.34	16.68 ± 0.06	g	p60	56156.239	57.71	17.89 ± 0.08	g	LCOGT
56108.212	14.34	17.05 ± 0.06	i	p60	56156.240	57.71	17.82 ± 0.05	g	LCOGT
56108.213	14.34	16.94 ± 0.06	r	p60	56156.240	57.71	17.46 ± 0.01	r	LCOGT
56108.214	14.34	16.85 ± 0.06	B	p60	56156.241	57.71	17.53 ± 0.02	r	LCOGT
56108.215	14.34	16.75 ± 0.06	g	p60	56156.242	57.71	17.69 ± 0.02	i	LCOGT
56113.202	18.85	17.06 ± 0.06	i	p60	56156.243	57.71	17.69 ± 0.03	i	LCOGT
56113.203	18.85	17.00 ± 0.06	r	p60	56159.199	60.38	17.55 ± 0.07	i	p60
56113.204	18.85	16.95 ± 0.07	B	p60	56161.176	62.17	17.48 ± 0.06	r	p60
56113.205	18.85	16.74 ± 0.06	g	p60	56161.177	62.17	17.98 ± 0.07	B	p60
56113.206	18.85	17.09 ± 0.06	i	p60	56161.178	62.17	17.75 ± 0.06	g	p60
56113.207	18.85	16.94 ± 0.06	r	p60	56161.236	62.22	17.93 ± 0.05	g	LCOGT
56113.208	18.85	16.97 ± 0.07	B	p60	56161.237	62.22	17.98 ± 0.06	g	LCOGT
56113.209	18.85	16.77 ± 0.06	g	p60	56161.239	62.22	17.80 ± 0.04	i	LCOGT
56118.253	23.41	17.11 ± 0.06	i	p60	56161.240	62.22	17.74 ± 0.03	i	LCOGT
56118.254	23.41	17.02 ± 0.06	r	p60	56165.167	65.77	17.47 ± 0.07	i	p60
56118.255	23.41	16.87 ± 0.06	g	p60	56177.147	76.59	17.61 ± 0.07	i	p60
56118.255	23.41	17.05 ± 0.06	B	p60	56177.148	76.59	17.70 ± 0.06	r	p60
56118.256	23.41	17.14 ± 0.06	i	p60	56177.149	76.59	18.33 ± 0.08	B	p60

Table D44. Continuation of Table D42.

MJD	Phase	m	Filter	Tel	MJD	Phase	m	Filter	Tel
56177.150	76.59	17.86 ± 0.06	g	p60	56266.472	157.24	19.08 ± 0.09	r	p60
56181.231	80.27	18.18 ± 0.07	g	LCOGT	56266.473	157.24	19.50 ± 0.12	g	p60
56181.233	80.28	17.79 ± 0.04	r	LCOGT	56268.466	159.04	19.98 ± 0.15	B	p60
56181.234	80.28	17.82 ± 0.03	r	LCOGT	56273.452	163.54	19.44 ± 0.10	r	p60
56181.235	80.28	18.05 ± 0.04	i	LCOGT	56273.454	163.54	19.74 ± 0.11	g	p60
56185.159	83.82	17.84 ± 0.07	i	p60	56281.429	170.75	19.57 ± 0.20	i	p60
56185.160	83.82	17.84 ± 0.07	r	p60	56281.431	170.75	19.42 ± 0.14	r	p60
56185.162	83.82	18.41 ± 0.08	B	p60	56283.425	172.55	19.46 ± 0.08	r	p60
56185.163	83.82	18.06 ± 0.07	g	p60	56283.428	172.55	20.07 ± 0.14	B	p60
56185.165	83.83	17.73 ± 0.07	i	p60	56283.429	172.55	19.72 ± 0.10	g	p60
56185.166	83.83	17.84 ± 0.07	r	p60	56289.531	178.06	19.02 ± 0.09	i	p60
56185.167	83.83	18.46 ± 0.09	B	p60	56297.386	185.15	19.60 ± 0.12	i	p60
56185.169	83.83	18.03 ± 0.07	g	p60	56297.388	185.16	19.59 ± 0.09	r	p60
56187.239	85.70	18.37 ± 0.07	g	LCOGT	56297.390	185.16	20.00 ± 0.15	B	p60
56187.240	85.70	18.47 ± 0.06	g	LCOGT	56297.392	185.16	19.88 ± 0.11	g	p60
56187.241	85.70	17.89 ± 0.02	r	LCOGT	56323.314	208.57	19.96 ± 0.18	i	p60
56196.215	93.80	18.10 ± 0.02	r	LCOGT	56323.315	208.57	20.36 ± 0.20	r	p60
56196.216	93.80	17.94 ± 0.03	r	LCOGT	56323.319	208.57	20.27 ± 0.21	g	p60
56196.217	93.80	18.42 ± 0.04	i	LCOGT	56324.311	209.47	20.21 ± 0.12	r	p60
56197.224	94.71	18.03 ± 0.02	r	LCOGT	56345.334	228.45	20.11 ± 0.18	i	p60
56197.225	94.72	18.14 ± 0.02	r	LCOGT	56345.336	228.45	20.32 ± 0.16	r	p60
56197.226	94.72	18.43 ± 0.04	i	LCOGT	56345.338	228.45	20.62 ± 0.32	B	p60
56197.226	94.72	18.43 ± 0.03	i	LCOGT	56345.340	228.45	20.71 ± 0.21	g	p60
56200.213	97.41	18.11 ± 0.02	r	LCOGT	56345.342	228.45	20.15 ± 0.17	i	p60
56200.214	97.41	18.14 ± 0.02	r	LCOGT	56345.344	228.46	20.27 ± 0.15	r	p60
56200.215	97.41	18.56 ± 0.11	i	LCOGT	56345.346	228.46	20.50 ± 0.29	B	p60
56201.113	98.23	18.69 ± 0.08	g	p60	56345.348	228.46	20.49 ± 0.18	g	p60
56201.115	98.23	18.08 ± 0.08	g	p60	56346.253	229.28	20.48 ± 0.25	i	p60
56202.112	99.13	17.86 ± 0.07	i	p60	56346.255	229.28	20.09 ± 0.17	r	p60
56202.113	99.13	18.06 ± 0.07	r	p60	56346.262	229.29	20.31 ± 0.22	g	p60
56214.101	109.95	18.23 ± 0.08	i	p60	56347.431	230.34	20.10 ± 0.26	i	p60
56214.103	109.95	18.22 ± 0.07	r	p60	56347.433	230.34	20.51 ± 0.27	r	p60
56214.104	109.96	18.96 ± 0.09	B	p60	56347.437	230.35	20.50 ± 0.31	g	p60
56214.106	109.96	18.45 ± 0.07	g	p60	56349.243	231.98	19.72 ± 0.26	i	p60
56237.549	131.12	18.67 ± 0.11	i	p60	56350.242	232.88	20.41 ± 0.30	r	p60
56245.535	138.34	18.66 ± 0.18	i	p60	56350.246	232.88	20.42 ± 0.36	g	p60
56245.538	138.34	19.70 ± 0.23	B	p60	56352.237	234.68	20.38 ± 0.21	r	p60
56245.539	138.34	19.17 ± 0.14	g	p60	56352.241	234.68	20.77 ± 0.33	g	p60
56250.514	142.83	19.12 ± 0.09	r	p60	56353.233	235.58	20.38 ± 0.14	r	p60
56251.511	143.73	19.09 ± 0.08	r	p60	56353.236	235.58	21.10 ± 0.31	B	p60
56252.509	144.63	19.04 ± 0.10	i	p60	56353.237	235.58	20.50 ± 0.15	g	p60
56252.510	144.63	19.84 ± 0.16	B	p60	56356.228	238.28	20.38 ± 0.17	i	p60
56252.512	144.64	19.47 ± 0.10	g	p60	56362.272	243.74	20.47 ± 0.14	r	p60
56262.535	153.69	19.33 ± 0.14	r	p60	56362.275	243.74	20.88 ± 0.26	B	p60
56262.537	153.69	20.06 ± 0.26	g	p60	56362.276	243.75	20.70 ± 0.15	g	p60
56265.478	156.34	19.44 ± 0.26	g	p60	56362.279	243.75	20.47 ± 0.14	r	p60

Table D45. Continuation of Table D42.

MJD	Phase	m	Filter	Tel	MJD	Phase	m	Filter	Tel
56362.281	243.75	20.84 ± 0.24	B	p60	56507.216	374.62	22.01 ± 0.28	r	p60
56362.283	243.75	20.70 ± 0.15	g	p60					
56362.479	243.93	20.62 ± 0.18	r	p48					
56362.509	243.96	20.34 ± 0.15	r	p48					
56362.539	243.98	20.50 ± 0.18	r	p48					
56364.203	245.49	20.18 ± 0.14	i	p60					
56366.489	247.55	20.32 ± 0.22	r	p48					
56366.500	247.56	20.48 ± 0.15	r	p48					
56366.511	247.57	20.70 ± 0.18	r	p48					
56366.522	247.58	20.52 ± 0.16	r	p48					
56369.539	250.30	20.43 ± 0.18	r	p48					
56370.309	251.00	20.61 ± 0.18	r	p60					
56370.310	251.00	20.71 ± 0.28	B	p60					
56371.249	251.85	21.16 ± 0.34	g	p60					
56372.197	252.70	20.36 ± 0.27	r	p60					
56373.179	253.59	20.65 ± 0.30	i	p60					
56373.181	253.59	20.43 ± 0.26	r	p60					
56374.178	254.49	20.11 ± 0.30	r	p60					
56374.513	254.79	20.39 ± 0.17	r	p48					
56375.291	255.50	20.58 ± 0.19	i	p60					
56375.293	255.50	21.24 ± 0.23	r	p60					
56375.295	255.50	20.89 ± 0.14	g	p60					
56376.170	256.29	20.80 ± 0.30	r	p60					
56376.506	256.59	20.93 ± 0.25	r	p48					
56382.171	261.71	20.91 ± 0.26	B	p60					
56385.515	264.73	20.39 ± 0.32	r	p48					
56386.171	265.32	21.13 ± 0.18	g	p60					
56388.496	267.42	21.10 ± 0.29	r	p60					
56388.497	267.42	21.25 ± 0.20	g	p60					
56390.279	269.03	20.63 ± 0.28	r	p60					
56392.268	270.83	21.12 ± 0.31	r	p60					
56409.274	286.18	20.72 ± 0.24	i	p60					
56412.465	289.06	21.43 ± 0.29	i	p60					
56413.448	289.95	21.50 ± 0.31	r	p60					
56416.395	292.61	21.82 ± 0.35	r	p60					
56416.396	292.61	21.80 ± 0.22	g	p60					
56422.435	298.06	21.29 ± 0.25	i	p60					
56422.440	298.07	22.23 ± 0.33	g	p60					
56425.342	300.69	21.85 ± 0.32	r	p60					
56431.387	306.15	21.33 ± 0.30	i	p60					
56432.325	306.99	21.51 ± 0.28	i	p60					
56452.323	325.05	21.89 ± 0.34	r	p60					
56459.237	331.29	21.31 ± 0.23	i	p60					
56460.294	332.25	21.38 ± 0.33	i	p60					
56470.268	341.25	21.76 ± 0.36	i	p60					
56471.211	342.11	22.11 ± 0.30	r	p60					

Table D46. PTF 12dam rest-frame g photometry data.

MJD	Phase	m_g	M_g	Tel	Ref	MJD	Phase	m_g	M_g	Tel	Ref
56025.328	-60.50	19.92 ± 0.22	-18.57	p48		56080.204	-10.95	16.91 ± 0.06	-21.57	p60	
56027.257	-58.75	19.82 ± 0.17	-18.66	p48		56080.207	-10.94	16.93 ± 0.06	-21.55	p60	
56027.286	-58.73	19.91 ± 0.16	-18.57	p48		56080.940	-10.28	16.93 ± 0.01	-21.55	LT+RATCam	IV
56027.315	-58.70	19.84 ± 0.15	-18.64	p48		56081.940	-9.38	16.91 ± 0.01	-21.57	LT+RATCam	IV
56030.480	-55.84	19.25 ± 0.17	-19.24	PS1	IV	56083.360	-8.10	16.89 ± 0.02	-21.59	LCOGT	
56033.489	-53.13	19.69 ± 0.13	-18.79	p48		56085.211	-6.43	16.89 ± 0.06	-21.59	p60	
56034.162	-52.52	19.76 ± 0.13	-18.72	p48		56085.214	-6.42	16.96 ± 0.06	-21.52	p60	
56034.194	-52.49	19.76 ± 0.13	-18.72	p48		56086.444	-5.31	16.82 ± 0.02	-21.66	LCOGT	
56034.256	-52.44	19.63 ± 0.12	-18.85	p48		56086.446	-5.31	16.85 ± 0.02	-21.63	LCOGT	
56036.166	-50.71	19.58 ± 0.13	-18.90	p48		56089.334	-2.70	16.81 ± 0.02	-21.68	LCOGT	
56036.208	-50.67	19.48 ± 0.12	-19.00	p48		56089.336	-2.70	16.81 ± 0.02	-21.67	LCOGT	
56036.371	-50.53	19.51 ± 0.12	-18.98	p48		56090.201	-1.92	16.85 ± 0.06	-21.63	p60	
56038.345	-48.74	19.18 ± 0.09	-19.30	p48		56090.205	-1.92	16.84 ± 0.06	-21.64	p60	
56038.375	-48.72	19.20 ± 0.09	-19.29	p48		56098.030	5.15	16.92 ± 0.01	-21.56	TNG+LRS	IV
56040.427	-46.86	19.09 ± 0.09	-19.40	p48		56098.294	5.39	16.94 ± 0.06	-21.54	p60	
56040.458	-46.84	19.03 ± 0.09	-19.46	p48		56098.297	5.39	16.91 ± 0.06	-21.57	p60	
56046.398	-41.47	18.36 ± 0.08	-20.13	p48		56103.212	9.83	16.94 ± 0.06	-21.54	p60	
56046.428	-41.44	18.37 ± 0.08	-20.11	p48		56103.226	9.84	17.10 ± 0.06	-21.39	p60	
56046.500	-41.38	18.10 ± 0.17	-20.39	PS1	IV	56104.020	10.56	17.03 ± 0.01	-21.46	WHT	IV
56048.432	-39.64	18.14 ± 0.08	-20.34	p48		56108.209	14.34	17.02 ± 0.06	-21.47	p60	
56048.466	-39.60	18.24 ± 0.07	-20.25	p48		56108.213	14.34	17.02 ± 0.06	-21.47	p60	
56048.497	-39.58	18.16 ± 0.08	-20.32	p48		56113.203	18.85	17.10 ± 0.06	-21.38	p60	
56058.475	-30.57	17.56 ± 0.07	-20.92	p48		56113.207	18.85	17.04 ± 0.06	-21.45	p60	
56059.275	-29.84	17.50 ± 0.06	-20.99	p48		56116.010	21.38	17.16 ± 0.01	-21.32	NOT	IV
56061.329	-27.99	17.44 ± 0.06	-21.04	p48		56118.254	23.41	17.14 ± 0.06	-21.34	p60	
56063.291	-26.22	17.34 ± 0.06	-21.14	p48		56118.257	23.41	17.11 ± 0.06	-21.37	p60	
56063.322	-26.19	17.32 ± 0.06	-21.17	p48		56128.030	32.24	17.30 ± 0.05	-21.18	GTC	IV
56063.352	-26.16	17.38 ± 0.06	-21.11	p48		56128.380	32.55	17.25 ± 0.02	-21.23	LCOGT	
56065.441	-24.28	17.28 ± 0.07	-21.20	p48		56128.381	32.55	17.28 ± 0.03	-21.21	LCOGT	
56066.380	-23.43	17.26 ± 0.06	-21.22	p48		56129.200	33.29	17.29 ± 0.06	-21.19	p60	
56066.414	-23.40	17.28 ± 0.06	-21.20	p48		56148.930	51.11	17.61 ± 0.01	-20.87	NOT	IV
56066.448	-23.37	17.26 ± 0.06	-21.22	p48		56149.244	51.39	17.51 ± 0.02	-20.98	LCOGT	
56068.221	-21.77	17.24 ± 0.06	-21.24	p60		56149.245	51.39	17.52 ± 0.01	-20.97	LCOGT	
56068.227	-21.76	17.17 ± 0.06	-21.31	p60		56152.243	54.10	17.57 ± 0.03	-20.91	LCOGT	
56068.477	-21.54	17.21 ± 0.06	-21.27	p48		56152.243	54.10	17.59 ± 0.02	-20.90	LCOGT	
56070.264	-19.92	17.06 ± 0.02	-21.42	LCOGT		56156.240	57.71	17.66 ± 0.01	-20.82	LCOGT	
56070.265	-19.92	17.05 ± 0.02	-21.43	LCOGT		56156.241	57.71	17.73 ± 0.02	-20.75	LCOGT	
56070.401	-19.80	17.11 ± 0.06	-21.37	p48		56160.920	61.93	17.79 ± 0.01	-20.69	WHT	IV
56070.436	-19.77	17.12 ± 0.06	-21.36	p48		56161.176	62.17	17.69 ± 0.06	-20.79	p60	
56070.469	-19.74	17.13 ± 0.06	-21.35	p48		56174.850	74.51	18.00 ± 0.01	-20.48	NOT	IV
56071.130	-19.14	17.16 ± 0.01	-21.33	GTC	IV	56177.148	76.59	17.93 ± 0.06	-20.55	p60	
56072.920	-17.52	17.11 ± 0.01	-21.38	WHT	IV	56181.233	80.28	18.02 ± 0.04	-20.46	LCOGT	
56075.235	-15.43	17.08 ± 0.06	-21.40	p60		56181.234	80.28	18.06 ± 0.03	-20.42	LCOGT	
56076.373	-14.41	16.99 ± 0.06	-21.49	p48		56185.160	83.82	18.08 ± 0.07	-20.40	p60	
56076.404	-14.38	17.03 ± 0.06	-21.46	p48		56185.166	83.83	18.08 ± 0.07	-20.40	p60	
56076.950	-13.89	16.97 ± 0.01	-21.51	LT+RATCam	IV	56187.241	85.70	18.13 ± 0.02	-20.35	LCOGT	

Table D47. Continuation of Table D46.

MJD	Phase	m_g	M_g	Tel	Ref	MJD	Phase	m_g	M_g	Tel	Ref
56191.860	89.87	18.37 ± 0.01	-20.11	WHT	IV	56374.513	254.79	20.62 ± 0.17	-17.87	p48	
56196.215	93.80	18.34 ± 0.02	-20.14	LCOGT		56375.293	255.50	21.47 ± 0.23	-17.02	p60	
56196.216	93.80	18.19 ± 0.03	-20.29	LCOGT		56376.170	256.29	21.02 ± 0.30	-17.46	p60	
56197.224	94.71	18.28 ± 0.02	-20.20	LCOGT		56376.506	256.59	21.15 ± 0.25	-17.34	p48	
56197.225	94.72	18.39 ± 0.02	-20.09	LCOGT		56385.515	264.73	20.61 ± 0.32	-17.87	p48	
56200.213	97.41	18.36 ± 0.02	-20.12	LCOGT		56388.496	267.42	21.32 ± 0.29	-17.16	p60	
56200.214	97.41	18.40 ± 0.02	-20.09	LCOGT		56390.279	269.03	20.85 ± 0.28	-17.63	p60	
56202.113	99.13	18.32 ± 0.07	-20.16	p60		56392.268	270.83	21.34 ± 0.31	-17.15	p60	
56214.103	109.95	18.49 ± 0.07	-19.99	p60		56413.448	289.95	21.72 ± 0.31	-16.76	p60	
56250.514	142.83	19.39 ± 0.09	-19.09	p60		56416.395	292.61	22.05 ± 0.35	-16.44	p60	
56251.511	143.73	19.36 ± 0.08	-19.12	p60		56425.342	300.69	22.08 ± 0.32	-16.40	p60	
56262.535	153.69	19.60 ± 0.14	-18.88	p60		56432.930	307.54	21.87 ± 0.09	-16.61	LT+RATCam	IV
56266.472	157.24	19.35 ± 0.09	-19.14	p60		56452.323	325.05	22.13 ± 0.34	-16.35	p60	
56273.452	163.54	19.71 ± 0.10	-18.77	p60		56452.960	325.63	22.47 ± 0.04	-16.01	WHT	IV
56281.431	170.75	19.68 ± 0.14	-18.80	p60		56471.211	342.11	22.35 ± 0.30	-16.13	p60	
56283.425	172.55	19.72 ± 0.08	-18.76	p60		56507.216	374.62	22.26 ± 0.28	-16.23	p60	
56285.210	174.16	19.44 ± 0.02	-19.04	LT+RATCam	IV						
56287.630	176.34	19.47 ± 0.09	-19.01	FTN	IV						
56297.388	185.16	19.85 ± 0.09	-18.64	p60							
56312.150	198.48	19.88 ± 0.04	-18.61	LT+RATCam	IV						
56320.210	205.76	19.94 ± 0.05	-18.54	LT+RATCam	IV						
56323.315	208.57	20.60 ± 0.20	-17.88	p60							
56324.311	209.47	20.46 ± 0.12	-18.03	p60							
56334.170	218.37	20.11 ± 0.04	-18.38	LT+RATCam	IV						
56345.336	228.45	20.56 ± 0.16	-17.93	p60							
56345.344	228.46	20.51 ± 0.15	-17.98	p60							
56346.255	229.28	20.33 ± 0.17	-18.16	p60							
56347.433	230.34	20.74 ± 0.27	-17.75	p60							
56350.242	232.88	20.64 ± 0.30	-17.85	p60							
56352.237	234.68	20.61 ± 0.21	-17.87	p60							
56353.233	235.58	20.61 ± 0.14	-17.88	p60							
56362.260	243.73	20.49 ± 0.04	-17.99	LT+RATCam	IV						
56362.272	243.74	20.69 ± 0.14	-17.79	p60							
56362.279	243.75	20.70 ± 0.14	-17.79	p60							
56362.479	243.93	20.84 ± 0.18	-17.64	p48							
56362.509	243.96	20.56 ± 0.15	-17.92	p48							
56362.539	243.98	20.73 ± 0.18	-17.75	p48							
56366.489	247.55	20.54 ± 0.22	-17.94	p48							
56366.500	247.56	20.70 ± 0.15	-17.78	p48							
56366.511	247.57	20.92 ± 0.18	-17.56	p48							
56366.522	247.58	20.74 ± 0.16	-17.74	p48							
56369.539	250.30	20.65 ± 0.18	-17.83	p48							
56370.309	251.00	20.84 ± 0.18	-17.65	p60							
56372.197	252.70	20.58 ± 0.27	-17.90	p60							
56373.181	253.59	20.65 ± 0.26	-17.83	p60							
56374.178	254.49	20.33 ± 0.30	-18.15	p60							

Table D48. PTF 12gty photometry data.

MJD	Phase	m	Filter	Tel	MJD	Phase	m	Filter	Tel
56086.286	-48.50	21.20 ± 0.36	r	p48	56159.279	13.53	20.23 ± 0.13	g	p60
56090.440	-44.97	20.91 ± 0.35	r	p48	56166.255	19.46	19.61 ± 0.10	i	p60
56092.374	-43.32	21.30 ± 0.36	r	p48	56166.257	19.46	19.90 ± 0.11	r	p60
56092.404	-43.30	20.95 ± 0.32	r	p48	56166.259	19.46	20.54 ± 0.29	g	p60
56097.373	-39.07	20.92 ± 0.35	r	p48	56166.262	19.47	19.52 ± 0.09	i	p60
56097.431	-39.02	20.30 ± 0.21	r	p48	56166.263	19.47	19.83 ± 0.10	r	p60
56099.391	-37.36	20.59 ± 0.25	r	p48	56166.266	19.47	20.25 ± 0.12	g	p60
56099.425	-37.33	20.56 ± 0.25	r	p48	56177.151	28.72	19.70 ± 0.10	i	p60
56100.314	-36.58	20.54 ± 0.21	r	p48	56177.167	28.73	19.72 ± 0.10	r	p60
56100.344	-36.55	20.52 ± 0.23	r	p48	56177.171	28.74	20.39 ± 0.15	g	p60
56102.311	-34.88	20.58 ± 0.25	r	p48	56185.171	35.53	19.77 ± 0.13	i	p60
56102.341	-34.85	20.49 ± 0.29	r	p48	56185.173	35.53	19.94 ± 0.14	r	p60
56102.370	-34.83	20.40 ± 0.24	r	p48	56186.137	36.35	20.07 ± 0.12	r	p60
56104.303	-33.19	20.60 ± 0.24	r	p48	56186.142	36.36	20.99 ± 0.21	g	p60
56104.351	-33.14	20.37 ± 0.22	r	p48	56187.138	37.20	20.18 ± 0.12	r	p60
56104.380	-33.12	20.68 ± 0.30	r	p48	56187.142	37.21	20.93 ± 0.17	g	p60
56106.301	-31.49	20.30 ± 0.21	r	p48	56198.182	46.59	20.32 ± 0.26	i	p60
56106.340	-31.45	20.57 ± 0.24	r	p48	56199.118	47.38	20.27 ± 0.14	i	p60
56106.370	-31.43	20.25 ± 0.19	r	p48	56199.120	47.39	20.67 ± 0.20	r	p60
56108.297	-29.79	20.51 ± 0.23	r	p48	56200.115	48.23	20.29 ± 0.13	i	p60
56108.326	-29.77	20.47 ± 0.25	r	p48	56200.117	48.23	20.55 ± 0.13	r	p60
56108.356	-29.74	20.62 ± 0.28	r	p48	56200.122	48.24	21.76 ± 0.29	g	p60
56112.234	-26.45	20.40 ± 0.23	r	p48	56201.116	49.08	20.74 ± 0.18	r	p60
56112.264	-26.42	20.02 ± 0.21	r	p48	56202.114	49.93	20.89 ± 0.18	r	p60
56117.344	-22.10	20.17 ± 0.19	r	p48	56202.119	49.94	21.08 ± 0.19	g	p60
56117.376	-22.08	19.82 ± 0.17	r	p48	56214.108	60.12	20.27 ± 0.12	i	p60
56119.295	-20.45	20.06 ± 0.21	r	p48	56214.110	60.12	20.58 ± 0.17	r	p60
56123.328	-17.02	19.95 ± 0.16	r	p48	56223.094	67.76	20.32 ± 0.14	i	p60
56123.357	-16.99	19.86 ± 0.17	r	p48	56223.097	67.76	20.65 ± 0.20	r	p60
56124.273	-16.22	20.02 ± 0.16	r	p48	56226.093	70.31	20.77 ± 0.17	i	p60
56124.311	-16.18	19.87 ± 0.18	r	p48	56226.095	70.31	20.97 ± 0.20	r	p60
56124.353	-16.15	19.98 ± 0.21	r	p48	56227.093	71.16	20.49 ± 0.19	i	p60
56129.307	-11.94	19.76 ± 0.14	r	p48	56227.095	71.16	21.26 ± 0.32	r	p60
56129.336	-11.91	19.79 ± 0.16	r	p48	56228.091	72.01	20.29 ± 0.13	i	p60
56129.366	-11.89	19.80 ± 0.21	r	p48	56228.093	72.01	21.00 ± 0.21	r	p60
56133.287	-8.56	19.77 ± 0.14	r	p48	56272.570	109.80	20.72 ± 0.20	i	p60
56133.317	-8.53	19.86 ± 0.17	r	p48	56283.540	119.12	21.36 ± 0.23	i	p60
56133.347	-8.50	19.72 ± 0.15	r	p48	56283.542	119.13	21.26 ± 0.23	r	p60
56136.315	-5.98	20.04 ± 0.21	r	p48	56289.541	124.22	21.40 ± 0.27	i	p60
56136.345	-5.96	19.56 ± 0.18	r	p48	56289.544	124.23	21.81 ± 0.34	r	p60
56138.341	-4.26	19.45 ± 0.08	i	p60	56297.510	130.99	21.48 ± 0.27	i	p60
56138.342	-4.26	19.45 ± 0.09	r	p60	56297.512	131.00	21.54 ± 0.27	r	p60
56148.299	4.20	19.52 ± 0.10	i	p60	56300.487	133.52	21.29 ± 0.32	r	p60
56148.304	4.21	20.35 ± 0.24	g	p60					
56159.274	13.53	19.71 ± 0.10	i	p60					
56159.275	13.53	19.72 ± 0.10	r	p60					

Table D49. PTF 12gty rest-frame g photometry data.

MJD	Phase	m_g	M_g	Tel	Ref	MJD	Phase	m_g	M_g	Tel	Ref
56086.286	-48.50	21.26 ± 0.36	-18.40	p48		56186.137	36.35	20.32 ± 0.12	-19.34	p60	
56090.440	-44.97	20.96 ± 0.35	-18.70	p48		56187.138	37.20	20.44 ± 0.12	-19.22	p60	
56092.374	-43.32	21.35 ± 0.36	-18.31	p48		56199.120	47.39	20.95 ± 0.20	-18.71	p60	
56092.404	-43.30	21.00 ± 0.32	-18.65	p48		56200.117	48.23	20.83 ± 0.13	-18.83	p60	
56097.373	-39.07	20.97 ± 0.35	-18.68	p48		56201.116	49.08	21.02 ± 0.18	-18.64	p60	
56097.431	-39.02	20.36 ± 0.21	-19.30	p48		56202.114	49.93	21.17 ± 0.18	-18.49	p60	
56099.391	-37.36	20.64 ± 0.25	-19.02	p48		56214.110	60.12	20.87 ± 0.17	-18.79	p60	
56099.425	-37.33	20.61 ± 0.25	-19.04	p48		56223.097	67.76	20.95 ± 0.20	-18.71	p60	
56100.314	-36.58	20.59 ± 0.21	-19.07	p48		56226.095	70.31	21.28 ± 0.20	-18.38	p60	
56100.344	-36.55	20.58 ± 0.23	-19.08	p48		56227.095	71.16	21.56 ± 0.32	-18.10	p60	
56102.311	-34.88	20.64 ± 0.25	-19.02	p48		56228.093	72.01	21.30 ± 0.21	-18.36	p60	
56102.341	-34.85	20.54 ± 0.29	-19.12	p48		56283.542	119.13	21.58 ± 0.23	-18.08	p60	
56102.370	-34.83	20.46 ± 0.24	-19.20	p48		56289.544	124.23	22.12 ± 0.34	-17.54	p60	
56104.303	-33.19	20.66 ± 0.24	-19.00	p48		56297.512	131.00	21.86 ± 0.27	-17.80	p60	
56104.351	-33.14	20.43 ± 0.22	-19.23	p48		56300.487	133.52	21.61 ± 0.32	-18.05	p60	
56104.380	-33.12	20.74 ± 0.30	-18.92	p48							
56106.301	-31.49	20.35 ± 0.21	-19.31	p48							
56106.340	-31.45	20.63 ± 0.24	-19.03	p48							
56106.370	-31.43	20.30 ± 0.19	-19.36	p48							
56108.297	-29.79	20.56 ± 0.23	-19.10	p48							
56108.326	-29.77	20.52 ± 0.25	-19.14	p48							
56108.356	-29.74	20.67 ± 0.28	-18.98	p48							
56112.234	-26.45	20.46 ± 0.23	-19.20	p48							
56112.264	-26.42	20.08 ± 0.21	-19.58	p48							
56117.344	-22.10	20.24 ± 0.19	-19.42	p48							
56117.376	-22.08	19.89 ± 0.17	-19.76	p48							
56119.295	-20.45	20.15 ± 0.21	-19.51	p48							
56123.328	-17.02	20.04 ± 0.16	-19.61	p48							
56123.357	-16.99	19.96 ± 0.17	-19.70	p48							
56124.273	-16.22	20.12 ± 0.16	-19.54	p48							
56124.311	-16.18	19.98 ± 0.18	-19.68	p48							
56124.353	-16.15	20.09 ± 0.21	-19.57	p48							
56129.307	-11.94	19.88 ± 0.14	-19.78	p48							
56129.336	-11.91	19.91 ± 0.16	-19.75	p48							
56129.366	-11.89	19.92 ± 0.21	-19.74	p48							
56133.287	-8.56	19.90 ± 0.14	-19.76	p48							
56133.317	-8.53	19.99 ± 0.17	-19.67	p48							
56133.347	-8.50	19.85 ± 0.15	-19.81	p48							
56136.315	-5.98	20.18 ± 0.21	-19.48	p48							
56136.345	-5.96	19.70 ± 0.18	-19.96	p48							
56138.342	-4.26	19.59 ± 0.09	-20.07	p60							
56159.275	13.53	19.93 ± 0.10	-19.73	p60							
56166.257	19.46	20.12 ± 0.11	-19.54	p60							
56166.263	19.47	20.05 ± 0.10	-19.61	p60							
56177.167	28.73	19.96 ± 0.10	-19.70	p60							
56185.173	35.53	20.19 ± 0.14	-19.47	p60							

Table D50. PTF 12hni photometry data.

MJD	Phase	m	Filter	Tel	MJD	Phase	m	Filter	Tel
56146.255	-7.23	18.45 ± 0.09	r	p48	56228.108	66.80	21.01 ± 0.25	r	p60
56146.319	-7.18	18.52 ± 0.08	r	p48	56228.177	66.86	21.16 ± 0.25	r	p48
56147.229	-6.35	18.49 ± 0.08	r	p48	56229.188	67.78	20.89 ± 0.27	r	p48
56147.294	-6.30	18.53 ± 0.08	r	p48	56231.104	69.51	20.47 ± 0.16	r	p48
56148.232	-5.45	18.52 ± 0.08	r	p48	56231.168	69.57	20.88 ± 0.25	r	p48
56148.296	-5.39	18.74 ± 0.07	r	p48	56232.155	70.46	20.43 ± 0.17	r	p48
56151.485	-2.50	18.67 ± 0.07	r	p60	56234.128	72.25	20.58 ± 0.17	i	p60
56166.233	10.83	18.55 ± 0.07	r	p48	56234.130	72.25	20.78 ± 0.15	r	p60
56167.276	11.78	18.59 ± 0.08	r	p48	56234.132	72.25	21.72 ± 0.32	B	p60
56167.347	11.84	18.62 ± 0.07	r	p48	56234.133	72.25	21.74 ± 0.23	g	p60
56176.256	19.90	18.59 ± 0.08	i	p60	56235.094	73.12	20.62 ± 0.17	i	p60
56176.257	19.90	18.79 ± 0.08	r	p60	56235.151	73.17	20.91 ± 0.16	r	p60
56176.259	19.90	19.86 ± 0.16	B	p60	56235.154	73.17	21.98 ± 0.27	g	p60
56176.261	19.91	19.43 ± 0.10	g	p60	56238.088	75.83	20.67 ± 0.19	i	p60
56179.143	22.51	18.99 ± 0.25	i	p60	56238.090	75.83	20.87 ± 0.18	r	p60
56179.144	22.51	18.87 ± 0.19	i	p60	56238.091	75.83	21.72 ± 0.34	B	p60
56179.145	22.51	19.03 ± 0.16	r	p60	56238.093	75.83	22.00 ± 0.29	g	p60
56179.168	22.53	19.52 ± 0.11	g	p60	56245.126	82.19	20.79 ± 0.19	i	p60
56179.169	22.54	18.89 ± 0.09	r	p60	56245.127	82.19	21.11 ± 0.19	r	p60
56179.171	22.54	19.83 ± 0.16	B	p60	56245.129	82.20	21.65 ± 0.31	B	p60
56179.172	22.54	19.53 ± 0.10	g	p60	56245.130	82.20	21.90 ± 0.27	g	p60
56185.180	27.97	19.28 ± 0.09	i	p60	56255.073	91.19	20.78 ± 0.27	i	p60
56185.182	27.97	19.24 ± 0.09	i	p60	56255.076	91.19	21.28 ± 0.29	r	p60
56185.183	27.97	19.35 ± 0.09	r	p60	56268.130	103.00	21.70 ± 0.27	g	p60
56185.185	27.98	20.34 ± 0.17	B	p60	56270.094	104.78	20.42 ± 0.17	i	p60
56185.187	27.98	19.89 ± 0.10	g	p60	56270.096	104.78	20.56 ± 0.16	r	p60
56200.134	41.50	20.17 ± 0.25	i	p60	56270.098	104.78	20.38 ± 0.16	i	p60
56200.136	41.50	20.43 ± 0.25	r	p60	56270.099	104.78	20.55 ± 0.16	r	p60
56201.131	42.40	20.75 ± 0.34	g	p60	56271.108	105.69	21.18 ± 0.28	g	p60
56214.127	54.15	19.94 ± 0.12	i	p60	56273.113	107.51	20.07 ± 0.14	i	p60
56214.128	54.16	20.56 ± 0.13	r	p60	56273.115	107.51	20.63 ± 0.17	r	p60
56214.132	54.16	21.87 ± 0.26	g	p60	56282.074	115.61	20.15 ± 0.19	i	p60
56217.112	56.85	20.23 ± 0.15	i	p60	56282.077	115.61	20.46 ± 0.18	r	p60
56217.113	56.86	20.50 ± 0.16	r	p60	56282.080	115.62	21.26 ± 0.27	g	p60
56217.117	56.86	21.36 ± 0.25	g	p60					
56217.118	56.86	20.28 ± 0.16	i	p60					
56217.120	56.86	20.52 ± 0.15	r	p60					
56217.123	56.86	21.68 ± 0.27	g	p60					
56220.103	59.56	20.30 ± 0.14	i	p60					
56220.104	59.56	20.58 ± 0.13	r	p60					
56220.108	59.56	21.16 ± 0.18	g	p60					
56220.110	59.57	20.15 ± 0.13	i	p60					
56220.112	59.57	20.67 ± 0.13	r	p60					
56220.113	59.57	21.64 ± 0.29	B	p60					
56220.115	59.57	21.17 ± 0.17	g	p60					
56228.106	66.80	20.34 ± 0.20	i	p60					

Table D51. PTF 12hni rest-frame g photometry data.

MJD	Phase	m_g	M_g	Telescope	Reference
56146.255	-7.23	18.44 ± 0.09	-20.00	p48	
56146.319	-7.18	18.51 ± 0.08	-19.93	p48	
56147.229	-6.35	18.48 ± 0.08	-19.96	p48	
56147.294	-6.30	18.52 ± 0.08	-19.92	p48	
56148.232	-5.45	18.51 ± 0.08	-19.93	p48	
56148.296	-5.39	18.74 ± 0.07	-19.70	p48	
56151.485	-2.50	18.68 ± 0.07	-19.76	p60	
56166.233	10.83	18.62 ± 0.07	-19.82	p48	
56167.276	11.78	18.66 ± 0.08	-19.79	p48	
56167.347	11.84	18.68 ± 0.07	-19.76	p48	
56176.257	19.90	18.89 ± 0.08	-19.55	p60	
56179.145	22.51	19.14 ± 0.16	-19.30	p60	
56179.169	22.54	19.00 ± 0.09	-19.44	p60	
56185.183	27.97	19.48 ± 0.09	-18.96	p60	
56200.136	41.50	20.59 ± 0.25	-17.85	p60	
56214.128	54.16	20.75 ± 0.13	-17.69	p60	
56217.113	56.86	20.70 ± 0.16	-17.74	p60	
56217.120	56.86	20.73 ± 0.15	-17.72	p60	
56220.104	59.56	20.79 ± 0.13	-17.65	p60	
56220.112	59.57	20.87 ± 0.13	-17.57	p60	
56228.108	66.80	21.23 ± 0.25	-17.21	p60	
56228.177	66.86	21.38 ± 0.25	-17.06	p48	
56229.188	67.78	21.12 ± 0.27	-17.33	p48	
56231.104	69.51	20.69 ± 0.16	-17.75	p48	
56231.168	69.57	21.11 ± 0.25	-17.34	p48	
56232.155	70.46	20.65 ± 0.17	-17.79	p48	
56234.130	72.25	21.01 ± 0.15	-17.43	p60	
56235.151	73.17	21.14 ± 0.16	-17.30	p60	
56238.090	75.83	21.10 ± 0.18	-17.34	p60	
56245.127	82.19	21.35 ± 0.19	-17.09	p60	
56255.076	91.19	21.53 ± 0.29	-16.91	p60	
56270.096	104.78	20.83 ± 0.16	-17.62	p60	
56270.099	104.78	20.81 ± 0.16	-17.63	p60	
56273.115	107.51	20.89 ± 0.17	-17.55	p60	
56282.077	115.61	20.73 ± 0.18	-17.71	p60	

Table D52. PTF 12mxx photometry data.

MJD	Phase	m	Filter	Tel	MJD	Phase	m	Filter	Tel
56239.096	-39.96	21.19 ± 0.31	r	p48	56283.800	-6.28	19.13 ± 0.07	g	LT
56243.141	-36.91	20.56 ± 0.20	g	p48	56283.800	-6.28	19.29 ± 0.09	r	LT
56243.178	-36.89	20.74 ± 0.22	g	p48	56283.800	-6.28	19.36 ± 0.10	i	LT
56245.207	-35.36	20.49 ± 0.17	g	p48	56284.180	-6.00	21.06 ± 0.62	UVW2	Swift/UVOT
56245.242	-35.33	20.38 ± 0.17	g	p48	56284.186	-5.99	19.23 ± 0.14	r	p60
56252.227	-30.07	20.17 ± 0.19	r	p48	56284.188	-5.99	19.26 ± 0.29	u	Swift/UVOT
56252.259	-30.04	20.34 ± 0.24	r	p48	56284.191	-5.99	19.14 ± 0.19	B	Swift/UVOT
56254.154	-28.62	20.34 ± 0.24	r	p48	56284.191	-5.99	19.75 ± 0.35	UVW1	Swift/UVOT
56254.193	-28.59	19.94 ± 0.17	r	p48	56284.195	-5.99	19.65 ± 0.32	UVM2	Swift/UVOT
56256.155	-27.11	19.84 ± 0.17	r	p48	56284.195	-5.99	19.33 ± 0.17	B	p60
56256.185	-27.09	19.72 ± 0.17	r	p48	56284.196	-5.99	19.42 ± 0.25	z	p60
56256.223	-27.06	19.82 ± 0.18	r	p48	56284.198	-5.98	19.27 ± 0.13	g	p60
56256.253	-27.04	19.75 ± 0.19	r	p48	56284.614	-5.67	21.53 ± 0.34	UVW1	Swift/UVOT
56257.142	-26.37	19.58 ± 0.15	r	p48	56284.616	-5.67	20.11 ± 0.20	u	Swift/UVOT
56257.172	-26.34	19.69 ± 0.17	r	p48	56284.617	-5.67	19.02 ± 0.15	B	Swift/UVOT
56265.139	-20.34	19.64 ± 0.11	r	p48	56284.618	-5.67	22.37 ± 0.36	UVW2	Swift/UVOT
56265.168	-20.32	19.53 ± 0.12	r	p48	56284.622	-5.66	21.59 ± 0.31	UVM2	Swift/UVOT
56268.093	-18.12	19.59 ± 0.11	r	p48	56287.061	-3.83	19.21 ± 0.09	g	LCOGT
56268.122	-18.09	19.62 ± 0.11	r	p48	56287.069	-3.82	19.08 ± 0.32	r	LCOGT
56271.100	-15.85	19.44 ± 0.12	r	p48	56287.075	-3.82	19.17 ± 0.01	i	LCOGT
56271.130	-15.83	19.35 ± 0.12	r	p48	56287.900	-3.19	19.32 ± 0.13	i	LT
56281.800	-7.79	19.08 ± 0.11	g	LT	56289.061	-2.32	19.25 ± 0.05	g	LCOGT
56282.060	-7.59	19.16 ± 0.05	g	LCOGT	56289.068	-2.31	19.23 ± 0.08	r	LCOGT
56282.067	-7.59	19.24 ± 0.06	r	LCOGT	56289.076	-2.31	19.32 ± 0.06	i	LCOGT
56282.073	-7.58	19.29 ± 0.10	i	LCOGT	56290.061	-1.57	19.21 ± 0.04	g	LCOGT
56282.082	-7.58	19.49 ± 0.11	i	p60	56290.068	-1.56	19.15 ± 0.08	r	LCOGT
56282.084	-7.58	19.24 ± 0.09	r	p60	56290.075	-1.56	19.32 ± 0.19	i	LCOGT
56282.085	-7.58	19.25 ± 0.12	B	p60	56290.900	-0.93	19.32 ± 0.08	i	LT
56282.087	-7.57	19.15 ± 0.09	g	p60	56290.900	-0.93	19.14 ± 0.08	g	LT
56282.088	-7.57	19.40 ± 0.11	i	p60	56290.900	-0.93	19.22 ± 0.08	r	LT
56282.090	-7.57	19.27 ± 0.09	r	p60	56291.061	-0.81	19.18 ± 0.04	g	LCOGT
56282.092	-7.57	19.37 ± 0.13	B	p60	56291.068	-0.81	19.18 ± 0.02	r	LCOGT
56282.093	-7.57	19.21 ± 0.09	g	p60	56291.075	-0.80	19.29 ± 0.02	i	LCOGT
56282.095	-7.57	19.39 ± 0.11	i	p60	56291.800	-0.26	19.25 ± 0.07	r	LT
56282.096	-7.57	19.32 ± 0.09	r	p60	56291.800	-0.26	19.39 ± 0.07	i	LT
56282.098	-7.57	19.40 ± 0.14	B	p60	56291.800	-0.26	19.20 ± 0.06	g	LT
56282.100	-7.56	19.62 ± 0.22	z	p60	56293.900	1.33	19.16 ± 0.13	r	LT
56282.101	-7.56	19.12 ± 0.09	g	p60	56293.900	1.33	19.34 ± 0.08	i	LT
56282.103	-7.56	19.45 ± 0.11	i	p60	56293.900	1.33	19.25 ± 0.07	g	LT
56282.105	-7.56	19.30 ± 0.10	r	p60	56295.061	2.20	19.30 ± 0.02	g	LCOGT
56282.106	-7.56	19.32 ± 0.13	B	p60	56295.068	2.21	19.22 ± 0.04	r	LCOGT
56282.108	-7.56	19.24 ± 0.19	z	p60	56295.075	2.21	19.26 ± 0.10	i	LCOGT
56282.109	-7.56	19.20 ± 0.10	g	p60	56295.800	2.76	19.27 ± 0.07	r	LT
56283.061	-6.84	19.17 ± 0.04	g	LCOGT	56295.800	2.76	19.22 ± 0.07	g	LT
56283.068	-6.83	19.17 ± 0.06	r	LCOGT	56295.800	2.76	19.36 ± 0.08	i	LT
56283.074	-6.83	19.31 ± 0.06	i	LCOGT	56296.800	3.51	19.23 ± 0.08	g	LT

Table D53. Continuation of Table D52.

MJD	Phase	m	Filter	Telescope
56296.800	3.51	19.37 ± 0.08	i	LT
56296.800	3.51	19.26 ± 0.07	r	LT
56298.061	4.46	19.32 ± 0.08	g	LCOGT
56298.068	4.47	19.25 ± 0.07	r	LCOGT
56298.073	4.47	19.26 ± 0.09	i	LCOGT
56300.061	5.97	19.35 ± 0.07	g	LCOGT
56300.068	5.97	19.14 ± 0.03	r	LCOGT
56300.074	5.98	19.19 ± 0.06	i	LCOGT
56300.800	6.52	19.31 ± 0.07	g	LT
56300.800	6.52	19.35 ± 0.07	i	LT
56300.800	6.52	19.28 ± 0.07	r	LT
56301.124	6.77	19.38 ± 0.10	i	p60
56301.125	6.77	19.33 ± 0.09	r	p60
56301.127	6.77	19.51 ± 0.12	B	p60
56301.129	6.77	19.15 ± 0.17	z	p60
56301.130	6.77	19.38 ± 0.09	g	p60
56303.800	8.78	19.35 ± 0.07	r	LT
56303.800	8.78	19.40 ± 0.07	g	LT
56303.800	8.78	19.42 ± 0.09	i	LT
56308.061	11.99	19.63 ± 0.05	g	LCOGT
56308.068	12.00	19.33 ± 0.05	r	LCOGT
56308.074	12.00	19.48 ± 0.10	i	LCOGT
56308.800	12.55	19.44 ± 0.08	i	LT
56308.800	12.55	19.53 ± 0.08	g	LT
56308.800	12.55	19.38 ± 0.08	r	LT

Table D54. PTF 12mxx rest-frame g photometry data.

MJD	Phase	m_g	M_g	Telescope	Reference
56239.096	-39.96	21.53 ± 0.31	-19.64	p48	
56252.227	-30.07	20.51 ± 0.19	-20.66	p48	
56252.259	-30.04	20.69 ± 0.24	-20.49	p48	
56254.154	-28.62	20.69 ± 0.24	-20.49	p48	
56254.193	-28.59	20.29 ± 0.17	-20.89	p48	
56256.155	-27.11	20.19 ± 0.17	-20.98	p48	
56256.185	-27.09	20.07 ± 0.17	-21.11	p48	
56256.223	-27.06	20.16 ± 0.18	-21.01	p48	
56256.253	-27.04	20.10 ± 0.19	-21.08	p48	
56257.142	-26.37	19.93 ± 0.15	-21.24	p48	
56257.172	-26.34	20.04 ± 0.17	-21.14	p48	
56265.139	-20.34	20.00 ± 0.11	-21.17	p48	
56265.168	-20.32	19.89 ± 0.12	-21.29	p48	
56268.093	-18.12	19.96 ± 0.11	-21.22	p48	
56268.122	-18.09	19.99 ± 0.11	-21.19	p48	
56271.100	-15.85	19.81 ± 0.12	-21.36	p48	
56271.130	-15.83	19.72 ± 0.12	-21.46	p48	
56282.067	-7.59	19.61 ± 0.06	-21.57	LCOGT	
56282.084	-7.58	19.62 ± 0.09	-21.56	p60	
56282.090	-7.57	19.65 ± 0.09	-21.53	p60	
56282.096	-7.57	19.71 ± 0.09	-21.47	p60	
56282.105	-7.56	19.68 ± 0.10	-21.49	p60	
56283.068	-6.83	19.54 ± 0.06	-21.64	LCOGT	
56283.800	-6.28	19.65 ± 0.09	-21.52	LT	
56284.186	-5.99	19.62 ± 0.14	-21.56	p60	
56287.069	-3.82	19.45 ± 0.32	-21.72	LCOGT	
56289.068	-2.31	19.60 ± 0.08	-21.58	LCOGT	
56290.068	-1.56	19.53 ± 0.08	-21.65	LCOGT	
56290.900	-0.93	19.59 ± 0.08	-21.59	LT	
56291.068	-0.81	19.56 ± 0.02	-21.62	LCOGT	
56291.800	-0.26	19.62 ± 0.07	-21.55	LT	
56293.900	1.33	19.54 ± 0.13	-21.64	LT	
56295.068	2.21	19.60 ± 0.04	-21.58	LCOGT	
56295.800	2.76	19.65 ± 0.07	-21.53	LT	
56296.800	3.51	19.64 ± 0.07	-21.53	LT	
56298.068	4.47	19.63 ± 0.07	-21.54	LCOGT	
56300.068	5.97	19.52 ± 0.03	-21.65	LCOGT	
56300.800	6.52	19.67 ± 0.07	-21.51	LT	
56301.125	6.77	19.73 ± 0.09	-21.45	p60	
56303.800	8.78	19.73 ± 0.07	-21.44	LT	
56308.068	12.00	19.73 ± 0.05	-21.45	LCOGT	
56308.800	12.55	19.78 ± 0.08	-21.40	LT	

Table D55. PTF 13ajg photometry data.

MJD	Phase	m	Filter	Tel	MJD	Phase	m	Filter	Tel
56362.453	-27.52	21.13 ± 0.25	r	p48	56399.440	-6.27	20.39 ± 0.15	r	p48
56362.512	-27.49	21.03 ± 0.22	r	p48	56400.346	-5.75	20.27 ± 0.17	r	p48
56363.426	-26.96	21.07 ± 0.27	r	p48	56400.377	-5.73	20.20 ± 0.16	r	p48
56363.455	-26.95	21.34 ± 0.34	r	p48	56400.407	-5.71	20.23 ± 0.14	r	p48
56363.484	-26.93	21.12 ± 0.23	r	p48	56401.383	-5.15	20.46 ± 0.15	r	p48
56365.544	-25.75	20.84 ± 0.28	r	p48	56401.413	-5.14	20.28 ± 0.15	r	p48
56369.418	-23.52	21.26 ± 0.29	r	p48	56401.443	-5.12	20.21 ± 0.14	r	p48
56369.448	-23.50	20.89 ± 0.20	r	p48	56402.354	-4.60	20.16 ± 0.16	r	p48
56369.477	-23.49	21.24 ± 0.23	r	p48	56402.384	-4.58	20.03 ± 0.14	r	p48
56370.519	-22.89	21.17 ± 0.31	r	p48	56402.414	-4.56	20.15 ± 0.15	r	p48
56374.414	-20.65	20.56 ± 0.22	r	p48	56403.353	-4.02	20.13 ± 0.16	r	p48
56374.444	-20.63	21.03 ± 0.28	r	p48	56403.382	-4.00	20.24 ± 0.13	r	p48
56374.474	-20.62	20.80 ± 0.21	r	p48	56403.412	-3.99	20.38 ± 0.18	r	p48
56375.416	-20.07	21.15 ± 0.36	r	p48	56404.351	-3.45	20.22 ± 0.18	r	p48
56375.446	-20.06	20.90 ± 0.24	r	p48	56404.381	-3.43	20.27 ± 0.14	r	p48
56375.475	-20.04	20.67 ± 0.23	r	p48	56404.410	-3.41	20.22 ± 0.13	r	p48
56376.421	-19.50	20.76 ± 0.24	r	p48	56405.362	-2.87	20.05 ± 0.19	r	p48
56376.451	-19.48	20.72 ± 0.22	r	p48	56405.392	-2.85	20.02 ± 0.19	r	p48
56376.481	-19.46	20.48 ± 0.21	r	p48	56405.435	-2.83	20.37 ± 0.23	r	p48
56382.381	-16.07	20.56 ± 0.26	r	p48	56412.345	1.15	20.09 ± 0.17	r	p48
56382.412	-16.05	20.43 ± 0.23	r	p48	56412.375	1.16	20.02 ± 0.15	r	p48
56385.371	-14.35	20.61 ± 0.21	r	p48	56412.404	1.18	20.50 ± 0.21	r	p48
56385.401	-14.34	20.44 ± 0.17	r	p48	56413.359	1.73	20.40 ± 0.17	r	p48
56385.431	-14.32	20.44 ± 0.20	r	p48	56413.389	1.75	20.17 ± 0.16	r	p48
56386.337	-13.80	20.27 ± 0.16	r	p48	56413.419	1.76	20.01 ± 0.15	r	p48
56386.366	-13.78	20.54 ± 0.16	r	p48	56414.457	2.36	20.15 ± 0.16	r	p48
56387.367	-13.21	20.56 ± 0.21	r	p48	56415.258	2.82	20.13 ± 0.16	r	p48
56387.397	-13.19	20.85 ± 0.20	r	p48	56415.385	2.89	20.17 ± 0.16	r	p48
56387.427	-13.17	20.22 ± 0.13	r	p48	56415.415	2.91	20.20 ± 0.16	r	p48
56388.484	-12.57	20.34 ± 0.15	r	p48	56416.317	3.43	20.40 ± 0.17	r	p48
56388.514	-12.55	20.45 ± 0.18	r	p48	56416.350	3.45	20.13 ± 0.12	r	p48
56389.359	-12.06	20.49 ± 0.16	r	p48	56416.384	3.47	20.39 ± 0.13	r	p48
56389.389	-12.05	20.42 ± 0.16	r	p48	56417.286	3.98	20.28 ± 0.15	r	p48
56389.419	-12.03	20.41 ± 0.15	r	p48	56417.325	4.01	20.24 ± 0.15	r	p48
56390.439	-11.44	20.41 ± 0.19	r	p48	56417.362	4.03	20.29 ± 0.15	r	p48
56392.331	-10.35	20.66 ± 0.23	r	p48	56422.356	6.90	20.23 ± 0.13	r	p48
56392.360	-10.34	20.53 ± 0.21	r	p48	56422.402	6.92	20.15 ± 0.12	r	p48
56392.389	-10.32	20.67 ± 0.23	r	p48	56422.433	6.94	20.53 ± 0.18	r	p48
56394.349	-9.20	20.50 ± 0.17	r	p48	56423.335	7.46	20.03 ± 0.13	r	p48
56395.301	-8.65	20.33 ± 0.15	r	p48	56423.365	7.48	20.40 ± 0.14	r	p48
56395.330	-8.63	20.10 ± 0.13	r	p48	56423.395	7.49	20.42 ± 0.16	r	p48
56396.294	-8.08	20.31 ± 0.14	r	p48	56424.297	8.01	20.23 ± 0.14	r	p48
56396.324	-8.06	20.40 ± 0.17	r	p48	56424.332	8.03	20.32 ± 0.13	r	p48
56396.355	-8.04	20.23 ± 0.14	r	p48	56424.370	8.06	20.27 ± 0.13	r	p48
56399.364	-6.31	20.30 ± 0.17	r	p48	56425.272	8.57	20.41 ± 0.15	r	p48
56399.409	-6.29	20.40 ± 0.17	r	p48	56425.363	8.63	20.29 ± 0.11	r	p48

Table D56. Continuation of Table D55.

MJD	Phase	m	Filter	Tel	MJD	Phase	m	Filter	Tel
56425.394	8.64	20.34 ± 0.15	r	p48	56452.281	24.09	21.09 ± 0.20	r	p48
56426.295	9.16	20.24 ± 0.15	r	p48	56453.208	24.63	20.97 ± 0.23	r	p48
56426.373	9.21	20.43 ± 0.15	r	p48	56453.277	24.67	21.12 ± 0.21	r	p48
56426.404	9.22	20.35 ± 0.15	r	p48	56454.210	25.20	21.07 ± 0.22	r	p48
56427.306	9.74	20.42 ± 0.18	r	p48	56454.276	25.24	21.60 ± 0.33	r	p48
56427.335	9.76	20.34 ± 0.16	r	p48	56455.190	25.76	21.15 ± 0.22	r	p48
56427.367	9.78	20.75 ± 0.18	r	p48	56455.279	25.82	21.54 ± 0.18	r	p48
56428.269	10.30	20.65 ± 0.20	r	p48	56456.204	26.35	21.22 ± 0.23	r	p48
56428.322	10.33	20.42 ± 0.15	r	p48	56456.283	26.39	21.61 ± 0.29	r	p48
56428.371	10.35	20.24 ± 0.14	r	p48	56457.196	26.92	21.35 ± 0.29	r	p48
56431.364	12.07	20.78 ± 0.20	r	p48	56457.270	26.96	21.56 ± 0.30	r	p48
56431.404	12.10	20.32 ± 0.14	r	p48	56458.202	27.50	21.85 ± 0.31	r	p48
56431.434	12.11	20.59 ± 0.17	r	p48	56458.269	27.53	21.42 ± 0.21	r	p48
56432.336	12.63	20.66 ± 0.22	r	p48	56459.193	28.06	21.43 ± 0.29	r	p48
56432.369	12.65	20.67 ± 0.24	r	p48	56459.277	28.11	21.35 ± 0.26	r	p48
56432.405	12.67	20.42 ± 0.14	r	p48	56460.207	28.65	21.08 ± 0.28	r	p48
56433.306	13.19	20.52 ± 0.22	r	p48	56461.194	29.21	21.00 ± 0.25	r	p48
56433.363	13.22	20.76 ± 0.25	r	p48	56461.251	29.25	21.20 ± 0.27	r	p48
56433.392	13.24	20.21 ± 0.15	r	p48	56462.214	29.80	21.51 ± 0.34	r	p48
56434.294	13.76	20.62 ± 0.26	r	p48	56463.243	30.39	21.21 ± 0.35	r	p48
56434.343	13.79	20.41 ± 0.25	r	p48	56469.185	33.81	21.67 ± 0.30	r	p48
56434.372	13.80	20.25 ± 0.18	r	p48	56469.224	33.83	21.00 ± 0.20	r	p48
56440.358	17.24	20.43 ± 0.27	r	p48	56471.206	34.97	21.60 ± 0.31	r	p48
56440.393	17.26	20.54 ± 0.30	r	p48	56471.243	34.99	21.43 ± 0.25	r	p48
56441.350	17.81	20.77 ± 0.30	r	p48	56472.230	35.56	20.92 ± 0.22	r	p48
56442.335	18.38	20.79 ± 0.23	r	p48	56474.203	36.69	21.37 ± 0.29	r	p48
56442.468	18.45	20.76 ± 0.22	r	p48	56477.315	38.48	21.26 ± 0.21	r	p48
56443.384	18.98	21.06 ± 0.23	r	p48	56486.243	43.61	22.03 ± 0.30	r	p48
56443.419	19.00	21.32 ± 0.28	r	p48	56488.327	44.81	21.51 ± 0.34	r	p48
56444.321	19.52	21.03 ± 0.23	r	p48					
56444.355	19.54	21.04 ± 0.26	r	p48					
56445.257	20.06	20.97 ± 0.16	r	p48					
56445.307	20.09	21.20 ± 0.20	r	p48					
56446.211	20.61	20.87 ± 0.17	r	p48					
56446.286	20.65	20.93 ± 0.17	r	p48					
56447.219	21.18	21.43 ± 0.21	r	p48					
56447.291	21.23	21.16 ± 0.17	r	p48					
56448.217	21.76	21.06 ± 0.20	r	p48					
56448.291	21.80	21.11 ± 0.20	r	p48					
56449.204	22.33	21.35 ± 0.24	r	p48					
56449.276	22.37	21.18 ± 0.18	r	p48					
56450.222	22.91	21.34 ± 0.28	r	p48					
56450.283	22.95	20.90 ± 0.14	r	p48					
56451.207	23.48	20.77 ± 0.17	r	p48					
56451.277	23.52	20.99 ± 0.19	r	p48					
56452.209	24.05	20.95 ± 0.20	r	p48					

Table D57. PTF 13ajg rest-frame g photometry data.

MJD	Phase	m_g	M_g	Tel	Ref	MJD	Phase	m_g	M_g	Tel	Ref
56362.453	-27.52	22.05 ± 0.25	-21.24	p48		56399.409	-6.29	21.13 ± 0.17	-22.17	p48	
56362.512	-27.49	21.95 ± 0.22	-21.35	p48		56399.440	-6.27	21.12 ± 0.15	-22.18	p48	
56363.426	-26.96	22.00 ± 0.27	-21.30	p48		56400.346	-5.75	21.00 ± 0.17	-22.30	p48	
56363.455	-26.95	22.26 ± 0.34	-21.03	p48		56400.377	-5.73	20.93 ± 0.16	-22.36	p48	
56363.484	-26.93	22.04 ± 0.23	-21.26	p48		56400.407	-5.71	20.95 ± 0.14	-22.34	p48	
56365.544	-25.75	21.77 ± 0.28	-21.53	p48		56401.383	-5.15	21.18 ± 0.15	-22.12	p48	
56369.418	-23.52	22.16 ± 0.29	-21.13	p48		56401.413	-5.14	21.00 ± 0.15	-22.29	p48	
56369.448	-23.50	21.79 ± 0.20	-21.50	p48		56401.443	-5.12	20.93 ± 0.14	-22.36	p48	
56369.477	-23.49	22.14 ± 0.23	-21.16	p48		56402.354	-4.60	20.88 ± 0.16	-22.41	p48	
56370.519	-22.89	22.06 ± 0.31	-21.24	p48		56402.384	-4.58	20.75 ± 0.14	-22.55	p48	
56374.414	-20.65	21.43 ± 0.22	-21.87	p48		56402.414	-4.56	20.87 ± 0.15	-22.43	p48	
56374.444	-20.63	21.89 ± 0.28	-21.40	p48		56403.353	-4.02	20.84 ± 0.16	-22.46	p48	
56374.474	-20.62	21.67 ± 0.21	-21.62	p48		56403.382	-4.00	20.95 ± 0.13	-22.34	p48	
56375.416	-20.07	22.01 ± 0.36	-21.29	p48		56403.412	-3.99	21.09 ± 0.18	-22.21	p48	
56375.446	-20.06	21.76 ± 0.24	-21.53	p48		56404.351	-3.45	20.93 ± 0.18	-22.36	p48	
56375.475	-20.04	21.53 ± 0.23	-21.77	p48		56404.381	-3.43	20.98 ± 0.14	-22.32	p48	
56376.421	-19.50	21.62 ± 0.24	-21.67	p48		56404.410	-3.41	20.93 ± 0.13	-22.36	p48	
56376.451	-19.48	21.58 ± 0.22	-21.72	p48		56405.362	-2.87	20.75 ± 0.19	-22.55	p48	
56376.481	-19.46	21.34 ± 0.21	-21.96	p48		56405.392	-2.85	20.73 ± 0.19	-22.57	p48	
56382.381	-16.07	21.38 ± 0.26	-21.92	p48		56405.435	-2.83	21.08 ± 0.23	-22.22	p48	
56382.412	-16.05	21.25 ± 0.23	-22.04	p48		56412.345	1.15	20.76 ± 0.17	-22.53	p48	
56385.371	-14.35	21.42 ± 0.21	-21.88	p48		56412.375	1.16	20.69 ± 0.15	-22.60	p48	
56385.401	-14.34	21.24 ± 0.17	-22.06	p48		56412.400	1.18	20.80 ± 0.06	-22.49	P60	V
56385.431	-14.32	21.24 ± 0.20	-22.06	p48		56412.404	1.18	21.17 ± 0.21	-22.13	p48	
56386.337	-13.80	21.07 ± 0.16	-22.22	p48		56413.359	1.73	21.06 ± 0.17	-22.24	p48	
56386.366	-13.78	21.34 ± 0.16	-21.95	p48		56413.389	1.75	20.84 ± 0.16	-22.46	p48	
56387.367	-13.21	21.35 ± 0.21	-21.95	p48		56413.419	1.76	20.67 ± 0.15	-22.63	p48	
56387.397	-13.19	21.64 ± 0.20	-21.66	p48		56414.457	2.36	20.82 ± 0.16	-22.48	p48	
56387.427	-13.17	21.01 ± 0.13	-22.28	p48		56415.258	2.82	20.78 ± 0.16	-22.52	p48	
56388.484	-12.57	21.13 ± 0.15	-22.17	p48		56415.385	2.89	20.82 ± 0.16	-22.47	p48	
56388.514	-12.55	21.24 ± 0.18	-22.06	p48		56415.415	2.91	20.85 ± 0.16	-22.44	p48	
56389.359	-12.06	21.27 ± 0.16	-22.03	p48		56416.317	3.43	21.05 ± 0.17	-22.25	p48	
56389.389	-12.05	21.20 ± 0.16	-22.09	p48		56416.350	3.45	20.78 ± 0.12	-22.51	p48	
56389.419	-12.03	21.19 ± 0.15	-22.11	p48		56416.384	3.47	21.04 ± 0.13	-22.25	p48	
56390.439	-11.44	21.19 ± 0.19	-22.10	p48		56417.286	3.98	20.93 ± 0.15	-22.37	p48	
56392.331	-10.35	21.44 ± 0.23	-21.86	p48		56417.325	4.01	20.89 ± 0.15	-22.41	p48	
56392.360	-10.34	21.30 ± 0.21	-22.00	p48		56417.362	4.03	20.94 ± 0.15	-22.36	p48	
56392.389	-10.32	21.44 ± 0.23	-21.86	p48		56418.100	4.45	20.92 ± 0.01	-22.38	NOT	V
56394.349	-9.20	21.25 ± 0.17	-22.04	p48		56422.356	6.90	20.85 ± 0.13	-22.44	p48	
56395.300	-8.65	21.05 ± 0.05	-22.25	P60	V	56422.402	6.92	20.77 ± 0.12	-22.52	p48	
56395.301	-8.65	21.09 ± 0.15	-22.21	p48		56422.433	6.94	21.15 ± 0.18	-22.14	p48	
56395.330	-8.63	20.85 ± 0.13	-22.44	p48		56423.335	7.46	20.66 ± 0.13	-22.64	p48	
56396.294	-8.08	21.06 ± 0.14	-22.24	p48		56423.365	7.48	21.03 ± 0.14	-22.27	p48	
56396.324	-8.06	21.15 ± 0.17	-22.14	p48		56423.395	7.49	21.05 ± 0.16	-22.25	p48	
56396.355	-8.04	20.97 ± 0.14	-22.32	p48		56423.400	7.50	20.93 ± 0.05	-22.37	P60	V
56399.364	-6.31	21.03 ± 0.17	-22.27	p48		56424.297	8.01	20.84 ± 0.14	-22.45	p48	

Table D58. Continuation of Table D57.

MJD	Phase	m_g	M_g	Tel	Ref	MJD	Phase	m_g	M_g	Tel	Ref
56424.332	8.03	20.93 ± 0.13	-22.36	p48		56447.291	21.23	21.69 ± 0.17	-21.60	p48	
56424.370	8.06	20.89 ± 0.13	-22.41	p48		56448.217	21.76	21.59 ± 0.20	-21.71	p48	
56425.272	8.57	21.03 ± 0.15	-22.27	p48		56448.291	21.80	21.63 ± 0.20	-21.67	p48	
56425.363	8.63	20.91 ± 0.11	-22.39	p48		56449.204	22.33	21.87 ± 0.24	-21.42	p48	
56425.394	8.64	20.95 ± 0.15	-22.34	p48		56449.276	22.37	21.71 ± 0.18	-21.59	p48	
56426.295	9.16	20.85 ± 0.15	-22.45	p48		56449.300	22.38	21.77 ± 0.06	-21.53	P60	V
56426.373	9.21	21.04 ± 0.15	-22.26	p48		56450.222	22.91	21.85 ± 0.28	-21.44	p48	
56426.404	9.22	20.96 ± 0.15	-22.33	p48		56450.283	22.95	21.42 ± 0.14	-21.88	p48	
56427.306	9.74	21.02 ± 0.18	-22.27	p48		56451.207	23.48	21.29 ± 0.17	-22.00	p48	
56427.335	9.76	20.94 ± 0.16	-22.36	p48		56451.277	23.52	21.51 ± 0.19	-21.78	p48	
56427.367	9.78	21.35 ± 0.18	-21.95	p48		56452.209	24.05	21.47 ± 0.20	-21.83	p48	
56428.269	10.30	21.26 ± 0.20	-22.04	p48		56452.281	24.09	21.60 ± 0.20	-21.70	p48	
56428.322	10.33	21.02 ± 0.15	-22.27	p48		56453.208	24.63	21.48 ± 0.23	-21.82	p48	
56428.371	10.35	20.84 ± 0.14	-22.46	p48		56453.277	24.67	21.63 ± 0.21	-21.67	p48	
56430.100	11.35	21.13 ± 0.02	-22.17	NOT	V	56454.210	25.20	21.57 ± 0.22	-21.72	p48	
56431.364	12.07	21.37 ± 0.20	-21.93	p48		56454.276	25.24	22.11 ± 0.33	-21.19	p48	
56431.400	12.09	21.02 ± 0.07	-22.28	P60	V	56455.190	25.76	21.65 ± 0.22	-21.65	p48	
56431.404	12.10	20.91 ± 0.14	-22.38	p48		56455.279	25.82	22.05 ± 0.18	-21.25	p48	
56431.434	12.11	21.18 ± 0.17	-22.11	p48		56455.400	25.89	21.97 ± 0.22	-21.32	P60	V
56432.300	12.61	21.17 ± 0.06	-22.13	P60	V	56456.200	26.35	21.98 ± 0.10	-21.31	P60	V
56432.336	12.63	21.25 ± 0.22	-22.04	p48		56456.204	26.35	21.72 ± 0.23	-21.58	p48	
56432.369	12.65	21.26 ± 0.24	-22.04	p48		56456.283	26.39	22.11 ± 0.29	-21.18	p48	
56432.405	12.67	21.00 ± 0.14	-22.29	p48		56457.196	26.92	21.84 ± 0.29	-21.45	p48	
56433.300	13.19	21.31 ± 0.12	-21.98	P60	V	56457.270	26.96	22.05 ± 0.30	-21.24	p48	
56433.306	13.19	21.10 ± 0.22	-22.20	p48		56458.202	27.50	22.34 ± 0.31	-20.95	p48	
56433.363	13.22	21.34 ± 0.25	-21.95	p48		56458.269	27.53	21.92 ± 0.21	-21.38	p48	
56433.392	13.24	20.79 ± 0.15	-22.50	p48		56459.193	28.06	21.92 ± 0.29	-21.38	p48	
56434.294	13.76	21.20 ± 0.26	-22.10	p48		56459.277	28.11	21.84 ± 0.26	-21.46	p48	
56434.343	13.79	20.99 ± 0.25	-22.31	p48		56460.207	28.65	21.57 ± 0.28	-21.73	p48	
56434.372	13.80	20.83 ± 0.18	-22.47	p48		56461.194	29.21	21.49 ± 0.25	-21.81	p48	
56440.300	17.21	21.64 ± 0.22	-21.66	P60	V	56461.251	29.25	21.68 ± 0.27	-21.61	p48	
56440.358	17.24	20.99 ± 0.27	-22.31	p48		56462.214	29.80	21.99 ± 0.34	-21.31	p48	
56440.393	17.26	21.10 ± 0.30	-22.20	p48		56463.243	30.39	21.69 ± 0.35	-21.61	p48	
56441.350	17.81	21.32 ± 0.30	-21.98	p48		56469.185	33.81	22.13 ± 0.30	-21.17	p48	
56442.335	18.38	21.34 ± 0.23	-21.96	p48		56469.224	33.83	21.46 ± 0.20	-21.84	p48	
56442.468	18.45	21.31 ± 0.22	-21.99	p48		56469.300	33.87	22.53 ± 0.35	-20.77	P60	V
56443.200	18.88	21.55 ± 0.13	-21.74	P60	V	56470.300	34.45	21.97 ± 0.13	-21.33	P60	V
56443.384	18.98	21.61 ± 0.23	-21.69	p48		56471.206	34.97	22.06 ± 0.31	-21.24	p48	
56443.419	19.00	21.86 ± 0.28	-21.43	p48		56471.243	34.99	21.89 ± 0.25	-21.41	p48	
56444.321	19.52	21.58 ± 0.23	-21.72	p48		56472.230	35.56	21.37 ± 0.22	-21.93	p48	
56444.355	19.54	21.59 ± 0.26	-21.71	p48		56474.203	36.69	21.82 ± 0.29	-21.48	p48	
56445.257	20.06	21.51 ± 0.16	-21.79	p48		56477.000	38.30	22.42 ± 0.05	-20.88	NOT	V
56445.307	20.09	21.74 ± 0.20	-21.56	p48		56477.315	38.48	21.70 ± 0.21	-21.59	p48	
56446.211	20.61	21.41 ± 0.17	-21.89	p48		56479.300	39.62	22.52 ± 0.25	-20.78	P60	V
56446.286	20.65	21.46 ± 0.17	-21.83	p48		56480.200	40.14	22.14 ± 0.14	-21.16	P60	V
56447.219	21.18	21.96 ± 0.21	-21.34	p48		56486.243	43.61	22.44 ± 0.30	-20.85	p48	

Table D59. Continuation of Table D57.

MJD	Phase	m_g	M_g	Telescope	Reference
56488.327	44.81	21.91 ± 0.34	-21.38	p48	
56544.300	76.97	24.04 ± 0.08	-19.25	Keck	V
56776.600	210.45	25.14 ± 0.09	-18.15	Keck	V
56869.400	263.78	26.40 ± 0.22	-16.89	Keck	V

Table D60. PTF 13bdll photometry data.

MJD	Phase	m	Filter	Tel	MJD	Phase	m	Filter	Tel
56387.271	-75.52	21.48 ± 0.30	r	p48	56470.235	-16.38	20.86 ± 0.17	i	p60
56390.286	-73.37	21.54 ± 0.33	r	p48	56470.237	-16.38	21.01 ± 0.17	r	p60
56414.258	-56.28	21.19 ± 0.26	r	p48	56470.241	-16.38	21.92 ± 0.30	g	p60
56415.281	-55.55	21.63 ± 0.36	r	p48	56471.196	-15.70	21.58 ± 0.21	g	p60
56416.218	-54.89	21.54 ± 0.30	r	p48	56474.217	-13.55	21.25 ± 0.31	g	p60
56416.248	-54.86	21.56 ± 0.32	r	p48	56480.206	-9.28	20.69 ± 0.16	i	p60
56416.277	-54.84	21.41 ± 0.28	r	p48	56480.209	-9.28	20.84 ± 0.17	r	p60
56417.185	-54.20	21.24 ± 0.25	r	p48	56480.213	-9.27	22.14 ± 0.34	g	p60
56417.252	-54.15	21.21 ± 0.25	r	p48	56490.219	-2.14	20.73 ± 0.23	i	p60
56423.224	-49.89	21.48 ± 0.30	r	p48	56490.221	-2.14	21.20 ± 0.30	r	p60
56423.253	-49.87	21.08 ± 0.25	r	p48					
56423.283	-49.85	21.19 ± 0.24	r	p48					
56424.184	-49.21	20.99 ± 0.21	r	p48					
56424.188	-49.21	20.95 ± 0.19	r	p48					
56424.239	-49.17	21.65 ± 0.31	r	p48					
56424.269	-49.15	21.05 ± 0.24	r	p48					
56425.198	-48.49	21.68 ± 0.33	r	p48					
56425.207	-48.48	21.43 ± 0.24	r	p48					
56425.234	-48.46	20.89 ± 0.20	r	p48					
56425.282	-48.43	21.19 ± 0.25	r	p48					
56426.214	-47.76	21.25 ± 0.29	r	p48					
56426.244	-47.74	21.17 ± 0.24	r	p48					
56426.274	-47.72	21.12 ± 0.25	r	p48					
56427.195	-47.06	21.16 ± 0.27	r	p48					
56427.237	-47.03	21.15 ± 0.33	r	p48					
56427.276	-47.00	21.47 ± 0.34	r	p48					
56428.177	-46.36	21.01 ± 0.26	r	p48					
56428.239	-46.32	21.14 ± 0.25	r	p48					
56428.279	-46.29	21.41 ± 0.35	r	p48					
56429.287	-45.57	21.40 ± 0.36	r	p48					
56444.230	-34.92	20.77 ± 0.21	r	p48					
56444.237	-34.91	20.96 ± 0.22	r	p48					
56444.265	-34.89	20.86 ± 0.25	r	p48					
56445.220	-34.21	20.96 ± 0.22	r	p48					
56445.262	-34.18	21.24 ± 0.27	r	p48					
56449.282	-31.32	21.17 ± 0.21	r	p60					
56450.329	-30.57	20.80 ± 0.23	i	p60					
56450.332	-30.57	21.61 ± 0.32	g	p60					
56451.313	-29.87	20.85 ± 0.19	i	p60					
56452.312	-29.16	21.32 ± 0.24	g	p60					
56453.282	-28.47	21.20 ± 0.21	g	p60					
56456.201	-26.39	21.02 ± 0.14	r	p60					
56457.195	-25.68	21.06 ± 0.20	i	p60					
56457.197	-25.68	21.72 ± 0.33	B	p60					
56462.282	-22.05	20.66 ± 0.29	r	p60					
56469.272	-17.07	21.03 ± 0.29	i	p60					

Table D61. PTF 13bdd rest-frame g photometry data.

MJD	Phase	m_g	M_g	Telescope	Reference
56387.271	-75.52	21.95 ± 0.30	-19.75	p48	
56390.286	-73.37	22.01 ± 0.33	-19.69	p48	
56414.258	-56.28	21.65 ± 0.26	-20.05	p48	
56415.281	-55.55	22.09 ± 0.36	-19.61	p48	
56416.218	-54.89	22.01 ± 0.30	-19.70	p48	
56416.248	-54.86	22.02 ± 0.32	-19.68	p48	
56416.277	-54.84	21.87 ± 0.28	-19.83	p48	
56417.185	-54.20	21.70 ± 0.25	-20.00	p48	
56417.252	-54.15	21.67 ± 0.25	-20.03	p48	
56423.224	-49.89	21.95 ± 0.30	-19.75	p48	
56423.253	-49.87	21.55 ± 0.25	-20.15	p48	
56423.283	-49.85	21.65 ± 0.24	-20.05	p48	
56424.184	-49.21	21.46 ± 0.21	-20.24	p48	
56424.188	-49.21	21.42 ± 0.19	-20.29	p48	
56424.239	-49.17	22.11 ± 0.31	-19.59	p48	
56424.269	-49.15	21.52 ± 0.24	-20.19	p48	
56425.198	-48.49	22.15 ± 0.33	-19.55	p48	
56425.207	-48.48	21.89 ± 0.24	-19.81	p48	
56425.234	-48.46	21.36 ± 0.20	-20.35	p48	
56425.282	-48.43	21.65 ± 0.25	-20.05	p48	
56426.214	-47.76	21.71 ± 0.29	-19.99	p48	
56426.244	-47.74	21.64 ± 0.24	-20.06	p48	
56426.274	-47.72	21.58 ± 0.25	-20.12	p48	
56427.195	-47.06	21.62 ± 0.27	-20.08	p48	
56427.237	-47.03	21.61 ± 0.33	-20.09	p48	
56427.276	-47.00	21.94 ± 0.34	-19.76	p48	
56428.177	-46.36	21.48 ± 0.26	-20.22	p48	
56428.239	-46.32	21.60 ± 0.25	-20.10	p48	
56428.279	-46.29	21.88 ± 0.35	-19.83	p48	
56429.287	-45.57	21.87 ± 0.36	-19.84	p48	
56444.230	-34.92	21.23 ± 0.21	-20.47	p48	
56444.237	-34.91	21.43 ± 0.22	-20.27	p48	
56444.265	-34.89	21.33 ± 0.25	-20.37	p48	
56445.220	-34.21	21.43 ± 0.22	-20.27	p48	
56445.262	-34.18	21.70 ± 0.27	-20.00	p48	
56449.282	-31.32	21.64 ± 0.21	-20.07	p60	
56456.201	-26.39	21.49 ± 0.14	-20.22	p60	
56462.282	-22.05	21.13 ± 0.29	-20.58	p60	
56470.237	-16.38	21.48 ± 0.17	-20.23	p60	
56480.209	-9.28	21.31 ± 0.17	-20.40	p60	
56490.221	-2.14	21.66 ± 0.30	-20.04	p60	

Table D62. PTF 13bjz photometry data.

MJD	Phase	m	Filter	Telescope
56424.171	-11.01	20.97 ± 0.13	r	p48
56425.163	-10.23	20.43 ± 0.12	r	p48
56426.181	-9.43	20.50 ± 0.17	r	p48
56427.163	-8.66	20.29 ± 0.16	r	p48
56428.206	-7.84	20.26 ± 0.13	r	p48
56433.197	-3.91	19.73 ± 0.13	r	p48
56434.213	-3.11	19.58 ± 0.10	r	p48
56443.178	3.94	19.55 ± 0.10	r	p48
56443.179	3.94	19.90 ± 0.11	r	p48
56443.237	3.98	19.70 ± 0.13	r	p48
56443.250	3.99	20.02 ± 0.15	r	p48
56444.170	4.72	19.98 ± 0.12	r	p48
56444.171	4.72	19.86 ± 0.09	r	p48
56444.270	4.80	19.72 ± 0.15	r	p48
56444.271	4.80	19.74 ± 0.15	r	p48
56445.173	5.51	19.67 ± 0.09	r	p48
56445.174	5.51	19.55 ± 0.10	r	p48
56445.282	5.59	20.13 ± 0.12	r	p48

Table D63. PTF 13bjz rest-frame g photometry data.

MJD	Phase	m_g	M_g	Telescope	Reference
56424.171	-11.01	21.27 ± 0.13	-19.43	p48	
56425.163	-10.23	20.73 ± 0.12	-19.97	p48	
56426.181	-9.43	20.80 ± 0.17	-19.90	p48	
56427.163	-8.66	20.59 ± 0.16	-20.11	p48	
56428.206	-7.84	20.57 ± 0.13	-20.14	p48	
56433.197	-3.91	20.05 ± 0.13	-20.66	p48	
56434.213	-3.11	19.90 ± 0.10	-20.80	p48	
56443.178	3.94	19.89 ± 0.10	-20.81	p48	
56443.179	3.94	20.24 ± 0.11	-20.47	p48	
56443.237	3.98	20.04 ± 0.13	-20.66	p48	
56443.250	3.99	20.36 ± 0.15	-20.34	p48	
56444.170	4.72	20.32 ± 0.12	-20.39	p48	
56444.171	4.72	20.20 ± 0.09	-20.50	p48	
56444.270	4.80	20.06 ± 0.15	-20.64	p48	
56444.271	4.80	20.08 ± 0.15	-20.62	p48	
56445.173	5.51	20.01 ± 0.09	-20.69	p48	
56445.174	5.51	19.90 ± 0.10	-20.81	p48	
56445.282	5.59	20.48 ± 0.12	-20.23	p48	

Table D64. PTF 13cjq photometry data.

MJD	Phase	m	Filter	Tel	MJD	Phase	m	Filter	Tel
56506.277	-0.00	20.05 ± 0.12	r	p48	56521.427	10.85	20.04 ± 0.10	r	p48
56506.314	0.03	20.02 ± 0.12	r	p48	56521.463	10.88	20.39 ± 0.12	r	p48
56506.435	0.11	20.07 ± 0.11	r	p48	56533.196	19.28	20.89 ± 0.24	i	p60
56507.336	0.76	20.01 ± 0.12	r	p48	56533.198	19.28	20.63 ± 0.17	r	p60
56507.421	0.82	20.11 ± 0.11	r	p48	56533.201	19.28	20.91 ± 0.16	g	p60
56507.458	0.85	20.05 ± 0.11	r	p48	56537.297	22.22	20.77 ± 0.14	i	p60
56508.359	1.49	20.05 ± 0.11	r	p48	56537.299	22.22	21.71 ± 0.22	B	p60
56508.437	1.55	20.19 ± 0.10	r	p48	56539.238	23.61	20.71 ± 0.11	r	p60
56508.476	1.57	20.09 ± 0.10	r	p48	56539.240	23.61	22.23 ± 0.33	B	p60
56509.377	2.22	20.06 ± 0.10	r	p48	56539.242	23.61	21.60 ± 0.15	g	p60
56509.434	2.26	20.04 ± 0.10	r	p48	56545.388	28.01	21.21 ± 0.21	i	p60
56509.473	2.29	20.26 ± 0.11	r	p48	56545.391	28.01	21.62 ± 0.20	r	p60
56510.375	2.93	20.00 ± 0.10	r	p48	56546.226	28.61	21.22 ± 0.28	i	p60
56510.428	2.97	20.19 ± 0.10	r	p48	56546.232	28.62	22.16 ± 0.26	g	p60
56510.467	3.00	20.28 ± 0.22	r	p48	56547.216	29.32	20.98 ± 0.17	i	p60
56511.370	3.65	20.13 ± 0.10	r	p48	56547.251	29.35	22.07 ± 0.23	g	p60
56511.433	3.69	20.10 ± 0.10	r	p48	56548.176	30.01	21.34 ± 0.30	i	p60
56511.471	3.72	20.07 ± 0.10	r	p48	56549.150	30.71	21.19 ± 0.28	i	p60
56512.374	4.37	20.03 ± 0.11	r	p48	56550.144	31.42	21.38 ± 0.28	i	p60
56512.429	4.41	20.05 ± 0.10	r	p48	56552.186	32.88	21.06 ± 0.36	i	p60
56512.467	4.43	20.13 ± 0.10	r	p48	56559.149	37.87	21.56 ± 0.26	r	p60
56513.369	5.08	20.03 ± 0.10	r	p48	56564.132	41.44	22.09 ± 0.33	r	p60
56513.428	5.12	20.20 ± 0.11	r	p48	56567.130	43.58	21.36 ± 0.23	i	p60
56513.466	5.15	20.16 ± 0.11	r	p48	56567.132	43.59	22.33 ± 0.36	r	p60
56514.367	5.79	20.15 ± 0.10	r	p48	56569.253	45.11	21.85 ± 0.29	i	p60
56514.426	5.84	20.26 ± 0.11	r	p48	56569.256	45.11	21.92 ± 0.21	r	p60
56514.462	5.86	20.04 ± 0.10	r	p48	56572.170	47.19	21.84 ± 0.30	i	p60
56515.366	6.51	20.13 ± 0.11	r	p48	56578.134	51.47	21.73 ± 0.31	r	p60
56515.423	6.55	20.20 ± 0.11	r	p48	56591.393	60.96	22.00 ± 0.32	r	p60
56515.460	6.58	20.20 ± 0.11	r	p48	56592.252	61.58	22.34 ± 0.32	r	p60
56516.362	7.22	20.02 ± 0.10	r	p48	56658.136	108.77	22.45 ± 0.35	i	p60
56516.416	7.26	20.10 ± 0.10	r	p48	56685.141	128.11	22.28 ± 0.32	r	p60
56516.454	7.29	20.11 ± 0.10	r	p48					
56517.355	7.93	20.14 ± 0.10	r	p48					
56517.410	7.97	19.99 ± 0.10	r	p48					
56517.447	8.00	20.06 ± 0.10	r	p48					
56518.348	8.65	20.08 ± 0.11	r	p48					
56518.402	8.68	20.26 ± 0.11	r	p48					
56518.439	8.71	20.07 ± 0.11	r	p48					
56519.341	9.36	20.20 ± 0.11	r	p48					
56519.412	9.41	20.18 ± 0.10	r	p48					
56519.449	9.43	20.05 ± 0.11	r	p48					
56520.351	10.08	20.37 ± 0.12	r	p48					
56520.428	10.14	20.19 ± 0.11	r	p48					
56520.465	10.16	20.16 ± 0.10	r	p48					
56521.368	10.81	20.10 ± 0.12	r	p48					

Table D65. PTF 13cjg rest-frame g photometry data.

MJD	Phase	m_g	M_g	Tel	Ref	MJD	Phase	m_g	M_g	Tel	Ref
56506.277	-0.00	20.50 ± 0.12	-21.16	p48		56521.427	10.85	20.49 ± 0.10	-21.17	p48	
56506.314	0.03	20.47 ± 0.12	-21.19	p48		56521.463	10.88	20.84 ± 0.12	-20.82	p48	
56506.435	0.11	20.52 ± 0.11	-21.14	p48		56533.198	19.28	21.08 ± 0.17	-20.58	p60	
56507.336	0.76	20.46 ± 0.12	-21.20	p48		56539.238	23.61	21.16 ± 0.11	-20.50	p60	
56507.421	0.82	20.56 ± 0.11	-21.10	p48		56545.391	28.01	22.07 ± 0.20	-19.59	p60	
56507.458	0.85	20.51 ± 0.11	-21.15	p48		56559.149	37.87	22.01 ± 0.26	-19.65	p60	
56508.359	1.49	20.50 ± 0.11	-21.16	p48		56564.132	41.44	22.54 ± 0.33	-19.12	p60	
56508.437	1.55	20.64 ± 0.10	-21.02	p48		56567.132	43.59	22.78 ± 0.36	-18.88	p60	
56508.476	1.57	20.54 ± 0.10	-21.12	p48		56569.256	45.11	22.37 ± 0.21	-19.29	p60	
56509.377	2.22	20.51 ± 0.10	-21.15	p48		56578.134	51.47	22.18 ± 0.31	-19.48	p60	
56509.434	2.26	20.49 ± 0.10	-21.17	p48		56591.393	60.96	22.45 ± 0.32	-19.21	p60	
56509.473	2.29	20.72 ± 0.11	-20.94	p48		56592.252	61.58	22.79 ± 0.32	-18.87	p60	
56510.375	2.93	20.45 ± 0.10	-21.21	p48		56685.141	128.11	22.74 ± 0.32	-18.92	p60	
56510.428	2.97	20.65 ± 0.10	-21.01	p48							
56510.467	3.00	20.73 ± 0.22	-20.93	p48							
56511.370	3.65	20.58 ± 0.10	-21.08	p48							
56511.433	3.69	20.55 ± 0.10	-21.11	p48							
56511.471	3.72	20.52 ± 0.10	-21.14	p48							
56512.374	4.37	20.48 ± 0.11	-21.18	p48							
56512.429	4.41	20.51 ± 0.10	-21.15	p48							
56512.467	4.43	20.58 ± 0.10	-21.08	p48							
56513.369	5.08	20.48 ± 0.10	-21.18	p48							
56513.428	5.12	20.66 ± 0.11	-21.00	p48							
56513.466	5.15	20.62 ± 0.11	-21.04	p48							
56514.367	5.79	20.60 ± 0.10	-21.06	p48							
56514.426	5.84	20.71 ± 0.11	-20.95	p48							
56514.462	5.86	20.50 ± 0.10	-21.16	p48							
56515.366	6.51	20.58 ± 0.11	-21.08	p48							
56515.423	6.55	20.66 ± 0.11	-21.00	p48							
56515.460	6.58	20.66 ± 0.11	-21.00	p48							
56516.362	7.22	20.48 ± 0.10	-21.18	p48							
56516.416	7.26	20.56 ± 0.10	-21.10	p48							
56516.454	7.29	20.57 ± 0.10	-21.09	p48							
56517.355	7.93	20.60 ± 0.10	-21.06	p48							
56517.410	7.97	20.45 ± 0.10	-21.21	p48							
56517.447	8.00	20.51 ± 0.10	-21.15	p48							
56518.348	8.65	20.54 ± 0.11	-21.12	p48							
56518.402	8.68	20.71 ± 0.11	-20.95	p48							
56518.439	8.71	20.52 ± 0.11	-21.14	p48							
56519.341	9.36	20.65 ± 0.11	-21.01	p48							
56519.412	9.41	20.63 ± 0.10	-21.03	p48							
56519.449	9.43	20.50 ± 0.11	-21.16	p48							
56520.351	10.08	20.83 ± 0.12	-20.83	p48							
56520.428	10.14	20.65 ± 0.11	-21.01	p48							
56520.465	10.16	20.61 ± 0.10	-21.05	p48							
56521.368	10.81	20.55 ± 0.12	-21.11	p48							

Table D66. PTF 13dcc photometry data.

MJD	Phase	m	Filter	Tel	MJD	Phase	m	Filter	Tel
56533.359	-55.21	19.68 ± 0.17	r	p48	56562.480	-34.86	19.81 ± 0.12	r	p48
56533.417	-55.17	19.73 ± 0.11	r	p48	56562.514	-34.83	19.72 ± 0.13	r	p48
56533.454	-55.14	19.76 ± 0.10	r	p48	56563.416	-34.20	19.74 ± 0.14	r	p48
56537.335	-52.43	19.81 ± 0.09	r	p60	56563.490	-34.15	19.75 ± 0.13	r	p48
56537.348	-52.42	19.66 ± 0.11	r	p48	56563.523	-34.13	19.91 ± 0.17	r	p48
56537.466	-52.34	19.86 ± 0.09	r	p48	56564.425	-33.50	19.80 ± 0.12	r	p48
56537.502	-52.31	19.70 ± 0.09	r	p48	56564.478	-33.46	19.95 ± 0.12	r	p48
56538.449	-51.65	19.80 ± 0.09	r	p48	56564.511	-33.44	19.87 ± 0.13	r	p48
56539.343	-51.03	19.66 ± 0.12	r	p48	56565.413	-32.81	19.78 ± 0.12	r	p48
56539.380	-51.00	19.79 ± 0.12	r	p48	56565.466	-32.77	19.88 ± 0.11	r	p48
56539.417	-50.97	19.80 ± 0.11	r	p48	56565.500	-32.75	19.86 ± 0.13	r	p48
56540.445	-50.26	19.98 ± 0.24	r	p48	56566.402	-32.11	19.82 ± 0.11	r	p48
56541.337	-49.63	19.73 ± 0.13	r	p48	56566.451	-32.08	19.79 ± 0.10	r	p48
56541.374	-49.61	19.55 ± 0.22	r	p48	56566.484	-32.06	19.85 ± 0.12	r	p48
56541.410	-49.58	19.38 ± 0.22	r	p48	56567.385	-31.43	19.77 ± 0.10	r	p48
56542.337	-48.93	19.77 ± 0.13	r	p48	56567.440	-31.39	19.76 ± 0.11	r	p48
56542.454	-48.85	19.69 ± 0.11	r	p48	56567.473	-31.37	19.86 ± 0.11	r	p48
56542.491	-48.83	19.71 ± 0.11	r	p48	56568.375	-30.74	19.93 ± 0.11	r	p48
56543.393	-48.20	19.84 ± 0.11	r	p48	56568.449	-30.68	19.83 ± 0.12	r	p48
56543.460	-48.15	19.91 ± 0.11	r	p48	56568.484	-30.66	19.83 ± 0.12	r	p48
56543.497	-48.12	19.74 ± 0.10	r	p48	56569.386	-30.03	19.77 ± 0.13	r	p48
56545.326	-46.84	19.55 ± 0.12	r	p48	56569.456	-29.98	19.84 ± 0.11	r	p48
56546.323	-46.15	19.76 ± 0.13	r	p48	56569.491	-29.96	19.76 ± 0.12	r	p48
56546.429	-46.07	19.86 ± 0.10	r	p48	56570.393	-29.33	19.83 ± 0.27	r	p48
56546.465	-46.05	19.86 ± 0.10	r	p48	56570.468	-29.27	19.39 ± 0.21	r	p48
56547.367	-45.42	19.79 ± 0.12	r	p48	56570.503	-29.25	19.94 ± 0.27	r	p48
56547.493	-45.33	19.80 ± 0.11	r	p48	56571.405	-28.62	20.01 ± 0.18	r	p48
56548.321	-44.75	19.82 ± 0.12	r	p48	56571.458	-28.58	19.72 ± 0.13	r	p48
56548.470	-44.65	19.76 ± 0.09	r	p48	56571.492	-28.56	20.08 ± 0.23	r	p48
56548.507	-44.62	19.71 ± 0.11	r	p48	56572.395	-27.93	19.83 ± 0.13	r	p48
56549.408	-43.99	19.88 ± 0.09	r	p48	56572.458	-27.88	19.85 ± 0.12	r	p48
56549.454	-43.96	19.82 ± 0.09	r	p48	56573.400	-27.22	19.83 ± 0.12	r	p48
56549.491	-43.93	19.76 ± 0.08	r	p48	56573.437	-27.20	19.98 ± 0.12	r	p48
56550.393	-43.30	19.77 ± 0.12	r	p48	56573.470	-27.17	19.99 ± 0.16	r	p48
56550.479	-43.24	19.83 ± 0.09	r	p48	56576.389	-25.13	19.83 ± 0.11	r	p48
56550.513	-43.22	19.81 ± 0.08	r	p48	56576.494	-25.06	19.90 ± 0.13	r	p48
56551.415	-42.59	19.78 ± 0.13	r	p48	56576.527	-25.04	19.78 ± 0.15	r	p48
56551.460	-42.56	19.86 ± 0.12	r	p48	56588.209	-16.87	19.76 ± 0.18	r	p48
56551.494	-42.53	19.83 ± 0.09	r	p48	56588.353	-16.77	20.05 ± 0.21	r	p48
56552.396	-41.90	19.76 ± 0.14	r	p48	56588.379	-16.75	19.76 ± 0.17	r	p48
56552.441	-41.87	19.88 ± 0.13	r	p48	56589.281	-16.12	19.62 ± 0.12	r	p48
56552.474	-41.85	19.80 ± 0.14	r	p48	56589.306	-16.11	19.93 ± 0.15	r	p48
56561.283	-35.69	19.81 ± 0.21	r	p48	56589.334	-16.09	19.76 ± 0.11	r	p48
56561.364	-35.64	19.87 ± 0.15	r	p48	56590.356	-15.37	19.74 ± 0.12	r	p48
56561.397	-35.61	19.85 ± 0.14	r	p48	56590.382	-15.35	19.72 ± 0.13	r	p48
56562.448	-34.88	19.90 ± 0.13	r	p48	56591.283	-14.73	19.75 ± 0.13	r	p48

Table D67. Continuation of Table D66.

MJD	Phase	<i>m</i>	Filter	Tel	MJD	Phase	<i>m</i>	Filter	Tel
56591.324	-14.70	19.64 ± 0.09	r	p48	56645.123	22.90	20.13 ± 0.19	g	p60
56591.349	-14.68	19.68 ± 0.09	r	p48	56647.133	24.31	19.75 ± 0.21	i	p60
56592.296	-14.02	19.61 ± 0.09	r	p48	56647.134	24.31	20.83 ± 0.29	r	p60
56592.389	-13.95	19.67 ± 0.11	r	p48	56647.138	24.31	20.46 ± 0.16	g	p60
56592.415	-13.93	19.71 ± 0.09	r	p48	56648.114	24.99	20.15 ± 0.15	i	p60
56596.187	-11.30	19.75 ± 0.16	r	p48	56648.116	25.00	20.02 ± 0.09	r	p60
56596.300	-11.22	19.66 ± 0.13	r	p48	56648.120	25.00	20.43 ± 0.10	g	p60
56596.326	-11.20	19.67 ± 0.12	r	p48	56655.200	29.95	19.99 ± 0.17	i	p60
56597.228	-10.57	19.54 ± 0.14	r	p48	56655.202	29.95	20.25 ± 0.16	r	p60
56597.312	-10.51	19.70 ± 0.13	r	p48	56655.207	29.95	20.85 ± 0.20	g	p60
56597.337	-10.49	19.55 ± 0.12	r	p48	56656.169	30.62	20.17 ± 0.15	i	p60
56598.240	-9.86	19.59 ± 0.15	r	p48	56656.171	30.63	20.25 ± 0.13	r	p60
56598.308	-9.82	19.62 ± 0.11	r	p48	56656.176	30.63	20.66 ± 0.14	g	p60
56598.334	-9.80	19.67 ± 0.12	r	p48	56657.131	31.30	20.14 ± 0.10	i	p60
56599.236	-9.17	19.58 ± 0.12	r	p48	56657.133	31.30	20.21 ± 0.08	r	p60
56599.277	-9.14	19.71 ± 0.11	r	p48	56657.138	31.30	20.62 ± 0.09	g	p60
56599.302	-9.12	19.61 ± 0.11	r	p48	56658.126	31.99	20.15 ± 0.10	i	p60
56600.245	-8.46	19.59 ± 0.10	r	p48	56658.129	31.99	20.25 ± 0.09	r	p60
56600.363	-8.38	19.54 ± 0.12	r	p48	56658.133	32.00	20.66 ± 0.10	g	p60
56600.388	-8.36	19.47 ± 0.21	r	p48	56659.202	32.74	20.21 ± 0.11	i	p60
56602.171	-7.12	19.55 ± 0.17	r	p48	56660.154	33.41	20.12 ± 0.11	i	p60
56602.228	-7.08	19.57 ± 0.20	r	p48	56660.156	33.41	20.29 ± 0.10	r	p60
56602.255	-7.06	19.54 ± 0.16	r	p48	56660.161	33.41	20.65 ± 0.10	g	p60
56603.168	-6.42	19.37 ± 0.14	r	p48	56662.209	34.85	20.38 ± 0.18	i	p60
56603.236	-6.37	19.44 ± 0.12	r	p48	56662.211	34.85	20.30 ± 0.13	r	p60
56603.295	-6.33	19.51 ± 0.11	r	p48	56662.216	34.85	20.82 ± 0.13	g	p60
56604.295	-5.63	19.60 ± 0.09	r	p48	56670.136	40.39	19.07 ± 0.34	i	p60
56604.412	-5.55	19.57 ± 0.09	r	p48	56671.191	41.12	20.41 ± 0.20	i	p60
56604.438	-5.53	19.58 ± 0.11	r	p48	56671.194	41.13	20.60 ± 0.19	r	p60
56605.339	-4.90	19.53 ± 0.11	r	p48	56672.195	41.83	20.88 ± 0.31	i	p60
56605.381	-4.87	19.62 ± 0.11	r	p48	56672.197	41.83	20.59 ± 0.26	r	p60
56605.407	-4.85	19.54 ± 0.10	r	p48	56673.185	42.52	20.60 ± 0.24	r	p60
56607.157	-3.63	19.82 ± 0.16	r	p48	56676.130	44.58	20.70 ± 0.13	i	p60
56607.295	-3.53	19.54 ± 0.12	r	p48	56676.132	44.58	21.33 ± 0.15	r	p60
56607.323	-3.51	19.47 ± 0.12	r	p48	56676.137	44.58	21.59 ± 0.14	g	p60
56608.225	-2.88	19.34 ± 0.11	r	p48	56683.250	49.55	21.13 ± 0.21	i	p60
56608.262	-2.86	19.60 ± 0.17	r	p48	56683.252	49.55	21.37 ± 0.24	r	p60
56608.292	-2.84	19.48 ± 0.15	r	p48	56685.127	50.86	21.41 ± 0.19	i	p60
56609.193	-2.21	19.64 ± 0.15	r	p48	56685.134	50.87	21.65 ± 0.25	r	p60
56609.341	-2.10	19.45 ± 0.12	r	p48	56697.144	59.26	21.43 ± 0.26	i	p60
56637.117	17.31	19.95 ± 0.18	i	p60	56697.146	59.26	21.51 ± 0.24	r	p60
56637.119	17.31	19.88 ± 0.18	r	p60	56701.150	62.06	22.29 ± 0.39	r	DCT
56637.123	17.31	20.14 ± 0.16	g	p60	56701.160	62.07	21.80 ± 0.32	i	DCT
56641.787	20.57	22.52 ± 0.41	UVW1	Swift/UVOT	56710.176	68.37	21.25 ± 0.26	i	p60
56643.118	21.50	22.48 ± 0.52	UVW1	Swift/UVOT	56908.400	206.91	23.45 ± 0.55	r	DCT
56645.119	22.90	19.93 ± 0.23	r	p60	57070.000	319.85	24.90 ± 0.10	r	HST

Table D68. PTF 13dcc rest-frame g photometry data.

MJD	Phase	m_g	M_g	Tel	Ref	MJD	Phase	m_g	M_g	Tel	Ref
56533.359	-55.21	20.18 ± 0.17	-21.70	p48		56562.480	-34.86	20.31 ± 0.12	-21.57	p48	
56533.417	-55.17	20.23 ± 0.11	-21.65	p48		56562.514	-34.83	20.21 ± 0.13	-21.66	p48	
56533.454	-55.14	20.26 ± 0.10	-21.62	p48		56563.416	-34.20	20.23 ± 0.14	-21.64	p48	
56537.335	-52.43	20.30 ± 0.09	-21.57	p60		56563.490	-34.15	20.25 ± 0.13	-21.63	p48	
56537.348	-52.42	20.16 ± 0.11	-21.72	p48		56563.523	-34.13	20.41 ± 0.17	-21.46	p48	
56537.466	-52.34	20.36 ± 0.09	-21.52	p48		56564.425	-33.50	20.30 ± 0.12	-21.58	p48	
56537.502	-52.31	20.19 ± 0.09	-21.68	p48		56564.478	-33.46	20.45 ± 0.12	-21.43	p48	
56538.449	-51.65	20.30 ± 0.09	-21.58	p48		56564.511	-33.44	20.37 ± 0.13	-21.50	p48	
56539.343	-51.03	20.16 ± 0.12	-21.72	p48		56565.413	-32.81	20.28 ± 0.12	-21.60	p48	
56539.380	-51.00	20.29 ± 0.12	-21.59	p48		56565.466	-32.77	20.38 ± 0.11	-21.49	p48	
56539.417	-50.97	20.30 ± 0.11	-21.58	p48		56565.500	-32.75	20.35 ± 0.13	-21.52	p48	
56540.445	-50.26	20.48 ± 0.24	-21.40	p48		56566.402	-32.11	20.31 ± 0.11	-21.56	p48	
56541.337	-49.63	20.23 ± 0.13	-21.65	p48		56566.451	-32.08	20.29 ± 0.10	-21.58	p48	
56541.374	-49.61	20.05 ± 0.22	-21.83	p48		56566.484	-32.06	20.34 ± 0.12	-21.53	p48	
56541.410	-49.58	19.88 ± 0.22	-22.00	p48		56567.385	-31.43	20.27 ± 0.10	-21.61	p48	
56542.337	-48.93	20.27 ± 0.13	-21.60	p48		56567.440	-31.39	20.26 ± 0.11	-21.62	p48	
56542.454	-48.85	20.19 ± 0.11	-21.69	p48		56567.473	-31.37	20.36 ± 0.11	-21.52	p48	
56542.491	-48.83	20.21 ± 0.11	-21.67	p48		56568.375	-30.74	20.42 ± 0.11	-21.45	p48	
56543.393	-48.20	20.33 ± 0.11	-21.54	p48		56568.449	-30.68	20.33 ± 0.12	-21.55	p48	
56543.460	-48.15	20.40 ± 0.11	-21.47	p48		56568.484	-30.66	20.33 ± 0.12	-21.55	p48	
56543.497	-48.12	20.23 ± 0.10	-21.64	p48		56569.386	-30.03	20.27 ± 0.13	-21.61	p48	
56545.326	-46.84	20.05 ± 0.12	-21.83	p48		56569.456	-29.98	20.34 ± 0.11	-21.53	p48	
56546.323	-46.15	20.26 ± 0.13	-21.62	p48		56569.491	-29.96	20.25 ± 0.12	-21.62	p48	
56546.429	-46.07	20.36 ± 0.10	-21.52	p48		56570.393	-29.33	20.32 ± 0.27	-21.55	p48	
56546.465	-46.05	20.36 ± 0.10	-21.52	p48		56570.468	-29.27	19.89 ± 0.21	-21.99	p48	
56547.367	-45.42	20.29 ± 0.12	-21.59	p48		56570.503	-29.25	20.44 ± 0.27	-21.43	p48	
56547.493	-45.33	20.29 ± 0.11	-21.58	p48		56571.405	-28.62	20.50 ± 0.18	-21.37	p48	
56548.321	-44.75	20.32 ± 0.12	-21.56	p48		56571.458	-28.58	20.22 ± 0.13	-21.66	p48	
56548.470	-44.65	20.26 ± 0.09	-21.61	p48		56571.492	-28.56	20.57 ± 0.23	-21.30	p48	
56548.507	-44.62	20.20 ± 0.11	-21.67	p48		56572.395	-27.93	20.33 ± 0.13	-21.55	p48	
56549.408	-43.99	20.37 ± 0.09	-21.50	p48		56572.458	-27.88	20.35 ± 0.12	-21.52	p48	
56549.454	-43.96	20.31 ± 0.09	-21.56	p48		56573.400	-27.22	20.32 ± 0.12	-21.55	p48	
56549.491	-43.93	20.26 ± 0.08	-21.62	p48		56573.437	-27.20	20.48 ± 0.12	-21.40	p48	
56550.393	-43.30	20.26 ± 0.12	-21.61	p48		56573.470	-27.17	20.49 ± 0.16	-21.38	p48	
56550.479	-43.24	20.33 ± 0.09	-21.55	p48		56576.389	-25.13	20.32 ± 0.11	-21.55	p48	
56550.513	-43.22	20.30 ± 0.08	-21.57	p48		56576.494	-25.06	20.40 ± 0.13	-21.48	p48	
56551.415	-42.59	20.27 ± 0.13	-21.60	p48		56576.527	-25.04	20.27 ± 0.15	-21.60	p48	
56551.460	-42.56	20.36 ± 0.12	-21.51	p48		56588.209	-16.87	20.25 ± 0.18	-21.63	p48	
56551.494	-42.53	20.32 ± 0.09	-21.55	p48		56588.353	-16.77	20.54 ± 0.21	-21.34	p48	
56552.396	-41.90	20.26 ± 0.14	-21.62	p48		56588.379	-16.75	20.25 ± 0.17	-21.63	p48	
56552.441	-41.87	20.38 ± 0.13	-21.50	p48		56589.281	-16.12	20.11 ± 0.12	-21.77	p48	
56552.474	-41.85	20.30 ± 0.14	-21.58	p48		56589.306	-16.11	20.42 ± 0.15	-21.45	p48	
56561.283	-35.69	20.31 ± 0.21	-21.57	p48		56589.334	-16.09	20.25 ± 0.11	-21.62	p48	
56561.364	-35.64	20.37 ± 0.15	-21.50	p48		56590.356	-15.37	20.23 ± 0.12	-21.65	p48	
56561.397	-35.61	20.35 ± 0.14	-21.52	p48		56590.382	-15.35	20.21 ± 0.13	-21.67	p48	
56562.448	-34.88	20.40 ± 0.13	-21.48	p48		56591.283	-14.73	20.24 ± 0.13	-21.63	p48	

Table D69. Continuation of Table D68.

MJD	Phase	m_g	M_g	Tel	Ref	MJD	Phase	m_g	M_g	Tel	Ref
56591.324	-14.70	20.13 ± 0.09	-21.74	p48		56657.133	31.30	20.67 ± 0.08	-21.20	p60	
56591.349	-14.68	20.17 ± 0.09	-21.71	p48		56658.129	31.99	20.71 ± 0.09	-21.16	p60	
56592.296	-14.02	20.09 ± 0.09	-21.78	p48		56660.156	33.41	20.75 ± 0.10	-21.12	p60	
56592.389	-13.95	20.16 ± 0.11	-21.72	p48		56662.211	34.85	20.77 ± 0.13	-21.11	p60	
56592.415	-13.93	20.19 ± 0.09	-21.68	p48		56671.194	41.13	21.06 ± 0.19	-20.82	p60	
56596.187	-11.30	20.23 ± 0.16	-21.64	p48		56672.197	41.83	21.05 ± 0.26	-20.82	p60	
56596.300	-11.22	20.14 ± 0.13	-21.73	p48		56673.185	42.52	21.06 ± 0.24	-20.82	p60	
56596.326	-11.20	20.15 ± 0.12	-21.72	p48		56676.132	44.58	21.79 ± 0.15	-20.09	p60	
56597.228	-10.57	20.02 ± 0.14	-21.85	p48		56683.252	49.55	21.83 ± 0.24	-20.05	p60	
56597.312	-10.51	20.19 ± 0.13	-21.69	p48		56685.134	50.87	22.11 ± 0.25	-19.76	p60	
56597.337	-10.49	20.04 ± 0.12	-21.84	p48		56697.146	59.26	21.97 ± 0.24	-19.91	p60	
56598.240	-9.86	20.07 ± 0.15	-21.81	p48		56701.150	62.06	22.75 ± 0.39	-19.13	DCT	
56598.308	-9.82	20.10 ± 0.11	-21.77	p48		56908.400	206.91	23.91 ± 0.55	-17.96	DCT	
56598.334	-9.80	20.16 ± 0.12	-21.72	p48		57070.000	319.85	25.37 ± 0.10	-16.51	HST	
56599.236	-9.17	20.06 ± 0.12	-21.82	p48							
56599.277	-9.14	20.19 ± 0.11	-21.69	p48							
56599.302	-9.12	20.09 ± 0.11	-21.78	p48							
56600.245	-8.46	20.07 ± 0.10	-21.81	p48							
56600.363	-8.38	20.02 ± 0.12	-21.86	p48							
56600.388	-8.36	19.95 ± 0.21	-21.93	p48							
56602.171	-7.12	20.03 ± 0.17	-21.84	p48							
56602.228	-7.08	20.06 ± 0.20	-21.82	p48							
56602.255	-7.06	20.02 ± 0.16	-21.86	p48							
56603.168	-6.42	19.85 ± 0.14	-22.02	p48							
56603.236	-6.37	19.92 ± 0.12	-21.95	p48							
56603.295	-6.33	19.99 ± 0.11	-21.89	p48							
56604.295	-5.63	20.08 ± 0.09	-21.79	p48							
56604.412	-5.55	20.05 ± 0.09	-21.82	p48							
56604.438	-5.53	20.06 ± 0.11	-21.81	p48							
56605.339	-4.90	20.02 ± 0.11	-21.86	p48							
56605.381	-4.87	20.10 ± 0.11	-21.77	p48							
56605.407	-4.85	20.02 ± 0.10	-21.85	p48							
56607.157	-3.63	20.30 ± 0.16	-21.57	p48							
56607.295	-3.53	20.02 ± 0.12	-21.85	p48							
56607.323	-3.51	19.95 ± 0.12	-21.93	p48							
56608.225	-2.88	19.82 ± 0.11	-22.05	p48							
56608.262	-2.86	20.08 ± 0.17	-21.80	p48							
56608.292	-2.84	19.96 ± 0.15	-21.92	p48							
56609.193	-2.21	20.12 ± 0.15	-21.76	p48							
56609.341	-2.10	19.93 ± 0.12	-21.94	p48							
56637.119	17.31	20.35 ± 0.18	-21.52	p60							
56645.119	22.90	20.39 ± 0.23	-21.48	p60							
56647.134	24.31	21.30 ± 0.29	-20.58	p60							
56648.116	25.00	20.48 ± 0.09	-21.39	p60							
56655.202	29.95	20.71 ± 0.16	-21.16	p60							
56656.171	30.63	20.71 ± 0.13	-21.16	p60							

Table D70. PTF 13ehe photometry data.

MJD	Phase	m	Filter	Tel	MJD	Phase	m	Filter	Tel
56621.333	-35.88	20.23 ± 0.19	r	p48	56702.250	24.35	19.80 ± 0.01	r	DCT
56626.540	-32.01	20.01 ± 0.13	r	p48	56702.500	24.54	19.75 ± 0.04	r	DCT
56639.194	-22.59	19.94 ± 0.19	r	p48	56702.500	24.54	20.25 ± 0.04	g	DCT
56639.249	-22.55	20.04 ± 0.25	r	p48	56702.500	24.54	19.65 ± 0.04	i	DCT
56640.177	-21.86	19.98 ± 0.24	r	p48	56703.151	25.02	19.76 ± 0.09	i	p60
56640.217	-21.83	19.86 ± 0.25	r	p48	56703.153	25.02	19.68 ± 0.09	r	p60
56640.302	-21.76	19.89 ± 0.26	r	p48	56703.157	25.02	20.34 ± 0.12	g	p60
56640.360	-21.72	19.92 ± 0.26	r	p48	56710.154	30.23	19.77 ± 0.09	i	p60
56640.404	-21.69	19.69 ± 0.23	r	p48	56710.156	30.23	19.76 ± 0.08	r	p60
56640.447	-21.66	19.54 ± 0.24	r	p48	56710.160	30.24	20.38 ± 0.09	g	p60
56640.490	-21.62	19.64 ± 0.21	r	p48	56910.490	179.36	22.09 ± 0.07	r	DCT
56640.531	-21.59	20.43 ± 0.33	r	p48	56910.500	179.37	22.05 ± 0.08	r	DCT
56647.487	-16.42	19.45 ± 0.16	r	p48	57070.000	298.10	23.98 ± 0.06	r	HST
56647.518	-16.39	19.60 ± 0.17	r	p48					
56647.551	-16.37	19.51 ± 0.17	r	p48					
56647.575	-16.35	19.64 ± 0.27	r	p48					
56648.357	-15.77	19.74 ± 0.10	r	p60					
56648.358	-15.77	19.83 ± 0.11	r	p60					
56662.178	-5.48	19.99 ± 0.20	i	p60					
56662.180	-5.48	19.62 ± 0.11	r	p60					
56662.184	-5.47	19.94 ± 0.10	g	p60					
56663.135	-4.77	19.73 ± 0.10	i	p60					
56667.465	-1.54	19.79 ± 0.15	r	p60					
56667.466	-1.54	19.96 ± 0.13	g	p60					
56671.174	1.22	19.68 ± 0.13	i	p60					
56672.168	1.96	19.81 ± 0.18	i	p60					
56673.090	2.64	19.78 ± 0.17	i	p60					
56673.094	2.65	20.04 ± 0.24	g	p60					
56675.188	4.20	19.58 ± 0.17	r	p48					
56675.236	4.24	19.48 ± 0.23	r	p48					
56675.299	4.29	19.24 ± 0.25	r	p48					
56675.342	4.32	19.34 ± 0.20	r	p48					
56675.395	4.36	19.41 ± 0.36	r	p48					
56675.436	4.39	19.75 ± 0.25	r	p48					
56675.478	4.42	19.69 ± 0.23	r	p48					
56675.523	4.45	19.49 ± 0.21	r	p48					
56680.095	7.86	19.70 ± 0.11	i	p60					
56680.096	7.86	19.66 ± 0.09	r	p60					
56680.101	7.86	19.99 ± 0.09	g	p60					
56685.098	11.58	19.62 ± 0.11	i	p60					
56685.100	11.58	19.69 ± 0.10	r	p60					
56685.104	11.59	20.03 ± 0.09	g	p60					
56697.114	20.53	19.69 ± 0.09	i	p60					
56697.115	20.53	19.70 ± 0.10	r	p60					
56697.120	20.53	20.23 ± 0.12	g	p60					
56702.250	24.35	20.79 ± 0.03	g	DCT					

Table D71. PTF 13ehe rest-frame g photometry data.

MJD	Phase	m_g	M_g	Telescope	Reference
56621.333	-35.88	20.62 ± 0.19	-20.67	p48	
56626.540	-32.01	20.40 ± 0.13	-20.90	p48	
56639.194	-22.59	20.33 ± 0.19	-20.97	p48	
56639.249	-22.55	20.43 ± 0.25	-20.86	p48	
56640.177	-21.86	20.37 ± 0.24	-20.93	p48	
56640.217	-21.83	20.25 ± 0.25	-21.04	p48	
56640.302	-21.76	20.28 ± 0.26	-21.01	p48	
56640.360	-21.72	20.31 ± 0.26	-20.98	p48	
56640.404	-21.69	20.08 ± 0.23	-21.22	p48	
56640.447	-21.66	19.93 ± 0.24	-21.37	p48	
56640.490	-21.62	20.03 ± 0.21	-21.26	p48	
56640.531	-21.59	20.82 ± 0.33	-20.47	p48	
56647.487	-16.42	19.85 ± 0.16	-21.45	p48	
56647.518	-16.39	20.00 ± 0.17	-21.29	p48	
56647.551	-16.37	19.91 ± 0.17	-21.38	p48	
56647.575	-16.35	20.04 ± 0.27	-21.26	p48	
56648.357	-15.77	20.13 ± 0.10	-21.16	p60	
56648.358	-15.77	20.23 ± 0.11	-21.06	p60	
56662.180	-5.48	20.03 ± 0.11	-21.26	p60	
56667.465	-1.54	20.20 ± 0.15	-21.09	p60	
56675.188	4.20	20.00 ± 0.17	-21.29	p48	
56675.236	4.24	19.90 ± 0.23	-21.39	p48	
56675.299	4.29	19.66 ± 0.25	-21.64	p48	
56675.342	4.32	19.76 ± 0.20	-21.53	p48	
56675.395	4.36	19.83 ± 0.36	-21.46	p48	
56675.436	4.39	20.17 ± 0.25	-21.12	p48	
56675.478	4.42	20.11 ± 0.23	-21.19	p48	
56675.523	4.45	19.92 ± 0.21	-21.38	p48	
56680.096	7.86	20.09 ± 0.09	-21.21	p60	
56685.100	11.58	20.12 ± 0.10	-21.17	p60	
56697.115	20.53	20.14 ± 0.10	-21.16	p60	
56702.250	24.35	20.24 ± 0.01	-21.05	DCT	
56702.500	24.54	20.19 ± 0.04	-21.10	DCT	
56703.153	25.02	20.12 ± 0.09	-21.18	p60	
56710.156	30.23	20.21 ± 0.08	-21.09	p60	
56910.490	179.36	22.58 ± 0.07	-18.72	DCT	
56910.500	179.37	22.54 ± 0.08	-18.76	DCT	
57070.000	298.10	24.44 ± 0.06	-16.86	HST	